A Computational Framework for Modelling Micro-scale Fluids in the Presence of Surface Tension

Ross J. D. Mackenzie

Infrastructure & Environment Research Division
School of Engineering

University of Glasgow

Submitted in fulfilment of the requirements for the Degree of Doctor of Philosophy

January 2015

Declaration

I declare that this thesis is a record of the original work carried out by myself under the supervision of Doctor Łukasz Kaczmarczyk and Professor Chris Pearce in the Infrastructure & Environment Division of the School of Engineering at the University of Glasgow, United Kingdom. This research was undertaken during the period of October 2010 to August 2014. The copyright of this thesis belongs to the author under the terms of the United Kingdom Copyright acts. Due acknowledgment must always be made of the use of any material contained in, or derived from this thesis. The thesis has not been presented elsewhere in consideration for a higher degree.

Ross Mackenzie

Abstract

Immunisation, pioneered by Edward Jenner (1749-1823), has saved millions of lives and has helped the human race survive several disease pandemics. Today, the immunisation industry conducts vast amounts of research, not only developing new vaccinations, but also new methods of diagnosis. Currently, blood samples are taken manually using a syringe, loaded into a centrifuge and spun for several hours to separate out the different parts of the blood sample. These parts can then be tested manually for a range of ailments. In some areas of the world, access to such a device is unavailable and even if it was, this can be a long, energy intensive and costly process. Hence, new faster methods involving the use of microchips and surface acoustic waves and are an inviting possibility.

Utilising the field of fluid dynamics, notably the work of Newton, Euler, Cauchy, Navier and Stokes, combined with modern computational methods allows for an engineering perspective to be taken on this problem. This thesis combines many novel contributions to create a computational modelling framework to model external excitation of axisymmetric micro-scale fluid droplets. In the present work fluid motion is governed by an axisymmetric form of the Navier-Stokes equations, with focus on incompressible Newtonian fluids, and this is presented in full. At the micro-scale, surface tension is the most dominant force, hence additional contributions are derived and included due to surface tension and contact line forces. Additionally, to reduce spurious oscillations within the pressure field, the pressure Laplacian stabilisation (PLS) technique is implemented. A derivation of the technique as well as an investigation into the effect of the stabilisation parameter is presented.

The kinematics of the system are of great importance. At the micro-scale, tracking of the surface of the fluid is highly desirable and most advantageous, and the choice of kinematic description must reflect this. Unlike more traditional computational methods adopting an Eulerian description or a Lagrangian description of the governing equations, the presented

computational framework makes use of the Arbitrary Lagrangian Eulerian (ALE) description. The ALE formulation avoids many of the drawbacks of traditional methods whilst allowing for accurate tracking of the fluid surface and minimising the requirement for frequent remeshing. Taking the current, deformed, configuration as the reference configuration in an Updated Lagrangian (UL) manner, combines into a kinematic description termed the Updated Arbitrary Lagrangian Eulerian (UALE) formulation. The physics underlying this formulation are presented in detail within this thesis.

Several problems, examining a range of droplet volume, contact angle and experimental configuration are presented to validate the computational framework against analytical solutions. Of the various problems examined, all show a very good correlation to analytical solutions. Differences, if any, are attributed to the density of the mesh, which is shown to alter the amplitude but not the frequency of oscillation, or over-simplification made in the analytical solutions.

Lastly, a new hypothesis is tested which until recently was extremely difficult to verify. The current hypothesis in the literature proposes that upon reaching the fluid-solid interface, surface acoustic waves propagate through the fluid causing motion. Conversely, the new hypothesis proposes that upon reaching the fluid-solid interface, surface acoustic waves propagate capillary waves up the surface of the droplet, changing the apparent wetting angle and inducing motion. This is implemented by changing the contact angle in time to simulate the action of surface acoustic waves and the resulting analysis recorded the occurrence of jetting thereby confirming the hypothesis. Further testing can be conducted and this technology utilised in the development of new disease diagnosis devices.

The computational framework has been very successful in modelling a range of micro-scale problems. Further development of this framework will allow for a greater understanding of the effect of surface acoustic waves on a fluid droplet. In turn, this will allow for the improved design of surface acoustic wave devices.

Acknowledgments

Firstly I should thank my supervisors Doctor Łukasz Kaczmarczyk and Professor Chris Pearce, who have been a tremendous help throughout my PhD. Without Łukasz's help with the computational aspect of this PhD, I would have struggled a great deal, and his insight into the underlying physics has been very valuable indeed. I thank him for being patient with me and believing that I could achieve our goals. Chris's ability to see a problem from a different angle has been highly advantageous throughout this PhD and his help and encouragement is much appreciated. I should also thank Doctor Julien Reboud and Professor Jon Cooper who provided laboratory data for the surface acoustic wave problems and Quentin Bausiere who assisted with the capillary problems.

Secondly, I wish to thank my family for all their help and support over the course of my PhD, especially my Mum and Dad and my sisters. Whilst my PhD may seem a world away from their working lives, they have encouraged me to always perform to my maximum and have supported me through the times when things were not going so smoothly.

Thirdly, I wish to thank my friends Nelly and Claire, Russell and Adriana, Euan, Gary and Alan M. who have provided much required escapism. A special mention to Graeme, Alan K., Caroline, Dimitrios X., Ignatios, Michael, Dimitrios K., Xue, Ali, Euan M., Julien, James, Doug, Elisa, Marnie, Melanie and Sarah. We have all helped each other along the way and I am sure I would not have enjoyed my PhD nearly as much if it was not for all of you.

Last, but my no means least, I wish to thank my fiancée Jay. Whilst I did not meet her until the end of my first year, she has provided masses of encouragement and support to help me reach this point. Her never-ending enthusiasm in my research has helped me overcome those days when nothing seems to be going right, and she has provided me with many fun times to distract me when in need. You make me happier every single day and I could not have done this without you Jay, thank you.

Contents

List of Figures

List of Tables

List of Algorithms

List of Symbols

$\bar{R}$	dimensionless radius
$\bar{Z}$	dimensionless height
Δh	height above a datum
ΔP	hydrostatic pressure
Δp	interfacial pressure difference
Δt	time step
Δt^*	time intervals at which data was recorded
$\delta\bar{\mathbf{n}}$	the unknown component of the normal
$\delta\hat{\mathbf{e}}$	unknown component of the deviatoric stress tensor
$\delta\mathbf{e}$	iterative change of the deviatoric stress tensor
$\mathbb{T}$	deviatoric stress tensor
$\bar{\mathbf{n}}$	the known component of the normal
$\hat{\mathbf{v}}$	vector of nodal mesh velocity
$\mathbf{a}$	vector of nodal acceleration
$\mathbf{a}_{n+1}$	current nodal acceleration
$\mathbf{b}$	body force
$\mathbf{c}$	convective velocity
$\mathbf{e}_i$	known component of the deviatoric stress tensor
$\mathbf{F}^{\mathbf{CL}}$	contact line force vector

$\mathbf{F}^{\mathbf{ST}}$ surface tension force vector

$\mathbf{f}_{...}$ force vector

$\mathbf{F}_{\mathbf{pen}}$ penatly force matrix

$\mathbf{f}$ body force

$\mathbf{J}$ the Jacobian

$\mathbf{K}^{\mathbf{CL}}$ contact line stiffness matrix

$\mathbf{K}^{\mathbf{ST}}$ surface tension stiffness matrix

$\mathbf{K}_{...}$ stiffness matrix

$\mathbf{K}_{\mathbf{pen}}$ penatly stiffness matrix

$\mathbf{M}_{...}$ mass matrix

$\mathbf{m}$ binormal of the curve C

$\mathbf{N}_{\mathbf{br}}$ radial component of the boundary edge shape functions

$\mathbf{N}_{\mathbf{b}}$ boundary edge shape functions

$\mathbf{N}_{\mathbf{r}}$ radial component of the element shape functions

$\mathbf{N}$ element shape functions

$\mathbf{n}$ unit normal

$\mathbf{N}_{12}$ shape function matrix for the surface of revolution generated by line 1-2

$\mathbf{N}_{1}$ shape function matrix for the contact line generated by the revolution of node 1

$\mathbf{p}$ momentum

$\mathbf{R}$ rotation matrix

$\mathbf{s}$ physical fluid property

$\mathbf{t}$ traction unit vector

$\mathbf{v}$ vector of nodal fluid velocity

$\mathbf{v}_{n+1}$ current nodal velocity

$\mathbf{v}_n$ previous nodal velocity

$\mathbf{w_p}$ weighting function in the pressure field

$\mathbf{w_v}$ weighting function in the velocity field

$\mathbf{w}$ weighting function

$\mathbf{X}$ material domain

$\mathbf{x}$ spatial domain

$\mathbf{x}_{n+1}$ current nodal displacement

$\mathbf{x}_n$ previous nodal displacement

$\partial u/\partial y$ local shear velocity

$\underline{\delta p}$ unknown vector of fluid pressure

$\underline{\delta \hat{\mathbf{v}}}$ unknown vector of mesh velocity

$\underline{\delta \mathbf{v}}$ unknown vector of fluid velocity

A amplitude of oscillation

A_{mt} component of the metric tensor

A_s surface area of the droplet subject to surface tension

B_{mt} component of the metric tensor

C boundary curve of the surface Γ

D duration of excitation

da elemental area

E dimensionless volume

E_k kinetic energy

E_p potential energy

$f(x,y,z,t)$ a property of the fluid

g gravitational acceleration

H mean curvature

h measure of mesh size

I the identity matrix

L length of linear element

l capillary length

p nodal fluid pressure

$P(w)$ operator applied to the test function

p_{ext} external pressure

p_{int} internal pressure

P_n n^{th} order Legendre polynomial

p_r, p_ϕ, p_z components of the pressure field in cylindrical coordinates

p_x, p_y, p_z components of the pressure field in cartesian coordinates

Q sources and sinks in the control volume

R unperturbed spherical radius

r radial coordinate

R_1, R_2 principal radii of curvature

r_k, z_k coordinates of node k

r_{n+1} radius at current time step

r_n radius at previous time step

T period of oscillation

t time

V volume

v_r, v_ϕ, v_z components of the velocity field in cylindrical coordinates

v_x, v_y, v_z components of the velocity field in cartesian coordinates

Greek Symbols

α_0 initial contact angle

α_e contact angle

$\bar{\tau}$ stabilisation parameter (intrinsic time)

β a scalar on the stabilisation parameter

χ mesh domain

$\Delta\alpha$ time dependent contact angle

$\delta\Omega$ bounding surfaces of the control volume

Γ domain surface

γ surface tension parameter

γ_{LG} liquid-gas interfacial surface tension

γ_{SG} solid-gas interfacial surface tension

γ_{SL} solid-liquid interfacial surface tension

$\gamma_{surfactant}$ lower value of surface tension due to interaction with a surfactant

κ user defined penalty factor

λ second viscosity coefficient

σ Cauchy stress tensor

μ fluid shear viscosity

μ_{mesh} mesh viscosity

∇_s surface gradient operator

Ω control volume

ω angular frequency

ϕ motion applied to a mesh

ρ fluid density

τ	fluid shear stress
θ	angular coordinate
θ_A	advancing contact angle
θ_R	receding contact angle

Chapter 1

Introduction

1.1 Aims and Scope of the Thesis

The phenomenon of surface tension surrounds us in our everyday lives. Caused by molecular cohesion, surface tension allows a liquid to resist external forces and governs the shape, size and behaviour of liquid droplets. It is present anywhere there is interaction between two fluids or a fluid and a solid and can be seen in many every day situations including insects resting on a water surface, in soap bubbles and the 'legs' of whisky. Additionally, surface tension is present in the cells in our bodies, and has a role in many of the biological processes that keep us alive. At micro-scales, surface tension is the most dominant force and therefore extremely important.

This thesis aims to develop a computational framework that can accurately predict surface tension forces and consequently the response of micro-scale fluid droplets when subject to gravity forces and surface acoustic waves (SAW). To be able to predict the response of micro-scale droplets subject to external excitation is of great benefit in our ultimate goal of providing modelling capability for the improved design of surface acoustic wave devices. Such devices are part of the growing sector of lab-on-a-chip technologies, refer to [12, 41, 59, 43, 22, 54] and the references therein.

Prototypes of SAW devices are expensive and small-scale manufacture is a long and complex

Figure 1.1: SAW device developed by the Bioelectronics Group

process. It is hoped that a computational framework that can predict the response of micro-scale fluid droplets will be not just of financial benefit but also of benefit in the understanding of fluid motion induced by external excitation. The devices currently under development by the Bioelectronics Group at the University of Glasgow, Figure 1.1, use SAW to spin micro-scale blood samples on disposable chips, centrifuging the components into separate parts. These parts can then be tested for various diseases with a much faster diagnosis time than current NHS techniques: 30 minutes versus 5-10 days[1]. Traditional centrifuges encounter difficulties when the number of cells is low, and damage to the cells can be caused. Much like using ultrasound to obtain an image of a fetus in the womb, SAW will not damage biological cells; it only acts to manipulate the position of the cells. Additionally, the SAW device is compact enough to be a desk-top item, something current centrifuges are not; current centrifuges are large, bulky machines which are energy hungry and very noisy. It is envisioned that in the near future, these devices will be at the forefront of General Practice diagnosis, with rapid diagnosis resulting in prompt treatment and reduced transmission to others. Undoubtably, this will reduce the duration of illness and save lives in the case of potentially fatal diseases. A further advantage is the ability to power the SAW device using a mobile phone or a small solar cell. The portability and ease of powering the device make it highly advantageous in disaster areas or Third World rural communities where the nearest sterile laboratory could be many hours travel away.

[1]Whilst times vary depending on the test undertaken and for each health board, 5-10 days is the time quoted in most instances by the NHS.

The computational framework discussed in this thesis brings together the work of many authors whilst aiming to maintain a solution scheme that is fast, efficient and reliable. By far the largest component of the framework is the solution of the Navier-Stokes equations for incompressible Newtonian fluids in an axisymmetric system. To eradicate oscillations within the pressure field, pressure stabilisation terms have been included in the framework. However, the most important component is that describing surface tension, and additional contributions are assembled into the force vector and stiffness matrix to account for this. Without an accurate depiction of surface tension at this scale, results cannot be trusted to be completely accurate. The finite element governing equations are written using an Updated Arbitrary Lagrangian Eulerian formulation and solved using an implicit trapezoidal integration scheme. Blood is a non-Newtonian fluid and whilst the framework is built around the analysis of Newtonian fluids, the framework has been developed in a way that extension to include non-Newtonian fluids is very straight-forward.

The quality of the finite element mesh is of great importance in the solution and, as such, mesh improvement in the form of Laplacian smoothing is used to minimise problems with the mesh.

In the following chapters, the physics behind the computational model will be covered in detail, followed by comprehensive validation of the model. Where appropriate, comparison to analytical solutions will be made, accompanied by discussion of the results with regard to the effectiveness and accuracy of the framework.

The computational framework is available to download, in various forms, from http://userweb.eng.gla.ac.uk/0404207m/index.html.

1.2 Outline of the Thesis

This thesis is split into numerous chapters that are independent with minimal cross referencing. However, Chapters 7 and 8 employ the ideas presented in the previous chapters to first validate and then experiment with the computational framework. The focus of each chapter is as follows:

CHAPTER 2 - A literature review is presented including a brief timeline of fluid mechanics from ancient times to the modern day. Computational discretisation methodologies are discussed along with the selected method used in this work. A review of previous surface tension and surface acoustic wave analyses will also be presented, along with their merits and faults.

CHAPTER 3 - A detailed derivation of the Navier-Stokes equations for incompressible Newtonian fluids is given alongside discussion of the assumptions made in terms of fluid stress and fluid pressure. A Galerkin weighted residual *weak form* of the Navier-Stokes equations for incompressible Newtonian fluids is also presented.

CHAPTER 4 - The computational solution strategy is outlined, comprising a kinematic description and a time integration scheme. Applying this strategy to the Galerkin weighted residual *weak form* of the Navier-Stokes equations for incompressible Newtonian fluids developed in the previous chapter produces a space and time discretised *weak form*. The method of extending the framework from 2D to axisymmetry is also detailed. The implementation of mesh optimisation using a Laplacian smoothing algorithm is outlined. The advantages and disadvantages of this implementation are noted.

CHAPTER 5 - The phenomenon of surface tension is discussed with reference to the Young-Laplace equation and the Young equation, followed by the derivation of the surface tension contributions to the force vector and stiffness matrix. The method of identifying mesh edges on the surface of the fluid is also discussed.

CHAPTER 6 - The various methods of stabilisation of the pressure field are discussed and the pressure stabilisation terms adopted in this work are derived in part. A comprehensive study of the effect of the pressure stabilisation parameter is undertaken with reference to its impact on, in the main, the pressure field and the droplet motion.

CHAPTER 7 - Bringing all previous chapters together, this chapter outlines the validation and verification of the computational framework. Several analyses are undertaken and, where appropriate, comparison is made to analytical solutions with any differences noted and justification given. Analyses examine quasi-static and dynamic situations as well as some more complex problems including zero-gravity environments, surfactants and capillary problems.

CHAPTER 8 - Further numerical testing is presented whereby droplets are subject to external excitation. The modelling procedure is outlined and comparison is made to laboratory testing. The effectiveness of the form of application of external excitation

is discussed. A new hypothesis on the action of surface acoustic waves on droplets is presented and testing undertaken. The validity of the hypothesis is discussed.

CHAPTER 9 - Concluding remarks on the effectiveness of the computational framework are presented alongside possible extensions to this work.

1.3 Notation

Within this thesis, matrix-vector notation will be used; all matrices and vectors are distinguished by bold-faced characters. A list of symbols is included for any symbol referred to on more than one occasion. In addition, Voigt notation is used in the derivation of the symmetric part of the deviatoric stress tensor.

Chapter 2

Literature Review

The objective of this chapter is to briefly detail the history of fluid mechanics through the ages, particularly the more recent development of computational schemes adopted to solve more complex fluid dynamics problems. Previous solution schemes examining problems including surface tension and surface acoustic waves are also reviewed.

2.1 The History of Fluid Mechanics

2.1.1 Ancient Times

Humans have had an understanding of fluids for millennia. Ancient civilizations used boats, irrigation schemes, water supply schemes and drainages schemes emphasizing that water was not only an important commodity but the flow of fluids was understood to a good extent. Additionally, the development of airborne weapons, such as arrows and spears, designed to travel through the air at speed and with accuracy demonstrates, to some extent, an understanding of fluid-structure interaction (FSI). The first dateable published work on fluids was that by Archimedes of Syracuse, entitled, *On Floating Bodies* [13]. Comprising two volumes and published in 250BC, the work examined the positions assumed by solid objects floating in liquid. The two most celebrated results of this work are the Archimedes' Principle:

> Any object, wholly or partially immersed in a fluid, is buoyed up by a force equal to the weight of the fluid displaced by the object
> - Archimedes of Syracuse

and the Principle of Flotation:

> Any floating object displaces its own weight in fluid
> - Archimedes of Syracuse

2.1.2 15th Century - 20th Century

Leonardo da Vinci (1452-1519) made several observations and experiments on fluid mechanics. A two volume translation of his works [42], contains details of an initial equation for the conservation of mass for one-dimensional incompressible flows, as well as the first published use of the word 'eddy' to describe fluid flow.

The inventor of the barometer, Torricelli (1608-1647) also studied wind movements and the speed of fluid flow. By using mercury in place of water (mercury is much denser than water), he discovered that, due to atmospheric pressure, the height of a fluid in a vertical tube sealed at one end and placed into a bath of mercury will fluctuate. This system became known as a Torricellian tube, with the vacuum created at the top of the sealed tube known as a Torricellian vacuum.

Pascal's (1623-1662) work concentrated on the principles of hydraulic fluids, his most important discoveries being the hydraulic press and, in terms of medicine, the syringe. Pascal proved that hydrostatic pressure is caused by the elevation of the fluid and not the weight of the fluid. His work also became intwined with that of Torricelli, as he initially discounted the idea of a vacuum present in a Torricellian tube. However, after various experiments, he gave a detailed account of why there was indeed a vacuum present in the tube [49]. Additionally, Pascal formulated the principle of transmission of fluid pressure, or Pascal's Law, Equation 2.1, which states that the pressure ratio in a confined incompressible fluid will remain constant if the applied pressure is transmitted equally in all directions within the fluid.

$$\Delta P = \rho g \Delta h \tag{2.1}$$

In the above equation, ΔP is the hydrostatic pressure relative to atmospheric pressure, ρ is the fluid density, g is gravitational acceleration and Δh is the height of fluid above a datum. An extremely important principle, Pascal's Law is used in a range of applications including modern vehicle braking systems.

Sir Isaac Newton (1642-1727), one of the most influential scientists of all time for his laws of motion, gravitational forces and calculus, also examined fluid viscosity. Newton derived, in differential form, a linear relation between shear strain rate and shear stress for fluids:

$$\tau = \mu \frac{\partial u}{\partial y} \tag{2.2}$$

where τ is the shear stress in the fluid, μ is the shear viscosity of the fluid (a scalar constant of proportionality), and $\partial u/\partial y$ is the local shear velocity, assuming the flow is moving along parallel lines and the y axis is perpendicular to the direction of flow and points in the direction of maximum shear velocity. In other words, the tensors describing viscous stresses and strain rate are related by a viscosity tensor that is constant and is independent of flow velocity and stress state. A fluid that holds to this relationship is said to be a Newtonian fluid. For non-Newtonian fluids, the viscosity is dependent on the shear rate or shear rate history; the relationship between the shear stress and shear strain rate is non-linear and may even be dependent on time, such as shear-thinning fluids and shear-thickening fluids. Several everyday liquids, such as custard, ketchup and blood, are non-Newtonian fluids.

Daniel Bernoulli (1700-1782) continued Newton's work on inviscid flows (where viscous forces are much smaller compared to inertial forces), deriving the Bernoulli Principle: an increase in the speed of an inviscid flow occurs alongside a decrease in fluid pressure or a decrease in potential energy. Euler (1707-1783), close friends with Bernoulli, took this work further, deriving the Euler equations for inviscid fluids:

$$\rho \left(\frac{\partial}{\partial t} + \mathbf{v} \cdot \nabla \right) \mathbf{v} + \nabla p = 0 \tag{2.3}$$

This is a variant of Newton's Second Law, ($\mathbf{F} = m\mathbf{a}$) where t is time, $\mathbf{v}$ is the vector of fluid velocity, ρ is the fluid density, and p is the fluid pressure.

Further work on inviscid flows was undertaken by d'Alembert (1717-1783), such as the d'Alembert Paradox; Lagrange (1736-1813), who wrote several papers on the pressure exerted by fluids in motion (as well as deriving the basis of the law of virtual work); Laplace (1749-1827), who applied calculus to the potential function (developed by Lagrange, Bernoulli and others), developing the Laplacian operator and thus continued the work of Euler; and finally Poisson (1781-1840), who continued the work of Laplace and also derived the Navier-Stokes equations independently of Navier.

Young (1773-1829) made several notable contributions to the scientific community, most notably in the fields of solid mechanics, vision, light and Egyptology. In terms of engineering, his most well-known contribution was to elasticity, and he derived the Young's modulus. Young also observed the relationship between the solid, liquid and gas phases and the associated contact angle, developing the theory of capillary phenomena on the principle of surface tension [70]. The relationship between the three phases and the contact angle is known as Young's equation, given in Equation 2.4. Laplace discovered the importance of meniscus radii in capillary action. Combined with the theory developed by Young and written in a mathematical context by Laplace, the Young-Laplace equation, Equation 2.5, describes the capillary pressure difference across an interface between two static fluids due to surface tension. The Young-Laplace equation is occasionally called the Young-Laplace-Gauss equation because it was Gauss (1777-1855) whom combined the work of Young and Laplace in 1830. Using the principle of virtual work devised by Johann Bernoulli (1667-1748), Gauss was able to derive the differential equation and boundary conditions.

$$\gamma_{\mathrm{SG}} = \gamma_{\mathrm{SL}} + \gamma_{\mathrm{LG}} \cos \alpha_e \tag{2.4}$$

$$\Delta p = -\gamma \nabla \cdot \mathbf{n} = 2\gamma H = \gamma \left(\frac{1}{R_1} + \frac{1}{R_2} \right) \tag{2.5}$$

The mathematician Cauchy (1789-1857), a pioneer of mathematical analysis, proposed a partial differential equation to describe non-relativistic momentum transport in a continuum. Named after him, the Cauchy momentum equation, Equation 2.6, considers the velocity vector field $\mathbf{v}$, the density of the continuum ρ, the stress tensor σ and body force $\mathbf{f}$. This is also a variant of Newton's Second Law.

$$\rho \frac{D\mathbf{v}}{Dt} = \nabla \cdot \sigma + \mathbf{f} \tag{2.6}$$

In terms of viscous flows, work was undertaken by Poiseuille (1797-1869) and Hagen (1797-1884), who are jointly recognised for developing a physical law relating to the pressure drop in fluid flowing through a long cylindrical pipe, such as arteries and veins. The GCS (gram-centimetre-second) unit of measurement of viscosity (Poise) is named after Poiseuille.

In terms of fluid flow, the biggest contributions arise from Navier (1785-1836) and Stokes (1819-1903). The Navier-Stokes equations arise from the work of their predecessors, especially Newton, Laplace, Euler, Lagrange, Cauchy and Poisson. Starting with Newton's Second Law ($\mathbf{F} = m\mathbf{a}$) and applying to fluid motion, alongside a pressure term and a viscous stress term, the Navier-Stokes equations are used in a range of applications. Navier was the

first to attempt to add a friction term to Euler's equation in 1822. In 1845 Stokes furthered this by using the absolute viscosity. The equations can, when accompanied by a conservation of mass equation and boundary conditions, describe both laminar and turbulent flows accurately. Chapter 3 derives the Navier-Stokes equations in full, alongside a narrative of the assumptions and simplifications made.

Reynolds (1842-1912) is best known for his work on the transition between laminar and turbulent flows and hence the Reynolds number. The Reynolds number is the ratio of inertial forces to viscous forces. As such, a viscous fluid has a low Reynolds number and an inviscid fluid has a high Reynolds number. He also developed Reynolds-averaging, a method of expressing quantities as the sum of the mean and fluctuating components, and this can be incorporated with the Navier-Stokes equations resulting in the so called Reynolds-averaged Navier-Stokes equations.

Strutt, the 3rd Baron Rayleigh (1842-1919) predicted the existence of a surface acoustic wave on the surface of solids. Named Rayleigh waves in his honour, they include both longitudinal and transverse waves that exponentially decrease in amplitude with distance from the surface. Surface particles are forced to move in ellipses, in planes normal to the surface and parallel to the direction of propagation, with one such example being ocean waves. Rayleigh also extended the idea of group velocity first proposed by Hamilton (1805-1865), and such a phenomena can be seen in the ripple of waves propagating from an object dropped in water, Figure 2.1.

Prandtl (1875-1953) worked on the phenomenon of boundary layers. He noticed that fluid flows with small viscosity can be separated into a thin viscous or boundary layer, and an almost inviscid outer layer. The boundary layer will occur near solid surfaces and interfaces. This phenomenon has been an important tool in the development of modern computational fluid dynamics (CFD).

Figure 2.1: Ripples in a pond [5]

2.2 Computational Fluid Dynamics

Since the advent of the computer age, computers are increasingly being used to solve fluid dynamics problems. At the root of all computational fluid dynamics (CFD) problems is the Navier-Stokes equations, which, with application of the Euler equation (Equation 2.3), can be simplified in terms of viscous effects. The Navier-Stokes equations can also be linearised for small perturbation problems. The method of solving a CFD problem involves discretising the volume of fluid using a mesh, defining the geometric boundaries of the domain, defining the governing physics (the Navier-Stokes equations), defining the initial and boundary conditions, solving the system of partial differential equations (PDEs) using an iterative solution scheme, and examining the results using a post-processing visualisation tool. There are a number of discretisation methods that can be utilised, such as the finite element method (FEM), the finite volume method (FVM), the finite difference method (FDM), the spectral element method (SEM), and the boundary element method (BEM). Each discretisation method has its advantages and disadvantages.

In the context of this work, the finite element method (FEM) is the chosen discretisation method for various reasons. Not only does this method offer one of the lowest storage requirements, it is also well-suited to complex geometries like those presented in this thesis. Additionally, use of the FEM will allow for this work to be incorporated into the work of

others in our research group with much more ease. It is envisioned that the parts of the computational framework relating to surface tension, for example, will be modular and therefore easily included in other frameworks, for example examining water percolation through porous media.

Initially developed for use in structural mechanics, the FEM can be used in a wide range of problems including CFD. Generally applying to displacement-based formulations, the FEM can take on many other forms including force-based, equilibrium and mixed methods, however, displacement-based formulations are the most common [17]. The domain of interest is subdivided into a number of simplified discrete components, each with their own set of equations relating back to the entire system. These equations are solved in an iterative scheme and then summed together to give the solution for the whole domain. In terms of advantages, the FEM is able to capture complex geometries, can handle the union of different material properties, and can capture local effects. Additionally, matrices computed in the FEM tend to be banded meaning low storage requirements and low computational time. Whilst much more stable than other methods, the FEM can be more computationally expensive, for example, in comparison to the FVM.

Discussed in more detail in Chapter 4, the choice of kinematic description is very important. Traditionally in fluid mechanics Eulerian formulations have been used to describe the system of equations. Whilst well suited to problems involving large deformation because the elements do not deform, this causes problems when the desire is to accurately track the surface of the fluid. As such, more recent computational models [28, 47, 57, 58, 27] have examined the options for alternative kinematic formulations.

2.3 The Particle Finite Element Method

The particle finite element method (PFEM), developed by Oñate et al. [47], is a computational framework designed to assess fluid-structure interaction (FSI). The PFEM is based on the use of an updated Lagrangian formulation of the governing equations to model the motion of nodes in the fluid and solid domains. As such, nodes are seen as particles and are allowed to move freely. Separation of nodes from the main domain is allowed with the aim of modelling individual fluid droplets. The nodes are connected using a mesh and the integral form of the governing equations are solved in the standard FEM manner. The finite calculus (FIC) method is included in the framework to deal with pressure stabilisation issues

from the incompressibility condition. In terms of applications, the PFEM is used for a range of problems including wave splashing and free surface motion.

The use of a Lagrangian formulation gives excellent results in terms of tracking individual particles, especially in situations where the fluid domain will separate due to violent interaction with a solid. However, as a consequence of using a Lagrangian formulation, elements can become highly distorted when assessing flows with varying velocities within the fluid domain. Therefore large scale remeshing is required and this can become computationally expensive when assessing particularly complex flow problems and interactions. Indeed, Oñate et al. even suggest creating an entirely new mesh after a prescribed number of time steps to combat these distortions. This leads to the possibility of obtaining highly undesirable mesh-dependent results.

2.4 Micro-Scale Analyses of Surface Tension

For small-scale analyses, Saksono and Perić, [57, 58, 51, 56] use a Lagrangian formulation based upon an axisymmetric system for assessing the equilibrium geometries of various droplets and liquid bridges. The governing equations of the system are formulated as a function of nodal positions rather than nodal velocities. Additional contributions to the stiffness matrix and force vector arise from the surface tension and contact line forces, derived directly from the *weak form* of the Young-Laplace equation. At the scale of interest, surface tension is the most dominant force, and is instrumental in the shape, size and behaviour of droplets. Therefore the additional contributions are required to ensure the framework is accurate. Whilst the framework is highly versatile and produces excellent results with regard to the level of correlation to analytical results, the initial FE mesh in each case is carefully selected to minimise the requirement for remeshing. In the examples examined, the motion of the mesh is known from analytical solutions and the mesh is selected with this motion in mind. Figure 2.2 demonstrates the finite element (FE) mesh used by Saksono and Perić in a typical problem; the mesh, constructed of quadrilateral elements, is non-uniform. The need to select an initial mesh is a major drawback when assessing problems where the deformation of the domain is unknown *a priori*, not to mention the time required to create a mesh that will produce the desired results.

Dettmer collaborated with Saksono and Perić to develop a numerical model for examining incompressible Newtonian flows on moving domains in the presence of surface tension [28].

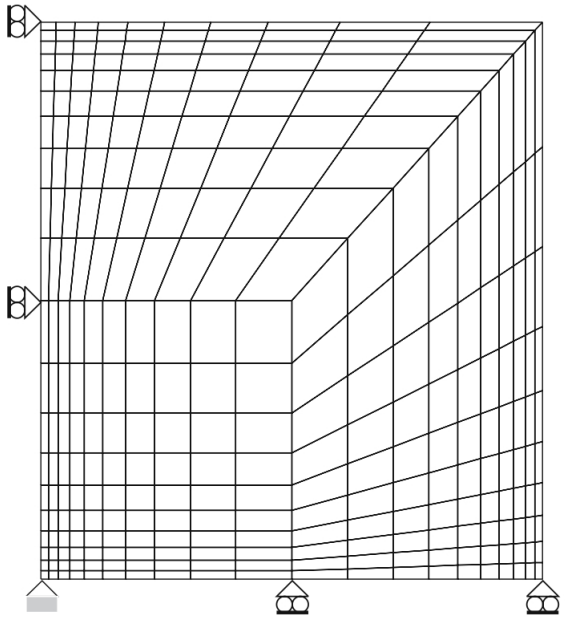

Figure 2.2: Typical finite element mesh used by Saksono and Perić [57]

The computational model uses an arbitrary Lagrangian Eulerian (ALE) scheme to solve the Galerkin/Least-squares stabilised equal order mixed velocity-pressure formulation of the incompressible Navier-Stokes equations. Surface tension is included in the system as derived by Saksono and Perić [51, 56] and described previously. The solution scheme is shown to be robust and accurate and computationally efficient, and does not require frequent remeshing, with analyses comparing equilibrium geometries of sessile droplets and liquid bridges to analytical solutions. However, for larger scale problems, there is an issue with convergence.

Dettmer and Perić take this work further by developing a partitioned solution scheme relying on the Newton-Raphson procedure to solve the sets of coupled equations [27]. This numerical model is used to solve the problems encountered previously, as well as dam break, sloshing, and capillary problems. The solutions are comparable to analytical solutions were applicable and the solution scheme is robust and accurate, however, it is noted that computational implementation is difficult.

Others have attempted computational modelling of surface tension, such as Brackbill et al. [23], Thürey et al. [65] and LeVeque and Li [39], amongst others. Refer to these papers and the references therein.

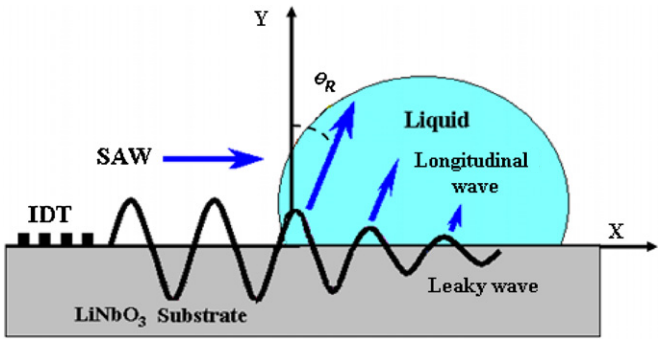

Figure 2.3: Typical set-up for SAW propagation into a liquid droplet [12]

2.4.1 Surface Acoustic Wave Analysis

Shiokawa et al. [60] conducted experiments over twenty years ago pertaining to the manipulation of liquid droplets using surface acoustic waves (SAW). Using a lithium niobate ($LiNbO_3$) substrate, the motion of the liquid droplets was found to be dependent on the chemical condition of the substrate. It was also shown that the SAW streaming force is strong enough to cause ejection of material from the liquid droplet.

Recently, work has been undertaken by Alghane et al. [12] using the FVM in OpenFOAM [1] examining the acoustic excitation of liquid droplets resting on a lithium niobate ($LiNbO_3$) surface. The 3D framework models surface acoustic waves (SAW) by application of a body force to the elements of the fluid volume located at the interface of the SAW and the fluid. Motion of the fluid is then found by solving the laminar incompressible Navier-Stokes equations. Figure 2.3 demonstrates the typical set up for such a system; an alternating electric field is applied to the interdigital transducer (IDT) converting the electric field to a SAW which propagates along the solid-air interface until it reaches the solid-liquid interface where it changes its mode to leaky SAW. Longitudinal waves are produced by this leaky SAW and they propagate into the fluid at the Rayleigh angle, θ_R; this creates a body force acting on the fluid. The magnitude of attenuation of the longitudinal waves depends on the properties of the substrate and the density of the liquid.

The framework produces good agreement when compared to experimental data, however calibration was required using experimental data before predictions could be made. Calibration may not always be possible nor practical and this is a major drawback of this framework.

2.5 Conclusions

This chapter examined a very brief history of fluid mechanics from ancient times to modern day computational fluid dynamics. By far the most influential work in this field is that by Navier and Stokes developing the Navier-Stokes equations. However, the importance of the work of their predecessors, especially Newton, Euler, Laplace, Cauchy, Poisson and Lagrange, in the development of the Navier-Stokes equations cannot be understated. Modern analysis of fluid problems involves computational schemes and the method of discretisation to be used in this framework was discussed. In the context of this work, the Finite Element Method has been chosen due to its low storage requirements, being well-suited to complex geometries and for incorporation of this work into the work of others in our research group.

The work of Oñate et al. on the Particle Finite Element method for assessing Fluid-Structure Interaction (FSI) and wave splashing shows the appropriateness of the FEM, in conjunction with a Lagrangian formulation, in this field. However, there are drawbacks of this solution scheme, namely, the need for frequent large-scale remeshing.

Saksono and Perić also use the FEM with a Lagrangian formulation to assess the role of surface tension in micro-fluids. Surface tension is extremely influential at this scale and therefore additional contributions from the surface tension force and the contact line force are assembled into the force vector and stiffness matrix. The resulting analyses give highly comparable equilibrium shapes to the analytical solutions. However, the need to carefully select an initial mesh is undesirable and limits the application of this scheme to problems where the deformation of the fluid is known.

Additions to this work in collaboration with Dettmer produced an accurate and robust solution scheme with results for various different scenarios comparable to analytical solutions. However, the model developed by Dettmer et al. has convergence issues for large scale analysis, and the model developed by Dettmer and Perić has difficulties in the computational implementation.

Lastly, the work of Shiokawa et al. and Alghane et al. has shown the possibilities of modelling surface acoustic wave attenuation of micro-scale droplets of liquid.

Chapter 3

The Physics of Fluid Motion

This chapter presents the governing partial differential equations for fluid motion, called the Navier-Stokes equations, both in their *strong* and *weak form* [11, 16, 66].

3.1 Rudimentary Mathematics

The Navier-Stokes equations describe conservation of momentum, energy and mass. This thesis is concerned with fluid motion at the micro-scale. It is assumed that the fluid is a continuum, and that no discrete particles exist in the fluid. Therefore, following the *continuum hypothesis*, the properties of the bulk of the fluid can be applied to any random point in the fluid by means of differentiation. To derive the Navier-Stokes equations, it is convenient to first introduce the concept of the material derivative and the Reynolds' transport theorem.

3.1.1 The Material Derivative

The material derivative is the derivative of a material property taken with respect to a moving coordinate system. For example, it may be necessary to determine the temperature evolution of a fluid 'parcel' in time, as it is moved along its path while following the fluid flow. The material derivative can be seen as the connection between Eulerian and Lagrangian mechanics. Defining $f(x,y,z,t)$ as a property of the fluid, the rate of change of f at a fixed position is $\partial f/\partial t$. The rate of change of f subject to a space and time dependent velocity field $\mathbf{v}$ is given as:

$$\frac{Df}{Dt} = \frac{d}{dt} f\left[x(t), y(t), z(t), t\right] \tag{3.1}$$

where $x(t)$, $y(t)$ and $z(t)$ change with time at the local flow velocity $\mathbf{v}$. Note:

$$u = \frac{dx}{dt} \qquad v = \frac{dy}{dt} \qquad w = \frac{dz}{dt} \tag{3.2}$$

Application of the chain rule of differentiation produces:

$$\begin{aligned} \frac{Df}{Dt} &= \frac{\partial f}{\partial x}\frac{dx}{dt} + \frac{\partial f}{\partial y}\frac{dy}{dt} + \frac{\partial f}{\partial z}\frac{dz}{dt} + \frac{\partial f}{\partial t} \\ &= u\frac{\partial f}{\partial x} + v\frac{\partial f}{\partial y} + w\frac{\partial f}{\partial z} + \frac{\partial f}{\partial t} \end{aligned} \tag{3.3}$$

Thus:

$$\frac{Df}{Dt} = \frac{\partial f}{\partial t} + (\mathbf{v}\cdot\nabla) f \tag{3.4}$$

The material derivative is also referred to as the convective derivative, substantive derivative, Lagrangian derivative, Stokes derivative or the total derivative.

3.1.2 Reynolds' Transport Theorem

An intensive property is a physical property of a system that is independent of the size of the system or the amount of material in the system, e.g. momentum. The Reynolds' transport theorem leads to a conservation equation and states that the rate of change in an intensive property $\mathbf{s}$ defined over a control volume Ω must be equal to the loss or gain through the boundaries of the control volume, plus what is created or destroyed by sources and sinks inside the control volume.

$$\frac{\partial}{\partial t}\int_{\Omega} \mathbf{s} dV = -\int_{\partial\Omega} \mathbf{sv}\cdot\mathbf{n} dA - \int_{\Omega} Q dV \tag{3.5}$$

where $\mathbf{n}$ is the outward-pointing unit-normal of Ω, Q is the sources and sinks in the control volume, and $\partial\Omega$ is the bounding surface of the control volume. The second term can be changed from a surface integral to a volume integral using the divergence theorem. The divergence theorem states that the outward flux of a vector through a closed surface is equal to the volume integral of the divergence of the vector, i.e. the net flow is equal to the sum of all sources minus the sum of all sinks. Applying the divergence theorem to the second term of Equation 3.5 gives:

$$\int_{\partial\Omega} \mathbf{sv}\cdot\mathbf{n} dA = \int_{\Omega} \nabla\cdot(\mathbf{sv})\, dV \tag{3.6}$$

Therefore, Equation 3.5 becomes:

$$\frac{\partial}{\partial t}\int_{\Omega} \mathbf{s} dV = -\int_{\Omega} \nabla\cdot(\mathbf{sv})\, dV - \int_{\Omega} Q dV \tag{3.7}$$

Now the left hand term of Equation 3.7 can be changed using Leibniz's Rule. This states that,

$$\frac{\partial}{\partial t}\int_{a(t)}^{b(t)} f(x,t)\,dx = \int_{a(t)}^{b(t)} \frac{\partial f}{\partial x}(x,t)\,dx \tag{3.8}$$

Applying this to the left hand term of Equation 3.7 gives:

$$\int_{\Omega} \frac{\partial \mathbf{s}}{\partial t} dV = -\int_{\Omega} \nabla \cdot (\mathbf{sv})\,dV - \int_{\Omega} Q dV \tag{3.9}$$

Rearranging:

$$\int_{\Omega} \left(\frac{\partial \mathbf{s}}{\partial t} + \nabla \cdot (\mathbf{sv}) + Q \right) dV = 0 \tag{3.10}$$

Therefore, the local form of Equation 3.10 is:

$$\frac{\partial \mathbf{s}}{\partial t} + \nabla \cdot (\mathbf{sv}) + Q = 0 \tag{3.11}$$

Equation 3.11 provides an expression that can be applied to the conservation of mass, momentum and energy.

3.2 The Navier-Stokes Equations

3.2.1 Conservation of Mass

If it is assumed that there are no sources or sinks of momentum in the control volume ($Q = 0$) and we apply Equation 3.11 for the scalar field density, we obtain the equation for conservation of mass:

$$\frac{\partial \rho}{\partial t} + \nabla \cdot (\rho \mathbf{v}) = 0 \tag{3.12}$$

3.2.2 Conservation of Momentum

Taking the momentum, $\mathbf{p}$, as an intensive property, to be equal to the product of fluid density and fluid velocity i.e. ($\mathbf{s} = \mathbf{p} = \rho \mathbf{v}$) and substituting into Equation 3.11:

$$\frac{\partial}{\partial t}(\rho \mathbf{v}) + \nabla \cdot (\rho \mathbf{vv}) + Q = 0 \tag{3.13}$$

Further, a body force **b**, which can be thought of as a source or sink of momentum per unit volume can be introduced. Expanding the above expression leads to:

$$\left(\frac{\partial \rho}{\partial t}\mathbf{v} + \frac{\partial \mathbf{v}}{\partial t}\rho\right) + (\mathbf{v}\mathbf{v}\cdot\nabla\rho + \rho\mathbf{v}\cdot\nabla\mathbf{v} + \rho\mathbf{v}\nabla\cdot\mathbf{v}) = \mathbf{b} \tag{3.14}$$

$$\mathbf{v}\left(\frac{\partial \rho}{\partial t} + \mathbf{v}\cdot\nabla\rho + \rho\nabla\cdot\mathbf{v}\right) + \rho\left(\frac{\partial \mathbf{v}}{\partial t} + \mathbf{v}\cdot\nabla\mathbf{v}\right) = \mathbf{b} \tag{3.15}$$

$$\mathbf{v}\left(\frac{\partial \rho}{\partial t} + \nabla\cdot(\rho\mathbf{v})\right) + \rho\left(\frac{\partial \mathbf{v}}{\partial t} + \mathbf{v}\cdot\nabla\mathbf{v}\right) \quad = \quad \mathbf{b} \tag{3.16}$$

Applying 3.12 to Equation 3.16 the first term in parenthesis disappears. Noting that the second term in parenthesis in Equation 3.16 is the material derivative of the velocity (Equation 3.4), the equation for conservation of momentum is:

$$\rho\frac{D\mathbf{v}}{Dt} \quad = \quad \mathbf{b} \tag{3.17}$$

3.2.3 General Form of Navier-Stokes Equations

Equation 3.17 is a general form of the Cauchy momentum equation, which can be further developed if it is assumed that the body force term **b** comprises two terms; a term to describe forces from stresses and a term to describe other forces such as gravity:

$$\mathbf{b} = \nabla\cdot\sigma + \mathbf{g} \tag{3.18}$$

where σ is the Cauchy stress tensor and **g** in this case represents the body force of gravity (i.e. $\rho g = \mathbf{g}$ vertical direction). The Cauchy stress tensor is:

$$\sigma = \begin{bmatrix} \sigma_{xx} & \tau_{xy} & \tau_{xz} \\ \tau_{yx} & \sigma_{yy} & \tau_{yz} \\ \tau_{zx} & \tau_{zy} & \sigma_{zz} \end{bmatrix} \tag{3.19}$$

Decomposing this into its volumetric and deviatoric components:

$$\sigma = -\begin{bmatrix} p & 0 & 0 \\ 0 & p & 0 \\ 0 & 0 & p \end{bmatrix} + \begin{bmatrix} \sigma_{xx}+p & \tau_{xy} & \tau_{xz} \\ \tau_{yx} & \sigma_{yy}+p & \tau_{yz} \\ \tau_{zx} & \tau_{zy} & \sigma_{zz}+p \end{bmatrix} \tag{3.20}$$

$$\sigma = -pI + \mathbb{T} \tag{3.21}$$

where I is the identity matrix and $\mathbb{T}$ is the deviatoric stress tensor. The pressure, p is equal to the negative of the mean stress:

$$p = -\frac{1}{3}(\sigma_{xx} + \sigma_{yy} + \sigma_{zz}) \tag{3.22}$$

At this point it is useful to note that several assumptions can now be made concerning the deviatoric stress tensor depending on the type of fluid. First, we will consider Newtonian fluids. A Newtonian fluid is one in which the viscous forces due to fluid flow are proportional to the strain rate at every point within the fluid. It is therefore possible to make the following assumptions [11, 66, 16]:

- the deviatoric stress tensor vanishes for a fluid at rest and depends only on the spatial derivatives of the flow velocity,
- the deviatoric stress tensor can be expressed as the product of the flow velocity gradient $\nabla\mathbf{v}$ with a viscosity tensor $\mathbf{A}$, such that $\mathbb{T} = \mathbf{A}(\nabla\mathbf{v})$,
- the fluid is isotropic (therefore $\mathbf{A}$ is an isotropic tensor),
- the deviatoric stress tensor is symmetric and can be expressed in terms of two viscosities μ and λ, where μ is known as the first viscosity coefficient, or simply the viscosity, and λ is the second viscosity coefficient.

Thus:

$$\mathbb{T} = 2\mu\mathbf{e} + \lambda\Delta I \tag{3.23}$$

where the rate of strain tensor is:

$$\mathbf{e} = \frac{1}{2}(\nabla\mathbf{v}) + \frac{1}{2}(\nabla\mathbf{v})^{\mathrm{T}} \tag{3.24}$$

and the rate of expansion of the fluid is Δ. The trace of the deviatoric stress tensor is zero, and so for three-dimensional flow $2\mu + 3\lambda = 0 \Longrightarrow \lambda = 2/3\mu$. Consider now an incompressible fluid, one in which the density is constant within an infinitesimal volume of fluid that moves with the fluid velocity. Therefore we can assume [11, 66, 16]:

- the viscosity μ is a constant,
- the bulk viscosity is zero, $\lambda = 0$,
- there are no sinks or sources of momentum because the density is constant, thus the divergence of the fluid velocity is zero, $\nabla \cdot \mathbf{v} = 0$.

The deviatoric stress tensor becomes:

$$\mathbb{T} = 2\mu\mathbf{e} \tag{3.25}$$

$$\mathbb{T} = 2\mu\left(\frac{1}{2}(\nabla\mathbf{v}) + \frac{1}{2}(\nabla\mathbf{v})^{\mathrm{T}}\right) \tag{3.26}$$

Substituting Equation 3.18 into Equation 3.17:

$$\rho\frac{D\mathbf{v}}{Dt} = \nabla\cdot\sigma + \mathbf{f} \tag{3.27}$$

Substituting Equations 3.21 and 3.26 into Equation 3.27:

$$\rho\left(\frac{\partial\mathbf{v}}{\partial t} + \mathbf{v}\cdot\nabla\mathbf{v}\right) = -\nabla p + \nabla\cdot\left(2\mu\left(\frac{1}{2}(\nabla\mathbf{v}) + \frac{1}{2}(\nabla\mathbf{v})^{\mathrm{T}}\right)\right) + \rho g \tag{3.28}$$

Simplifying, the final form of the Navier-Stokes equations is:

$$\rho\left(\frac{\partial\mathbf{v}}{\partial t} + \mathbf{v}\cdot\nabla\mathbf{v}\right) = -\nabla p + 2\mu\nabla^2\mathbf{v} + \rho g \tag{3.29}$$

3.3 The Weak Form of the Navier-Stokes Equations for an Incompressible Fluid

Equation 3.29 is the *strong form* of the Navier-Stokes equations; the equations hold for the entire domain and must be satisfied at every point within the domain. Transforming to a *weak form* of the partial differential equations, the solution is required to hold in a weighted residual sense in the domain. The *weak form* provides a much more convenient starting point from which to construct a finite element (FE) formulation.

3.3.1 Conservation of Mass in the Weak Form

Beginning with Equation 3.12 and applying the incompressibility condition (density is constant), the conservation of mass reduces to:

$$\nabla\cdot\mathbf{v} = 0 \tag{3.30}$$

Therefore, the Galerkin weighted residual form of the conservation of mass in the spatial domain is:

$$R_v(\mathbf{v}) = \int_{V(\mathbf{x})} \mathbf{w_p} tr\left(\frac{\partial\mathbf{v}}{\partial\mathbf{x}}\right) dV \tag{3.31}$$

The weighting function for the pressure field is represented by $\mathbf{w_p}$. A weighting function tests that the equation is satisfied in an average sense, rather than at each point in the domain. The following chapter details the terms within this equation and identifies the solution scheme adopted to solve this equation.

3.3.2 Conservation of Momentum in the Weak Form

The terms in parenthesis in Equation 3.29 are known collectively as the acceleration $\mathbf{a}$. The first term is known as the unsteady acceleration and the second term is known as the convective acceleration. Substituting the acceleration for these terms in parenthesis, the Galerkin weighted residual form of the conservation of momentum, Equation 3.29, in the spatial domain is:

$$R_v(\mathbf{v},p) = \int_{V(\mathbf{x})} \rho \mathbf{w_v} \cdot \mathbf{a} - tr\left(\frac{\partial \mathbf{w_v}}{\partial \mathbf{x}}\right) p + 2\mu \left(\frac{\partial \mathbf{w_v}}{\partial \mathbf{x}} : \mathbf{e}\right) - \mathbf{w_v} \cdot \mathbf{b}\, dV \tag{3.32}$$

The weighting function for the velocity field is represented by $\mathbf{w_v}$. The following chapter details the terms within this equation as well as the solution scheme adopted to solve this equation.

3.4 Conclusions

This chapter has discussed the material derivative, Reynolds' transport theorem, the conservation of mass and momentum and the assumptions made regarding the deviatoric stress tensor, finally arriving at the common form of the Navier-Stokes equations for an incompressible Newtonian fluid. *Weak forms* of the conservation of mass and the conservation of momentum were then given. The next chapter will develop a computational strategy for solving these equations, before discretising the equations firstly in time to form a semi-discretised form, and then in space using the finite element method.

Chapter 4

Computational Solution Strategy

The domain of the problems to be examined in this thesis are discretised into a finite element (FE) mesh consisting of three-noded triangular elements. Moreover, the geometric domain of each droplet is constantly changing in time and this requires a suitable kinematic description if the computational model is to be both robust and accurate. Several options are available for the kinematic description, some more suitable than others. Each option will be described in detail, examining the advantages and disadvantages of each. After selecting a kinematic description, the time integration scheme will be outlined. Together, this solution strategy can be applied to the *weak form* of the Navier-Stokes equations to develop a system of equations that can be solved computationally.

4.1 Eulerian Formulations

For some time Eulerian formulations (also known as spatial descriptions) have been the formulation of choice when assessing fluid mechanics problems. Eulerian meshes are well suited to problems involving very large deformations because the elements do not deform with the material and retain their original shape [20]. This formulation examines a specific location in the space through which the fluid flows as time passes; this space is known as the control volume. The mesh points remain stationary and fluid particles move through the mesh and as such, individual particles can only be traced within the control volume; their behaviour before entering and after exiting the control volume is unknown. Figure 4.1 shows a diagrammatic representation of a mesh with respect to Eulerian coordinates $\mathbf{x}$; on the left is an initial mesh and on the right is the deformed mesh after motion ϕ is applied.

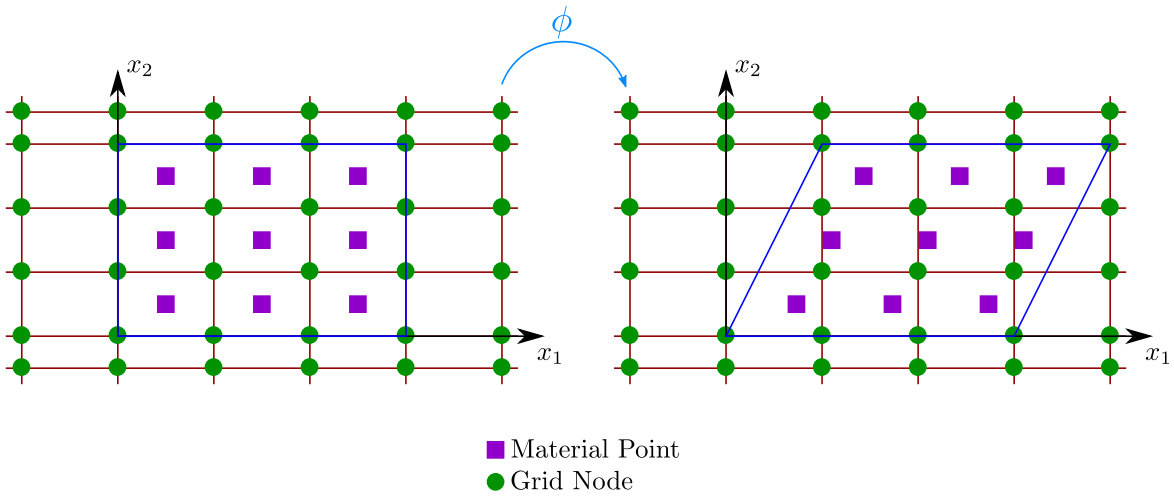

Figure 4.1: Eulerian description

It can be seen that the nodes remain stationary whilst the material points have moved. The problems to be assessed later inherently depend on accurate tracking of the droplet surface, and additionally the interior of the droplet will undergo large deformation. Since an Eulerian formulation cannot trace specific particles through time, it is not ideally suited to fluid free surface tracking problems, but is more suited towards the large deformation of the droplet interior (since the mesh will not experience any distortion).

4.2 Lagrangian Formulations

Typically used in solid mechanics, Lagrangian formulations (also known as material descriptions) easily deal with complicated boundaries and follow material points, therefore history-dependent materials can be accurately assessed. Each node within the FE mesh represents an individual fluid particle and the control volume is moved in context with a given particle; hence the motion of the particle can be followed in time and its behaviour constantly known. Figure 4.2 shows a mesh with respect to the Lagrangian coordinates $\mathbf{X}$; when motion ϕ is applied to the mesh, both the material points and the mesh nodes move together. Being able to follow the surface of the droplet in time is necessary for the problems to be undertaken and hence this would be the formulation of choice, as seen in the work of Oñate et al. [47], and Saksono and Perić, [57, 58]. However, a consequence of using a Lagrangian mesh is that when the mesh undergoes large deformation, the elements incur large distortions, thereby inducing errors in the numerical solution and ultimately failure of the analysis. A favoured option to mitigate this problem is the use of remeshing but this can add to the computational time and complexity.

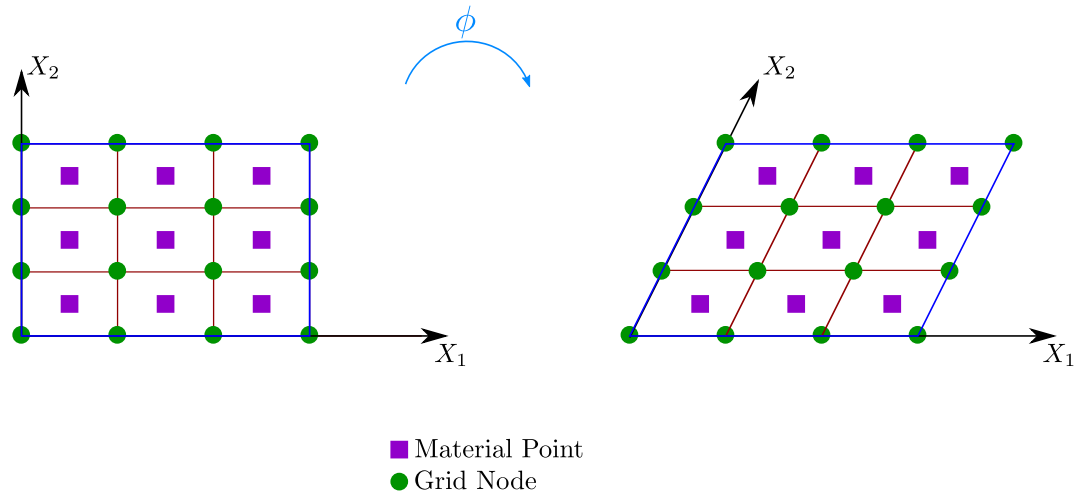

Figure 4.2: Lagrangian description

4.3 Arbitrary Lagrangian Eulerian Formulations

Examining the advantages and disadvantages of both Eulerian and Lagrangian formulations, it becomes apparent that neither formulation will give entirely satisfactory results for the problem at hand. However, the introduction of a control volume that can move freely in space and independently of the material, effectively combines the best features of both a pure Eulerian formulation and a pure Lagrangian formulation. This resulting Arbitrary Lagrangian Eulerian (ALE) formulation allows nodes to remain stationary in an Eulerian manner, to move with the continuum in a Lagrangian manner, or to move arbitrarily. Thus, ALE can handle greater distortions than a pure Lagrangian formulation and handle individual particle tracking in greater detail than a pure Eulerian formulation. It is for these reasons that an ALE formulation is chosen in this thesis.

ALE was first proposed for use in finite volume and finite difference problems with contributions from, among others, Franck and Lazarus [32], Noh [46] and Hirt et al. [33]. Early applications can be found in the work of Belytschko and Kennedy [19] and Donea et al. [30] to name a few.

In addition to the spatial domain, $\mathbf{x}$, and the material domain, $\mathbf{X}$, the ALE formulation requires a third domain. This domain is called the mesh domain, χ. Figure 4.3 shows a mapping from one domain to another. Therefore, each node in the mesh has additional degrees of freedom relating to the velocity of the mesh, $\hat{\mathbf{v}}$, alongside those for material velocity, $\mathbf{v}$,

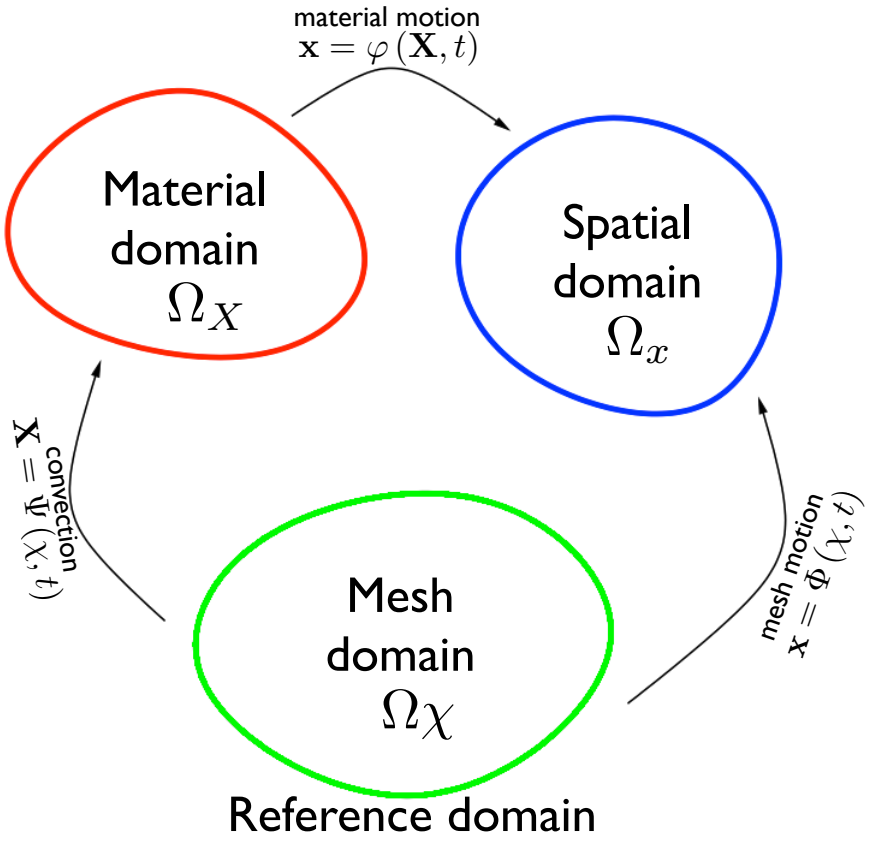

Figure 4.3: The three domains required in ALE

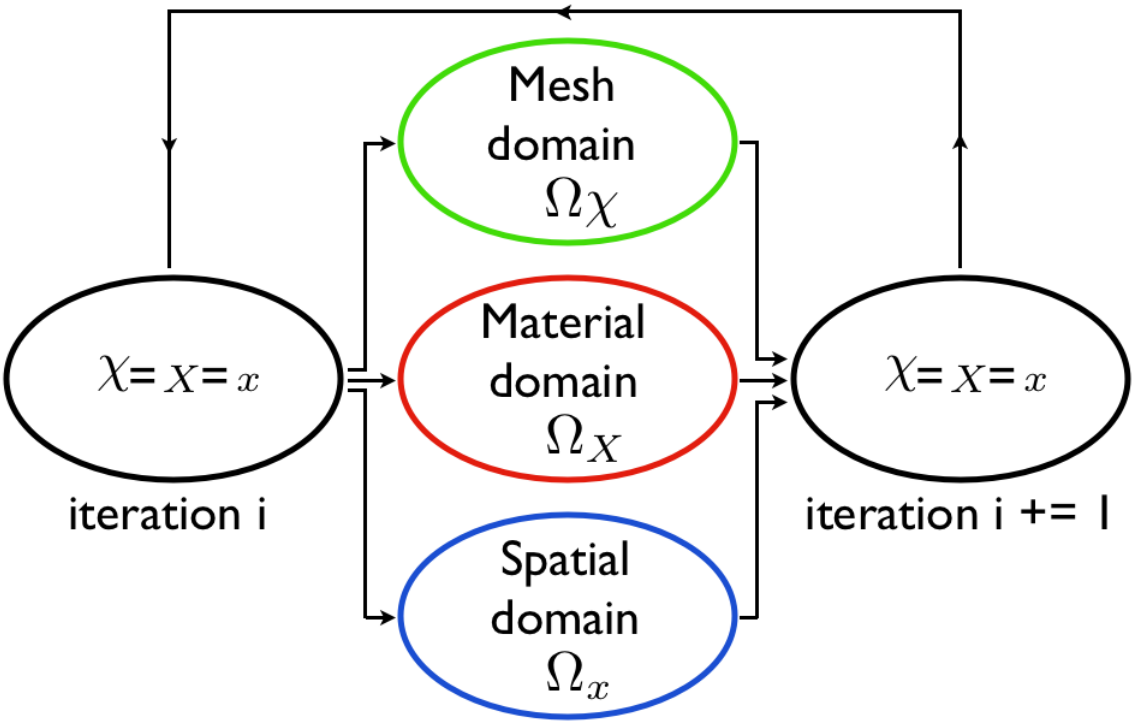

Figure 4.4: UALE iterative solving procedure

and, in the cases to be presented later, pressure, p. Each point in the mesh domain is related to a material point and each material point occupies some point in space. Before motion occurs, all three domains are equivalent. Motion occurs and we solve for the mesh velocity in the mesh domain as we integrate over the volume of the element, Figure 4.4. One can then map to the material domain to solve for material velocity and pressure (using $\mathbf{X} = \psi(\chi, t)$), and map to the spatial domain to solve for position (using $\mathbf{x} = \varphi(X, t)$). When the mesh velocity is zero, the formulation is purely Eulerian, when the mesh and material velocity are equal, the formulation is purely Lagrangian, and if the material and mesh velocities are not equal and the mesh velocity is non-zero, the formulation is 'arbitrary'.

When solving an ALE formulation, it is necessary to decide whether to adopt a staggered (S-ALE) solution strategy or a monolithic one (M-ALE). In the former, three consecutive steps are required [37]. First, a Lagrangian step where the mesh nodes move in a Lagrangian manner tracking the material; second, a rezone step where the nodes move in order to improve the mesh quality; and lastly, a remapping step where the solution is transferred from the old mesh to the new mesh. The interpolation of the solution from the old mesh to the new, however, can generate errors and introduce non-linearities during the change in mesh. In the latter approach (M-ALE), the physical equations and the mesh motion equations are coupled and solved simultaneously. Although this method results in a much larger matrix, the equations are properly linearised and quadratic convergence can be maintained [14]. The M-ALE approach is adopted in this thesis.

4.4 Updated Arbitrary Lagrangian Eulerian Formulations

When developing Lagrangian formulations, there are two common approaches: Total (TL) formulations and Updated (UL) formulations:

- In a TL formulation the derivatives and integrals are taken with respect to the Lagrangian (or material) coordinates, $\mathbf{X}$, [20]. The initial undeformed configuration is the reference configuration at all times and all equations relate to this configuration. TL formulations are most often applied to solid mechanics problems featuring elastic materials with finite displacements and finite strains [31]. When applying to fluid-flow problems or problems with changes in topology, TL formulations are unreliable because of high mesh distortion. In terms of computational schemes, TL formulations have low storage requirements, however the implementation is more involved.

- In an UL formulation the derivatives and integrals are taken with respect to the Eulerian (or spatial) coordinates, **x**, [20]. Unlike a TL formulation, the reference configuration is updated throughout the analysis. UL formulations are most often applied to solid mechanics problems with finite displacements and large strains; they are very good at assessing fluid-flow and changes in topology [31]. Moreover, UL formulations have high storage requirements when used in computational schemes as it is necessary to remember the previous stress state, but implementation is generally more straightforward than TL.

Irrespective of the approach adopted, the end result is the same. In this thesis, we adopt an UL formulation for the Lagrangian part of the ALE formulation and this combination has been termed as an 'Updated Arbitrary Lagrangian Eulerian' (UALE) formulation. Thus, our reference configuration is the current deformed configuration, updated each time step.

4.5 Time Integration Scheme

Now that a kinematic description has been chosen, and before the *weak form* of the conservation of mass and the conservation of momentum can be further examined, a solution scheme must be adopted. The *weak form* of the Navier-Stokes equations is expressed in terms of the fluid velocity and fluid pressure. The solution scheme adopted solves for the velocity and pressure in time using an iterative Newton-Raphson method. The accelerations are written in terms of the velocity only. We use an implicit time integration scheme consisting of a trapezoidal rule, as shown in Figure 4.5 to solve for the velocity, i.e. the velocity $\hat{\mathbf{v}}_{n+1}$ at time t_{n+1} is equal to the sum of the velocity $\hat{\mathbf{v}}_n$ at the previous time step t_n and the time-averaged sum of the incremental change and iterative change in velocity. In the 2D formulation con-

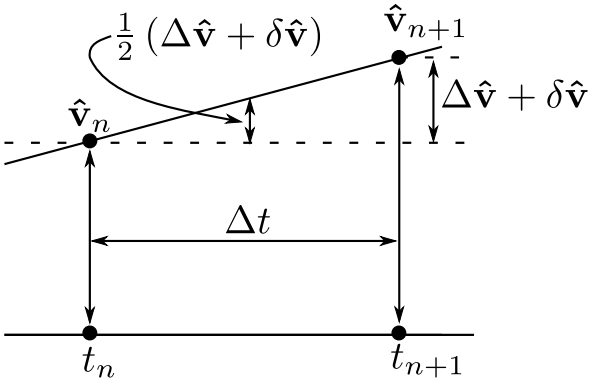

Figure 4.5: Trapezoidal integration scheme

sidered here, there are five degrees of freedom per node: horizontal and vertical fluid velocity (material velocity), fluid pressure, and horizontal and vertical mesh velocity, $\mathbf{v}$, p and $\hat{\mathbf{v}}$ respectively. The governing PDEs are nonlinear in nature and are solved implicitly using an incremental-iterative Newton-Raphson scheme. Given the solution at time t_n, $(\mathbf{v}_n, p_n, \hat{\mathbf{v}}_n)$, the solution at time t_{n+1} is formed using the Newton-Raphson scheme. Within each time step the increment in $\mathbf{v}$, p and $\hat{\mathbf{v}}$ are iteratively updated, thus the solution at time t_{n+1} and iteration $i+1$ is:

$$\mathbf{v}_{n+1}^{i+1} = \mathbf{v}_n + \Delta\mathbf{v}_{n+1}^{i+1} = \mathbf{v}_n + \Delta\mathbf{v}_{n+1}^{i} + \delta\mathbf{v} = \mathbf{v}_i + \delta\mathbf{v} \tag{4.1}$$

$$p_{n+1}^{i+1} = p_n + \Delta p_{n+1}^{i+1} = p_n + \Delta p_{n+1}^{i} + \delta p = p_i + \delta p \tag{4.2}$$

$$\hat{\mathbf{v}}_{n+1}^{i+1} = \hat{\mathbf{v}}_n + \Delta\hat{\mathbf{v}}_{n+1}^{i+1} = \hat{\mathbf{v}}_n + \Delta\hat{\mathbf{v}}_{n+1}^{i} + \delta\hat{\mathbf{v}} = \hat{\mathbf{v}}_i + \delta\hat{\mathbf{v}} \tag{4.3}$$

where $\delta\mathbf{v}$, δp and $\delta\hat{\mathbf{v}}$ are the iterative change in velocity, pressure and mesh velocity at time t_{n+1}, iteration $i+1$ and represent the fundamental unknowns. The subscript $(\ldots)_{n+1}$ has been omitted from the penultimate terms for convenience. The new position of a node is calculated at each iteration as:

$$\begin{aligned} \mathbf{x}_{n+1}^{i+1} &= \mathbf{x}_n + \Delta t\hat{\mathbf{v}}_n + \frac{\Delta t}{2}\Delta\hat{\mathbf{v}}_{n+1}^{i+1} \\ &= \mathbf{x}_n + \Delta t\hat{\mathbf{v}}_n + \frac{\Delta t}{2}\left(\Delta\hat{\mathbf{v}}_{n+1}^{i} + \delta\hat{\mathbf{v}}\right) \end{aligned} \tag{4.4}$$

where Δt is the time step. As a consequence of using an UALE formulation, the mesh velocity and the incremental change in mesh velocity are set equal to zero at the beginning of each iteration, with the iterative change in mesh velocity non-zero. Therefore, differentiating Equation 4.4 with respect to the mesh domain:

$$\left(\frac{\partial\mathbf{x}}{\partial\chi}\right)_{n+1}^{i+1} = \frac{\partial}{\partial\chi}\left(\chi + \Delta t\cancel{\hat{\mathbf{v}}} + \frac{\Delta t}{2}\cancel{\Delta\hat{\mathbf{v}}} + \frac{\Delta t}{2}\delta\hat{\mathbf{v}}\right) = \frac{\partial\chi(\chi,t)}{\partial\chi} + \frac{\Delta t}{2}\frac{\partial\delta\hat{\mathbf{v}}}{\partial\chi} \tag{4.5}$$

$$\left(\frac{\partial\mathbf{x}}{\partial\chi}\right)_{n+1}^{i+1} = 1 + \frac{\Delta t}{2}\frac{\partial\delta\hat{\mathbf{v}}}{\partial\chi} \tag{4.6}$$

Now, the gradient of the fluid (material) velocity in the spatial domain is:

$$\left(\frac{\partial\mathbf{v}}{\partial\mathbf{x}}\right)_{n+1}^{i+1} = \frac{\partial\mathbf{v}}{\partial\chi}\frac{\partial\chi}{\partial\mathbf{x}} = \frac{\partial\mathbf{v}}{\partial\chi}\left(\frac{\partial\mathbf{x}}{\partial\chi}\right)^{-1} \tag{4.7}$$

Therefore we require the inverse of Equation 4.6 to calculate the gradient of the velocity. Following a derivation from Bonet and Wood [21] as shown in Appendix A:

$$\left(\frac{\partial \mathbf{x}}{\partial \chi}\right)^{-1} = \frac{\partial \chi}{\partial \mathbf{x}} = 1 - \frac{\Delta t}{2}\frac{\partial \delta \hat{\mathbf{v}}}{\partial \chi} \tag{4.8}$$

Hence, the gradient of the fluid velocity in the reference configuration is:

$$\left(\frac{\partial \mathbf{v}}{\partial \mathbf{x}}\right)_{n+1}^{i+1} = \frac{\partial \mathbf{v}}{\partial \chi}\left(1 - \frac{\Delta t}{2}\frac{\partial \delta \hat{\mathbf{v}}}{\partial \chi}\right) = \frac{\partial \mathbf{v}}{\partial \chi} - \frac{\Delta t}{2}\frac{\partial \mathbf{v}}{\partial \chi}\frac{\partial \delta \hat{\mathbf{v}}}{\partial \chi} \tag{4.9}$$

Similarly, the gradient of the fluid pressure in the reference configuration is:

$$\left(\frac{\partial p}{\partial \mathbf{x}}\right)_{n+1}^{i+1} = \frac{\partial p}{\partial \chi}\frac{\partial \chi}{\partial \mathbf{x}} = \frac{\partial p}{\partial \chi}\left(1 - \frac{\Delta t}{2}\frac{\partial \delta \hat{\mathbf{v}}}{\partial \chi}\right) = \frac{\partial p}{\partial \chi} - \frac{\Delta t}{2}\frac{\partial p}{\partial \chi}\frac{\partial \delta \hat{\mathbf{v}}}{\partial \chi} \tag{4.10}$$

The acceleration, $\mathbf{a}$, of each node during each iteration can be written in terms of velocity:

$$\begin{aligned}
\mathbf{a}_{n+1}^{i+1} &= \frac{\partial \mathbf{v}}{\partial t} + \frac{\partial \mathbf{v}}{\partial \mathbf{x}}\mathbf{c} \\
&= \frac{\partial \mathbf{v}}{\partial t} + \frac{\partial \mathbf{v}}{\partial \chi}\frac{\partial \chi}{\partial \mathbf{x}}\mathbf{c} \\
&= \frac{\partial \mathbf{v}}{\partial t} + \frac{\partial \mathbf{v}}{\partial \chi}\left(1 - \frac{\Delta t}{2}\frac{\partial \delta \hat{\mathbf{v}}}{\partial \chi}\right)\mathbf{c} \\
&= \frac{\partial \mathbf{v}}{\partial t} + \frac{\partial \mathbf{v}}{\partial \chi}\mathbf{c} - \frac{\Delta t}{2}\frac{\partial \mathbf{v}}{\partial \chi}\frac{\partial \delta \hat{\mathbf{v}}}{\partial \chi}\mathbf{c}
\end{aligned} \tag{4.11}$$

where $\mathbf{c}$ is the convective velocity, the difference in material and mesh velocities:

$$\mathbf{c} = \mathbf{v} - \hat{\mathbf{v}} \tag{4.12}$$

The terms of the acceleration can be broken down further as shown in Appendix A. The final form of the acceleration is:

$$\begin{aligned}\mathbf{a}_{n+1}^{i+1} &= \frac{\Delta \mathbf{v}}{\Delta t}+\frac{\delta \mathbf{v}_i}{\Delta t} \\ &+\frac{\partial \mathbf{v}_i}{\partial \chi}\mathbf{v}_i+\frac{\partial \mathbf{v}_i}{\partial \chi}\delta \mathbf{v}_i+\frac{\partial \delta \mathbf{v}}{\partial \chi}\mathbf{v}_i-\frac{\partial \mathbf{v}_i}{\partial \chi}\hat{\mathbf{v}}_i-\frac{\partial \mathbf{v}_i}{\partial \chi}\delta \hat{\mathbf{v}}_i-\frac{\partial \delta \mathbf{v}}{\partial \chi}\hat{\mathbf{v}}_i \\ &-\frac{\Delta t}{2}\frac{\partial \mathbf{v}_i}{\partial \chi}\frac{\partial \delta \hat{\mathbf{v}}}{\partial \chi}\mathbf{v}_i+\frac{\Delta t}{2}\frac{\partial \mathbf{v}_i}{\partial \chi}\frac{\partial \delta \hat{\mathbf{v}}}{\partial \chi}\hat{\mathbf{v}}_i \end{aligned} \tag{4.13}$$

From this point onwards, it is convenient to omit the step subscript and iteration superscript.

4.6 Semi-Discretised Weak Form of the Navier-Stokes Equations

From the previous chapter, the *weak form* of the conservation of mass for an incompressible Newtonian fluid is:

$$R_v(\mathbf{v},\hat{\mathbf{v}}) = \int_{V(\mathbf{x})} \mathbf{w}_\mathbf{p} tr\left(\frac{\partial \mathbf{v}}{\partial \mathbf{x}}\right) dV \tag{4.14}$$

and the *weak form* of the conservation of momentum for an incompressible Newtonian fluid is:

$$R_v(\mathbf{v},\hat{\mathbf{v}},p) = \int_{V(\mathbf{x})} \rho \mathbf{w}_\mathbf{v}\cdot\mathbf{a} - tr\left(\frac{\partial \mathbf{w}_\mathbf{v}}{\partial \mathbf{x}}\right)p + 2\mu\left(\frac{\partial \mathbf{w}_\mathbf{v}}{\partial \mathbf{x}} : \mathbf{e}\right) - \mathbf{w}_\mathbf{v}\cdot\mathbf{b}\, dV \tag{4.15}$$

Now that we have examined a suitable solution scheme, we can discretise these *weak forms* in time.

4.6.1 Conservation of Mass

Applying Equation 4.8 to Equation 4.14 to map from the spatial domain to the reference domain, the semi-discretised *weak form* of the conservation of mass becomes:

$$R_v(\mathbf{v},\hat{\mathbf{v}}) = \int_V \mathbf{w}_\mathbf{p} tr\left(\frac{\partial \mathbf{v}}{\partial \chi}-\frac{\Delta t}{2}\frac{\partial \mathbf{v}}{\partial \chi}\frac{\partial \delta \hat{\mathbf{v}}}{\partial \chi}\right) dV \tag{4.16}$$

Recalling Equations 4.1, 4.2 and 4.3, the semi-discretised *weak form* in the reference domain in a cartesian system becomes:

$$\begin{aligned} R_v(\mathbf{v},\hat{\mathbf{v}}) &= \int_V \mathbf{w}_\mathbf{p} tr\left(\frac{\partial \mathbf{v}_i}{\partial \chi}\right) dV + \int_V \mathbf{w}_\mathbf{p} tr\left(\frac{\partial \delta \mathbf{v}}{\partial \chi}\right) dV \\ &- \int_V \mathbf{w}_\mathbf{p} tr\left(\frac{\Delta t}{2}\frac{\partial \mathbf{v}_i}{\partial \chi}\frac{\partial \delta \mathbf{v}}{\partial \chi}\right) dV \end{aligned} \tag{4.17}$$

4.6.2 Conservation of Momentum

The symmetric part of the deviatoric stress tensor can be mapped from the spatial domain to the reference domain using Equation 4.8 and it can be expanded into known and unknown components where $\mathbf{e}_i$ involves only the known fluid velocity, $\delta\mathbf{e}$ only the incremental change in fluid velocity, and $\delta\hat{\mathbf{e}}$ only the iterative change in mesh velocity (see Appendix B):

$$\mathbf{e} = \mathbf{e}_i + \delta\mathbf{e} + \delta\hat{\mathbf{e}} \tag{4.18}$$

where:

$$\mathbf{e}_i = symm\left[\frac{\partial \mathbf{v}_i}{\partial \chi} - \frac{1}{3}tr\left(\frac{\partial \mathbf{v}_i}{\partial \chi}\right)\right] \tag{4.19}$$

$$\delta\mathbf{e} = symm\left[\frac{\partial \delta\mathbf{v}}{\partial \chi} - \frac{1}{3}tr\left(\frac{\partial \delta\mathbf{v}}{\partial \chi}\right)\right] \tag{4.20}$$

$$\delta\hat{\mathbf{e}} = -symm\left[\frac{\Delta t}{2}\frac{\partial \mathbf{v}_i}{\partial \chi}\frac{\partial \delta\hat{\mathbf{v}}}{\partial \chi} - \frac{1}{3}tr\left(\frac{\Delta t}{2}\frac{\partial \mathbf{v}_i}{\partial \chi}\frac{\partial \delta\hat{\mathbf{v}}}{\partial \chi}\right)\right] \tag{4.21}$$

The Applying Equation 4.8 to Equation 4.15 to map from the spatial domain to the reference domain, and recalling Equations 4.1, 4.2 and 4.3, the semi-discretised *weak form* in the reference domain in a cartesian system becomes:

$$\begin{aligned} R_v(\mathbf{v},\hat{\mathbf{v}},p) \;=\; & \int_V \rho \mathbf{w}_\mathbf{v}\cdot\mathbf{a}\,dV \\ & - \int_V \left(tr\left(\frac{\partial \mathbf{w}_\mathbf{v}}{\partial \chi}\right) p_i + tr\left(\frac{\partial \mathbf{w}_\mathbf{v}}{\partial \chi}\right)\delta p - tr\left(\frac{\Delta t}{2}\frac{\partial \mathbf{w}_\mathbf{v}}{\partial \chi}\frac{\partial \delta\hat{\mathbf{v}}}{\partial \chi}\right) p_i \right) dV \\ & + \int_V \left(2\mu\left(\frac{\partial \mathbf{w}_\mathbf{v}}{\partial \chi}\right) : \mathbf{e}_i + 2\mu\left(\frac{\partial \mathbf{w}_\mathbf{v}}{\partial \chi}\right) : \delta\mathbf{e} + 2\mu\left(\frac{\partial \mathbf{w}_\mathbf{v}}{\partial \chi}\right) : \delta\hat{\mathbf{e}} \right) dV \\ & + \int_V \left(-2\mu\left(\frac{\Delta t}{2}\frac{\partial \mathbf{w}_\mathbf{v}}{\partial \chi}\frac{\partial \delta\hat{\mathbf{v}}}{\partial \chi}\right) : \mathbf{e}_i - \mathbf{w}_\mathbf{v}\cdot\mathbf{b} \right) dV \end{aligned} \tag{4.22}$$

where the acceleration $\mathbf{a}$ is given in Equation 4.13.

4.7 Extension to Axisymmetry

4.7.1 Cylindrical Coordinate System

The problems to be examined in this work are axisymmetric in nature as both the structure (the fluid droplet) and the loading (gravity, surface acoustic waves, *etc*) are axisymmetric; all radial planes are assumed to act identically and deformation is only allowed in plane (the r-z

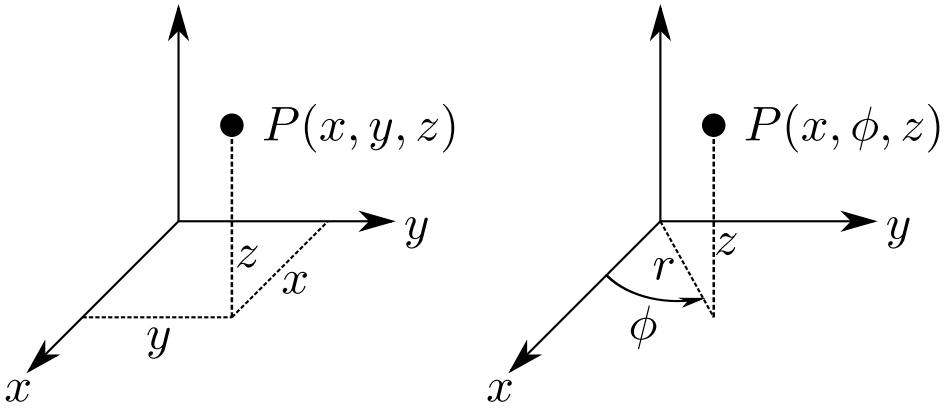

(a) Cartesian coordinate system (b) Cylindrical coordinate system

Figure 4.6: Coordinate systems

plane). The computational framework was initially developed for 2D plane-strain analysis. Thus the system of equations are now adapted to a cylindrical coordinate system.

A cylindrical coordinate system describes a point in space using the distance r from a chosen reference axis, the angle ϕ from this axis, and the perpendicular distance z from a chosen reference plane that is perpendicular to the reference axis, (r, ϕ, z), see Figure 4.6b. One can map between coordinate systems as follows:

$$x = r\cos\phi \qquad y = r\sin\phi \qquad z = z \tag{4.23}$$

$$r = \sqrt{x^2 + y^2} \qquad y = \begin{cases} 0 & \text{if } x = 0 \text{ and } y = 0 \\ \arcsin\left(\frac{y}{r}\right) & \text{if } x \geq 0 \\ -\arcsin\left(\frac{y}{r}\right) + \pi & \text{if } x < 0 \end{cases} \qquad z = z \tag{4.24}$$

Mapping from cylindrical to cartesian systems requires the Jacobian:

$$\mathbf{J} = \begin{bmatrix} \frac{\partial x}{\partial r} & \frac{\partial x}{\partial \phi} & \frac{\partial x}{\partial z} \\ \frac{\partial y}{\partial r} & \frac{\partial y}{\partial \phi} & \frac{\partial y}{\partial z} \\ \frac{\partial z}{\partial r} & \frac{\partial z}{\partial \phi} & \frac{\partial z}{\partial z} \end{bmatrix} = \begin{bmatrix} \cos\phi & -r\sin\phi & 0 \\ \sin\phi & r\cos\phi & 0 \\ 0 & 0 & 1 \end{bmatrix} \tag{4.25}$$

The inverse of the Jacobian is found to be:

$$\mathbf{J}^{-1} = \begin{bmatrix} \cos\phi & \sin\phi & 0 \\ -\dfrac{\sin\phi}{r} & \dfrac{\cos\phi}{r} & 0 \\ 0 & 0 & 1 \end{bmatrix} \tag{4.26}$$

The *weak form* of the governing equations require the calculation of the divergence of the pressure field and the velocity field. The divergence of the pressure field in cartesian coordinates is:

$$\nabla \cdot \mathbf{p} = \frac{\partial p_x}{\partial x} + \frac{\partial p_y}{\partial y} + \frac{\partial p_z}{\partial z} \tag{4.27}$$

where p_x, p_y and p_z are the components of the pressure field in cartesian coordinates, and the divergence of the velocity field in cartesian coordinates is:

$$\nabla \cdot \mathbf{v} = \frac{\partial v_x}{\partial x} + \frac{\partial v_z}{\partial z} \tag{4.28}$$

where v_x, v_y and v_z are the components of the velocity field in cartesian coordinates and there is no tangential velocity, i.e. $v_y = 0$. However, we require the divergence of the pressure field and velocity field in cylindrical coordinates. Examining the pressure field first, and looking at the gradient of the pressure field for reasons that will soon become apparent, following the derivation in Appendix C, the gradient of the pressure field is calculated in cylindrical coordinates as:

$$\frac{\partial p}{\partial \mathbf{x}} = \frac{\partial p}{\partial r}\hat{\mathbf{r}} + \frac{1}{r}\frac{\partial p}{\partial \phi}\hat{\phi} + \frac{\partial p}{\partial z}\hat{\mathbf{z}} \tag{4.29}$$

where $\hat{\mathbf{r}}$, $\hat{\phi}$ and $\hat{\mathbf{z}}$ are the unit vectors in cylindrical coordinates. Hence, the divergence of the pressure field in cylindrical coordinates, following Appendix C, is calculated as:

$$\nabla \cdot \mathbf{p} = \left(\frac{\partial p_r}{\partial r} + \frac{p_r}{r}\right) + \frac{1}{r}\frac{\partial p_\phi}{\partial \phi} + \frac{\partial p_z}{\partial z} \tag{4.30}$$

where p_r, p_ϕ and p_z are the components of the pressure field in cylindrical coordinates. Following a similar derivation, and assuming the tangential velocity is zero, i.e. $v_\phi = 0$, the divergence of the velocity field in cylindrical coordinates is:

$$\nabla \cdot \mathbf{v} = \left(\frac{\partial v_r}{\partial r} + \frac{v_r}{r}\right) + \frac{\partial v_z}{\partial z} \tag{4.31}$$

where v_r, v_ϕ and v_z are the components of the velocity field in cylindrical coordinates. Comparing the cartesian and cylindrical forms of the divergence of the two fields of interest, it

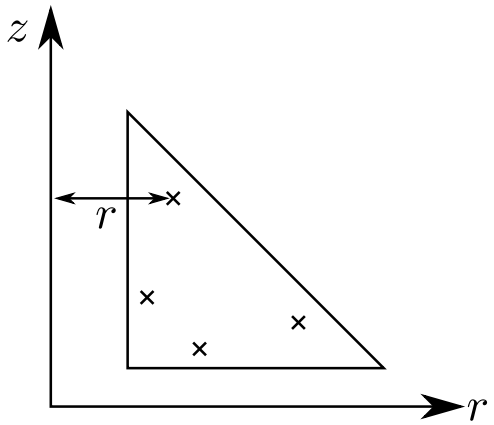

Figure 4.7: The radius of a Gauss point

can easily be seen that there is one additional term in each that requires to be calculated. It is of vital importance that these additional terms are included in the framework when changing to a cylindrical coordinate system.

4.7.2 Non-Linearity of the Radius and Normal

The above semi-discretised *weak form* of the conservation of mass and momentum is integrated over the volume of an element in a cartesian system. However, with the change to a cylindrical system, the *weak form* must now also be integrated radially, i.e. from 0 to $2\pi r$. Hence, the integral over the volume changes to a double integral, for example:

$$\int_V (\ldots)\, dV = 2\pi r \int_r \int_z (\ldots)\, dr dz \tag{4.32}$$

Care must be taken, however, due to the additional non-linearity provided from a constantly changing radius arising from the use of an UALE formulation. Furthermore, additional terms arise for the divergence of the pressure and the divergence of the velocity, Equations 4.30 and 4.31. Given that the symmetric part of the deviatoric stress tensor is dependent on the gradient of velocity, it would likewise require additional terms when in a cylindrical coordinate system. However, following the derivation in Appendix B, it becomes apparent that no additional terms are required.

The radius, r_{n+1}, is taken as the distance from each elemental Gauss point (four-point Gauss quadrature is used) to the vertical axis, see Figure 4.7. The radius changes as the mesh moves due to the use of an UALE formulation and so the radius is calculated as follows:

$$\begin{aligned} r_{n+1}^{i+1} &= r_n + \Delta r_{n+1} \\ &= r_n + \left(\hat{\mathbf{v}}_n^0 \Delta t + \Delta \hat{\mathbf{v}}_{n+1}^i \frac{\Delta t}{2} + \delta \hat{\mathbf{v}}_{n+1}^{i+1} \frac{\Delta t}{2} \right) \\ &= r_n + \frac{\Delta t}{2} \left(\hat{\mathbf{v}}_i \right)_r + \frac{\Delta t}{2} \left(\delta \hat{\mathbf{v}} \right)_r \end{aligned} \tag{4.33}$$

where r_n is the radius from the previous time step and the subscript $(\ldots)_r$ denotes only the radial component (i.e. the first component) of the mesh velocity is required. The second term in the above equation is considered when updating the coordinates (see Equation 4.4), and thus, the calculation of the radius reduces to:

$$r_{n+1}^{i+1} = r_n + \frac{\Delta t}{2} \left(\delta \hat{\mathbf{v}} \right)_r \tag{4.34}$$

and so:

$$2\pi r = 2\pi r_{n+1}^{i+1} = 2\pi r_n + \Delta t \pi \left(\delta \hat{\mathbf{v}} \right)_r \tag{4.35}$$

Therefore, after the integration from 0 to $2\pi r$ all existing terms will have two components, one dependent on the radius in the previous time step, and one dependent on the iterative change in mesh velocity in the radial direction. For force terms this will result in the scaling of the force vector by $2\pi r_n$ plus the creation of a new stiffness matrix due to the unknown iterative change in mesh velocity. The product of the iterative change in mesh velocity with itself is very small indeed and therefore negligible ($\delta \hat{\mathbf{v}} \cdot \delta \hat{\mathbf{v}} = 0$), and therefore for stiffness terms the second component is ignored.

Additionally, some of the new terms arising from the change to axisymmetry are divided by the radius. Taking the derivative of the inverse of the radius leads to:

$$\frac{d}{dr} \left(\frac{1}{r} \right) = -\frac{1}{r^2} \tag{4.36}$$

and linearising using a Taylor series expansion:

$$\left(\frac{1}{r} \right)_{n+1}^{i+1} = \frac{1}{r_n} - \frac{\Delta t}{2} \frac{1}{r_n^2} \left(\delta \hat{\mathbf{v}} \right)_r \tag{4.37}$$

The normal, $\mathbf{n}$, although unchanged from cartesian to cylindrical coordinate systems, is also constantly changing as the mesh moves. In an axisymmetric system, the coordinates of node k are given as (r_k, z_k) and the normal to the edge of an element defined by nodes 1 and 2 is

calculated from:

$$\mathbf{n} = \begin{bmatrix} z_1 - z_2 \\ r_2 - r_1 \end{bmatrix} = \begin{bmatrix} (z_1)_{n+1}^{i+1} - (z_2)_{n+1}^{i+1} \\ (r_2)_{n+1}^{i+1} - (r_1)_{n+1}^{i+1} \end{bmatrix} \tag{4.38}$$

where:

$$\begin{aligned} (z_1)_{n+1}^{i+1} &= (z_1)_n + \left(\hat{\mathbf{v}}_n^0\right)_1^z \Delta t + \left(\Delta\hat{\mathbf{v}}_{n+1}^i\right)_1^z \frac{\Delta t}{2} + \left(\delta\hat{\mathbf{v}}_{n+1}^{i+1}\right)_1^z \frac{\Delta t}{2} \\ &= (z_1)_n + (\hat{\mathbf{v}}_i)_1^z \frac{\Delta t}{2} + (\delta\hat{\mathbf{v}})_1^z \frac{\Delta t}{2} \\ &= (z_1)_n + (\delta\hat{\mathbf{v}})_1^z \frac{\Delta t}{2} \end{aligned} \tag{4.39}$$

and similar for the other coordinates. Therefore:

$$\begin{aligned} \mathbf{n} &= \begin{bmatrix} \left((z_1)_n + (\delta\hat{\mathbf{v}})_1^z \frac{\Delta t}{2}\right) - \left((z_2)_n + (\delta\hat{\mathbf{v}})_2^z \frac{\Delta t}{2}\right) \\ \left((r_2)_n + (\delta\hat{\mathbf{v}})_2^r \frac{\Delta t}{2}\right) - \left((r_1)_n + (\delta\hat{\mathbf{v}})_1^r \frac{\Delta t}{2}\right) \end{bmatrix} \\ &= \begin{bmatrix} (z_1 - z_2)_n \\ (r_2 - r_1)_n \end{bmatrix} + \frac{\Delta t}{2} \begin{bmatrix} (\delta\hat{\mathbf{v}})_1^z - (\delta\hat{\mathbf{v}})_2^z \\ (\delta\hat{\mathbf{v}})_2^r - (\delta\hat{\mathbf{v}})_1^r \end{bmatrix} \\ &= \bar{\mathbf{n}} + \frac{\Delta t}{2}\delta\bar{\mathbf{n}} \end{aligned} \tag{4.40}$$

where $(z_k)_n$ is the position of node z_k from the previous time step. Hence, any term containing the normal (see Chapter 6) will have two components; one from the previous state and one dependent on the iterative change in mesh velocity. As before, this second component is negligible for stiffness terms, but in the case of force terms, the second component results in the creation of new stiffness terms.

Additionally, when assessing singular edges of an element, the radius is measured from the centre of the linear element to the vertical radial axis, see Figure 4.8. In this case, the radius is found from:

$$r_{n+1} = \frac{(r_1)_{n+1}^{i+1} + (r_2)_{n+1}^{i+1}}{2} \tag{4.41}$$

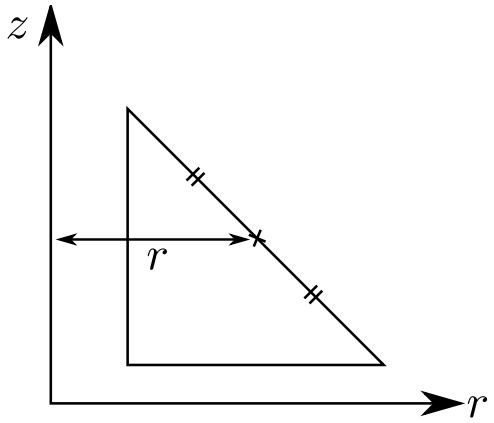

Figure 4.8: Axisymmetric finite element, r depicts the radius

where:

$$\begin{aligned}(r_1)_{n+1}^{i+1} &= r_1 + \left(\hat{\mathbf{v}}_n^0\right)_1^r \Delta t + \left(\Delta\hat{\mathbf{v}}_n^0\right)_1^r \frac{\Delta t}{2} + \left(\delta\hat{\mathbf{v}}_n^0\right)_1^r \frac{\Delta t}{2} \\ &= r_1 + (\delta\hat{\mathbf{v}})_1^r \frac{\Delta t}{2} \end{aligned} \tag{4.42}$$

and therefore:

$$\begin{aligned} r_{n+1} &= \frac{r_1 + (\delta\hat{\mathbf{v}})_1^r \frac{\Delta t}{2} + r_2 + (\delta\hat{\mathbf{v}})_2^r \frac{\Delta t}{2}}{2} \\ &= \frac{r_1 + r_2}{2} + \frac{\Delta t}{4}\left((\delta\hat{\mathbf{v}})_1^r + (\delta\hat{\mathbf{v}})_2^r\right) \\ &= r_n + \frac{\Delta t}{4}\delta r \end{aligned} \tag{4.43}$$

Hence:

$$2\pi r_{n+1} = 2\pi r_n + \frac{\Delta t}{2}\pi\delta r \tag{4.44}$$

4.8 Time and Space Discretised Weak Form

Integrating the semi-discretised *weak form* of the conservation of mass in Equation 4.17 from 0 to $2\pi r$ (using Equation 4.35) and including the additional term in the calculation of the divergence of the velocity (Equation 4.31), after some extensive mathematics (see Appendix D), the finalised *weak form* becomes:

$$
\begin{aligned}
R_v(\mathbf{v},\hat{\mathbf{v}}) &= 2\pi\int_r\int_z \mathbf{w_p} r_n \frac{\partial \mathbf{v}_i}{\partial \chi} : \mathbf{I}\,dr dz + \Delta t\pi \int_r\int_z \mathbf{w_p}\frac{\partial \mathbf{v}_i}{\partial \chi} : \mathbf{I}\mathbf{N_r}\underline{\delta\hat{\mathbf{v}}}dr dz \\
&\quad +2\pi\int_r\int_z \mathbf{w_p} r_n \frac{\partial \mathbf{N}}{\partial \chi} : \mathbf{I}\underline{\delta\mathbf{v}}dr dz - 2\pi\int_r\int_z \mathbf{w_p} r_n \frac{\Delta t}{2}\left[\frac{\partial \mathbf{v}_i}{\partial \chi}\right]^{\mathrm{T}} : \frac{\partial \mathbf{N}}{\partial \chi}\underline{\delta\hat{\mathbf{v}}}dr dz \\
&\quad +2\pi\int_r\int_z \mathbf{w_p}\cdot(v_i)_r dr dz + 2\pi\int_r\int_z (\mathbf{w_p}\cdot\mathbf{N_r})\,\underline{\delta\mathbf{v}}dr dz
\end{aligned} \tag{4.45}
$$

which, with some rearranging, simplifies to:

$$
R_v(\mathbf{v},\hat{\mathbf{v}}) = \mathbf{f_{pv}} + \mathbf{f_{pv}^{axi}} + \left(\mathbf{K_{pv}} + \mathbf{K_{pv}^{axi}}\right)\underline{\delta\mathbf{v}} + \left(\mathbf{K_{p\hat{v}}} + \mathbf{K_{pv}^{fr}}\right)\underline{\delta\hat{\mathbf{v}}} \tag{4.46}
$$

where $\mathbf{K}_{...}$ is a stiffness matrix, $\mathbf{f}_{...}$ is a force vector, $\mathbf{N}$ is the element shape functions, $\mathbf{N_r}$ is the radial component (i.e. the first component) of the element shape functions, and $\underline{\delta\mathbf{v}}$ and $\underline{\delta\hat{\mathbf{v}}}$ are the unknown vectors of fluid and mesh velocity. Applying the same steps to the semi-discretised *weak form* of the conservation of momentum in Equation 4.22, and including the additional term in the calculation of the divergence of the pressure (Equation 4.30) and the full form of the acceleration from Equation 4.13, after some extensive mathematics (see Appendix D), the finalised form becomes:

$$
\begin{aligned}
R_v(\mathbf{v},\hat{\mathbf{v}},p) \;=\;& 2\pi\int_r\int_z r_n\rho\mathbf{w_v}\left(\frac{\Delta\mathbf{v}}{\Delta t}+\frac{\partial\mathbf{v}_i}{\partial\chi}(\mathbf{v}_i-\hat{\mathbf{v}}_i)\right)-r_n(\mathbf{w_v}\cdot\mathbf{b})\,dVrdz\\
&+\Delta t\pi\int_r\int_z\left(\rho\mathbf{w_v}\left(\frac{\Delta\mathbf{v}}{\Delta t}+\frac{\partial\mathbf{v}_i}{\partial\chi}(\mathbf{v}_i-\hat{\mathbf{v}}_i)\right)-\mathbf{w_v}\cdot\mathbf{b}\right)\mathbf{N_r}\underline{\delta\hat{\mathbf{v}}}drdz\\
&+2\pi\int_r\int_z r_n\rho\mathbf{w_v}\left(\frac{\mathbf{N}}{\Delta t}+\frac{\partial\mathbf{v}_i}{\partial\chi}\mathbf{N}+\frac{\partial\mathbf{N}}{\partial\chi}(\mathbf{v}_i-\hat{\mathbf{v}}_i)\right)\underline{\delta\mathbf{v}}drdz\\
&+2\pi\int_r\int_z r_n\rho\mathbf{w_v}\left(\frac{\Delta t}{2}\frac{\partial\mathbf{v}_i}{\partial\chi}\frac{\partial\mathbf{N}}{\partial\chi}(\hat{\mathbf{v}}_i-\mathbf{v}_i)-\frac{\partial\mathbf{v}_i}{\partial\chi}\mathbf{N}\right)\underline{\delta\hat{\mathbf{v}}}drdz\\
&-2\pi\int_r\int_z r_n\frac{\partial\mathbf{w_v}}{\partial\chi}:\mathbf{I}p_i drdz-\Delta t\pi\int_r\int_z\left(\frac{\partial\mathbf{w_v}}{\partial\chi}:\mathbf{I}p_i\right)\mathbf{N_r}\underline{\delta\hat{\mathbf{v}}}drdz\\
&-2\pi\int_r\int_z r_n\frac{\partial\mathbf{w_v}}{\partial\chi}:\mathbf{I}\mathbf{N}\underline{\delta p}drdz+2\pi\int_r\int_z r_n\frac{\Delta t}{2}\left[\frac{\partial\mathbf{w_v}}{\partial\chi}\right]^{\mathrm{T}}:p_i\frac{\partial\mathbf{N}}{\partial\chi}\underline{\delta\hat{\mathbf{v}}}drdz\\
&+2\pi\int_r\int_z 2\mu r_n\frac{\partial\mathbf{w_v}}{\partial\chi}:(\mathbf{e}_i+\delta\mathbf{e}+\delta\hat{\mathbf{e}})\,drdz\\
&+\Delta t\pi\int_r\int_z\left(2\mu\frac{\partial\mathbf{w_v}}{\partial\chi}:\mathbf{e}_i\right)\mathbf{N_r}\underline{\delta\hat{\mathbf{v}}}drdz\\
&-2\pi\int_r\int_z 2\mu r_n\frac{\Delta t}{2}\left(\frac{\partial\mathbf{w_v}}{\partial\chi}(\mathbf{e}_i)^{\mathrm{T}}\right):\frac{\partial\mathbf{N}}{\partial\chi}\underline{\delta\hat{\mathbf{v}}}drdz-2\pi\int_r\int_z(w_v\cdot p_i)_r\,drdz\\
&-2\pi\int_r\int_z(w_v\cdot\mathbf{N_r})\,\underline{\delta p}drdz+2\pi\int_r\int_z\frac{2\mu}{r_n}(w_v\cdot v_i)_r\,drdz\\
&-2\pi\int_r\int_z\frac{\mu\Delta t}{r_n^2}(w_v\cdot v_i)_r\mathbf{N_r}\underline{\delta\hat{\mathbf{v}}}drdz+2\pi\int_r\int_z\frac{2\mu}{r_n}(w_v\cdot\mathbf{N_r})\,\underline{\delta\mathbf{v}}drdz \qquad (4.47)
\end{aligned}
$$

In the framework adopted, one solves for velocities and not accelerations, therefore the change in acceleration requires to be written in terms of velocity. One can write the acceleration as the time-derivative of the time-averaged velocity, where v_{n-1} is the previous velocity and v_n is the current velocity.

$$
\mathbf{a}=\frac{\partial\mathbf{v}}{\partial t}=\frac{\partial}{\partial t}\left(\frac{(v_{n-1}+v_n)}{2}\right)\Longrightarrow\delta a=\frac{\delta\mathbf{v}}{2\Delta t} \qquad (4.48)
$$

Equation 4.47 simplifies to (see Appendix D):

$$\begin{aligned} R_v(\mathbf{v},\hat{\mathbf{v}},p) &= \frac{1}{2\Delta t}\left(\mathbf{M_{vv}}\underline{\delta \mathbf{v}_i}+\mathbf{M_{v\hat{v}}}\underline{\delta \hat{\mathbf{v}}}\right)+\left(\mathbf{K_{vv}}+\mathbf{K_{vv}^{axi}}\right)\underline{\delta \mathbf{v}_i}+\left(\mathbf{K_{vp}}+\mathbf{K_{vp}^{axi}}\right)\underline{\delta p} \\ &+\left(\mathbf{K_{vp\hat{v}}}+\mathbf{K_{v\hat{v}}}+\mathbf{K_{v\hat{v}}^{axi}}+\mathbf{K_{vv}^{fr}}+\mathbf{K_{vm}^{fr}}+\mathbf{K_{vp}^{fr}}\right)\underline{\delta \hat{\mathbf{v}}} \\ &+\mathbf{f_{vv}}+\mathbf{f_{vv}^{axi}}+\mathbf{f_{vm}}+\mathbf{f_{vp}}+\mathbf{f_{vp}^{axi}} \end{aligned} \tag{4.49}$$

where $\mathbf{M}_{...}$ is a mass matrix and $\underline{\delta p}$ is the unknown vector of fluid pressure. In diagrammatic form, the system of governing equations derived thus far is shown below:

$$\begin{bmatrix} \mathbf{A_{vv}} & \mathbf{A_{vp}} & \mathbf{A_{v\hat{v}}} \\ \mathbf{A_{pv}} & \mathbf{A_{pp}} & \mathbf{A_{p\hat{v}}} \\ \mathbf{A_{\hat{v}v}} & \mathbf{A_{\hat{v}p}} & \mathbf{A_{\hat{v}\hat{v}}} \end{bmatrix} \begin{bmatrix} \underline{\delta \mathbf{v}} \\ \underline{\delta \mathbf{p}} \\ \underline{\delta \hat{\mathbf{v}}} \end{bmatrix} = - \begin{bmatrix} \mathbf{F_v} \\ \mathbf{F_p} \\ \mathbf{F_{\hat{v}}} \end{bmatrix}$$

Figure 4.9: Diagrammatic form of the system of governing equations

where $\underline{\delta \mathbf{v}}$, $\underline{\delta \mathbf{p}}$ and $\underline{\delta \hat{\mathbf{v}}}$ are the unknown iterative updates to the nodal fluid velocity, fluid pressure and mesh velocity and:

$$\mathbf{A_{vv}} = \frac{\mathbf{M_{vv}}}{2\Delta t}+\mathbf{K_{vv}}+\mathbf{K_{vv}^{axi}} \tag{4.50}$$

$$\mathbf{A_{vp}} = \mathbf{K_{vp}}+\mathbf{K_{vp}^{axi}} \tag{4.51}$$

$$\mathbf{A_{v\hat{v}}} = \frac{\mathbf{M_{v\hat{v}}}}{2\Delta t}+\mathbf{K_{v\hat{v}}}+\mathbf{K_{v\hat{v}}^{axi}}+\mathbf{K_{vp\hat{v}}}+\mathbf{K_{vv}^{fr}}+\mathbf{K_{vm}^{fr}}+\mathbf{K_{vp}^{fr}} \tag{4.52}$$

$$\mathbf{A_{pv}} = \mathbf{K_{pv}}+\mathbf{K_{pv}^{axi}} \tag{4.53}$$

$$\mathbf{A_{pp}} = 0 \tag{4.54}$$

$$\mathbf{A_{p\hat{v}}} = \mathbf{K_{p\hat{v}}}+\mathbf{K_{pv}^{fr}} \tag{4.55}$$

$$\mathbf{A_{\hat{v}p}} = 0 \tag{4.56}$$

$$\mathbf{F_v} = \mathbf{f_{vv}} + \mathbf{f_{vv}^{axi}} + \mathbf{f_{vm}} + \mathbf{f_{vp}} + \mathbf{f_{vp}^{axi}} \tag{4.57}$$

$$\mathbf{F_p} = \mathbf{f_{pv}} + \mathbf{f_{pv}^{axi}} \tag{4.58}$$

Additional terms will be added to some of the above groups in the following chapters. The first row of global system is reserved for momentum terms and the second row is reserved for mass terms and pressure stabilisation terms. In the third row, the term $\mathbf{A_{\hat{v}p}}$ is zero for all entries, the terms $\mathbf{A_{\hat{v}\hat{v}}}$ and $\mathbf{F_{\hat{v}}}$ are reserved for mesh improvement, and the term $\mathbf{A_{\hat{v}v}}$ is involved with the ALE formulation.

4.9 Mesh Optimisation via Laplacian Smoothing

The quality of the FE mesh must be maintained to prevent highly distorted elements effecting the solution and as such Laplacian smoothing has been implemented to optimise the mesh. Laplacian smoothing is widely used to calculate the updated nodal positions in a monolithic ALE formulation (M-ALE). Essentially, Laplacian smoothing changes the position of nodes without changing the mesh connectivity. Internal nodes are moved to a position that is the average of the neighbouring nodes. Figure 4.10 demonstrates that Laplacian smoothing is optimising the mesh throughout an analysis, aiming to achieve equal distances between nodes at all times.

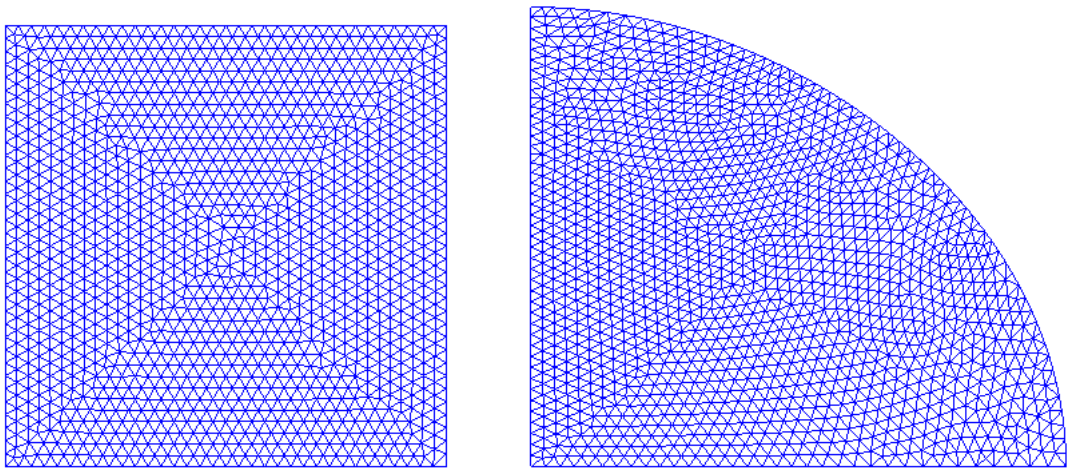

(a) Initial mesh (b) Mesh at equilibrium

Figure 4.10: Example of mesh optimisation using Laplacian smoothing; note the approximate equal distance between mesh nodes

The implementation of Laplacian smoothing in this thesis is straightforward but requires the

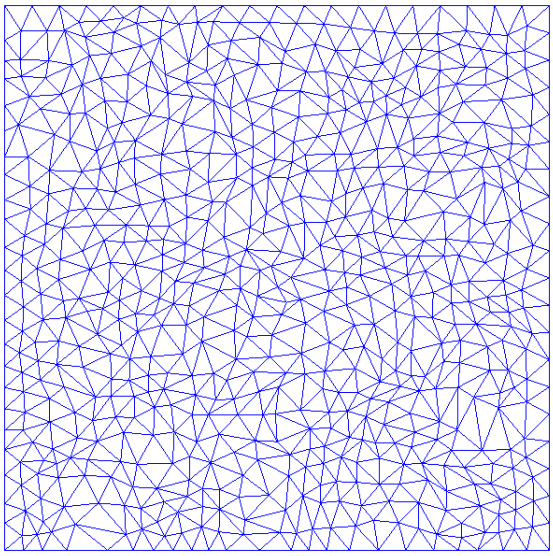

Figure 4.11: Inappropriate choice of mesh viscosity

use of a user defined variable called the mesh viscosity, μ_{mesh}. The mesh viscosity controls the speed at which the mesh moves independently from the fluid. Trial and error is required to obtain a value of μ_{mesh} that is sufficient in allowing the mesh to move not too quickly nor too slowly. This can be very difficult in situations where different parts of the fluid are moving at different speeds. Figure 4.11 demonstrates the effect a poor choice of mesh viscosity has on the mesh; notice several areas of severe mesh distortion. Additionally many elements have low interior angles and this creates problems in terms of discretisation errors, interpolation errors and conditioning of the stiffness matrix.

Alongside the difficulty in selecting a value of mesh viscosity, there are several other disadvantages of the current implementation:

- analyses terminate prematurely due to issues with the mesh, primarily due to μ_{mesh} and a high number of edge flips,
- excessive and unnecessary nodal displacements can be induced in a mesh because Laplacian smoothing wrongly assumes a good mesh must have equidistant nodes,
- every nodal displacement produces non-linearities which have a negative effect on the rate of convergence and the efficiency of the solution,
- Laplacian smoothing is not effective for non-convex domains as elements can become inverted,

- Laplacian smoothing is also not effective in 3D, causing mesh shrinkage after repeated iterations,
- local mesh refinement is not possible.

In addition to Laplacian smoothing, a simple mesh refinement algorithm is also used in the computational framework. The algorithm loops over all edges in the FE mesh and for each edge, calculates the ratio of the current length of the edge to the average edge length at the beginning of the analysis. If an edge has a high ratio, a new node is added at the midpoint of the edge, and if an edge has a low ratio, one of the two nodes on this edge is deleted from the mesh. The degrees of freedom of new nodes are interpolated from the original nodes on the edge. Whilst this process is not entirely physical as elements can be created or destroyed thus effecting the volume of fluid, element distortion is kept to a minimum. The point at which to decide if an edge is too long or too short is entirely subjective and some fine-tuning is required.

With these drawbacks in mind, and the desire to extend this framework into 3D in the future, Kelly [36] has proposed two alternative methods, mesh quality improvement and mesh quality preservation. The former uses an area-length ratio quality measure to calculate the quality of an element and an objective function that uses a log-barrier to penalise the worst elements in the mesh. A log-barrier function expresses the quality of every element as a function of the worst element in the solution space. This method was successful in reducing the level of remeshing and reducing volume loss, however, there was a major detrimental effect on the average time step and therefore this method was deemed too aggressive in this setting. The latter uses the same area-length ratio quality measure as previously to relate the current quality to the initial quality on an element-by-element basis, before being substituted into the same objective function. This means that if an element's quality remains constant, no attempt is made to improve it. This method almost eradicated volume loss, whilst the time step was much closer to that experienced when using Laplacian smoothing. However, due to the reduction in time step, Laplacian smoothing is recommended until the framework extends to 3D problems. However all analyses undertaken in this thesis will make use of Laplacian smoothing.

4.10 Conclusions

This chapter has discussed the kinematic description selected and the solution scheme adopted to solve the Navier-Stokes equations for an incompressible Newtonian fluid. A semi-

discretised *weak form* of the conservation of mass and momentum for a cartesian coordinate system were developed based upon this solution scheme before being further developed into an axisymmetric system that is implemented in the computational framework. The extension from cartesian to axisymmetric form of the Navier-Stokes equations takes account of integrating over the radial domain whilst acknowledging the non-linearity of the radius and normal due to an UALE formulation and the additional terms required when calculating the gradient of the velocity and the gradient of the pressure.

Lastly, the Laplacian smoothing method of mesh optimisation was outlined and an example of the type of mesh produced was shown. The importance of the mesh viscosity variable was highlighted alongside other disadvantages. Whilst the Laplacian smoothing algorithm is straightforward and produces good meshes, ultimately it must be replaced before the framework can be extended into 3D.

Chapter 5

Fluids at the Micro-scale

The objective of this chapter is to present the underlying physics behind the micro-scale behaviour of fluids. The Young-Laplace equation and Young's equation will be discussed in detail with emphasis on the influence of surface tension at micro-scale. Some examples of surface tension in action will also be presented. In particular, the computational model developed in the previous chapters will be extended to incorporate surface tension.

5.1 Surface Tension Phenomenon

The phenomenon of surface tension surrounds us in our everyday lives. Surface tension is a property of the fluid surface, caused by molecular cohesion, that allows the fluid to resist external force. Molecules in the main body of fluid are completely surrounded by similar molecules and are pulled equally in every direction resulting in a zero net force. However, molecules on the fluid surface are only surrounded on one side and therefore have a non-zero net force and will be pulled downwards towards the main fluid body, Figure 5.1. This is surface tension and manifests in a curving of the fluid surface. The surface tension of a droplet is powerful enough to govern the shape, size and behaviour of the droplet; in zero-gravity environments droplets will conform to near perfect spheres, this being the shape with the minimum surface area and therefore the minimum out-of-balance force. Surface tension is measured in force per unit length and its value depends on the fluid type and temperature, with the surface tension increasing with decreasing temperature. Surface tension is negligible at very large scales; however, in the context of this work, micro-scale droplets (10^{-9} L to

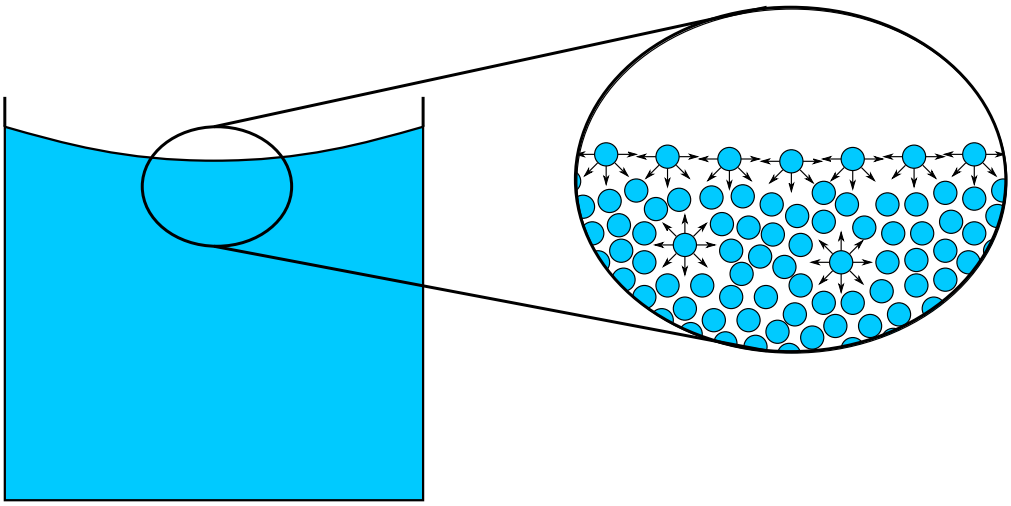

Figure 5.1: Water at molecular level

10^{-6} L) will be examined and at this scale, surface tension is by far the most dominant force and is extremely important in the determination of droplet shape and motion.

Surface tension plays a huge role in our everyday lives. From drinking a glass of wine to washing the dishes, from insects landing on the surface of a pond to its role within our blood cells, without surface tension life could not exist. See Figure 5.2 for some examples of surface tension.

5.1.1 Surface Tension and Wetting

Young (1773-1829) was the first person to develop a theory on surface tension, although Hauksbee (1660-1713) was one of the first to conduct experiments and make observations. Jurin (1684-1750) repeated the experiments of Hauksbee and observed that the height of fluid in a capillary tube is inversely proportional to the diameter of the tube. Laplace (1749-1827) produced a mathematical description of the theory developed by Young. Gauss (1777-1855) unified the work of Young and Laplace, and using the principle of virtual work derived by Johann Bernoulli (1667-1748), derived both the differential equation and boundary conditions. The Young-Laplace equation is a nonlinear partial differential equation that describes the pressure difference, Δp, across an interface between two fluids.

$$\Delta p = -\gamma \nabla \cdot \mathbf{n} = 2\gamma H = \gamma \left(\frac{1}{R_1} + \frac{1}{R_2} \right) \tag{5.1}$$

(a) Droplets of water falling from a tap [4]

(b) Bubbles in washing up liquid [3]

(c) Wasp resting on water surface [8]

(d) Water droplets on a leaf [10]

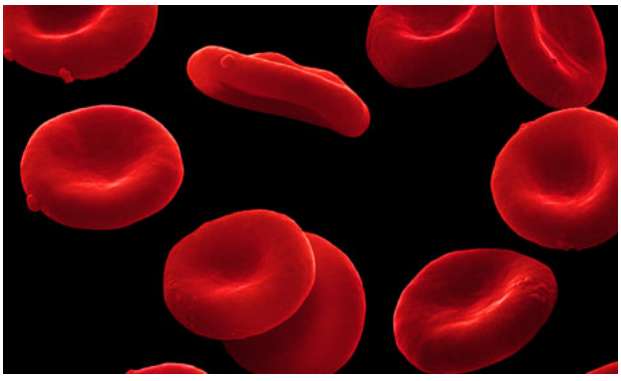

(e) Red blood cells [61]

Figure 5.2: Examples of surface tension in everyday life

where γ is the surface tension parameter, $\mathbf{n}$ is the unit normal to the interface, H is the mean curvature of the interface and R_1 and R_2 are the principal radii of curvature. Thus it can be seen that the pressure difference is a function of the surface tension of the fluid and the geometry of the interface. As a consequence of the pressure difference being dependent on the curvature of the interface, the angle at which the interface lies is also important. Known as the equilibrium contact angle, it is the angle at which the two fluids meet when in an equilibrium state and Young's equation describes the relationship between the surface tensions of the solid, liquid and gas phases in terms of this angle:

$$\gamma_{SG} = \gamma_{SL} + \gamma_{LG} \cos \alpha_e \tag{5.2}$$

where α_e is the equilibrium contact angle, γ_{SG} is the surface tension between the solid-gas interface, γ_{SL} is the surface tension between the solid-liquid interface, and finally γ_{LG} is the surface tension between the liquid-gas interface. Tadmor [62], however, argues that droplets have a range of contact angles, ranging from the advancing contact angle θ_A to the receding contact angle θ_R, the respective maximum and minimum obtainable angles. Imperfections in the smoothness of the solid surface causes differences in the three-phase contact line, the line at which air, water and the solid surface meet. This in turn causes the angle to change depending on local conditions. Thus, it is very important to take into consideration the condition of the solid surface and any imperfections in the surface.

Here it is necessary to define hydrophobic and hydrophilic surfaces. A hydrophobic surface is a surface that is difficult to wet as fluid molecules are repelled by the molecules composing the surface. Liquids resting on such surfaces have high contact angles, for example water droplets on ceramic surfaces. Conversely, hydrophilic surfaces are very easy to wet as they are composed of molecules that attract liquid molecules, and as such, liquids resting on hydrophilic surfaces have low contact angles. An example would be water droplets resting on a polymer. In general for contact angles less than 90° surfaces are considered hydrophilic, and greater than 90° surfaces are considered hydrophobic, see Figure 5.3. The leaves of the Lotus plant are considered to be superhydrophobic surfaces because water droplets resting on the leaves have contact angles greater than 150°.

5.1.2 The Effect of Surfactants on Surface Tension

Everyday household products such as soaps, detergents and emulsions are classed as surfactants. Surfactants contain both a water soluble and a water insoluble part since they are comprised of both hydrophilic and hydrophobic components, see Figure 5.4. Compounds

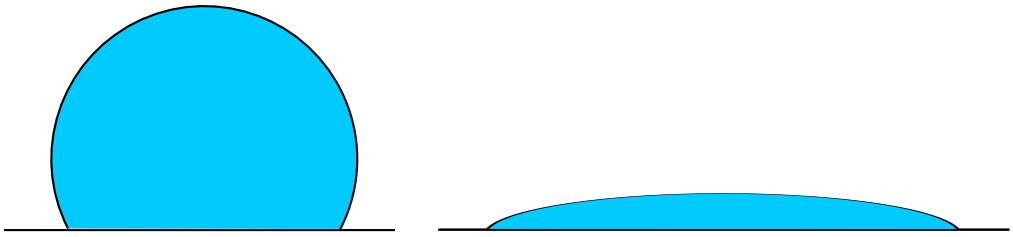

(a) Hydrophobic surface (b) Hydrophilic surface

Figure 5.3: Example of hydrophobic and hydrophilic surfaces

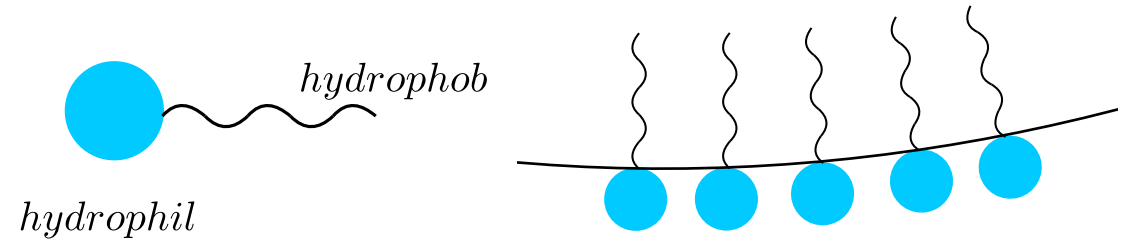

(a) Surfactant with hydrophilic head and hydrophobic tail (b) Surfactant interaction with water

Figure 5.4: Surfactants

with both hydrophilic and hydrophobic parts are termed amphiphilic. Surfactants will adsorb at interfaces between air and water and will diffuse in water. The result is a change in the properties of the water at the surface; surface tension will be reduced by a third or more depending on the concentration of the surfactant. This lowering of surface tension plays a key role in cleaning and washing, paint, ink, toothpaste, shampoo and many more household items and industrial processes. For example, insoluble particles become soluble in water after the addition of soap, and these newly water soluble particles can then be washed away.

5.1.3 Capillary Action

Capillary action is the ability of a liquid to flow through narrow vertical channels. The liquid flows in opposition to gravity, and this is caused by intermolecular forces between the liquid and the surrounding surfaces. If the diameter of a vertical channel is small enough, the combination of adhesive forces and cohesive forces (i.e. surface tension) between the channel and the liquid cause the liquid to rise within the channel. Examples of capillary action can be found in nature and in the human body; for example, plants use capillaries to move water from the ground to the tip of the highest leaf. The height of the meniscus in a capillary tube, Figure 5.5, is found from Equation 5.3 [16], where γ is surface tension, α is the contact angle, ρ is the fluid density, g is gravitational acceleration and r is the radius of

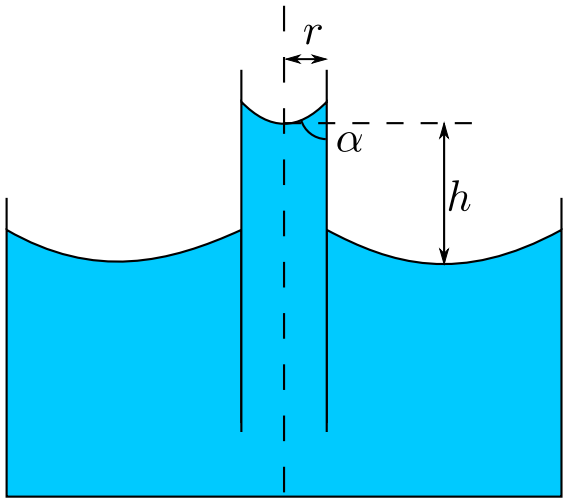

Figure 5.5: Capillary tube in a beaker of water

the tube.

$$h = \frac{2\gamma\cos\alpha}{\rho g r} \tag{5.3}$$

Therefore, the narrower the capillary tube, the higher the liquid will rise. Only the contact angle between the meniscus in the tube and the tube walls is required in the calculation, however, there are of course two additional contact angles in the system shown in Figure 5.5; between the outside wall of the tube and the beaker meniscus, and between the beaker wall and beaker meniscus.

5.2 Surface Tension and Contact Line Contributions

The following contributions to the system of equations from the surface tension force and contact line force have been derived by Saksono and Perić directly from the Young-Laplace equation. Refer to [57] for more detail.

5.2.1 Development of the Space and Time Discretised Form

The Cauchy stress tensor $\sigma(\mathbf{x},t)$ is defined such that $\mathbf{t}(\mathbf{x},t,\mathbf{n}) = \sigma\mathbf{n}$ where $\mathbf{t}(\mathbf{x},t,\mathbf{n})$ is the traction unit vector and $\mathbf{n}$ is the unit normal. Recalling the Young-Laplace equation, Equation 5.1:

$$\Delta p = 2\gamma H \tag{5.4}$$

The mean curvature can be defined in terms of the surface gradient operator ∇_s:

$$H = -\frac{\nabla_s \cdot \mathbf{n}}{2} \tag{5.5}$$

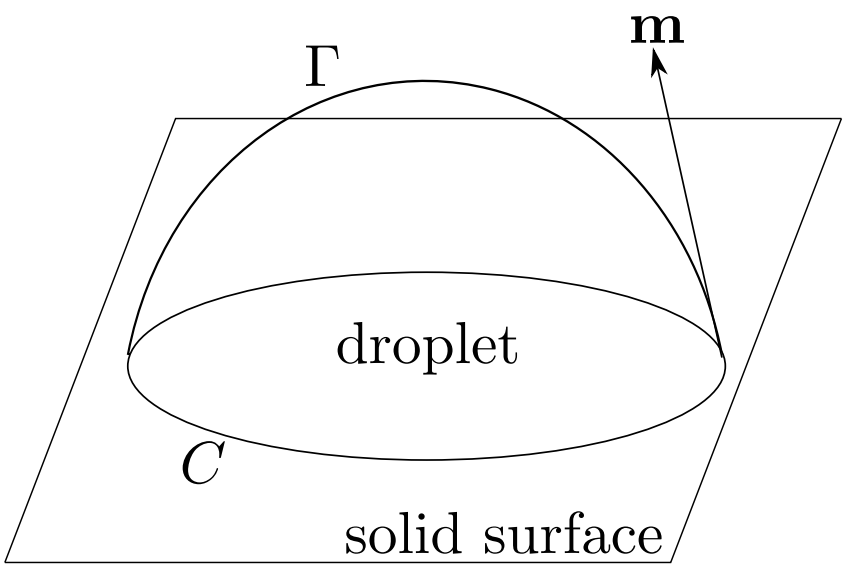

Figure 5.6: Typical droplet showing boundary curve C, droplet surface Γ and the binormal of the boundary curve $\mathbf{m}$

Therefore:

$$\Delta p = -\gamma \nabla_s \cdot \mathbf{n} \tag{5.6}$$

where $\nabla_s = (\mathbf{I} - \mathbf{n} \otimes \mathbf{n}) \nabla$. Expressing the pressure difference as the difference between the external pressure p_{ext} and internal pressure p_{int}, it is possible to express the continuity of forces across the fluid-gas interface as:

$$\sigma \mathbf{n} = -p_{\text{int}} \mathbf{n} = -p_{\text{ext}} \mathbf{n} + 2\gamma H \mathbf{n} \qquad \text{on } \Gamma \tag{5.7}$$

where Γ is the surface of the domain. The *weak form* of the right hand side of this momentum balance equation leads to the following expression:

$$\int_\Gamma p_{\text{ext}} \mathbf{n} \cdot \mathbf{w} da - \int_\Gamma 2\gamma H \mathbf{n} \cdot \mathbf{w} da \tag{5.8}$$

where $\mathbf{w}$ is a weighting function. The first integral has already been considered within the Navier-Stokes equations (Section 3.2.3) and therefore only the second integral is developed further here. Using the divergence theorem on the surface Γ, see Weatherburn [68], the second integral becomes:

$$-\int_\Gamma 2\gamma H \mathbf{n} \cdot \mathbf{w} da = \int_\Gamma \gamma \nabla_s \cdot \mathbf{w} da - \int_C \gamma \mathbf{w} \cdot \mathbf{m} ds \tag{5.9}$$

where C is the boundary curve of the surface Γ and $\mathbf{m}$ is the binormal of C, a vector tangent to the surface and orthogonal to the curve, see Figure 5.6. Following standard procedure, the

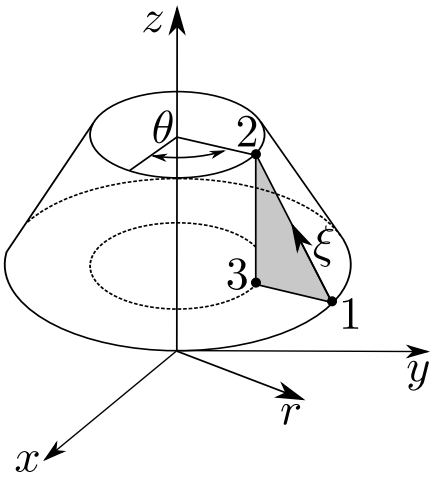

Figure 5.7: Axisymmetric triangular element

finite element form of these two new integrals gives the final form to include in the system of equations. The first integral on the right hand side of Equation 5.9 represents the contribution from the surface tension force, whilst the second integral represents the contribution from the contact line force:

$$\int_\Gamma \gamma \nabla_s \cdot \mathbf{w} da \Rightarrow \int_\Gamma \gamma \{\nabla_s \cdot \mathbf{N}_{12}\} da = \mathbf{F}^{\mathbf{ST}} \tag{5.10}$$

$$\int_C \gamma \mathbf{w} \cdot \mathbf{m} ds \Rightarrow \int_C \gamma [\mathbf{N}_1]^{\mathrm{T}} \{\mathbf{m}\} ds = \mathbf{F}^{\mathbf{CL}} \tag{5.11}$$

with $\mathbf{N}_{12}$ and $\mathbf{N}_1$ representing the FE shape functions for a linear element and a node respectively, and $\mathbf{F}^{\mathbf{ST}}$ and $\mathbf{F}^{\mathbf{CL}}$ representing the surface tension and contact line force vectors. Thus, the surface tension force is an internal force integrated over the surface of the domain, and the contact line force is an external force integrated over the contact line. It can be seen that Equations 5.10 and 5.11 have been derived from the Young-Laplace equation which was previously found to describe the pressure difference across an interface in terms of the mean curvature H. Thus, these equations are directly related to the curvature of the interface.

5.2.2 Surface Tension Force Contributions

The problems to be assessed are all axisymmetric in nature, i.e. both the structure and loading are axisymmetric and every radial plane is assumed to act identically with deformation only allowed in plane (r-z plane). In an axisymmetric analysis, both the out-of-plane stress and out-of-plane strain are non-zero. Consider a three-noded element with nodes 1, 2, 3, with nodes 1 and 2 on the fluid surface as shown in Figure 5.7. Line 1-2 is therefore subject to surface tension. The shape function matrix for the surface of revolution generated by line

1-2, $\mathbf{N}_{12}$ is:

$$\mathbf{N}_{12}(\xi,\theta) = \begin{bmatrix} \frac{1}{2}(1-\xi)\cos\theta & 0 & \frac{1}{2}(1+\xi)\cos\theta & 0 \\ \frac{1}{2}(1-\xi)\sin\theta & 0 & \frac{1}{2}(1+\xi)\sin\theta & 0 \\ 0 & \frac{1}{2}(1-\xi) & 0 & \frac{1}{2}(1+\xi) \end{bmatrix} \tag{5.12}$$

The position of a single point on this line can be expressed:

$$\mathbf{x}(\xi,\theta) = \mathbf{N}_{12} \begin{bmatrix} r_1 \\ z_1 \\ r_2 \\ z_2 \end{bmatrix} \tag{5.13}$$

where the angular component is constant, because nodes 1, 2 and 3 are in plane, and therefore not included. The coordinates of node k are represented by (r_k, z_k). A metric tensor which we use to measure distances in cylindrical space is defined by Weatherburn [68]:

$$A_{\mathrm{mt}} = \frac{\partial^2 \mathbf{x}}{\partial \xi^2} \qquad B_{\mathrm{mt}} = \frac{\partial^2 \mathbf{x}}{\partial \theta^2} \tag{5.14}$$

The three-noded element can be divided into a number of very small elemental areas da each given by:

$$da = \sqrt{A_{\mathrm{mt}} B_{\mathrm{mt}}}\, d\xi\, d\theta \tag{5.15}$$

For the axisymmetric surface in consideration, the surface gradient, from Weatherburn [68] and derived in Appendix E, takes the form:

$$\nabla_s = \frac{1}{A_{\mathrm{mt}}} \frac{\partial \mathbf{x}(\xi,\theta)}{\partial \xi} \frac{\partial}{\partial \xi} + \frac{1}{B_{\mathrm{mt}}} \frac{\partial \mathbf{x}(\xi,\theta)}{\partial \theta} \frac{\partial}{\partial \theta} \tag{5.16}$$

Hence:

$$\nabla_s \cdot \mathbf{N}_{12} = \frac{1}{A_{\mathrm{mt}}} \frac{\partial \mathbf{N}_{12}^{\mathrm{T}}}{\partial \xi} \frac{\partial \mathbf{x}(\xi,\theta)}{\partial \xi} + \frac{1}{B_{\mathrm{mt}}} \frac{\partial \mathbf{N}_{12}^{\mathrm{T}}}{\partial \theta} \frac{\partial \mathbf{x}(\xi,\theta)}{\partial \theta} \tag{5.17}$$

Refer to Appendix E for the derivation of the terms A_{mt} and B_{mt} and the derivatives of ${\mathbf{N}_{12}}^{\mathrm{T}}$. Therefore, the surface tension force vector is calculated from:

$$\begin{aligned}
\mathbf{F}^{\mathbf{ST}} &= \int_{\Gamma} \{\nabla_s \cdot \mathbf{N}_{12}\}\, da \\
&= \int_{-1}^{1}\int_{0}^{2\pi} \left\{ \frac{1}{A_{\mathrm{mt}}} \frac{\partial \mathbf{N}_{12}^{\mathrm{T}}}{\partial \xi} \frac{\partial \mathbf{x}(\xi,\theta)}{\partial \xi} + \frac{1}{B_{\mathrm{mt}}} \frac{\partial \mathbf{N}_{12}^{\mathrm{T}}}{\partial \theta} \frac{\partial \mathbf{x}(\xi,\theta)}{\partial \theta} \right\} \sqrt{A_{\mathrm{mt}} B_{\mathrm{mt}}}\, d\xi\, d\theta \\
&= \int_{-1}^{1}\int_{0}^{2\pi} \left\{ \frac{\sqrt{A_{\mathrm{mt}} B_{\mathrm{mt}}}}{A_{\mathrm{mt}}} \frac{\partial \mathbf{N}_{12}^{\mathrm{T}}}{\partial \xi} \frac{\partial \mathbf{x}(\xi,\theta)}{\partial \xi} \right. \\
&\quad \left. + \frac{\sqrt{A_{\mathrm{mt}} B_{\mathrm{mt}}}}{B_{\mathrm{mt}}} \frac{\partial \mathbf{N}_{12}^{\mathrm{T}}}{\partial \theta} \frac{\partial \mathbf{x}(\xi,\theta)}{\partial \theta} \right\} d\xi\, d\theta
\end{aligned} \tag{5.18}$$

Following some mathematical manipulation, see Appendix E, the surface tension force vector takes the form:

$$\mathbf{F}^{\mathbf{ST}} = \frac{\pi\gamma(r_1+r_2)}{L} \begin{bmatrix} r_1 - r_2 \\ z_1 - z_2 \\ r_2 - r_1 \\ z_2 - z_1 \end{bmatrix} + \pi\gamma L \begin{bmatrix} 1 \\ 0 \\ 1 \\ 0 \end{bmatrix} \tag{5.19}$$

where L is the length of the linear element, $L = \sqrt{(r_1 - r_2)^2 + (z_1 - z_2)^2}$. Taking the directional derivative of Equation 5.19 in the direction of displacement results in the surface tension contribution to the stiffness matrix $\mathbf{K}^{\mathbf{ST}}$:

$$\mathbf{K}^{\mathbf{ST}} = \mathbf{K}_{\mathbf{I}}^{\mathbf{ST}} + \mathbf{K}_{\mathbf{II}}^{\mathbf{ST}} + \mathbf{K}_{\mathbf{III}}^{\mathbf{ST}} \tag{5.20}$$

where:

$$\mathbf{K}_{\mathbf{I}}^{\mathbf{ST}} = \frac{\pi\gamma}{L} \begin{bmatrix} 2r_1 & 0 & -2r_2 & 0 \\ (z_1 - z_2) & (r_1 + r_2) & (z_1 - z_2) & -(r_1 + r_2) \\ -2r_1 & 0 & 2r_2 & 0 \\ (z_2 - z_1) & -(r_1 + r_2) & (z_2 - z_1) & (r_1 + r_2) \end{bmatrix} \tag{5.21}$$

$$\mathbf{K}_{\mathbf{II}}^{\mathbf{ST}} = -\frac{\pi\gamma(r_1+r_2)}{L^3} \begin{bmatrix} r_1 - r_2 \\ z_1 - z_2 \\ r_2 - r_1 \\ z_2 - z_1 \end{bmatrix} \begin{bmatrix} r_1 - r_2 \\ z_1 - z_2 \\ r_2 - r_1 \\ z_2 - z_1 \end{bmatrix}^{\mathrm{T}} \tag{5.22}$$

$$\mathbf{K}_{\mathbf{III}}^{\mathbf{ST}} = \frac{\pi\gamma}{L} \begin{bmatrix} 1 \\ 0 \\ 1 \\ 0 \end{bmatrix} \begin{bmatrix} r_1 - r_2 \\ z_1 - z_2 \\ r_2 - r_1 \\ z_2 - z_1 \end{bmatrix}^{\mathrm{T}} \tag{5.23}$$

5.2.3 Contact Line Force Contributions

If node 1, Figure 5.7, is on the contact line, the revolution of node 1 around the vertical axis creates the contact line. The shape function matrix for this contact line generated by the revolution of node 1, $\mathbf{N}_1$ is:

$$\mathbf{N}_1(\xi,\theta) = \begin{bmatrix} \frac{1}{2}(1-\xi)\cos\theta & 0 \\ \frac{1}{2}(1-\xi)\sin\theta & 0 \\ 0 & \frac{1}{2}(1-\xi) \end{bmatrix} \tag{5.24}$$

The vector $\mathbf{m}$, the binormal of the contact line, see Figure 5.6, is a function of the contact angle and is independent of displacement:

$$\mathbf{m} = \begin{bmatrix} \cos\theta\cos\alpha \\ \sin\theta\cos\alpha \\ -\sin\alpha \end{bmatrix} \tag{5.25}$$

Unlike previously where the angular component was constant for the three-noded element and so was not included, the angular component is included here as it will change depending on the location. Evaluating for $\xi = -1$ and assuming $ds = (1-\xi)\, r_1 d\theta$, the contact line force vector for node 1 is:

$$\begin{aligned} \mathbf{F}^{\mathbf{CL}} &= \int_C \gamma [\mathbf{N}_1]^{\mathrm{T}} \{\mathbf{m}\}\, ds \\ &= \int_0^{2\pi} \begin{bmatrix} \cos\theta & \sin\theta & 0 \\ 0 & 0 & 1 \end{bmatrix} \begin{bmatrix} \cos\theta\cos\alpha \\ \sin\theta\cos\alpha \\ -\sin\alpha \end{bmatrix} r_1 d\theta \\ &= 2\pi\gamma r_1 \begin{bmatrix} \cos\alpha \\ -\sin\alpha \end{bmatrix} \end{aligned} \tag{5.26}$$

There are no contributions from the contact line to node 2. Once again, the contribution to the stiffness matrix, for the contact line force, is found by taking the directional derivative of

the above equation in the direction of displacement:

$$\mathbf{K}^{\mathbf{CL}} = 2\pi\gamma \begin{bmatrix} \cos\alpha & 0 \\ -\sin\alpha & 0 \end{bmatrix} \tag{5.27}$$

5.3 Identification of the Surface Edges of the Droplet

The surface tension and contact line force vectors and stiffness matrices are only applied to the surface of the droplet, i.e. the edges of elements on the surface of the mesh. Within the computational framework, an alpha shapes algorithm is used to remesh every time step. An alpha shape is a group of piecewise linear curves associated with the shape of a finite set of points. Motion occurs within a time step and the system of equations are solved and the mesh is moved to the solution position. Within the computational framework developed, information is only stored on the nodes (for example velocities, pressures, density), hence, CGAL can be used to remesh using an alpha shapes algorithm without the loss of any data. The new mesh, still containing all data, is then passed to the next time step and this process is repeated.

An additional algorithm has been written to identify such edges at the beginning of each time step. Before the algorithm is reproduced, it is important to state the boundary conditions given to nodes at the very beginning of a typical analysis. Boundary conditions are defined as *fixed_x* for nodes fixed horizontally, *fixed_y* for nodes fixed vertically, *fluid* for all nodes describing the fluid (in all the cases to be examined in later chapters, all nodes are recognised as fluid nodes), and *fluid_surface* for those nodes on the surface of the fluid. The appropriate boundary conditions are stored in a *tag* in MOAB [63] called *type*. For example, Figure 5.8 shows the FE mesh and boundary conditions for a sessile droplet on a flat surface. Note that the problem is axisymmetric in nature. From the figure, it can be seen that each surface edge has only one adjacent triangular element and this piece of information is used in the following algorithm.

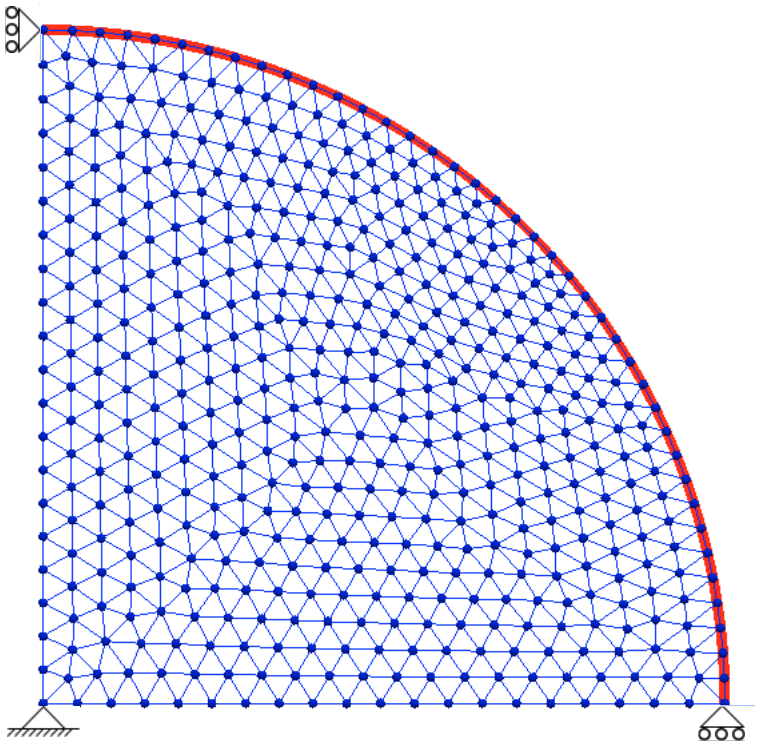

Figure 5.8: FE mesh and boundary conditions, with element edges on the fluid surface highlighted

Input: all mesh elements and vertices
Output: the range of mesh edges on the surface of the fluid
Define: ranges *all_elems*, *all_verts*, *perimeterverts*, *surface_edges*, *actualsurfedges*;
Identify all triangular elements and insert into *all_elems* (MOAB);
Identify connected vertices to *all_elems* and insert into *all_verts* (MOAB);
for *all_verts i* **do**
    Read *type* tag (MOAB);
    if *type = fluid_surface (already present from CGAL)* **then**
        Insert vertice *i* into *perimeterverts* (MOAB);
        Remove *fluid_surface* from tag (MOAB);
    end
    if *type = fixed_x* **or** *type = fixed_y* **then**
        Remove vertice *i* from *perimeterverts* (MOAB);
    end
end
Identify adjacent edges to *perimeterverts* and insert into *surface_edges* (MOAB);
for *surface_edges j* **do**
    Define: range *adjac_elems*;
    Define: entity handle *conn*;
    Identify adjacent elements to *j* and insert into *adjac_elems* (MOAB);
    Identify connected vertices to *j* and insert into *conn* (MOAB);
    if *conn* $\neq 2$ exit the code;
    Read *type* tag for *conn* (MOAB);
    if *adjac_elems = 1* **then**
        Add tag *fluid_surface* to *j* (MOAB);
        Insert *j* into *actualsurfedges* (MOAB);
        Add tag *fluid_surface* to *conn* (MOAB);
    end
end
if *actualsurfedges* = 0, exit the code;

Algorithm 5.1: Identification of those mesh edges on the surface of the fluid

The first step in algorithm 5.1 is to define various ranges in which different parts of the mesh will be stored at different times. Next, MOAB is used to identify all triangular elements, and then identify all the vertices connected to these elements. Then the algorithm loops over these vertices, reading the boundary conditions of each vertice. If the vertice is tagged with the *fluid_surface* boundary condition, (already present from CGAL [6]), this boundary condition is removed and it is placed into a range. However, if the vertice is fixed in the

horizontal or vertical directions, it is removed from this range. The current range, therefore, contains all the vertices on the fluid surface other than that on the contact line and that on the axis of symmetry. The algorithm now uses MOAB [44] to identify all edges of the mesh connected to these vertices. Then, the algorithm loops over this new range of edges, using MOAB [44] to identify all triangular elements and vertices connected to these edges. If the number of adjacent elements to an edge is equal to one, this edge is on the fluid surface and therefore we add the *fluid_surface* boundary condition to the edge and its two vertices, and we place the edge in a new meshset.

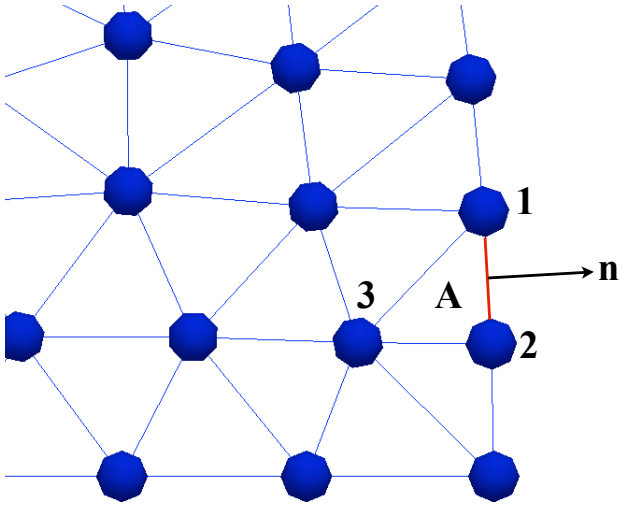

Figure 5.9: Ordering of nodes convention

Once all element edges on the surface of the fluid have been identified at the beginning of each time step, those edges are stored in a separate meshset in MOAB. This meshset is used to calculate $\mathbf{K}^{\mathbf{ST}}$ and $\mathbf{K}^{\mathbf{CL}}$ and then $\mathbf{F}^{\mathbf{ST}}$ and $\mathbf{F}^{\mathbf{CL}}$ for each edge where appropriate. An element node numbering convention is important to ensure that for all elements, the surface tension force components and contact line components are correctly calculated. All edges of triangles on the fluid surface are locally labelled nodes 1 and 2. The convention used states that for a given edge, for example the highlighted edge of element A in Figure 5.9, when the outward pointing normal is rotated clockwise by 90°, it points to node 2. The remaining node on the edge is therefore node 1 and the last node comprising the surface element is node 3. Numbering of element nodes needs to be consistent to prevent the components from the surface tension force vector, for example, being calculated in the wrong direction.

When identifying the edge on the contact line (if indeed there is a contact line, for example, in zero-gravity problems there is not), a similar algorithm is used. The range of vertices on the contact line is used to then calculate the force contribution and the stiffness contribution

from the contact line force. Additionally, the contact line force vector and stiffness matrix are rotated if the surface upon which the droplet rests is not flat. The geometry of the solid surface is known *a priori* and allows for the equation of the line describing the solid surface to be determined, for example, in Figure 5.8, the equation of the solid surface is $z = 0$. The coordinate of the contact point is determined and hence the gradient of the line describing the solid surface at the contact point can be calculated by taking the derivative of the line equation and substituting the contact point coordinates. From the gradient of the solid surface the angle of inclination can be calculated and hence the force vector and stiffness matrix in the global sense are found using a rotation matrix $\mathbf{R}$, following Algorithm 5.2.

Input: nodal coordinates for surface edge on contact line, equation of line describing the surface, $\mathbf{F}^{\mathbf{CL}}_{\mathbf{local}}$, $\mathbf{K}^{\mathbf{CL}}_{\mathbf{local}}$

Output: $\mathbf{F}^{\mathbf{CL}}_{\mathbf{global}}$, $\mathbf{K}^{\mathbf{CL}}_{\mathbf{global}}$

Calculate gradient at contact point, m;

Calculate angle of inclination, $\theta = \tan^{-1}(m)$;

if $m > 0$ **then**

$$\mathbf{R} = \begin{bmatrix} \cos\theta & -\sin\theta & 0 & 0 \\ \sin\theta & \cos\theta & 0 & 0 \\ 0 & 0 & \cos\theta & -\sin\theta \\ 0 & 0 & \sin\theta & \cos\theta \end{bmatrix};$$

else if $m < 0$ **then**

$$\mathbf{R} = \begin{bmatrix} \cos\theta & \sin\theta & 0 & 0 \\ -\sin\theta & \cos\theta & 0 & 0 \\ 0 & 0 & \cos\theta & \sin\theta \\ 0 & 0 & -\sin\theta & \cos\theta \end{bmatrix};$$

else

$m = 0$, no rotation required, $\mathbf{R} = \mathbf{I}$;

end

$\mathbf{F}^{\mathbf{CL}}_{\mathbf{global}} = \mathbf{R}\mathbf{F}^{\mathbf{CL}}_{\mathbf{local}}$;

$\mathbf{K}^{\mathbf{CL}}_{\mathbf{global}} = \mathbf{R}^{\mathrm{T}}\mathbf{K}^{\mathbf{CL}}_{\mathbf{local}}\mathbf{R}$;

Algorithm 5.2: Rotation of the local contact line force vector and stiffness matrix

5.4 Conclusions

The concept of surface tension has been introduced and the Young-Laplace equation and Young's equation were described. The difference between hydrophobic and hydrophilic surfaces was described and developed to give examples of surfactants, fluids with both hydrophobic and hydrophilic parts, which lower the surface tension of water. The work of Saksono and Perić was then derived in part, with the contributions to the force vector and stiffness matrix due to the surface tension force and the contact line force directly related to the Young-Laplace equation and thus the curvature of the interface. These contributions were given in a *weak form* before being further developed to show the actual nodal contributions.

Finally, the algorithms to identify the element edges on the surface of the mesh, to identify the surface edge on the contact line and to rotate the local contact line force vector and stiffness matrix to a global sense were described. These algorithms make use of MOAB [44] to identify the elements of the mesh required.

Chapter 6

Pressure Stabilisation

This chapter outlines the need for pressure stabilisation and briefly discusses the many methods available. The method of choice shall then be outlined and the pressure stabilisation terms included in the computational framework will be derived. Comprehensive testing of the pressure stabilisation terms shall also be undertaken to examine their effect.

6.1 The Requirement for Pressure Stabilisation

In the computational framework derived in the previous chapters, we use equal order interpolation functions for velocities and pressures as we want to calculate the velocity and pressure on the mesh nodes. Within the literature, [25], [34], [64], [50], [67], [48], it is noted that when using equal order interpolation functions for pressures and velocities within a Galerkin variational form, spurious oscillations occur in the solution space. Without some form of mitigation of these oscillations, the solutions can be meaningless. A large number of the analyses to be undertaken in the following chapters will examine the equilibrium shape of a water droplet. The initial geometry of the droplets in these analyses is a cylinder, however, due to the axisymmetric nature of the problem, only one half of a slice through the droplet need be assessed, refer to Figure 6.1. The initial cylindrical shape gives the droplet the potential energy to achieve its equilibrium geometry which, in this case, will be part of a circle. Figure 6.2a demonstrates one such analysis at step 3220, $t = 0.1$ seconds when pressure stabilisation is not included. The figure shows the warped pressure field for a slice through the droplet centre. The solution uses equal-order interpolations for velocities and pressures resulting in large peaks and troughs appearing in the pressure field; these instabilities will

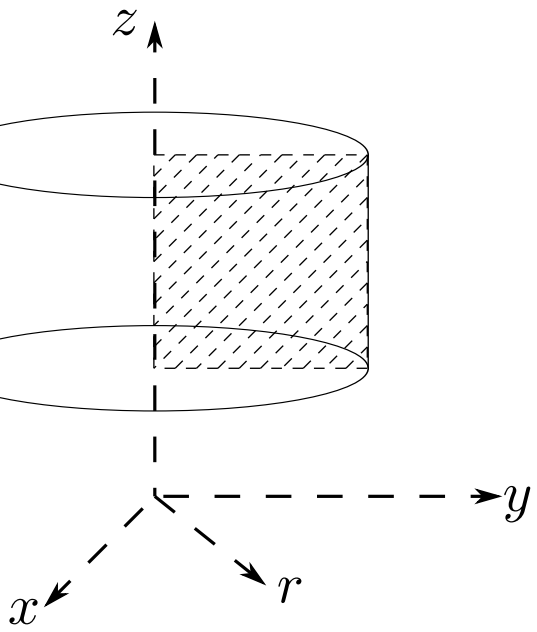

Figure 6.1: Cylindrical droplet with cross-section highlighted

affect the overall outcome and therefore reliability of the solution. Conversely, Figure 6.2b shows a second analysis at step 4240, $t = 0.1$ seconds with the inclusion of pressure stabilisation that will be derived in this chapter; note the smoothness of the pressure field over the entirety of the cross-section. Due to adaptive time stepping, the step number at $t = 0.1$ seconds differs for the two examples shown. Over the last 30 to 40 years, several stabilisation procedures have been proposed, and the various methods will be discussed here in brief.

6.2 Pressure Stabilisation Methods

Brezzi [24] and Babuška [15] showed that a stabilisation method is convergent if the combination of interpolation functions for pressures and velocities satisfy the *Babuška-Brezzi* condition (also known as the *inf-sup* condition). The *inf-sup* condition ensures that the finite element solution is the optimal solution, and is stable and solvable. Oscillations within the solution space are caused by methods in violation to this condition. Hence, most traditional schemes select combinations that satisfy this condition in the knowledge that the resulting solution will be stable. More recently, other methods of stabilisation have been proposed that allow for combinations that do not satisfy the condition. This means that sets of interpolation functions that were in violation of the *inf-sup* condition can now be used which, in some cases, leads to more computationally convenient solutions [34].

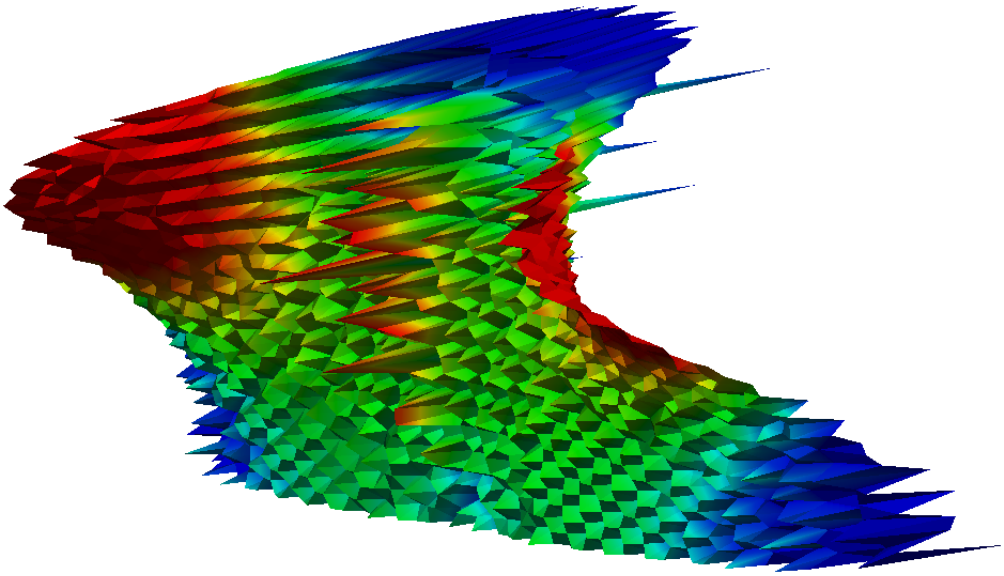

(a) Pressure field without stabilisation

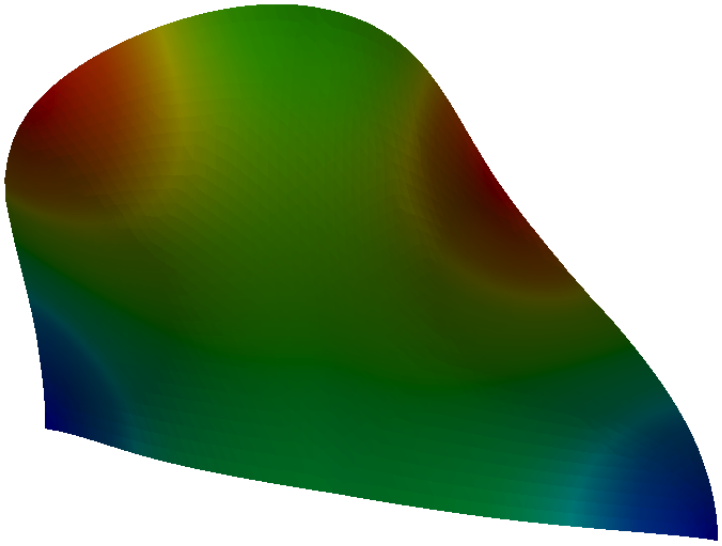

(b) Pressure field with stabilisation

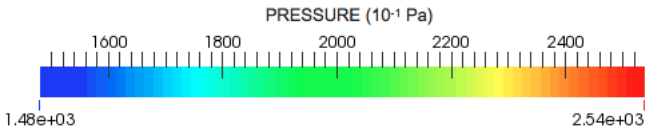

Figure 6.2: Oscillations within the pressure field at $t = 0.1$ seconds

Tezduyar [64] states that numerical instabilities can arise from two areas: poor combinations of interpolation functions, manifesting in oscillations in the pressure field; and from the advection terms of the governing equations, manifesting in oscillations in the velocity field. The latter is, however, more prevalent in flows with high Reynolds numbers and can be discounted in the context of this thesis. Tezduyar continues that such oscillations are not just inherent in the FEM but appear in other discretisation methods such as the FVM and the FDM; hence changing to an alternative discretisation method will not generally remove the need for stabilisation.

Most stabilisation techniques take the form of an operator (the type of operator is technique specific) applied to the approximation function, $P(w)$, a stabilisation parameter, $\bar{\tau}$ (also known as intrinsic time), and the residual of the differential equation, $R(u)$.

$$\sum_{e} \int_{\Omega^e} P(w)\, \bar{\tau} R(u)\, d\Omega \tag{6.1}$$

Stabilisation methods are classed by the definition of the operator $P(w)$. The most common method of stabilisation is Galerkin/Least-squares (GLS) methods because it introduces minimal excess diffusion and therefore there is a minimal loss of accuracy [29], [64]. It is worth noting that, depending on the problem, oscillations can be removed by excessive mesh refinement. By implementing successively denser mesh, the contribution from the stabilisation terms becomes smaller and smaller until it is negligible and the solution converges [26]. Hence, the addition of the stabilisation terms is verified. However, excessive mesh refinement is not always possible nor computationally practical in terms of solution time and cost.

6.2.1 Streamline-Upwind/Petrov-Galerkin and Related Methods

Brooks and Hughes [26] proposed the streamline-upwind/Petrov-Galerkin (SUPG) formulation of pressure stabilisation. This method utilises the reduction of diffusion from the streamline upwind concept in combination with the consistent Petrov-Galerkin weighted residual formulation. The outcome is weighting functions that are modified by adding a perturbation, see Equation 6.2, acting in the direction of flow only; the perturbations are in the form of diffusion (viscosity) in the direction of flow. The SUPG method has been shown to perform well and removes spurious oscillations whilst maintaining accuracy [26].

$$P(w) = \mathbf{a} \cdot \nabla w \tag{6.2}$$

Similar to SUPG is the pressure-stabilised/Petrov-Galerkin (PSPG) method as described by Brezzi and Pitkäranta [25], which examines two methods of stabilising the Stokes equations. The first method involves adding bubble functions (higher-order polynomials which vanish on element boundaries) to the velocity field to stabilise the pair of velocity and pressure spaces. The second method involves adding a stabilising term to the discrete equations with no change to the discrete pressure or velocity fields. The second method, whilst stabilising the formulation, affects the consistency of the formulation because the stabilisation term is not symmetric. This lack of symmetry introduces computational difficulties in determining the stability of this technique [29].

Hughes et al. [34] continued this work on PSPG formulations and developed a formulation for improving stability without experiencing the consistency problems affecting Brezzi and Pitkäranta. This new formulation suggests additional terms derived directly from a perturbation of the weighting function, allowing for previously unstable equal order interpolation functions in violation of the *Babuška-Brezzi* condition to be used for velocities and pressures. The resulting additional term has the form:

$$\bar{\tau}\nabla\mathbf{w}\cdot\nabla p \qquad \text{where } \bar{\tau} = \frac{\beta h^2}{2\mu} \tag{6.3}$$

where h is a measure of mesh size, μ is the fluid viscosity and β is a scalar. The value of the scalar β is selected to improve the stability of the Galerkin formulation without any compromise in the formulation's consistency. Hughes et al. show that this additional term allows for the use of combinations of pressure and velocity with C^0 approximation fields and also the use of equal order interpolations, both unstable when trying to satisfy the *Babuška-Brezzi* condition.

Pastor et al. [50] noted that the most efficient codes have matching interpolation spaces for pressures and velocities. For formulations with equal order interpolation, Pastor et al. derived a PSPG stabilisation term directly from the momentum equation with use of the volumetric strain and the pressure wave equation. The resulting term is a pressure Laplacian scaled by a stabilisation parameter, in a similar manner to Hughes et al.

$$\bar{\tau}\nabla^2 p \qquad \text{where } \bar{\tau} = \frac{\beta h^2}{\mu} \tag{6.4}$$

Truty [67] utilises this method in his work on porous media, demonstrating the versatility of

this method to different flow problems.

6.2.2 Galerkin/Least-squares Method

The Galerkin/Least-squares (GLS) method imposes the stabilisation term on an element by element basis, in partnership with a weighted least-squares formulation of the original differential equation [29]. The symmetric nature of the stabilisation term applied to the left-hand side of the system of equations is advantageous in introducing stability as it removed the computational difficulties encountered by Brezzi and Pitkäranta [25]. There is little difference between SUPG and GLS methods [29], and in some cases, such as convection-diffusion problems and problems using linear elements, the two methods are equivalent.

6.2.3 Pressure Laplacian Stabilisation (PLS) Method

Oñate et al. [48] introduced the pressure Laplacian stabilisation (PLS) technique. Pressure stabilisation is achieved via a higher-order Finite Calculus (FIC) approach whilst the convective effects are ignored. Higher-order balance statements are applied to a finite domain to produce a stabilised form of the governing differential equations and a standard Galerkin formulation is then applied. This leads to a similar pressure Laplacian term as seen in the work of Hughes et al. [34], Equation 6.3, and Pastor et al. [50], Equation 6.4, and an additional boundary pressure stabilisation term, both added to the conservation equations. The boundary term is important in terms of accuracy, particularly in problems involving free surface flow. All the stabilisation terms are scaled by the stabilisation parameter $\bar{\tau}$, which, as before, is dependent on the fluid viscosity and the mesh size. As the problems assessed in the following chapters involve free surface flows and the surface of the fluid is a major point of interest, we adopt the stabilisation terms as proposed by Oñate et al. in this work. Moreover, in terms of its simplistic nature, the PLS technique will be computationally easier and faster to implement into the system of equations than other methods.

6.3 Time and Space Discretised Form of the Pressure Stabilisation Terms

In the PLS technique [48], the mass balance equation (Equation 3.30), in the absence of body forces and assuming steady-state conditions, transforms to the stabilised mass balance equation. A Finite Calculus (FIC) form of the mass balance equation is developed using a higher-order Taylor series expansion. Integrating by parts produces the following, where Γ

is the boundary of the domain:

$$\int_V \mathbf{w_p} tr\left(\frac{\partial \mathbf{v}}{\partial \mathbf{x}}\right) dV - \int_V \bar{\tau} \frac{\partial \mathbf{w_p}}{\partial \mathbf{x}} : \frac{\partial p}{\partial \mathbf{x}} dV + \int_\Gamma \bar{\tau} \mathbf{w_p} \mathbf{n} \frac{\partial p}{\partial \mathbf{x}} d\Gamma \tag{6.5}$$

where:

$$\bar{\tau} = \frac{\beta h^2}{16\mu} \tag{6.6}$$

The first integral is the conservation of mass, considered in Chapter 3. The last two integrals are the traditional pressure Laplacian of pressure stabilisation techniques, and an additional boundary term respectively. Both are scaled by the stabilisation parameter $\bar{\tau}$, given in Equation 6.6, which is dependent on the mesh size h, the fluid dynamic viscosity μ and a user defined variable β; the effect of the magnitude of β will be investigated in the following section. For simplicity, the mesh size h is defined as the diameter of the circumscribed circle for an element, see Figure 6.3.

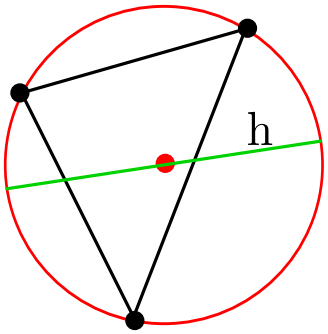

Figure 6.3: Diameter of the circumscribed circle for an element

Both integrals are evaluated in the spatial domain and so to map these to the reference (mesh) domain, requires the use of Equation 4.8, for example:

$$\begin{aligned}
\left(\frac{\partial \mathbf{w_p}}{\partial \mathbf{x}}\right)_{n+1}^{i+1} &= \frac{\partial \mathbf{w_p}}{\partial \chi} \frac{\partial \chi}{\partial \mathbf{x}} \\
&= \frac{\partial \mathbf{w_p}}{\partial \chi} \left(\frac{\partial \mathbf{x}}{\partial \chi}\right)^{-1} \\
&= \frac{\partial \mathbf{w_p}}{\partial \chi} \left(1 - \frac{\Delta t}{2} \frac{\partial \delta \hat{\mathbf{v}}}{\partial \chi}\right) \\
&= \frac{\partial \mathbf{w_p}}{\partial \chi} - \frac{\Delta t}{2} \frac{\partial \mathbf{w_p}}{\partial \chi} \frac{\partial \delta \hat{\mathbf{v}}}{\partial \chi}
\end{aligned} \tag{6.7}$$

Examining the pressure Laplacian first, which is calculated on an element by element basis:

$$\begin{aligned}\int_V \bar{\tau}\frac{\partial \mathbf{w_p}}{\partial \mathbf{x}} : \frac{\partial p}{\partial \mathbf{x}} dV &= \bar{\tau}\int_V \left(\frac{\partial \mathbf{w_p}}{\partial \chi}\frac{\partial \chi}{\partial \mathbf{x}} : \frac{\partial p}{\partial \chi}\frac{\partial \chi}{\partial \mathbf{x}}\right) dV \\ &= \bar{\tau}\int_V \left(\frac{\partial \mathbf{w_p}}{\partial \chi} - \frac{\Delta t}{2}\frac{\partial \mathbf{w_p}}{\partial \chi}\frac{\partial \delta\hat{\mathbf{v}}}{\partial \chi}\right) : \left(\frac{\partial p}{\partial \chi} - \frac{\Delta t}{2}\frac{\partial p}{\partial \chi}\frac{\partial \delta\hat{\mathbf{v}}}{\partial \chi}\right) dV \\ &= \bar{\tau}\int_V \frac{\partial \mathbf{w_p}}{\partial \chi} : \frac{\partial p}{\partial \chi} dV - \bar{\tau}\int_V \frac{\partial \mathbf{w_p}}{\partial \chi} : \left(\frac{\Delta t}{2}\frac{\partial p}{\partial \chi}\frac{\partial \delta\hat{\mathbf{v}}}{\partial \chi}\right) dV \\ &\quad -\bar{\tau}\int_V \left(\frac{\Delta t}{2}\frac{\partial \mathbf{w_p}}{\partial \chi}\frac{\partial \delta\hat{\mathbf{v}}}{\partial \chi}\right) : \frac{\partial p}{\partial \chi} dV \end{aligned} \tag{6.8}$$

and now using the solution for $p = p_i + \delta p$ at time t_{n+1} and iteration $i+1$ from Equation 4.2:

$$\begin{aligned}\int_V \bar{\tau}\frac{\partial \mathbf{w_p}}{\partial \mathbf{x}} : \frac{\partial p}{\partial \mathbf{x}} dV &= \bar{\tau}\int_V \frac{\partial \mathbf{w_p}}{\partial \chi} : \frac{\partial p_i}{\partial \chi} dV + \bar{\tau}\int_V \frac{\partial \mathbf{w_p}}{\partial \chi} : \frac{\partial \delta p}{\partial \chi} dV \\ &\quad -\bar{\tau}\int_V \frac{\partial \mathbf{w_p}}{\partial \chi} : \left(\frac{\Delta t}{2}\frac{\partial p_i}{\partial \chi}\frac{\partial \delta\hat{\mathbf{v}}}{\partial \chi}\right) dV \\ &\quad -\bar{\tau}\int_V \left(\frac{\Delta t}{2}\frac{\partial \mathbf{w_p}}{\partial \chi}\frac{\partial \delta\hat{\mathbf{v}}}{\partial \chi}\right) : \frac{\partial p_i}{\partial \chi} dV \end{aligned} \tag{6.9}$$

Integrating over the element from 0 to $2\pi r$ for axisymmetric conditions (see Equation 4.35) leads to:

$$
\begin{aligned}
2\pi r\int_r\int_z \bar{\tau}\frac{\partial \mathbf{w_p}}{\partial \mathbf{x}} : \frac{\partial p}{\partial \mathbf{x}} dr dz &= 2\pi\bar{\tau}\int_r\int_z r_n \frac{\partial \mathbf{w_p}}{\partial \chi} : \frac{\partial p_i}{\partial \chi} dr dz \\
&\quad + \left(\bar{\tau}\int_r\int_z \frac{\partial \mathbf{w_p}}{\partial \chi} : \frac{\partial p_i}{\partial \chi} dr dz\right)\left(\Delta t \pi \left(\delta\hat{\mathbf{v}}\right)_r\right) \\
&\quad + 2\pi\bar{\tau}\int_r\int_z r_n \frac{\partial \mathbf{w_p}}{\partial \chi} : \frac{\partial \delta p}{\partial \chi} dr dz \\
&\quad - 2\pi\bar{\tau}\int_r\int_z r_n \frac{\partial \mathbf{w_p}}{\partial \chi} : \left(\frac{\Delta t}{2}\frac{\partial p_i}{\partial \chi}\frac{\partial \delta\hat{\mathbf{v}}}{\partial \chi}\right) dr dz \\
&\quad - 2\pi\bar{\tau}\int_r\int_z r_n \left(\frac{\Delta t}{2}\frac{\partial \mathbf{w_p}}{\partial \chi}\frac{\partial \delta\hat{\mathbf{v}}}{\partial \chi}\right) : \frac{\partial p_i}{\partial \chi} dr dz \\
&= 2\pi\bar{\tau}\int_r\int_z r_n \frac{\partial \mathbf{w_p}}{\partial \chi} : \frac{\partial p_i}{\partial \chi} dr dz \\
&\quad + \Delta t\bar{\tau}\int_r\int_z \frac{\partial \mathbf{w_p}}{\partial \chi} : \frac{\partial p_i}{\partial \chi}\mathbf{N_r} dr dz \underline{\delta\hat{\mathbf{v}}} \\
&\quad + 2\pi\bar{\tau}\int_r\int_z r_n \frac{\partial \mathbf{w_p}}{\partial \chi} : \frac{\partial \mathbf{N}}{\partial \chi} dr dz \underline{\delta p} \\
&\quad - 2\pi\bar{\tau}\int_r\int_z r_n \left[\frac{\partial \mathbf{w_p}}{\partial \chi} : \left(\frac{\Delta t}{2}\frac{\partial p_i}{\partial \chi}\frac{\partial \mathbf{N}}{\partial \chi}\right)\right. \\
&\quad \left. + \left(\frac{\Delta t}{2}\frac{\partial \mathbf{w_p}}{\partial \chi}\frac{\partial \mathbf{N}}{\partial \chi}\right) : \frac{\partial p_i}{\partial \chi}\right] dr dz \underline{\delta\hat{\mathbf{v}}}
\end{aligned} \tag{6.10}
$$

where $\mathbf{N}$ represents the element shape functions and $\mathbf{N_r}$ represents the radial component, i.e. the first component, of the element shape functions. The above simplifies to:

$$
2\pi r\int_r\int_z \bar{\tau}\frac{\partial \mathbf{w_p}}{\partial \mathbf{x}} : \frac{\partial p}{\partial \mathbf{x}} dr dz = \mathbf{f^s_{pp}} + \mathbf{K^{s,fr}_{pp}}\underline{\delta\hat{\mathbf{v}}} + \mathbf{K^s_{pp}}\underline{\delta p} + \mathbf{K^s_{p\hat{v}}}\underline{\delta\hat{\mathbf{v}}} \tag{6.11}
$$

where $\mathbf{K}_{...}$ is a stiffness matrix and $\mathbf{f}_{...}$ is a force vector. Examining the boundary term, which is calculated on a boundary edge by edge basis, next:

$$
\begin{aligned}
\int_\Gamma \bar{\tau}\mathbf{w_p}\mathbf{n}\frac{\partial p}{\partial \mathbf{x}} d\Gamma &= \bar{\tau}\int_\Gamma \mathbf{w_p}\mathbf{n}\frac{\partial p}{\partial \chi}\frac{\partial \chi}{\partial \mathbf{x}} d\Gamma \\
&= \bar{\tau}\int_\Gamma \mathbf{w_p}\mathbf{n}\frac{\partial p}{\partial \chi} d\Gamma - \bar{\tau}\frac{\Delta t}{2}\int_\Gamma \mathbf{w_p}\mathbf{n}\frac{\partial p}{\partial \chi}\frac{\partial \delta\hat{\mathbf{v}}}{\partial \chi} d\Gamma
\end{aligned} \tag{6.12}
$$

and now using the solution for $p = p^{i+1}_{n+1}$ at time t_{n+1} and iteration $i+1$ from Equation 4.2:

$$
\int_\Gamma \bar{\tau}\mathbf{w_p}\mathbf{n}\frac{\partial p}{\partial \mathbf{x}} d\Gamma = \bar{\tau}\int_\Gamma \mathbf{w_p}\mathbf{n}\frac{\partial p_i}{\partial \chi} d\Gamma + \bar{\tau}\int_\Gamma \mathbf{w_p}\mathbf{n}\frac{\partial \delta p}{\partial \chi} d\Gamma - \bar{\tau}\frac{\Delta t}{2}\int_\Gamma \mathbf{w_p}\mathbf{n}\frac{\partial p_i}{\partial \chi}\frac{\partial \delta\hat{\mathbf{v}}}{\partial \chi} d\Gamma \tag{6.13}
$$

Integrating from 0 to $2\pi r$ (see Equation 4.44) and considering the non-linearity caused by

the normal (see Equation 4.40) leads to:

$$
\begin{aligned}
2\pi r\int_r\int_z \bar{\tau}\mathbf{w_p}\mathbf{n}\frac{\partial p}{\partial \mathbf{x}}drdz &= 2\pi\bar{\tau}\int_r\int_z r_n\mathbf{w_p}\bar{\mathbf{n}}\frac{\partial p_i}{\partial\chi}drdz+\frac{\Delta t}{2}\pi\bar{\tau}\int_r\int_z \mathbf{w_p}\bar{\mathbf{n}}\frac{\partial p_i}{\partial\chi}\delta rdrdz\\
&\quad +2\pi\bar{\tau}\int_r\int_z r_n\mathbf{w_p}\bar{\mathbf{n}}\frac{\partial\delta p}{\partial\chi}drdz\\
&\quad -\Delta t\pi\bar{\tau}\int_r\int_z r_n\mathbf{w_p}\bar{\mathbf{n}}\frac{\partial p_i}{\partial\chi}\frac{\partial\delta\hat{\mathbf{v}}}{\partial\chi}drdz\\
&\quad +\Delta t\pi\bar{\tau}\int_r\int_z r_n\mathbf{w_p}\frac{\partial p_i}{\partial\chi}\delta\bar{\mathbf{n}}drdz\\
&= 2\pi\bar{\tau}\int_r\int_z r_n\mathbf{w_p}\bar{\mathbf{n}}\frac{\partial p_i}{\partial\chi}drdz\\
&\quad +\frac{\Delta t}{2}\pi\bar{\tau}\int_r\int_z \mathbf{w_p}\bar{\mathbf{n}}\frac{\partial p_i}{\partial\chi}\mathbf{N_{br}}drdz\underline{\delta\hat{\mathbf{v}}}\\
&\quad +2\pi\bar{\tau}\int_r\int_z r_n\mathbf{w_p}\bar{\mathbf{n}}\frac{\partial\mathbf{N}}{\partial\chi}drdz\underline{\delta p}\\
&\quad -\Delta t\pi\bar{\tau}\int_r\int_z r_n\mathbf{w_p}\bar{\mathbf{n}}\frac{\partial p_i}{\partial\chi}\frac{\partial\mathbf{N}}{\partial\chi}drdz\underline{\delta\hat{\mathbf{v}}}\\
&\quad +\Delta t\pi\bar{\tau}\int_r\int_z r_n\mathbf{w_p}\frac{\partial p_i}{\partial\chi}\mathbf{N_b}drdz\underline{\delta\hat{\mathbf{v}}}
\end{aligned}
\tag{6.14}
$$

where $\mathbf{N_b}$ represents the linear shape functions for a boundary edge and $\mathbf{N_{br}}$ represents the radial component i.e. the first component, of these shape functions. The above simplifies to:

$$
2\pi r\int_r\int_z \bar{\tau}\mathbf{w_p}\mathbf{n}\frac{\partial p}{\partial\mathbf{x}}drdz=\mathbf{f^b_{pp}}+\mathbf{K^{b,fr}_{pp}}\underline{\delta\hat{\mathbf{v}}}+\mathbf{K^b_{pp}}\underline{\delta p}-\mathbf{K^b_{p\hat{v}}}\underline{\delta\hat{\mathbf{v}}}+\mathbf{K^{b,n}_{pp}}\underline{\delta\hat{\mathbf{v}}} \tag{6.15}
$$

Combining Equations 6.11 and 6.15, and simplifying:

$$
\left(\mathbf{K^s_{p\hat{v}}}-\mathbf{K^b_{p\hat{v}}}+\mathbf{K^{s,fr}_{pp}}+\mathbf{K^{b,fr}_{pp}}+\mathbf{K^{b,n}_{pp}}\right)\underline{\delta\hat{\mathbf{v}}}+\left(\mathbf{K^s_{pp}}+\mathbf{K^b_{pp}}\right)\underline{\delta p}=-\left(\mathbf{f^s_{pp}}+\mathbf{f^b_{pp}}\right) \tag{6.16}
$$

Reviewing the diagrammatic form of the system of governing equations from Chapter 4, additional terms can now be added to the corresponding group:

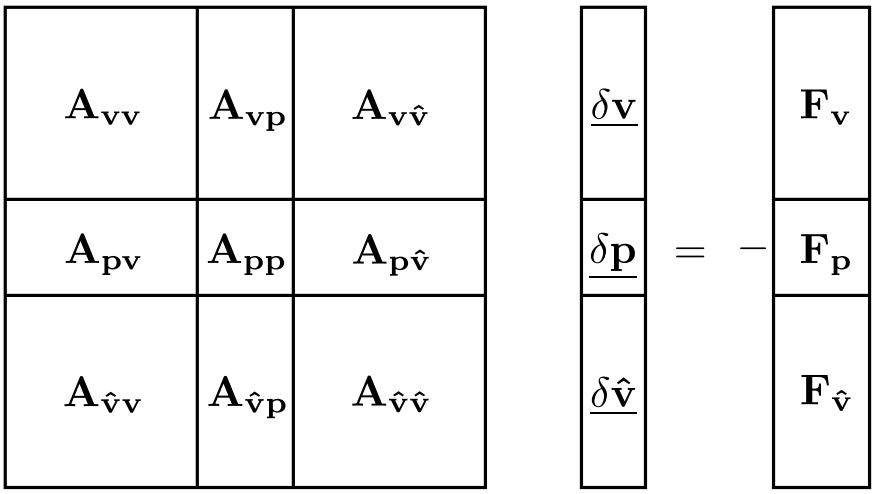

Figure 6.4: Diagrammatic form of the system of governing equations

where:

$$\mathbf{A_{vv}} = \frac{\mathbf{M_{vv}}}{2\Delta t} + \mathbf{K_{vv}} + \mathbf{K_{vv}^{axi}} \tag{6.17}$$

$$\mathbf{A_{vp}} = \mathbf{K_{vp}} + \mathbf{K_{vp}^{axi}} \tag{6.18}$$

$$\mathbf{A_{v\hat{v}}} = \frac{\mathbf{M_{v\hat{v}}}}{2\Delta t} + \mathbf{K_{v\hat{v}}} + \mathbf{K_{v\hat{v}}^{axi}} + \mathbf{K_{vp\hat{v}}} + \mathbf{K_{vv}^{fr}} + \mathbf{K_{vm}^{fr}} + \mathbf{K_{vp}^{fr}} \tag{6.19}$$

$$\mathbf{A_{pv}} = \mathbf{K_{pv}} + \mathbf{K_{pv}^{axi}} \tag{6.20}$$

$$\mathbf{A_{pp}} = \mathbf{K_{pp}^{s}} + \mathbf{K_{pp}^{b}} \tag{6.21}$$

$$\mathbf{A_{p\hat{v}}} = \mathbf{K_{p\hat{v}}} + \mathbf{K_{pv}^{fr}} + \mathbf{K_{p\hat{v}}^{s}} + \mathbf{K_{p\hat{v}}^{b}} + \mathbf{K_{pp}^{s,fr}} + \mathbf{K_{pp}^{b,fr}} + \mathbf{K_{pp}^{b,n}} \tag{6.22}$$

$$\mathbf{A_{\hat{v}p}} = 0 \tag{6.23}$$

$$\mathbf{F_v} = \mathbf{f_{vv}} + \mathbf{f_{vv}^{axi}} + \mathbf{f_{vm}} + \mathbf{f_{vp}} + \mathbf{f_{vp}^{axi}} \tag{6.24}$$

$$\mathbf{F_p} = \mathbf{f_{pv}} + \mathbf{f_{pv}^{axi}} + \mathbf{f_{pp}^{s}} + \mathbf{f_{pp}^{b}} \tag{6.25}$$

The accuracy of the terms was checked using a finite difference approach and by the use of successively denser mesh, therefore removing the contribution from the terms. Algorithm 6.1 details the system of identifying element edges on the boundary of the fluid. This is done in a similar manner as the algorithm in the previous chapter to identify the surface edges, identifying the correct edges by examining their boundary conditions and the number of adjacent elements.

Input: all mesh vertices
Output: the range of mesh edges on the boundary of the fluid
Define: ranges *all_elems*, *all_verts*, *perimeter_verts*, *perimeter_edges*;
Identify all triangular elements and insert into *all_elems* (MOAB);
Identify connected vertices to *all_elems* and insert into *all_verts* (MOAB);
for *all_verts i* **do**
    Read *type* tag (MOAB);
    if *type* = *fluid_surface* **or** *type* = *fixed_x* **or** *type* = *fixed_y* **then**
        Insert vertice *i* into *perimeter_verts* (MOAB);
    end
end
Identify all edges connected to *perimeter_verts* and insert into *perimeter_edges*;
Define: range *adjac_tris*;
for *perimeter_edges i* **do**
    Identify adjacent elements and place into *adjac_tris* (MOAB);
    if *adjac_tris* == *1* **then**
        Insert edge *i* into *boundary_edges* (MOAB);
    end
end

Algorithm 6.1: Identification of those mesh edges on the boundary of the fluid

6.4 Influence of the Pressure Stabilisation Parameter

A study into the effect of the user defined variable β in the pressure stabilisation parameter $\bar{\tau}$ is now undertaken. The value of β will be selected in the range of 1×10^{-3} to 1×10^{3}. All other parameters, such as viscosity and density, are kept constant so that direct comparison can be made. The parameters to be used in the analyses are listed in Table 6.1.

Parameter	Value
Fluid dynamic viscosity, μ	$1.01 \times 10^2\,\mathrm{dyne \cdot s/cm^2}$
Fluid density, ρ	$0.998\,\mathrm{g/cm^3}$
Surface tension, γ	$73\,\mathrm{dyne/cm}$
Contact angle, α	90°
Mesh viscosity, μ_{mesh}	$1 \times 10^{-2}\,\mathrm{dyne \cdot s/cm^2}$
Gravitational acceleration, g	$-981\,\mathrm{cm/s^2}$

Table 6.1: Fluid parameters for pressure stabilisation analyses

In order to allow the droplet to achieve its equilibrium geometry faster and without any dynamic oscillations, (see Chapter 7 for further explanation) the fluid dynamic viscosity is chosen to be much higher than that for water and is in fact more like honey.

To assess the effect of pressure stabilisation, the maximum and minimum pressures as well as average computational time and any anomalies are studied. Timings are given for a single Intel Xeon processor running on a Linux server. The computational time is the average of five analyses conducted under the same conditions for each of the values of β to a point 0.1 seconds into the analysis. Only half of the cross-section is created in Cubit using a finite element mesh comprising 1026 nodes and 1934 elements (5130 degrees of freedom), with the boundary conditions shown in Figure 6.5. For post-processing the geometry is mirrored about the axis of symmetry to give the full cross-section.

From Figure 6.6 and Table 6.2 it can be seen that for $\beta < 1.0$, whilst these analyses are among the quickest, there remain peaks and troughs within the pressure field, as well as a spurious ridge along the axisymmetric boundary. The range of high to low pressure is the greatest. For $1.0 \leq \beta \leq 100.0$ there are no major peaks or troughs and the pressure field is much smoother. However, there remains a ridge along the axisymmetric boundary. When $\beta \geq 500.0$ the ridge disappears and the pressure field becomes fully smooth, but with the drawback of the computational time increasing. Whilst there is very little difference between the two upper values examined, 500.0 and 1000.0, the computational time is respectively 27.9% and 26.6% greater than for $\beta = 1.0$.

There is little difference in the calculated contact angle in the range of parameter examined and negligible difference in the eventual equilibrium shape when steady state conditions are

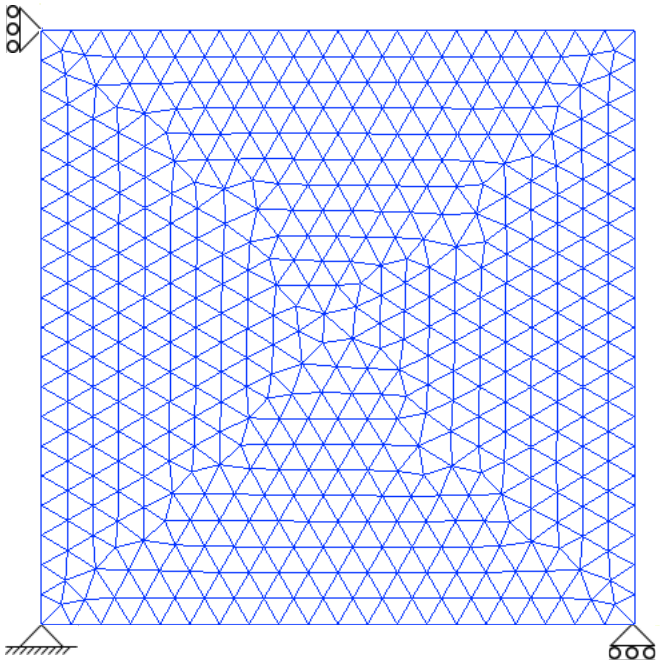

Figure 6.5: Initial FE mesh and boundary conditions for stabilisation analyses

achieved. However, it would seem that there comes a value of β at which the pressure field is misrepresented, much like increasing the number of finite elements around a stress concentration. It is therefore suggested that, for this problem, β is kept within the range 1.0 to 500.0 as this will provide a reasonably smooth pressure field whilst keeping analysis time to a minimum. Of course, if a fully smooth pressure field is required then a large value ($\beta \geq 500$) should be used. However, there is no indication at which value of β the pressure field is numerically correct. Obviously, this range of pressure stabilisation parameter is for the problem at hand and care must be taken for different problems to ensure that the value chosen produces as smooth a pressure field as required. Table 6.2 summarises all the data collected, Figure 6.7 conveys the relationship between the magnitude of the parameter (log scale) and the average computational time, and Figure 6.8 demonstrates representative time steps for two of the analyses conducted. The time steps shown are for for steps 60 and 61 with $\beta = 0$ and $\beta = 1000$; note the differences in time, droplet height and radius and time step. Both show quadratic convergence.

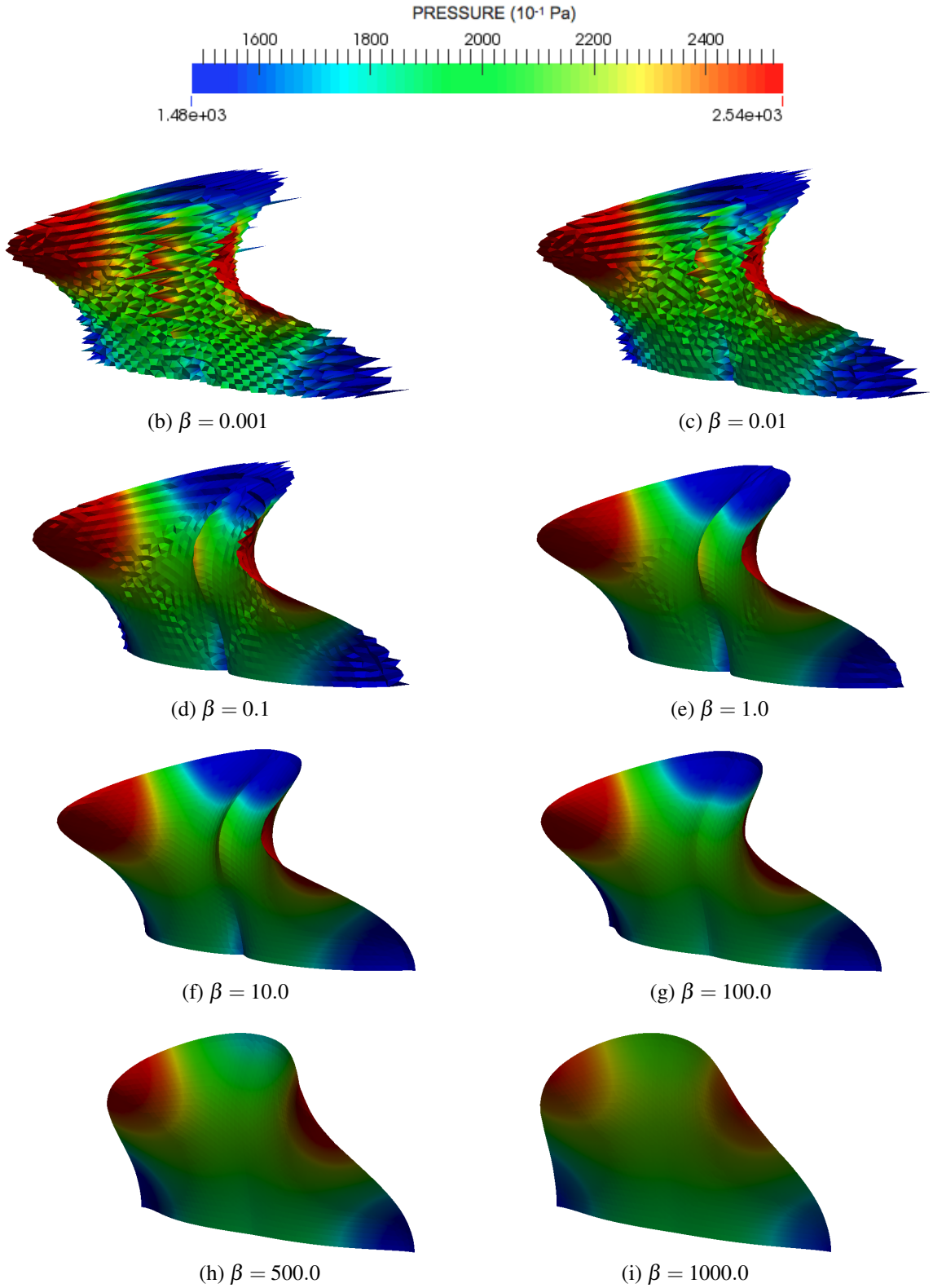

(b) $\beta = 0.001$ (c) $\beta = 0.01$

(d) $\beta = 0.1$ (e) $\beta = 1.0$

(f) $\beta = 10.0$ (g) $\beta = 100.0$

(h) $\beta = 500.0$ (i) $\beta = 1000.0$

Figure 6.6: Visual study of the effect of the parameter β at $t = 0.1\,sec$ on the pressure field

Parameter β	Average computational time (sec)	Contact angle α	Maximum pressure (Pa)	Minimum pressure (Pa)
0	0.851	89.492°	253	150
0.001	0.869	89.491°	252	158
0.01	0.856	89.488°	251	168
0.1	0.867	89.482°	250	175
1.0	0.880	89.477°	250	185
10	1.049	89.472°	247	190
100	1.108	89.458°	241	194
500	1.126	89.392°	232	201
1000	1.115	89.328°	227	205

Table 6.2: Numerical study of effect of parameter β at $t = 0.1\,sec$

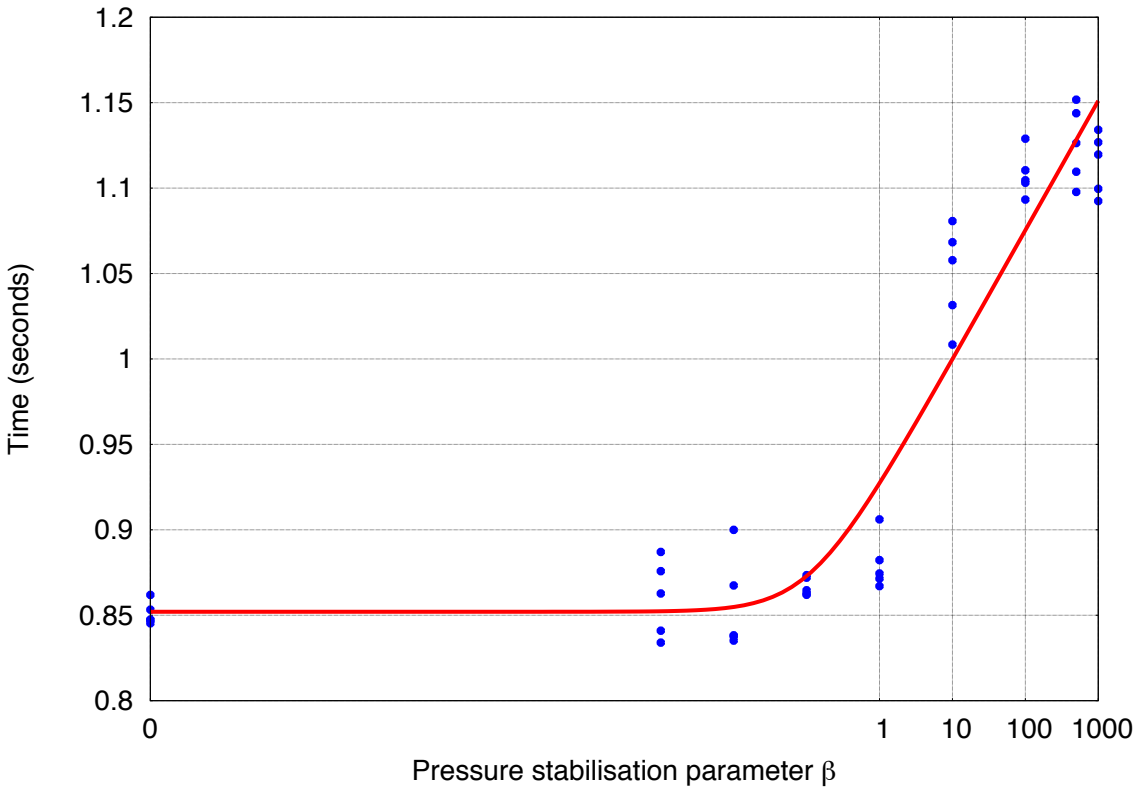

Figure 6.7: Average computational time for the range of pressure stabilisation parameters

```
SURFACE EDGES FOUND = 58        BOUNDARY EDGES FOUND = 116
step = 60, time = 0.000090532692273814
  0 SNES Function norm 8.972383822277e-03
  1 SNES Function norm 8.350495856622e-07
  2 SNES Function norm 1.259873967288e-09
  3 SNES Function norm 5.044653230315e-10
Nonlinear solve converged due to CONVERGED_FNORM_ABS
Number of Newton iterations = 3
AAA     step= 60   time= 0.000090532692273814  H= 0.0588518177  R= 0.0588387759  phi= 89.999464
V= 0.0006396388 == -0.0000015%   gy= -9.81000e+02  New dt = 0.000012413550641851
-----------------------------------------------------------------------------------------------

SURFACE EDGES FOUND = 58        BOUNDARY EDGES FOUND = 116
step = 61, time = 0.000102946242915665
  0 SNES Function norm 8.963974623541e-03
  1 SNES Function norm 8.131755772095e-07
  2 SNES Function norm 1.150895549079e-09
  3 SNES Function norm 4.985341438699e-10
Nonlinear solve converged due to CONVERGED_FNORM_ABS
Number of Newton iterations = 3
AAA     step= 61   time= 0.000102946242915665  H= 0.0588545379  R= 0.0588399613  phi= 89.999399
V= 0.0006396388 == -0.0000015%   gy= -9.81000e+02  New dt = 0.000012413550641851
```

(a) Representative time steps for $\beta = 0$

```
SURFACE EDGES FOUND = 58        BOUNDARY EDGES FOUND = 116
step = 60, time = 0.000052304669968147
  0 SNES Function norm 1.087598074101e-02
  1 SNES Function norm 3.643311178638e-07
  2 SNES Function norm 1.037358251232e-09
  3 SNES Function norm 2.708128791089e-10
Nonlinear solve converged due to CONVERGED_FNORM_ABS
Number of Newton iterations = 3
AAA     step= 60   time= 0.000052304669968147  H= 0.0588430316  R= 0.0588348889  phi= 89.999816
V= 0.0006396389 == -0.0000005%   gy= -9.81000e+02  New dt = 0.000004655081490694
-----------------------------------------------------------------------------------------------

SURFACE EDGES FOUND = 58        BOUNDARY EDGES FOUND = 116
step = 61, time = 0.000056959751458842
  0 SNES Function norm 1.087380960540e-02
  1 SNES Function norm 3.634664127258e-07
  2 SNES Function norm 1.038720884847e-09
  3 SNES Function norm 2.682495926167e-10
Nonlinear solve converged due to CONVERGED_FNORM_ABS
Number of Newton iterations = 3
AAA     step= 61   time= 0.000056959751458842  H= 0.0588441607  R= 0.0588353654  phi= 89.999798
V= 0.0006396389 == -0.0000005%   gy= -9.81000e+02  New dt = 0.000004655081490694
```

(b) Representative time steps for $\beta = 1000$

Figure 6.8: Representative time steps for pressure stabilisation analyses

6.5 Conclusions

The pressure stabilisation terms included in the computational framework are those from the PLS technique proposed by Oñate et al. [48] and are derived directly from the mass and momentum balance equations. The mapping of these terms from the spatial to reference domains, and taking account of the axisymmetry of the problem and the non-linearity of the radius, produced one force term and three stiffness terms to be calculated for each triangular element, and one force term and four stiffness terms to be calculated for each boundary edge. Each of these terms is scaled by the stabilisation parameter $\bar{\tau}$, dependent on the mesh size, the fluid viscosity and a user defined scalar β.

A comprehensive study into the effect of the parameter β has shown a high value leads to a smooth pressure field but a higher computational time and vice versa. For the FE mesh examined, a value of β in the range $1.0 \leq \beta \leq 500.0$ is suggested. Using a value at the lower end of the suggested range results in a pressure field that is relatively smooth whilst remaining computationally inexpensive, and a value at the higher end of the suggested range results in a fully smooth pressure field but a solution that is computationally more expensive; the computational time is on average 27.9% longer.

As aforementioned, there is no way of determining the most appropriate value of β *a priori*. Selected with certain problems and ease of implementation in mind, the PLS technique is very good at smoothing the pressure field; care must be taken if the aim of an analysis is to obtain pressure values.

In the analyses in the following chapters, the parameter $\beta = 1.0$ is used to keep computational time low, whilst providing an adequately smooth pressure field.

Chapter 7

Validation and Verification of the Computational Framework

This chapter details the various areas of validation and verification undertaken to ensure that the computational framework developed in the previous chapters produces reliable results. All areas determine the equilibrium geometry of droplets which can be compared to analytical solutions but with various boundary conditions and experimental configurations. Firstly, quasi-static analyses are undertaken whereby the fluid viscosity is artificially increased to reduce oscillations within the fluid and the equilibrium shape is determined and compared to analytical solutions. Then, the fluid viscosity is set to that for water and the period of oscillation is predicted and compared to analytical solutions. In addition, other more complex problems including surfactants and capillary tubes are examined and compared to analytical solutions where appropriate. Success in all these areas will allow for further problems to be examined involving external excitation.

7.1 Quasi-Static Analysis of Sessile Droplets

A sessile droplet will conform to a geometry that is part of a sphere when it is in equilibrium. Hence, by starting at a non-equilibrium geometry, for example, with a cylindrical cross-section, the droplet has the potential energy to achieve its equilibrium geometry. The surface tension forces present in the fluid will pull the droplet into a geometry where the external and internal forces balance. In normal circumstances, the droplet will oscillate into this position, however, to quickly ensure that the computational framework is accurate, the

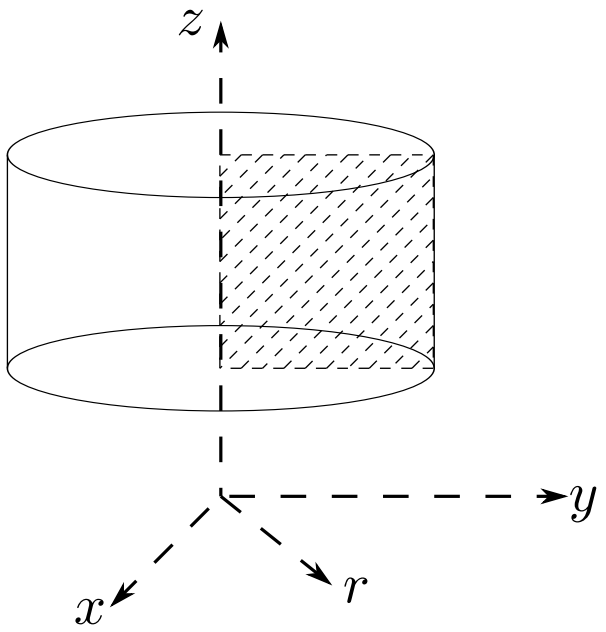

Figure 7.1: Cylindrical droplet with cross-section highlighted

fluid dynamic viscosity is increased to that for thick honey, $1.002 \times 10^2\,\mathrm{dyne}\cdot\mathrm{s/cm^2}$ (c.f. $1.002 \times 10^{-2}\,\mathrm{dyne}\cdot\mathrm{s/cm^2}$ for water). This increase in dynamic viscosity makes the fluid much thicker and much harder to flow, resulting in the droplet conforming to its equilibrium geometry without any oscillation. From here, the dynamic viscosity shall be termed the viscosity, and no reference to the kinematic viscosity shall be made.

Several droplets of varying size resting on a flat surface, all of which begin with an initial cylindrical shape, subject to gravity forces are analysed, see Figure 7.1. Due to the axisymmetrical nature of this problem only an axisymmetric slice need be modelled. Firstly, the analytical solution shall be discussed before comparison to the results from the computational framework.

7.1.1 Analytical Solution for the Equilibrium Shape of Sessile Droplets

An analytical solution for the equilibrium shape of sessile droplets has been developed by Pozrikidis [52]. The analytical solution is found from the Young-Laplace equation (see Chapter 5). The Young-Laplace equation is parameterised resulting in a number of ordinary differential equations and these differential equations can be solved using numerical integration. The resulting solution of these differential equations gives the dimensionless height and radius for a given dimensionless volume. It is important at this time to define the

capillary length, l, a physical constant with dimensions of length dependent on the surface tension of the fluid, the fluid density and gravity.

$$l = \left(\frac{\gamma}{\rho g}\right)^{\frac{1}{2}} \tag{7.1}$$

In the problems to be examined, for liquid water at $20°C$, $\gamma = 73\,\text{dyne/cm}$, $\rho = 0.998\,\text{g/cm}^3$ and $g = 981\,\text{cm/s}^2$, the capillary length is $0.273\,\text{cm}$ or $2.73\,\text{mm}$. Thus, to obtain a droplet with dimensionless units, both the radius and height of the droplet are divided by the capillary length. The dimensionless volume E can be expressed as :

$$E = \frac{V}{\pi l^3} \tag{7.2}$$

where V is the volume of the droplet. As the droplets to be examined are axisymmetric in nature, Algorithm 7.1 is used to calculate the initial dimensions of the cross-section for either an assumed cylindrical or semi-circular initial shape. The algorithm assumes that the droplet cross-section has equal height and radius and therefore the area of the cross-section is found from either $A = r^2$ or $A = \pi r^3/4$. The centroid of the cross-section is then calculated and used in Pappuss' centroid theorem to formulate an expression for the volume of revolution of the cross-section. This expression can be rearranged to calculate the radius, r. In this vein, several droplets of varying dimensionless volume have been examined and a comparison between the equilibrium geometry from both the computational framework and the analytical solution can now be made. The magnitude of the dimensionless volume has been selected to allow direct comparison with the analytical solution postulated by Pozrikidis [52]. The surface acoustic wave analysis to be undertaken in the next chapter is for a droplet of volume $10\,\mu\text{L}$, $(E = 0.156)$, and therefore it is important to check volumes of the same magnitude as this; hence, dimensionless volumes of $E = 0.01$, $E = 0.1$ and $E = 1.0$ are assessed, and Figure 7.2 demonstrates the difference in size for equilibrium geometries with contact angles of $90°$ and $135°$. For post-processing the geometry is mirrored about the axis of symmetry to give the full cross-section.

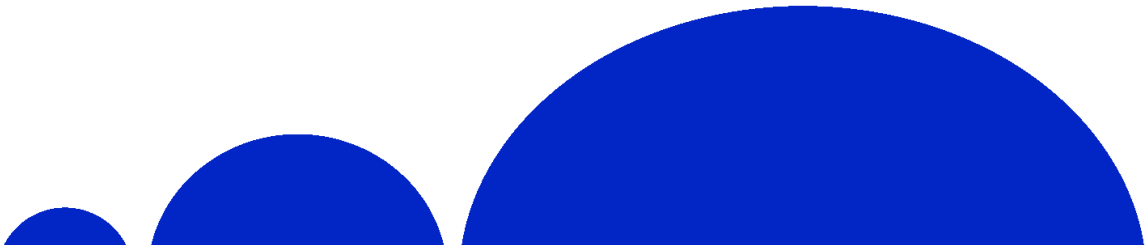

(a) Dimensionless volumes $E = 0.01$, $E = 0.1$ and $E = 1.0$ at equilibrium with 90° contact angle

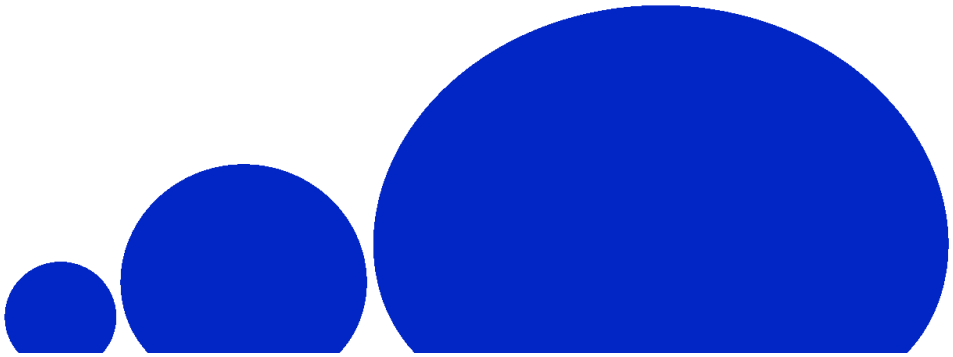

(b) Dimensionless volumes $E = 0.01$, $E = 0.1$ and $E = 1.0$ at equilibrium with 135° contact angle

Figure 7.2: Comparison of equilibrium geometries for the range of volumes examined

Input: Desired dimensionless volume E
Output: Initial dimensions r,z and volume V
Calculate the required volume using $V = E\pi l^3$;
if *initial shape is assumed cylindrical the cross-section is a square* **then**
  $r = z$ and therefore area, $A = r^2$;
  Distance from line of axisymmetry to centroid of cross-section, $\bar{y} = r/2$;
  Using Pappuss' centroid theorem, $V = 2\pi\bar{y}A = \pi r^3$;
  Rearranging, $r = \sqrt[3]{V/\pi}$;
end
if *initial shape is assumed semi-circular ($\alpha = 90°$) the cross-section is a quarter of a circle* **then**
  $r = z$ and therefore area, $A = \pi r^3/4$;
  Distance from line of axisymmetry to centroid of cross-section, $\bar{y} = 4r/3\pi$;
  Using Pappuss' centroid theorem, $V = 2\pi\bar{y}A = 2\pi r^3/3$;
  Rearranging, $r = \sqrt[3]{3V/2\pi}$;
end

Algorithm 7.1: Calculation of initial cross-section dimensions

7.1.2 Static Droplet with Dimensionless Volume 0.01

A dimensionless volume of $E = 0.01$ equates to an actual volume of 639.6 nL. To put this into perspective, there are approximately 1.56 million droplets this size in 1 litre. Droplets are examined for a range of equilibrium contact angles, 45°, 90° and 135°. A finite element mesh consisting of 504 nodes and 926 triangular elements (2520 degrees of freedom) is created in Cubit [7], with an initial cylindrical shape. Table 7.1 lists the parameters to be used for this volume, including fluid viscosity and fluid density. The user defined pressure stabilisation parameter β is given the value of 1.0 to give an appropriately smooth pressure field whilst keeping computational time to a minimum. Figure 7.3 depicts the boundary conditions applied to the mesh.

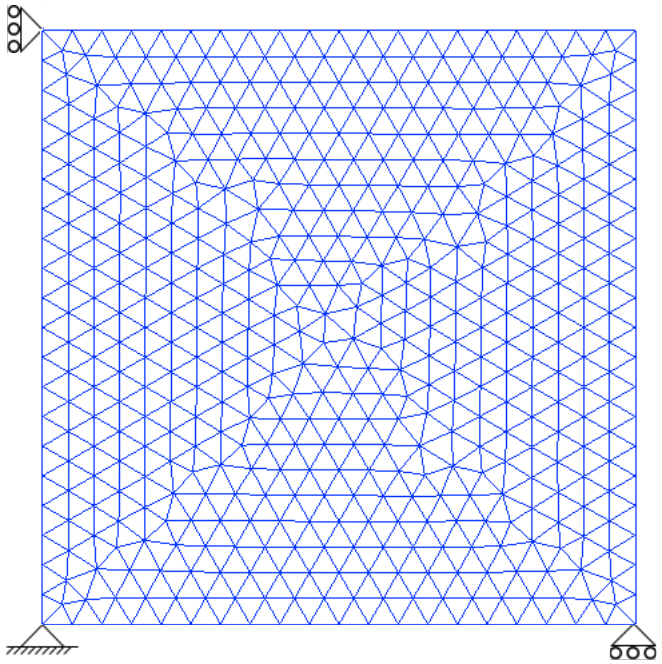

Figure 7.3: Typical initial FE mesh and boundary conditions for sessile droplet analyses

Parameter	Value
Fluid viscosity, μ	$1.01 \times 10^2\,\mathrm{dyne \cdot s/cm^2}$
Fluid density, ρ	$0.998\,\mathrm{g/cm^3}$
Surface tension, γ	$73\,\mathrm{dyne/cm}$
Stabilisation parameter, β	1.0
Mesh viscosity, μ_{mesh}	$1 \times 10^{-2}\,\mathrm{dyne \cdot s/cm^2}$
Gravitational acceleration, g	$-981\,\mathrm{cm/s^2}$

Table 7.1: Parameters for static analysis of sessile droplets

All three of the contact angles assessed achieve equilibrium geometry very quickly. Figures 7.4, 7.5, and 7.6 demonstrate the geometric evolution from the initial starting position to equilibrium. The colour contours demonstrate the pressure field with blue low pressure and red high pressure. The values of pressure are not relevant at this time. It was noted during the analyses for 45° and 135° equilibrium contact angles that the geometry evolves very quickly into a shape that achieves approximately the desired equilibrium contact angle. Once the equilibrium contact angle has been achieved, the bulk of the fluid then evolves into a geometry that maintains this angle. Thus, the equilibrium contact angle is achieved first, and the equilibrium geometry follows. This can be seen in the figures for these two equilibrium contact angles.

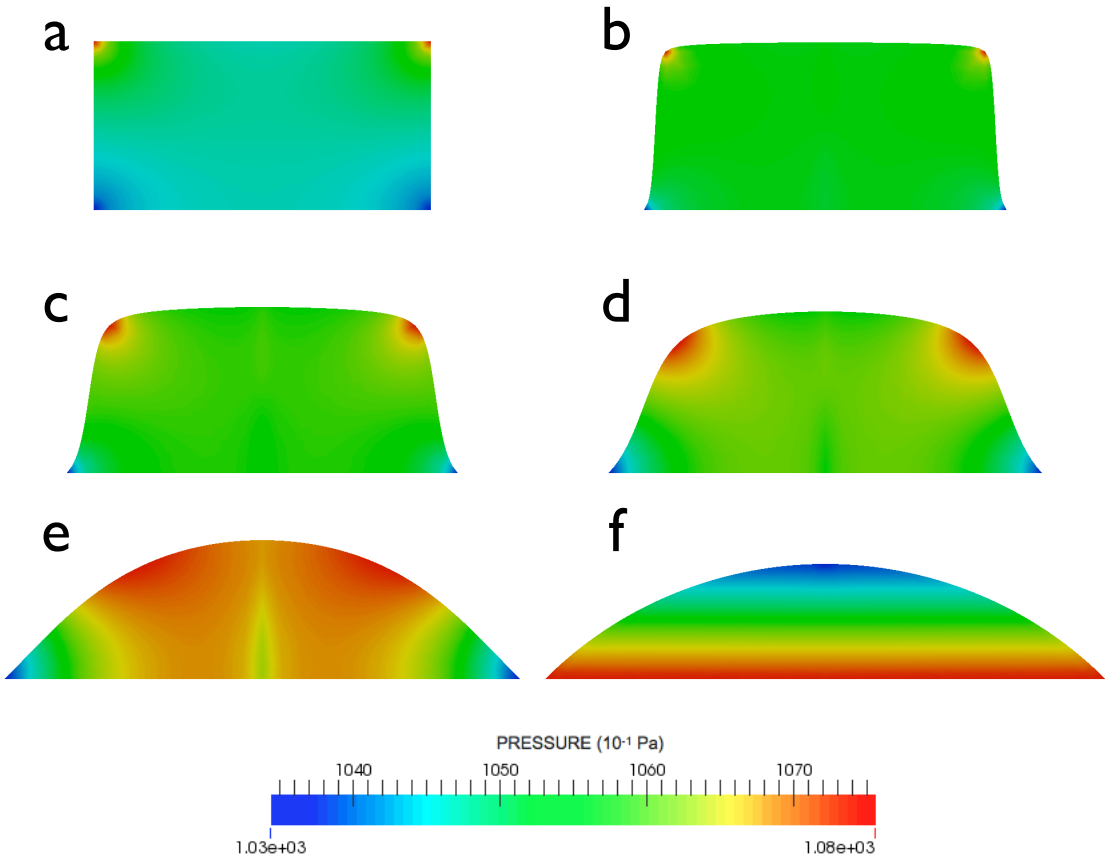

Figure 7.4: Static droplet geometry evolution for 45° contact angle, $E = 0.01$ with pressure contours: (a) t = 0 ms, (b) t = 5.8 ms, (c) t = 17.0 ms, (d) t = 39.0 ms, (e) t = 131.8 ms, (f) t = 933.9 ms

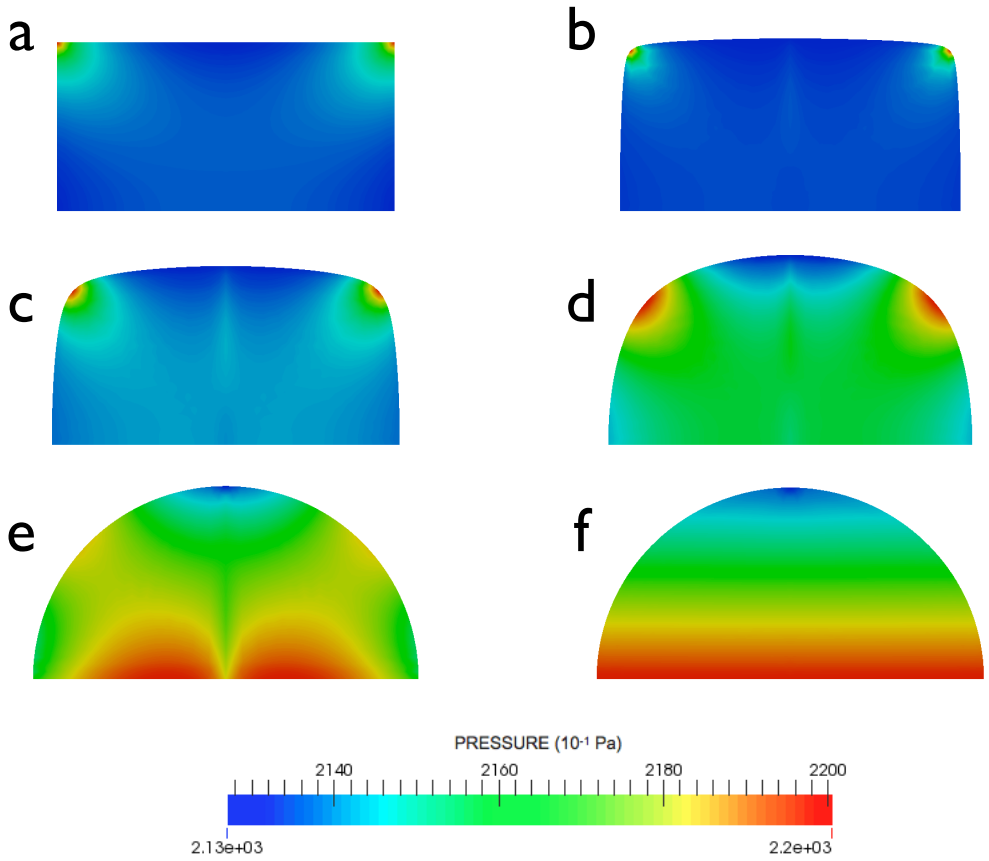

Figure 7.5: Static droplet geometry evolution for 90° contact angle, $E = 0.01$ with pressure contours: (a) t = 0 ms, (b) t = 6.2 ms, (c) t = 19.0 ms, (d) t = 55.4 ms, (e) t = 212.5 ms, (f) t = 1.96 s

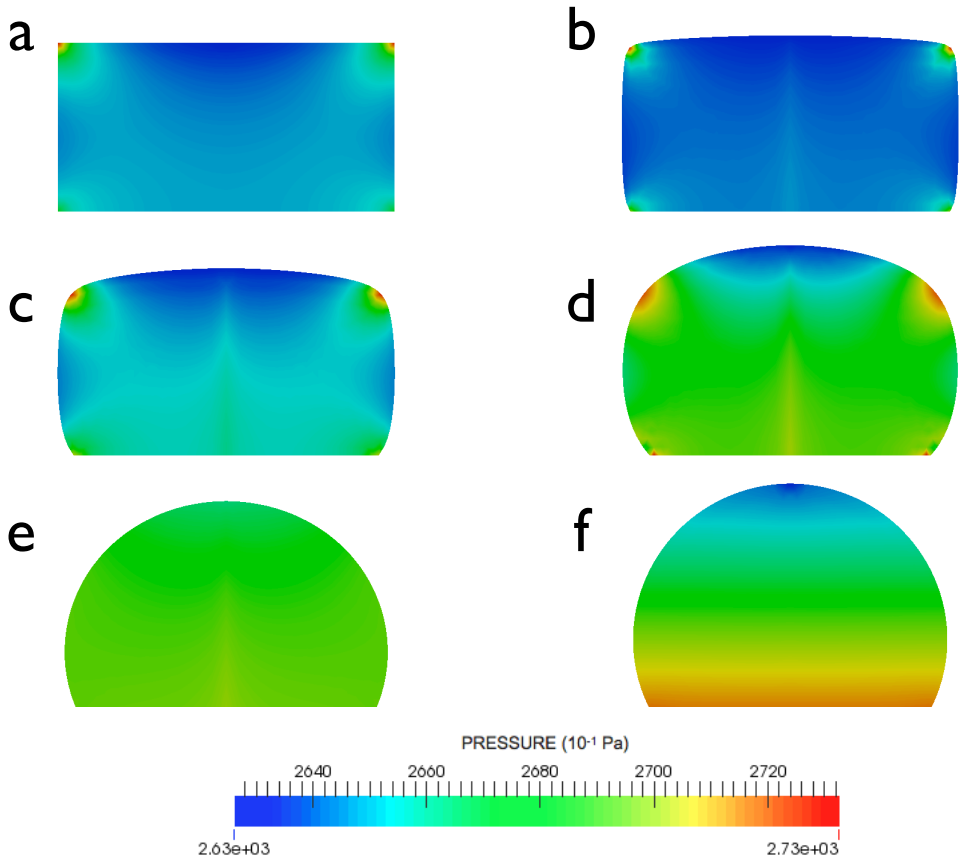

Figure 7.6: Static droplet geometry evolution for 135° contact angle, $E = 0.01$ with pressure contours: (a) t = 0 ms, (b) t = 5.5 ms, (c) t = 15.9 ms, (d) t = 42.9 ms, (e) t = 135.8 ms, (f) t = 662.9 ms

The final calculated contact angles from the computational analyses are 44.4°, 89.4°, and 133.1°. Increasing the number of mesh elements will bring the computational contact angle closer to that desired, but will result in an increased computational time. However, comparison to the analytical equilibrium shape shows a good correlation for each of the droplets. Figure 7.7 demonstrates the dimensionless radius, $\bar{R}$, plotted against dimensionless height, $\bar{Z}$ and therefore the shape of the droplets. There is a very good agreement between the calculated geometry and the analytical solutions, and any discrepancy between solutions can be explained by the coarseness of the FE mesh. It should be noted that there is negligible volume change over the course of the analyses, with changes of less than 0.08% occurring in each case.

In terms of the form of convergence, Figure 7.8 shows four consecutive representative steps for the analysis with a 90° contact angle. It can be seen that the convergence is quadratic, with the residual after each Newton iteration shown. Additional data noted at each step

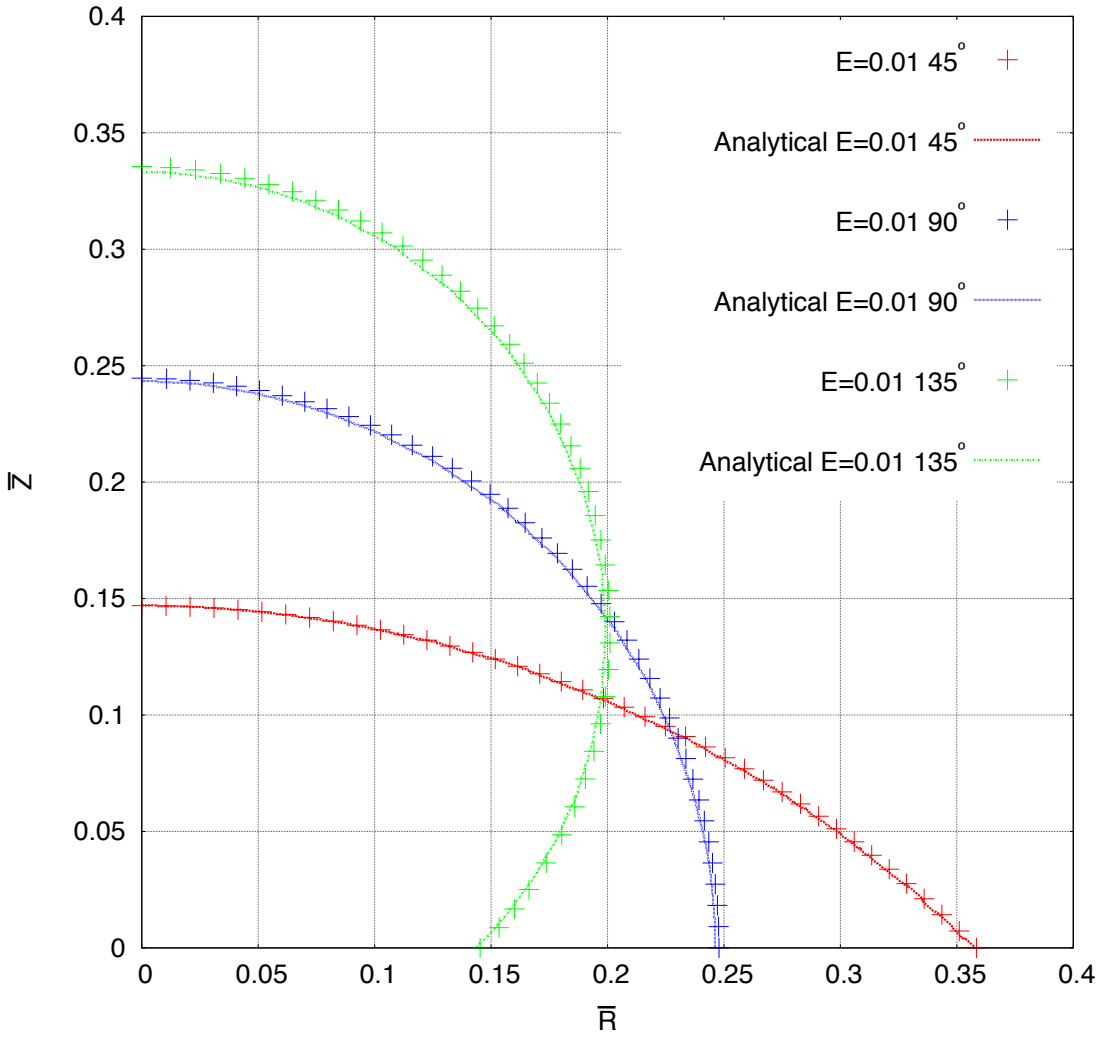

Figure 7.7: Comparison of computational and analytical equilibrium geometry for a range of contact angle, $E = 0.01$

```
SURFACE EDGES FOUND = 40        BOUNDARY EDGES FOUND = 80
step = 62, time = 0.000099369671273734
  0 SNES Function norm 9.956034015356e-03
  1 SNES Function norm 2.336220622678e-06
  2 SNES Function norm 1.435070641180e-09
  3 SNES Function norm 8.185706258816e-10
Nonlinear solve converged due to CONVERGED_FNORM_ABS
Number of Newton iterations = 3
AAA     step= 62   time= 0.000099369671273734  H= 0.0588525906  R= 0.0588408155  phi= 89.998809
V= 0.0006396388 == -0.0000019%   gy= -9.81000e+02 New dt = +1.35142e-05
-----------------------------------------------------------------------------------------------

SURFACE EDGES FOUND = 40        BOUNDARY EDGES FOUND = 80
step = 63, time = 0.000112883833482060
  0 SNES Function norm 9.932817732250e-03
  1 SNES Function norm 2.330454993195e-06
  2 SNES Function norm 1.212442409879e-09
  3 SNES Function norm 8.154376219128e-10
Nonlinear solve converged due to CONVERGED_FNORM_ABS
Number of Newton iterations = 3
AAA     step= 63   time= 0.000112883833482060  H= 0.0588553639  R= 0.0588422449  phi= 89.998656
V= 0.0006396388 == -0.0000019%   gy= -9.81000e+02 New dt = +1.35142e-05
-----------------------------------------------------------------------------------------------

SURFACE EDGES FOUND = 40        BOUNDARY EDGES FOUND = 80
step = 64, time = 0.000126397995690386
  0 SNES Function norm 9.909956404627e-03
  1 SNES Function norm 2.325507673453e-06
  2 SNES Function norm 1.208171845533e-09
  3 SNES Function norm 8.131235471925e-10
Nonlinear solve converged due to CONVERGED_FNORM_ABS
Number of Newton iterations = 3
AAA     step= 64   time= 0.000126397995690386  H= 0.0588581365  R= 0.0588436742  phi= 89.998503
V= 0.0006396388 == -0.0000019%   gy= -9.81000e+02 New dt = +1.35142e-05
-----------------------------------------------------------------------------------------------

SURFACE EDGES FOUND = 40        BOUNDARY EDGES FOUND = 80
step = 65, time = 0.000139912157898712
  0 SNES Function norm 9.887256003365e-03
  1 SNES Function norm 2.320669090700e-06
  2 SNES Function norm 1.204124304980e-09
  3 SNES Function norm 8.108006440501e-10
Nonlinear solve converged due to CONVERGED_FNORM_ABS
Number of Newton iterations = 3
AAA     step= 65   time= 0.000139912157898712  H= 0.0588609084  R= 0.0588451034  phi= 89.998350
V= 0.0006396388 == -0.0000019%   gy= -9.81000e+02 New dt = +1.35142e-05
```

Figure 7.8: Four representative steps for static analysis of $E = 0.01$ and 90° contact angle

includes the current time, the height of the droplet, the radius of the droplet, the current contact angle, the current volume and percentage volume loss, gravitational acceleration and the new adaptive time step.

7.1.3 Static Droplet with Dimensionless Volume 0.1

A similar droplet with dimensionless volume of $E = 0.1$ is now considered, with an actual volume of $6.396\,\mu$L. Approximately $156,338$ droplets this size are in 1 litre. The range of equilibrium contact angles to be examined is $60°$, $90°$ and $145°$ using a denser finite element mesh consisting of 1401 nodes and 2664 triangular elements (7005 degrees of freedom). Once again, the mesh initially has a cylindrical shape. The same parameters are used as previously and are listed in Table 7.1 and the same boundary conditions as shown in Figure 7.3. The evolution manifested in much the same manner as before, with the desired contact angle being approximately achieved followed by the fluid evolving into a geometry that maintains this angle. The final calculated equilibrium contact angles from the computational analyses are $59.6°$, $89.3°$, and $146.1°$ with no volume change of more than 0.01% occurring. Comparison to the analytical solution shows a generally good correlation, especially for a contact angle of $90°$, see Figure 7.12.

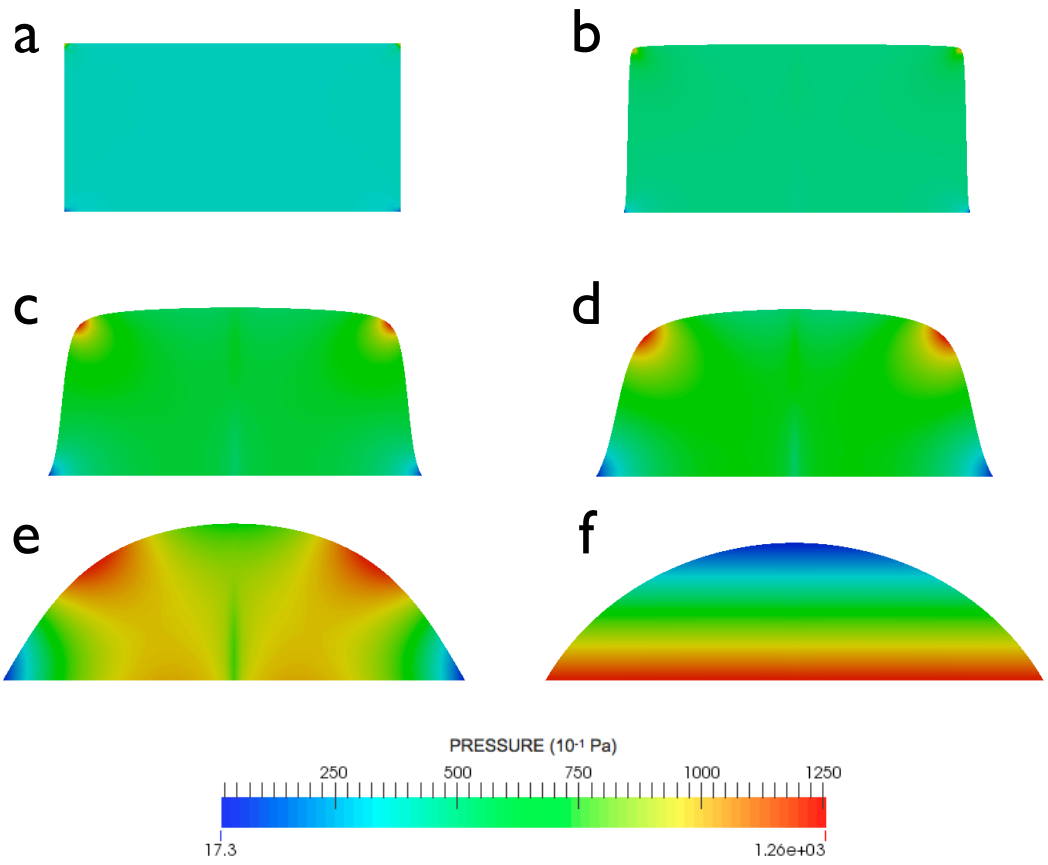

Figure 7.9: Static droplet geometry evolution for $60°$ contact angle, $E = 0.1$ with pressure contours: (a) t = 0 ms, (b) t = 6.0 ms, (c) t = 30.3 ms, (d) t = 60.1 ms, (e) t = 215.6 ms, (f) t = 1.41 s

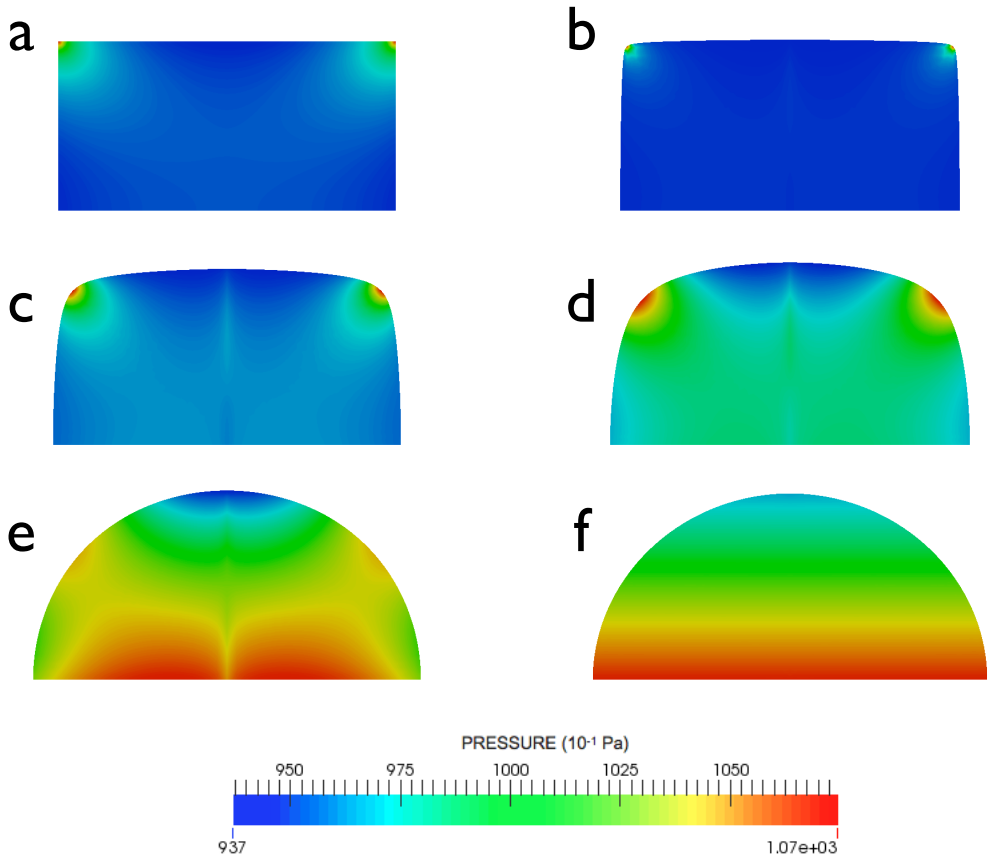

Figure 7.10: Static droplet geometry evolution for 90° contact angle, $E = 0.1$ with pressure contours: (a) t = 0 ms, (b) t = 6.5 ms, (c) t = 34.9 ms, (d) t = 78.3 ms, (e) t = 303.0 ms, (f) t = 1.62 s

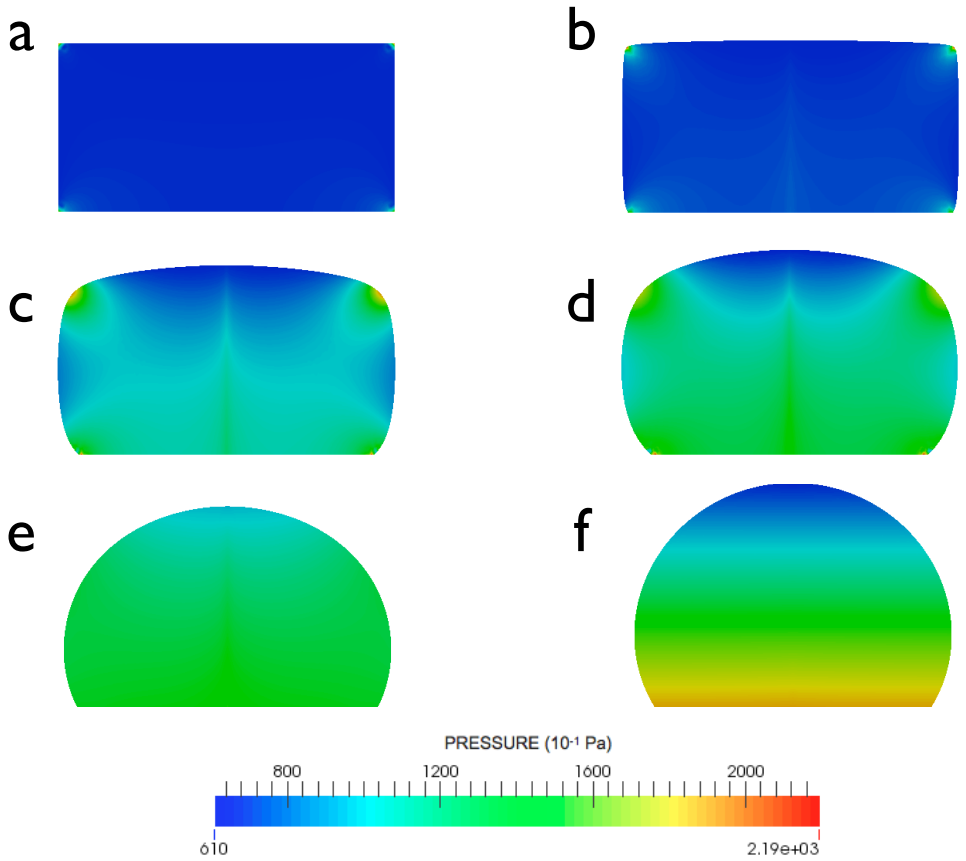

Figure 7.11: Static droplet geometry evolution for 145° contact angle, $E = 0.1$ with pressure contours: (a) t = 0 ms, (b) t = 6.7 ms, (c) t = 38.8 ms, (d) t = 75.4 ms, (e) t = 219.8 ms, (f) t = 1.27 s

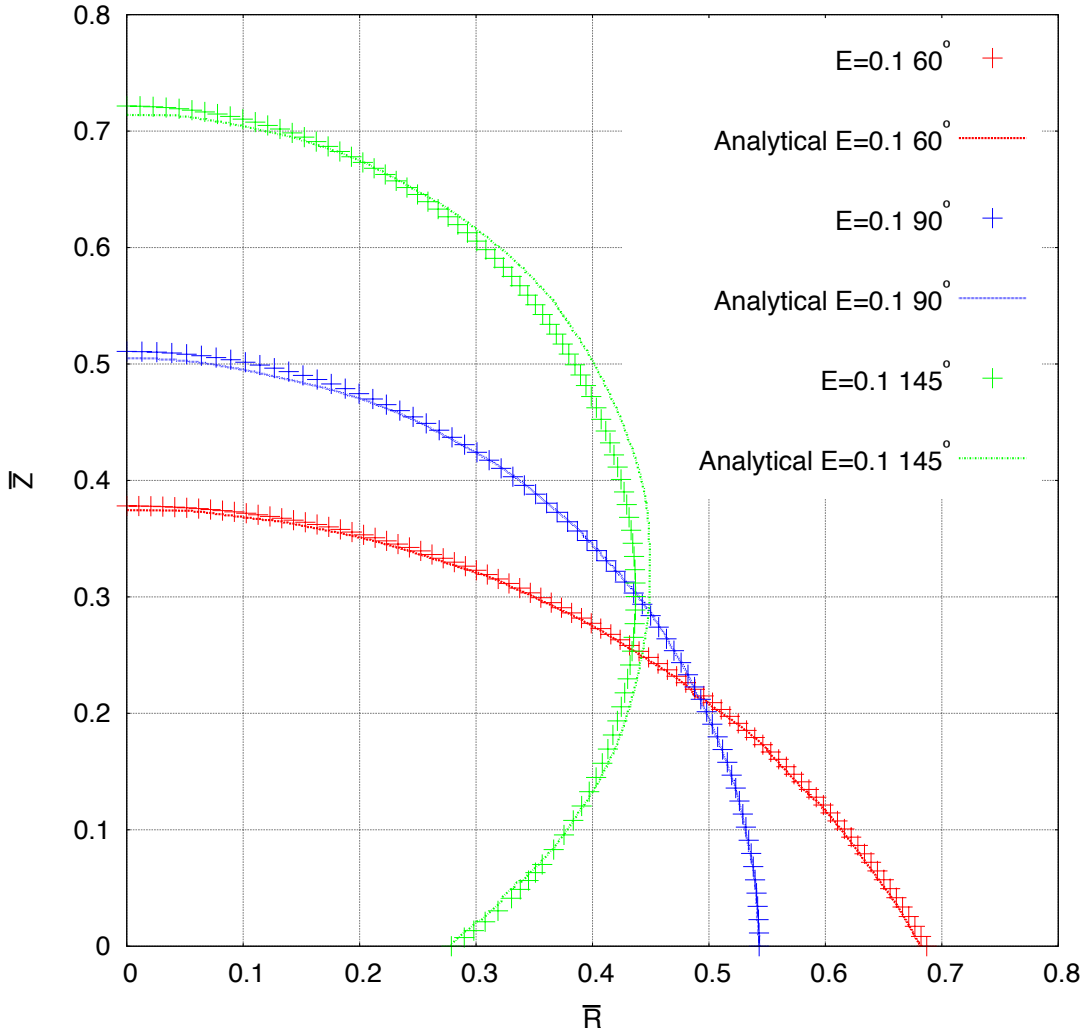

Figure 7.12: Comparison of computational and analytical equilibrium geometry for a range of contact angle, $E = 0.1$

7.1.4 Static Droplet with Dimensionless Volume 1.0

The third droplet assessed has a dimensionless volume of $E = 1.0$ which equates to an actual volume of $63.96\,\mu$L; approximately $15,633$ droplets this size are in 1 litre. Droplets are examined for a range of equilibrium contact angles - 40°, 90° and 150° - using a finite element mesh consisting of 1571 nodes and 2996 triangular elements (7855 degrees of freedom). The boundary conditions applied are those shown in Figure 7.3 and the parameters used are those listed in Table 7.1. Figures 7.13, 7.14 and 7.15 show the evolution of the droplets to equilibrium and it is immediately clear that the droplets are flatter at the top. This is because gravity has much more influence on this larger volume compared to the smaller volumes. The pressure field is shown in these figures, but the magnitude of the pressures is not im-

portant at this time. The final computed contact angles from the computational analyses are 39.5°, 89.1°, and 148.2°, with no volume change of more than 0.018% occurring. Figure 7.16 shows a good correlation between the computational geometries and the analytical geometries, especially for 40° and 90° contact angles.

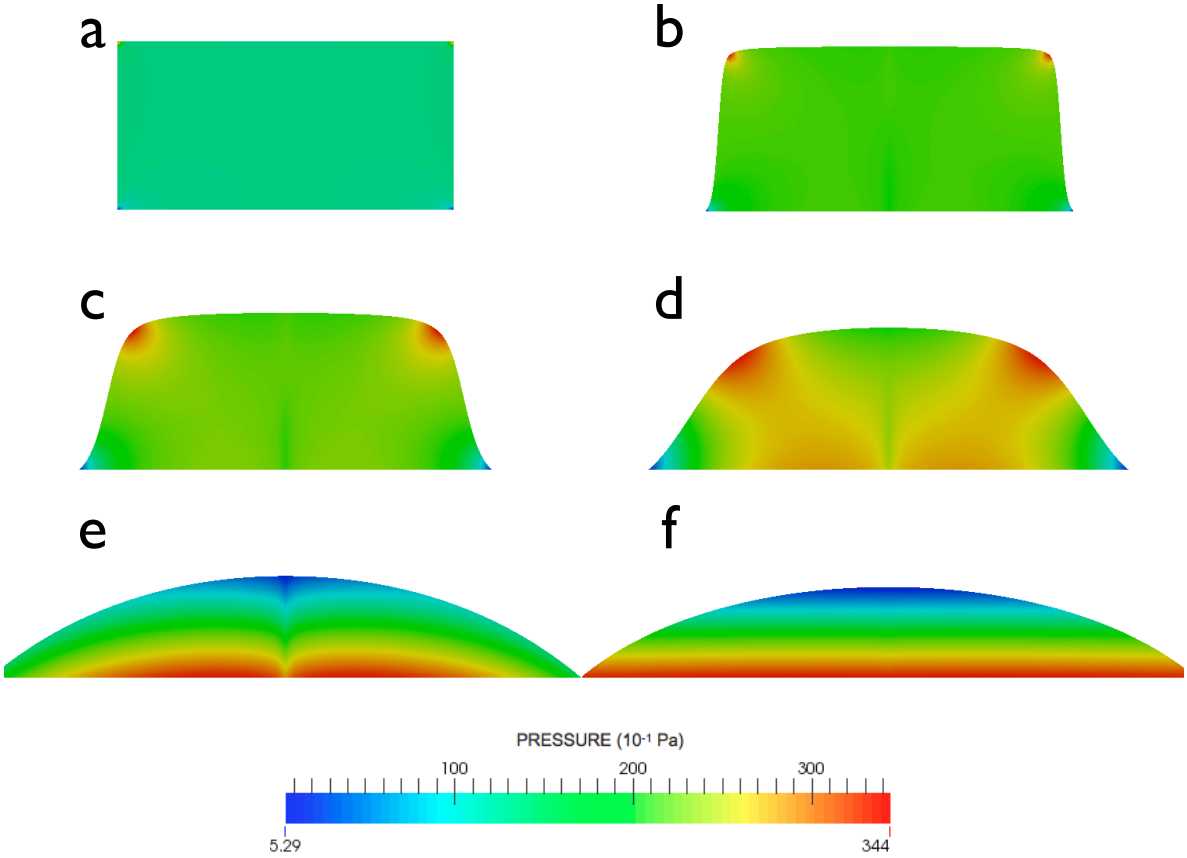

Figure 7.13: Static droplet geometry evolution for 40° contact angle, $E = 1.0$ with pressure contours: (a) t = 0 ms, (b) t = 30.6 ms, (c) t = 93.3 ms, (d) t = 242.1 ms, (e) t = 1.03 s, (f) t = 2.85 s

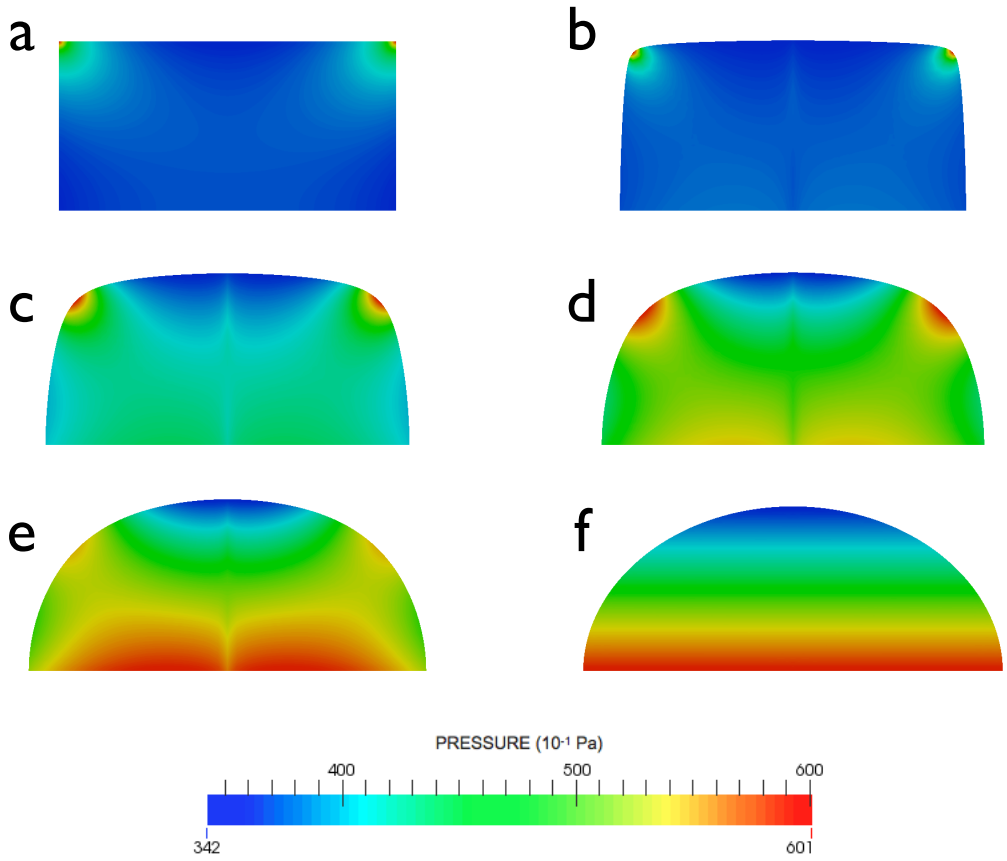

Figure 7.14: Static droplet geometry evolution for 90° contact angle, $E = 1.0$ with pressure contours: (a) t = 0 ms, (b) t = 36.1 ms, (c) t = 119.1 ms, (d) t = 225.8 ms, (e) t = 364.5 ms, (f) t = 1.10 s

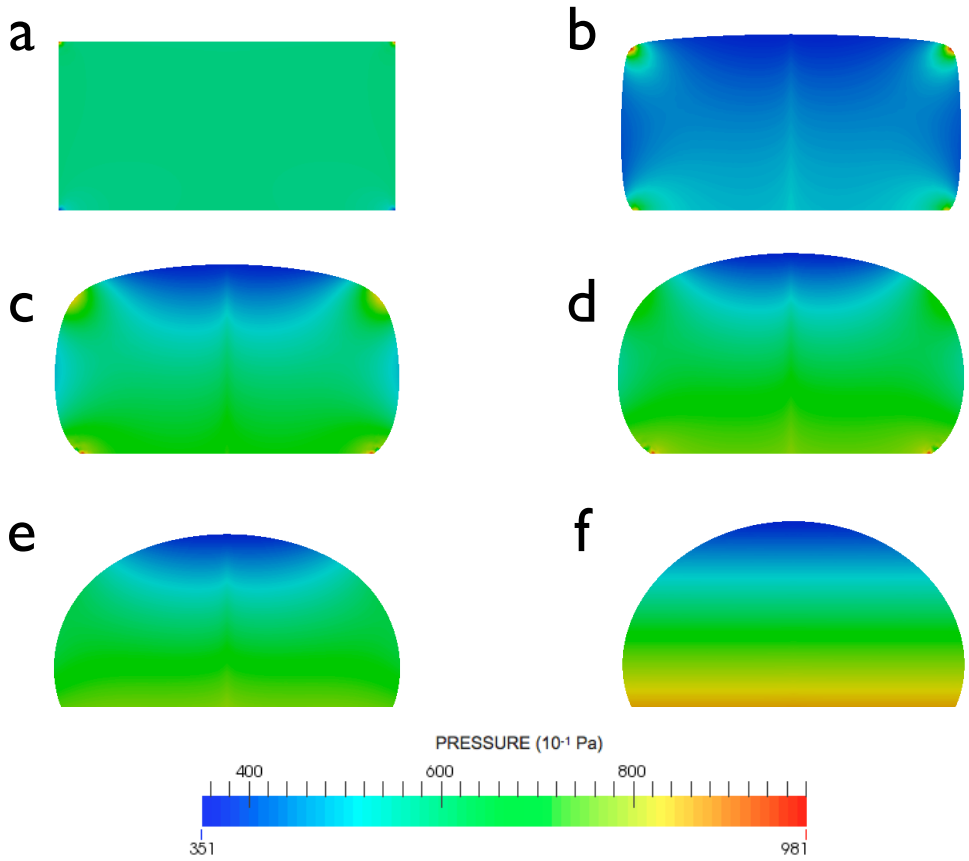

Figure 7.15: Static droplet geometry evolution for 150° contact angle, $E = 1.0$ with pressure contours: (a) t = 0 ms, (b) t = 36.2 ms, (c) t = 121.7 ms, (d) t = 223.9 ms, (e) t = 377.4 ms, (f) t = 1.40 s

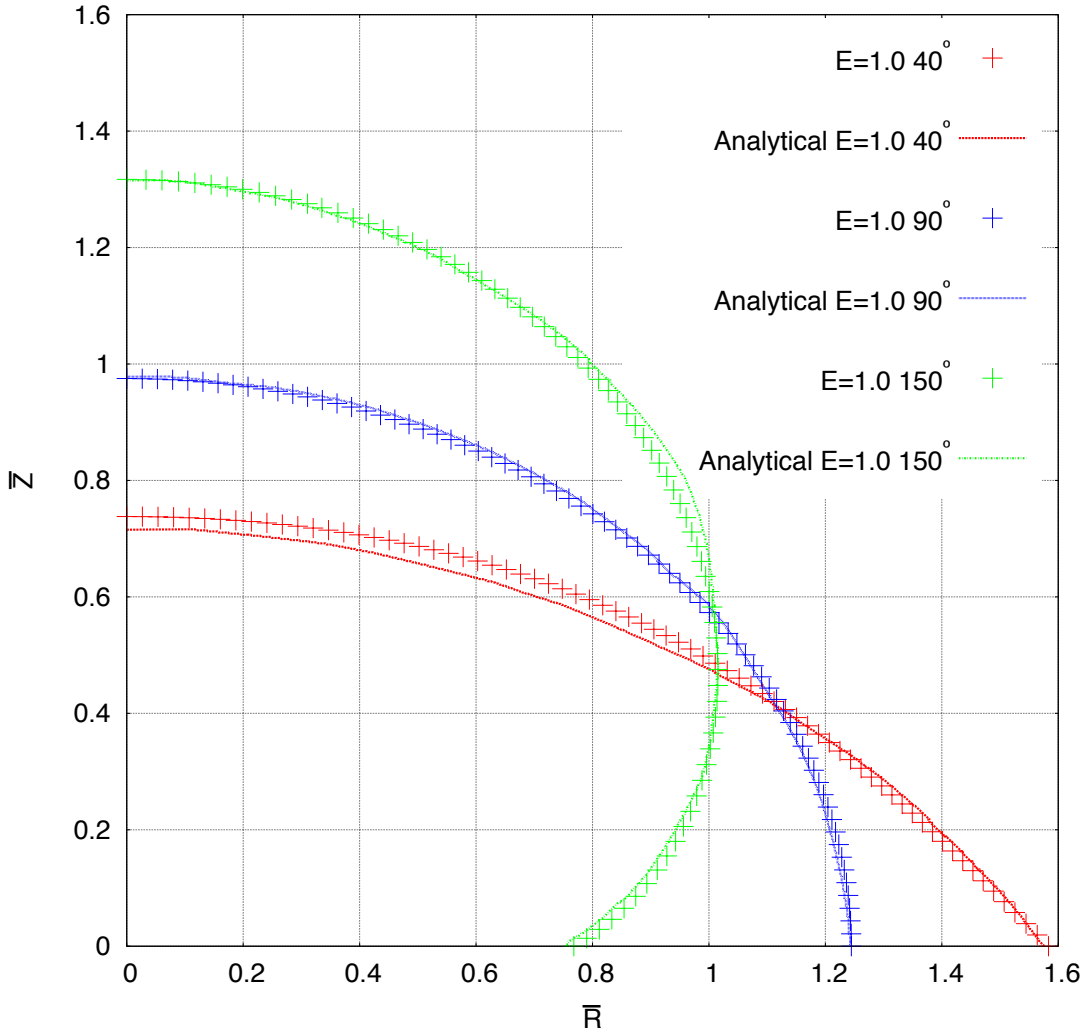

Figure 7.16: Comparison of computational and analytical equilibrium geometry for a range of contact angle, $E = 1.0$

In terms of the form of convergence, Figure 7.17 shows four consecutive representative steps for the analysis with a 90° contact angle. It can be seen that the convergence is quadratic, with the residual after each Newton iteration shown. Additional data noted at each step includes the current time, the height of the droplet, the radius of the droplet, the current contact angle, the current volume and percentage volume loss, gravitational acceleration and the new adaptive time step.

```
SURFACE EDGES FOUND = 72        BOUNDARY EDGES FOUND = 144
step = 137, time = 0.001137435897486613
  0 SNES Function norm 2.467462053401e-02
  1 SNES Function norm 6.767842070339e-06
  2 SNES Function norm 1.086044014302e-09
  3 SNES Function norm 9.024287980241e-10
Nonlinear solve converged due to CONVERGED_FNORM_ABS
Number of Newton iterations = 3
AAA     step= 137   time= 0.001137435897486613  H= 0.2731501840  R= 0.2732777659  phi= 89.995452
V= 0.0639638858 == -0.0000001%   gy= -9.81000e+02 New dt = +1.26930e-05
-----------------------------------------------------------------------------------------------

SURFACE EDGES FOUND = 72        BOUNDARY EDGES FOUND = 144
step = 138, time = 0.001150128860759803
  0 SNES Function norm 2.461193692809e-02
  1 SNES Function norm 6.761254102138e-06
  2 SNES Function norm 1.092754672388e-09
  3 SNES Function norm 9.011205319899e-10
Nonlinear solve converged due to CONVERGED_FNORM_ABS
Number of Newton iterations = 3
AAA     step= 138   time= 0.001150128860759803  H= 0.2731508710  R= 0.2732804355  phi= 89.995399
V= 0.0639638858 == -0.0000001%   gy= -9.81000e+02 New dt = +1.26930e-05
-----------------------------------------------------------------------------------------------

SURFACE EDGES FOUND = 72        BOUNDARY EDGES FOUND = 144
step = 139, time = 0.001162821824032992
  0 SNES Function norm 2.454945861545e-02
  1 SNES Function norm 6.754045157971e-06
  2 SNES Function norm 1.093357689294e-09
  3 SNES Function norm 8.995923344411e-10
Nonlinear solve converged due to CONVERGED_FNORM_ABS
Number of Newton iterations = 3
AAA     step= 139   time= 0.001162821824032992  H= 0.2731515578  R= 0.2732831052  phi= 89.995346
V= 0.0639638858 == -0.0000001%   gy= -9.81000e+02 New dt = +1.26930e-05
-----------------------------------------------------------------------------------------------

SURFACE EDGES FOUND = 72        BOUNDARY EDGES FOUND = 144
step = 140, time = 0.001175514787306182
  0 SNES Function norm 2.448720567451e-02
  1 SNES Function norm 6.746955184429e-06
  2 SNES Function norm 1.093734298685e-09
  3 SNES Function norm 8.980654267858e-10
Nonlinear solve converged due to CONVERGED_FNORM_ABS
Number of Newton iterations = 3
AAA     step= 140   time= 0.001175514787306182  H= 0.2731522445  R= 0.2732857748  phi= 89.995292
V= 0.0639638858 == -0.0000001%   gy= -9.81000e+02 New dt = +1.26930e-05
```

Figure 7.17: Four representative steps for static analysis of $E = 1.0$ and 90° contact angle

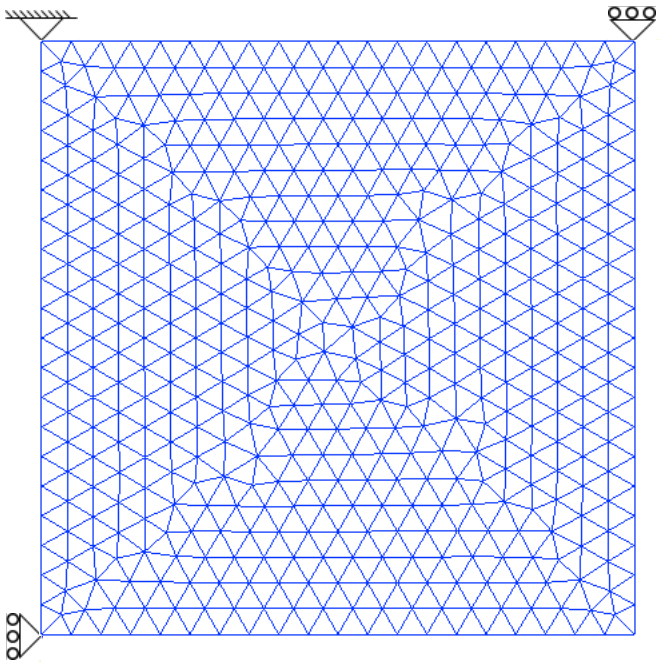

Figure 7.18: Typical initial FE mesh and boundary conditions for hanging droplet analyses

7.1.5 Static Hanging Droplets

Droplets of liquid hang from surfaces in many everyday situations, the obvious example being water taps. Utilising the same mesh as the first case ($E = 0.01$) and the parameters as listed in Table 7.1 but applying different boundary conditions (see Figure 7.18) allows for the examination of a droplet hanging from a surface under gravitational forces. An equilibrium contact angle of 90° is considered. Figure 7.19 demonstrates the evolution of this droplet from the initial geometry to equilibrium, and Figure 7.20 shows that the final geometry (vertical coordinate scaled by -1) of the droplet is approximately identical to that for the upright droplet, with both showing good correlation to the analytical solution.

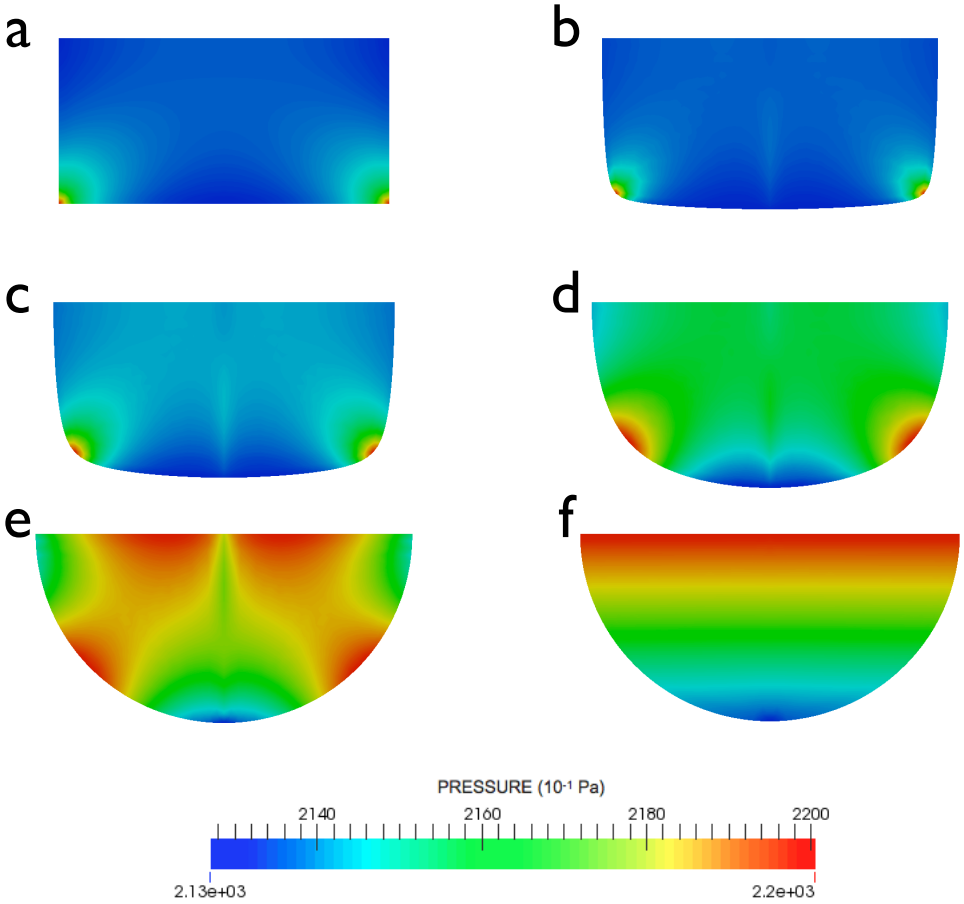

Figure 7.19: Static droplet geometry evolution for hanging droplet, 90° contact angle, $E = 0.01$ with pressure contours: (a) t = 0 ms, (b) t = 10.5 ms, (c) t = 24.1 ms, (d) t = 43.2 ms, (e) t = 189.0 ms, (f) t = 676.0 ms

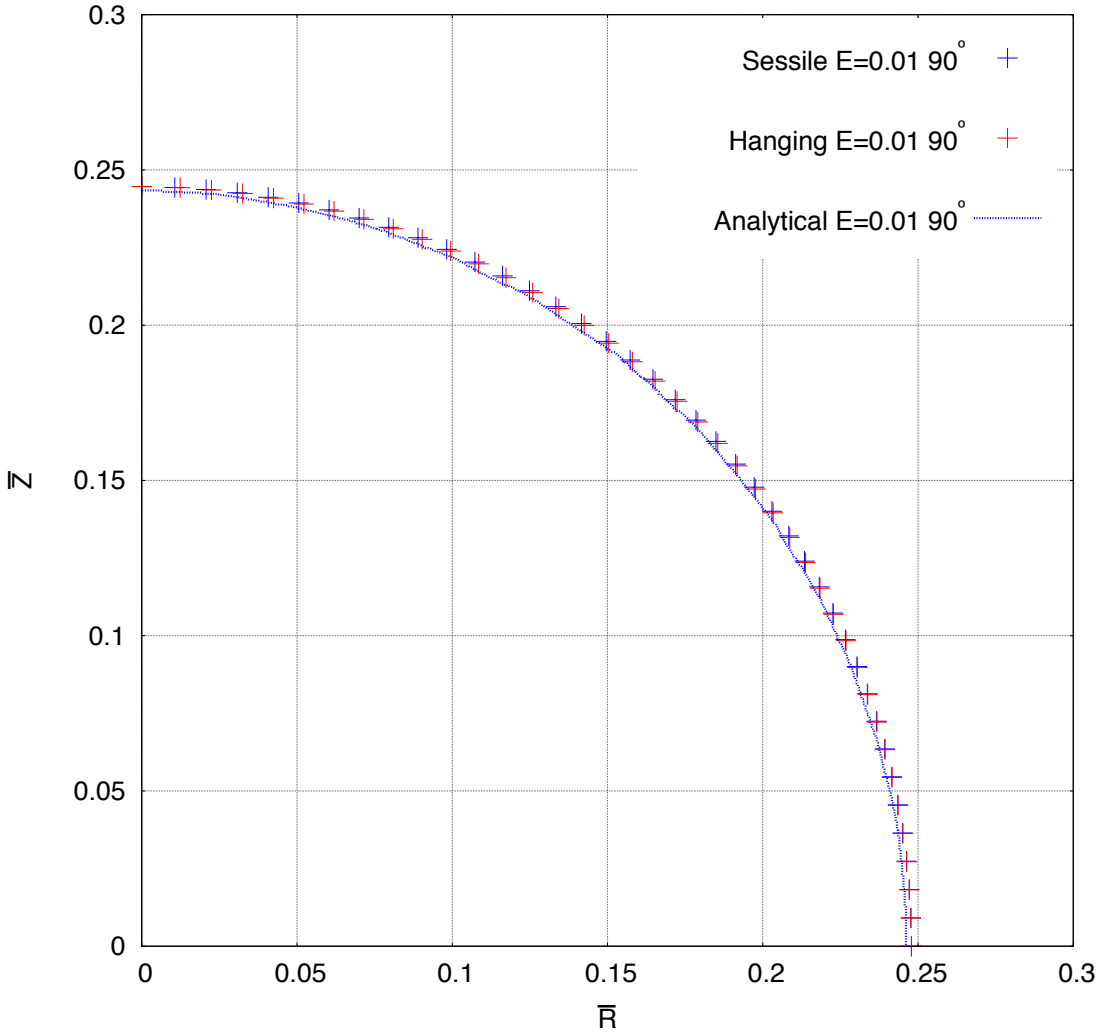

Figure 7.20: Comparison of computational and analytical equilibrium geometry of a hanging droplet, 90° contact angle, $E = 0.01$

The fact that both the upright and hanging droplets result in approximately identical equilibrium geometries demonstrates that gravity has little influence on the geometry given the small volume under consideration and that surface tension is the dominant action.

7.2 Dynamic Analysis of Floating Droplets

All of the problems examined up to this point have focused on a comparison of the predicted static equilibrium shape with an analytical solution. The manner in which a droplet geometry evolves and, for example, oscillates towards its equilibrium position will now be assessed. Only then, safe in the knowledge that the framework predicts both the correct equilibrium geometry and the form of oscillation, can more complex dynamic problems be examined.

In zero-gravity environments, surface tension will force a droplet to conform to a near perfect sphere. Starting at a non-equilibrium geometry, the droplet has the potential energy it requires to achieve its equilibrium shape. Three water droplets, of approximately the same volume, but of different starting geometry, are examined in a zero-gravity environment not only for the equilibrium geometry but also for the period of oscillation. Due to the axisymmetrical nature of this problem only half the domain cross-section need be modelled. First, the analytical solution shall be discussed before comparison to the results from the computational framework.

7.2.1 Comparison with the Analytical Solution for the Equilibrium Shape of Floating Droplets

Whilst ignoring viscous effects and assuming small amplitude oscillations, Rayleigh [53] determined the period of oscillation for water droplets floating in zero-gravity. The oscillating motion of the droplet in polar coordinates (r,θ) is given by:

$$r(t) = R + A\sin\omega t P_n(cos\theta) \tag{7.3}$$

where R is the unperturbed spherical radius, A is the amplitude and P_n is the n^{th} order Legendre polynomial, and n is the prescribed mode of oscillation. Rayleigh [53] showed that the angular frequency ω (measured in radians/second) can be calculated as:

$$\omega = \sqrt{n(n-1)(n+2)\left(\frac{\gamma}{\rho R^3}\right)} \tag{7.4}$$

Therefore, the period of oscillation T (measured in seconds) can be found from:

$$T = \frac{2\pi}{\omega} \tag{7.5}$$

Table 7.2 lists the frequency and period for the first three non-trivial modes of oscillation, $n = 2,3,4$, for $R = 0.0125\,\text{cm}$ and $A = 0.2R$.

Oscillation mode n	Analytical angular frequency ω (radians/second)	Analytical period T (seconds)
2	17,309.17	3.63×10^{-4}
3	33,519.06	1.87×10^{-4}
4	51,927.50	1.21×10^{-4}

Table 7.2: Analytical frequency and period

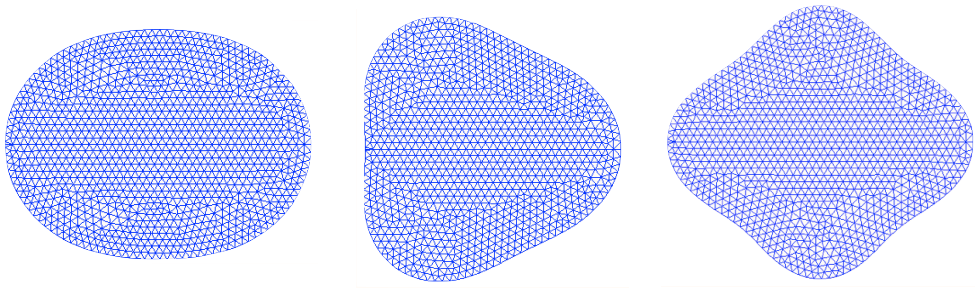

(a) n=2 (b) n=3 (c) n=4

Figure 7.21: Initial geometry of floating droplets; the geometric centre of the droplets is fixed

To compare the computational model with this analytical solution, a droplet geometry for each mode of oscillation ($n = 2, 3, 4$) was created. The initial geometry was determined from Equation 7.3; this non-equilibrium configuration provides potential energy to the droplet. Note, there is no contribution from the contact line as the droplets are floating in zero-gravity. The initial geometry of each droplet is meshed in Cubit [7] with approximately 580 nodes and 1067 triangular elements (2900 degrees of freedom), with the geometric centre fixed to avoid rigid body motion and the analysis performed using the parameters listed in Table 7.3, where the fluid parameters are those for liquid water at $20°C$. A constant time step of 1×10^{-7} sec was used in the following analyses for comparisons to be made more easily. Figure 7.21 shows each of the three droplets at time $t = 0$.

Parameter	Value
Fluid viscosity, μ	$1.01 \times 10^{-2}\,\text{dyne} \cdot \text{s/cm}^2$
Fluid density, ρ	$0.998\,\text{g/cm}^3$
Surface tension, γ	73 dyne/cm
Contact angle, α	Not required
Stabilisation parameter, β	1.0
Mesh viscosity, μ_{mesh}	$1 \times 10^{-3}\,\text{dyne} \cdot \text{s/cm}^2$
Gravitational acceleration, g	$0\,\text{cm/s}^2$
Time step, Δt	1×10^{-7} sec

Table 7.3: Parameters for dynamic analysis of floating droplets

The viscosity acts as a natural damper and so the three droplets all oscillate toward their equilibrium geometry, which in this case is a circle given that we are assessing an axisymmetric cross-section. Figures 7.22, 7.23 and 7.24, depict the evolution of the finite element mesh

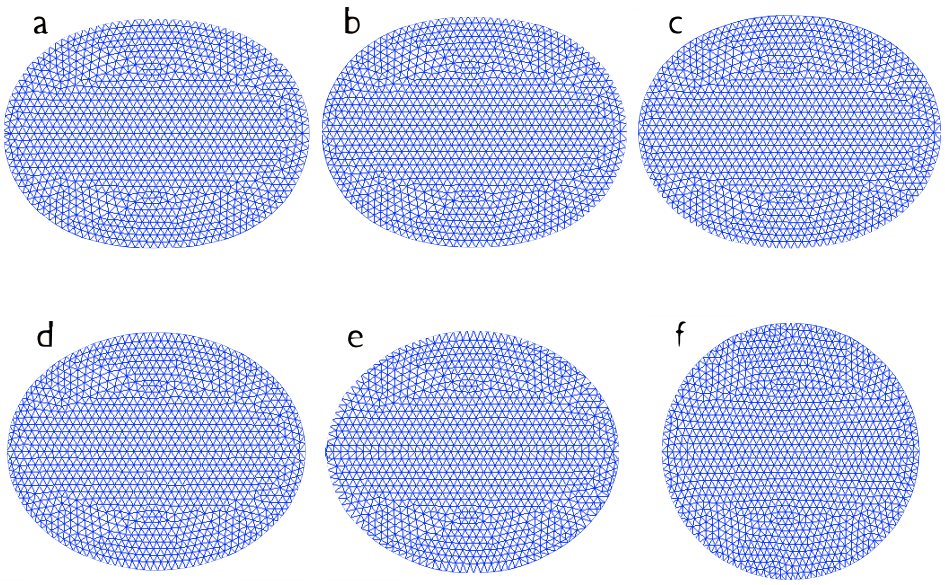

Figure 7.22: Droplet oscillations for $n = 2$ mode at various time instants: (a) $t = 0$, (b) $t = T/8$, (c) $t = T/4$, (d) $t = 3T/8$, (e) $t = T/2$, (f) $t = \infty$

for droplets with $n = 2$, $n = 3$ and $n = 4$ respectively before conforming to a near-perfect circle when steady state conditions are achieved. Capillary waves were observed on the surface of each droplet. To obtain the computational period, a point on the droplet is traced in time providing periods of oscillation of 3.74×10^{-4} seconds, 1.92×10^{-4} seconds and 1.23×10^{-4} seconds for $n = 2,3,4$ respectively. Figures 7.25, 7.26 and 7.27 show the comparison between the computed period of oscillation and the analytical period of oscillation for $n = 2,3,4$ respectively; the vertical black line in each figure demonstrates the analytical period and the dotted line demonstrates the calculated period. It can be seen that for each mode of oscillation, the computed period is very close indeed to the analytical period, with the computed period being slightly longer. The difference between the computed and analytical period is less than 3% for each mode of oscillation. This difference is due to the fact that Rayleigh neglects viscous effects and assumes small amplitude oscillations while the computational framework includes viscous effects and assumes large deformations. Volume change during these simulations is negligible with a 0.004% gain for $n = 2$, 0.013% loss for $n = 3$, and 0.008% loss for $n = 4$.

Examining Figures 7.25, 7.26 and 7.27 closer, it can be seen that the amplitude reduces significantly within the first period. For example, for $n = 2$ the amplitude reduces from

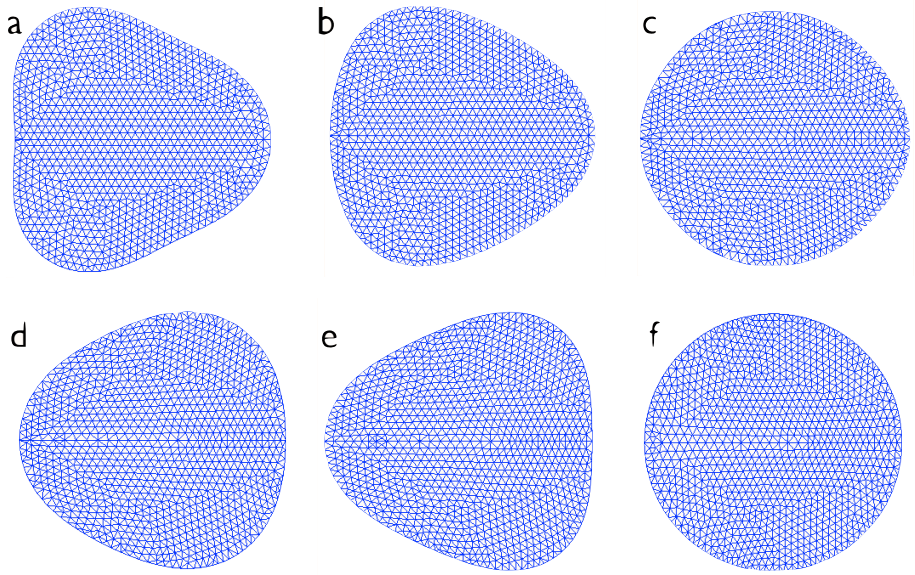

Figure 7.23: Droplet oscillations for $n = 3$ mode at various time instants: (a) $t = 0$, (b) $t = T/8$, (c) $t = T/4$, (d) $t = 3T/8$, (e) $t = T/2$, (f) $t = \infty$

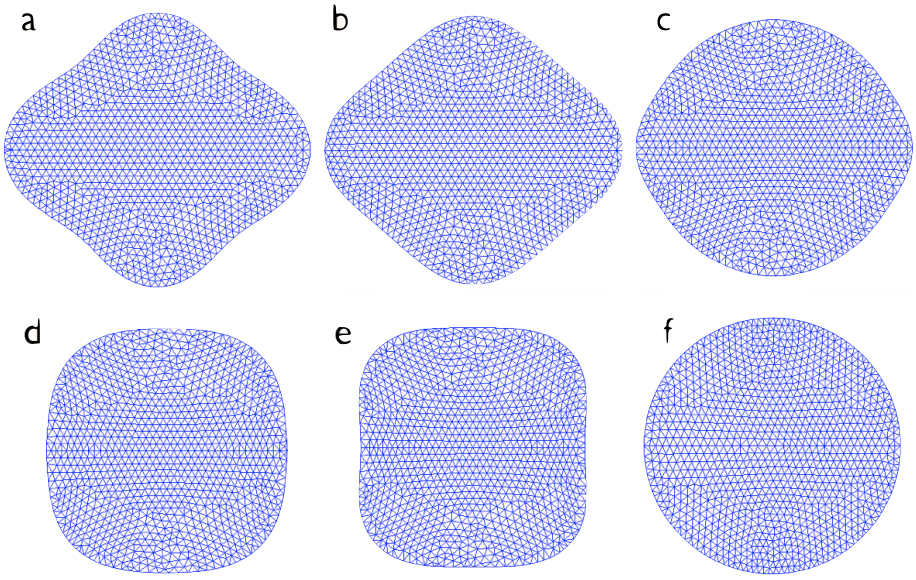

Figure 7.24: Droplet oscillations for $n = 4$ mode at various time instants: (a) $t = 0$, (b) $t = T/8$, (c) $t = T/4$, (d) $t = 3T/8$, (e) $t = T/2$, (f) $t = \infty$

≈ 0.00125cm to ≈ 0.001cm; a reduction of approximately 20%. The reason for this is unclear, however, it could be due to the coarseness of the mesh or the size of the time step.

For the given values of radius and amplitude under investigation ($R = 0.0125$ cm and $A = 0.2R$), the results from the computational framework correspond to the computational model by Saksono and Perić [58] which used a Lagrangian description. However, Saksono and Perić carefully select a mesh for the problem at hand with prior knowledge of the motion expected, whilst the computational framework developed does not have this constraint.

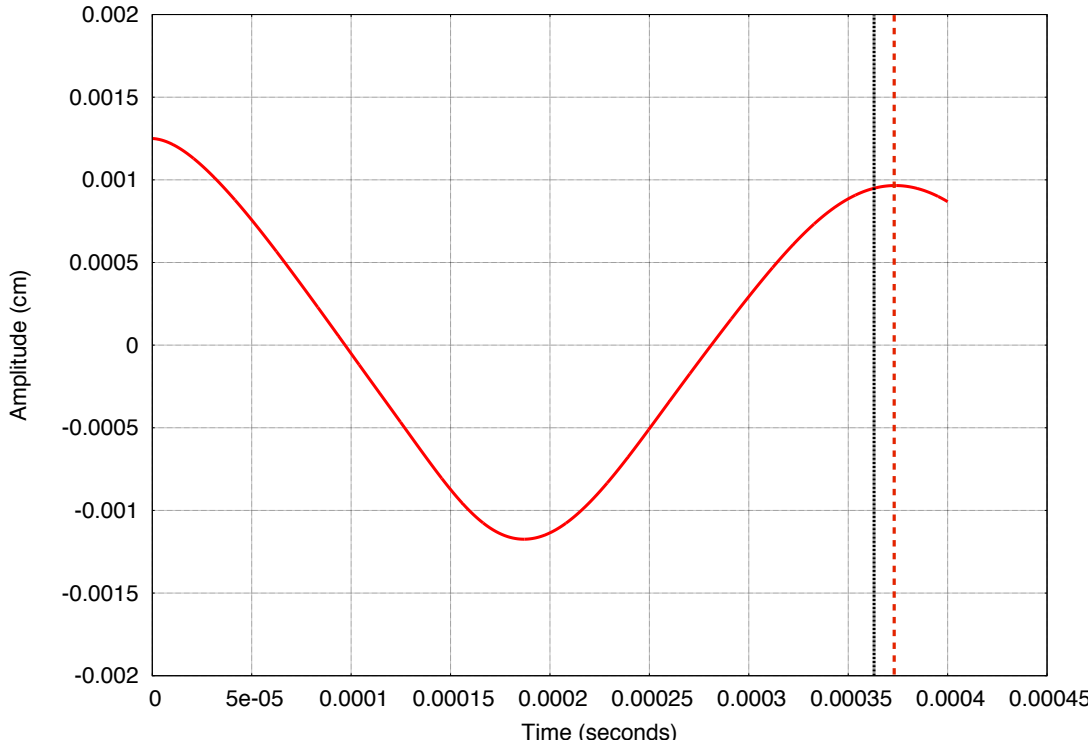

Figure 7.25: Comparison of computational and analytical period for $n = 2$ mode of oscillation

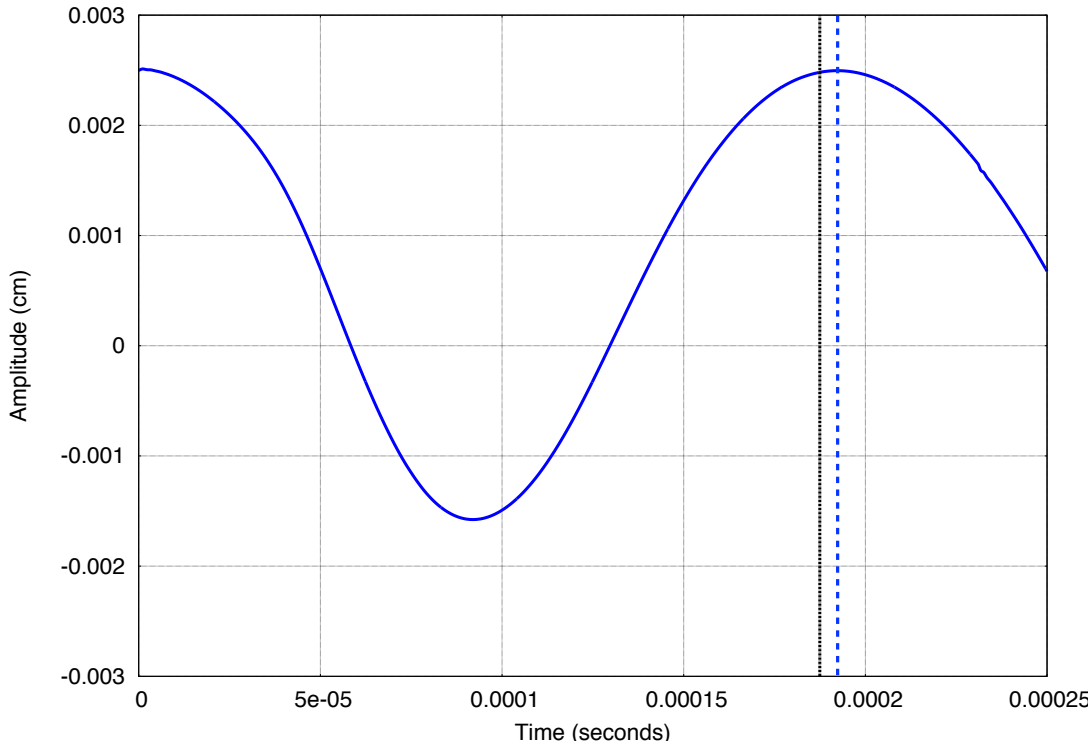

Figure 7.26: Comparison of computational and analytical period for $n = 3$ mode of oscillation

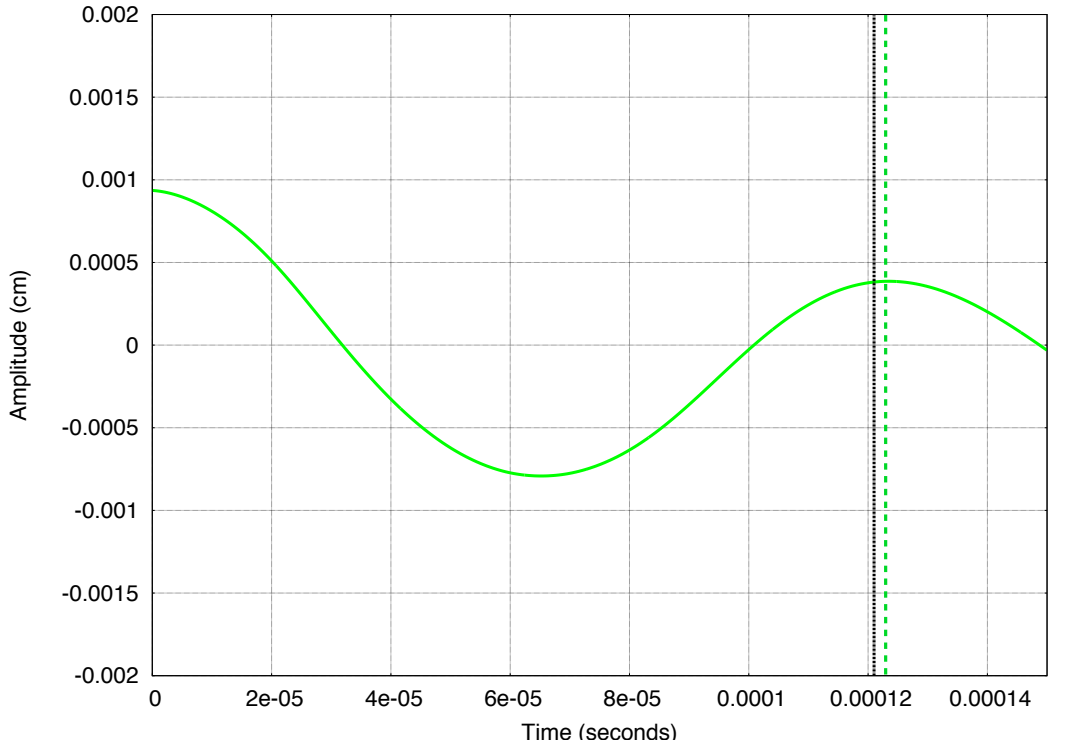

Figure 7.27: Comparison of computational and analytical period for $n = 4$ mode of oscillation

Parameter	Value
Fluid viscosity, μ	$1.01 \times 10^{-2}\,\mathrm{dyne \cdot s/cm^2}$
Fluid density, ρ	$0.998\,\mathrm{g/cm^3}$
Surface tension, γ	$73\,\mathrm{dyne/cm}$
Stabilisation parameter, β	1.0
Mesh viscosity, μ_{mesh}	$1 \times 10^{-4}\,\mathrm{dyne \cdot s/cm^2}$
Gravitational acceleration, g	$-981\,\mathrm{cm/s^2}$

Table 7.4: Parameters for dynamic analysis of sessile droplets

7.3 Further Dynamic Analysis

Now that the framework has been shown to correctly predict the period of oscillation, this thesis will return to sessile droplets, before examining more complex problems such as surfactants, hanging droplets and capillary action.

The viscosity of water ($1.002 \times 10^{-2}\,\mathrm{dyne \cdot s/cm^2}$) is applied for all subsequent analyses in this chapter. As seen in the previous examples, the viscosity acts as a natural damper. Table 7.4 lists the parameters used in the following analyses. The change in the fluid viscosity is accompanied by a change in mesh viscosity to ensure that the mesh does not move too slowly nor too quickly, see Chapter 4 Section 4.9. Only the two smaller droplets from the quasi-static case will be examined, i.e. $E = 0.01$ and $E = 0.1$, as these are closer in size to the problems investigated in the following chapter.

7.3.1 Dynamic Droplet with Dimensionless Volume 0.01

The droplet initially has the same cylindrical shape as seen in the previous quasi-static example for the same volume. The same mesh is used consisting of 504 nodes and 926 triangular elements (2520 degrees of freedom) and the desired contact angle is 90°. Over the first 0.01 seconds, the droplet undergoes violent oscillations. The droplet then achieves an equilibrium semi-circular shape at approximately 0.129 seconds. Figure 7.28 demonstrates the change in height of the droplet during the first 0.01 seconds and the violent oscillations over the first few hundredths of a second can be clearly seen. During this time the height of the droplet changes from 0.0588 cm at the start of the analysis to a maximum of 0.0982 cm and a minimum of 0.0574 cm. After 17.5 ms, the oscillation becomes periodic (the period is approximately 4.4 ms) and ever decaying with time, with the droplet eventually achieving its equilibrium geometry. Figure 7.29 depicts the geometric evolution of the cross-section of

the droplet in time. The pressure field is also shown, the magnitude of which is not relevant at this time. The equilibrium geometry is shown in Figure 7.30 and compared to that using a quasi-static analysis and the analytical solution; there is a very good correlation between the geometries. Over the course of the simulation, there is a 0.67% loss of volume from the droplet.

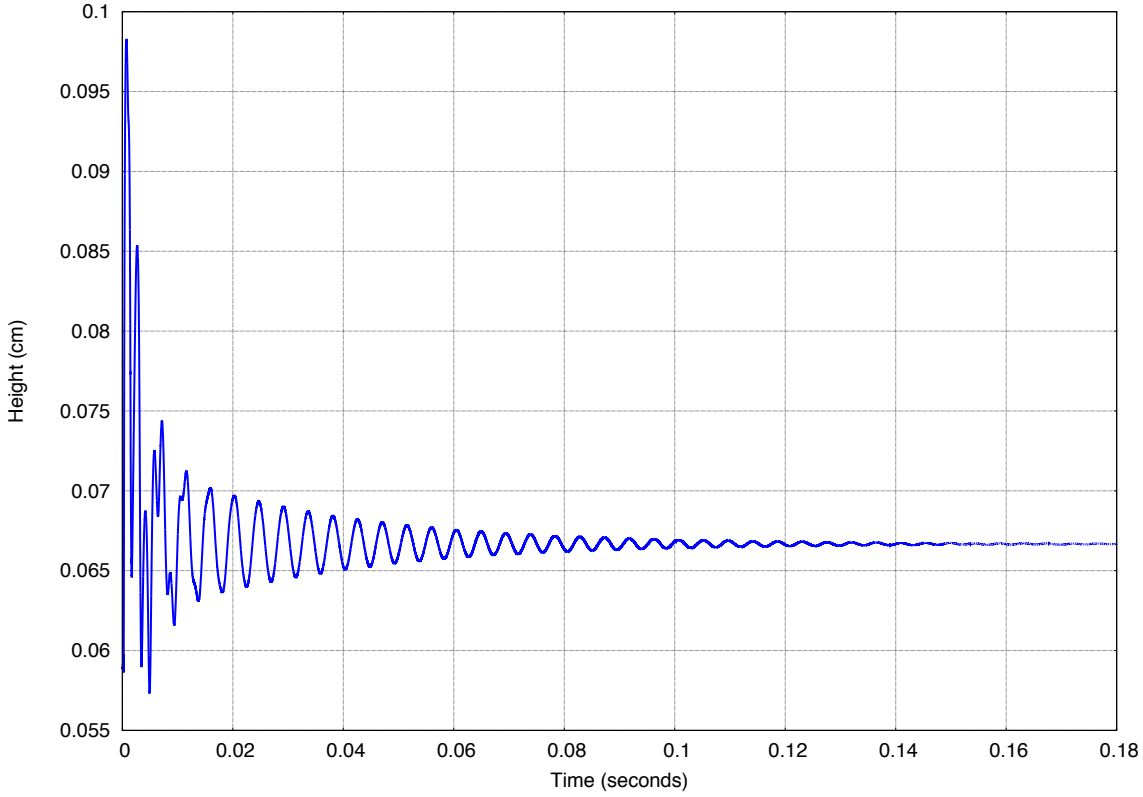

Figure 7.28: Dynamic droplet height in time for $E = 0.01$

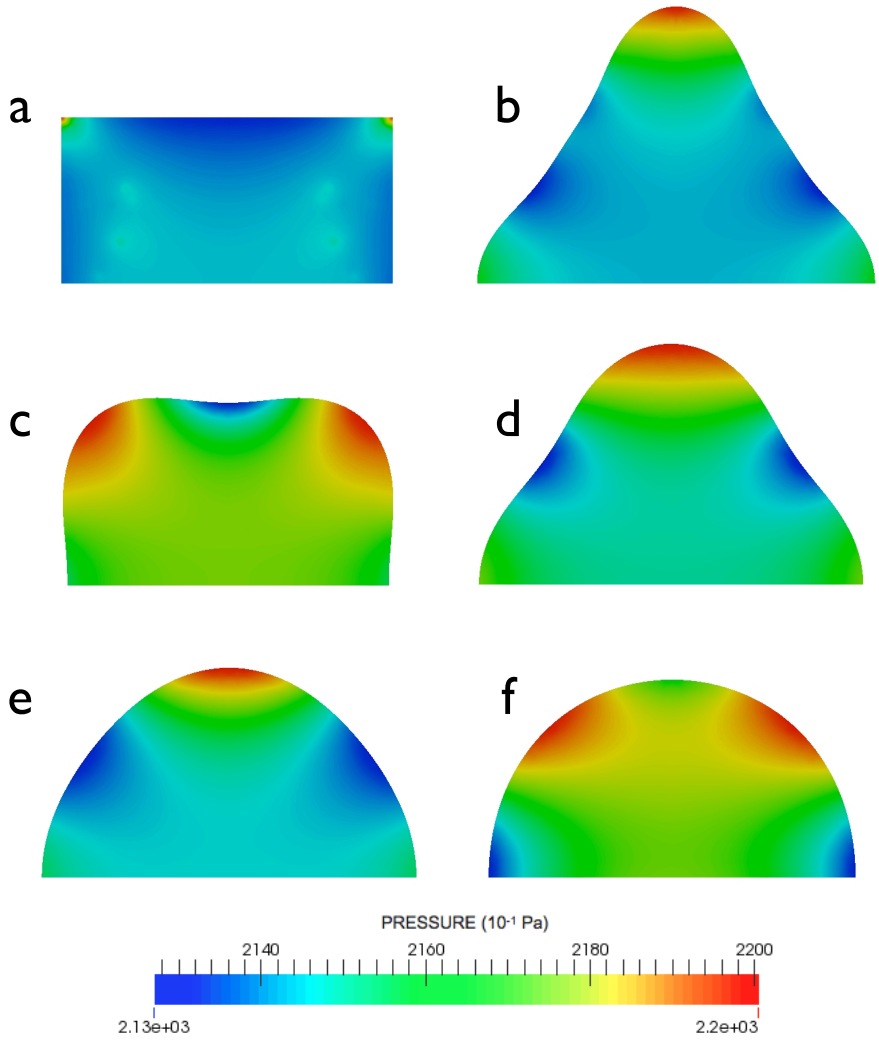

Figure 7.29: Dynamic droplet geometry evolution in first 0.01 seconds for 90° contact angle, $E = 0.01$ with pressure contours: (a) t = 0 ms, (b) t = 0.73 ms, (c) t = 1.7 ms, (d) t = 2.7 ms, (e) t = 7.2 ms, (f) t = 11.3 ms

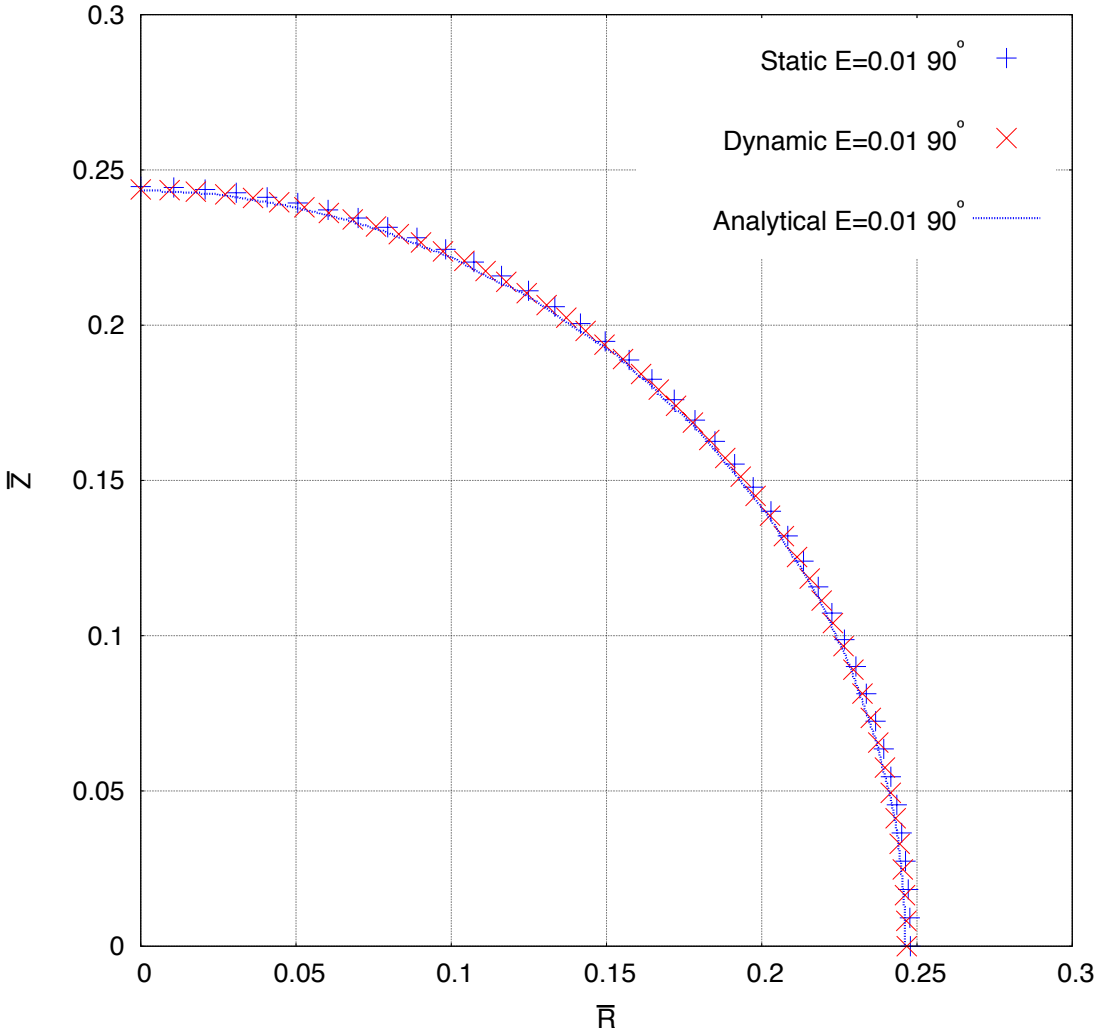

Figure 7.30: Comparison of computational and analytical equilibrium geometry for $E = 0.01$, 90° contact angle for quasi-static and dynamic methods

It is also useful to examine the kinetic and potential energy of the system. The kinetic energy, E_k, is calculated from the velocity of the fluid and the density of the fluid, whilst the potential energy, E_p, is calculated from the surface area, A_s, subject to surface tension. Both are measured in *ergs*, equivalent to 10^{-7} joules.

$$E_k = \frac{1}{2}\rho \mathbf{v}^2 \tag{7.6}$$

$$E_p = \frac{1}{2}A_s\gamma \tag{7.7}$$

Figure 7.31a shows the change in kinetic energy over time, whilst Figure 7.31b shows the change in potential energy over time; both also show the change in droplet height over time. As expected, as the droplet height oscillates, as does the potential energy in the system. The

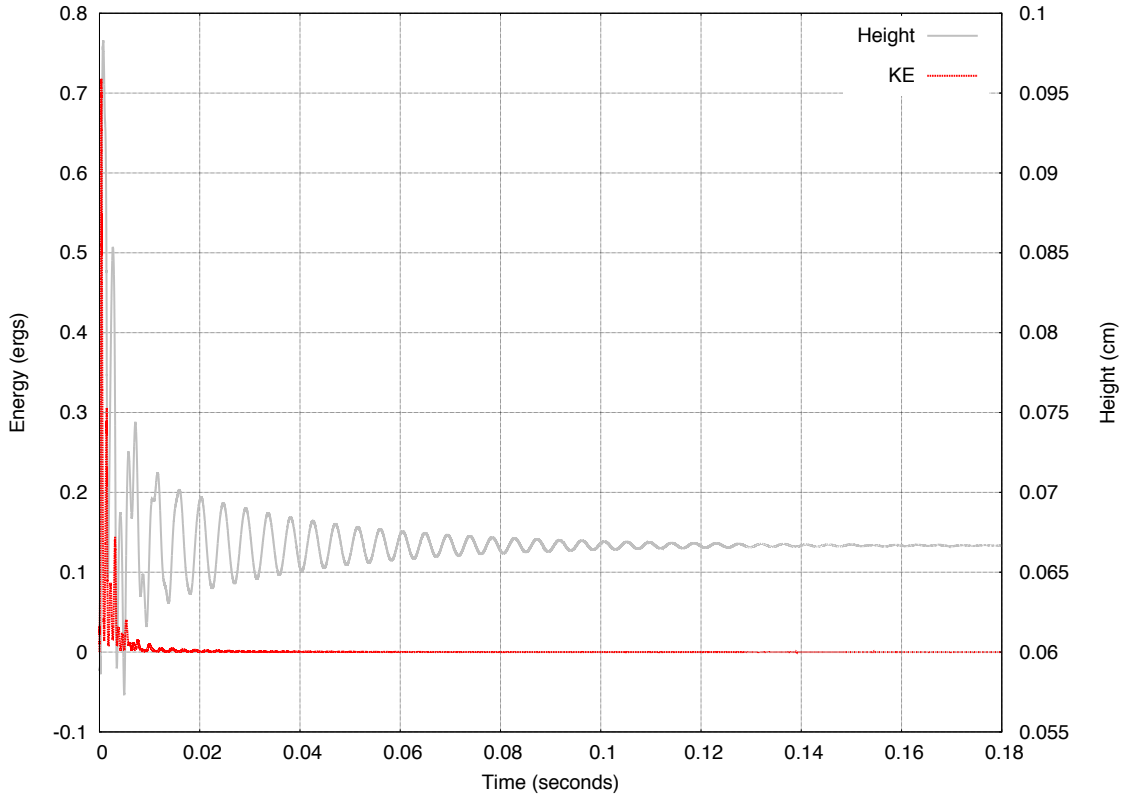

(a) Kinetic energy and height for $E = 0.01$

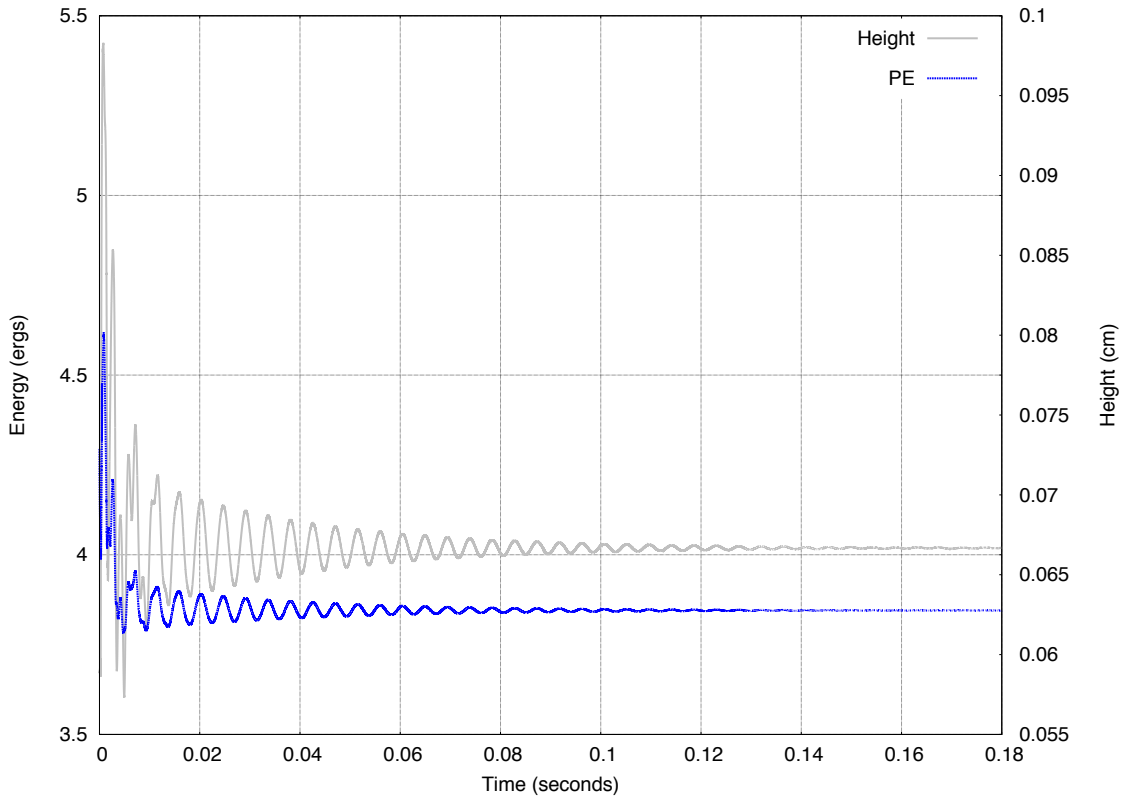

(b) Potential energy and height for $E = 0.01$

Figure 7.31: Change in droplet energy in time for $E = 0.01$

kinetic energy increases drastically during the initial oscillations of the droplet and then, as the oscillations reduce in magnitude, so does the kinetic energy with only very minor changes recorded.

In terms of the form of convergence, Figure 7.32 shows four consecutive representative steps for the analysis with a 90° contact angle. It can be seen that the convergence is quadratic, with the residual after each Newton iteration shown. Additional data noted at each step includes the current time, the height of the droplet, the radius of the droplet, the current contact angle, the current volume and percentage volume loss, gravitational acceleration and the new adaptive time step.

7.3.2 Dynamic Droplet with Dimensionless Volume 0.1

Beginning once again from the initial cylindrical shape and using the same mesh as previously for $E = 0.1$ with 1401 nodes and 2664 triangular elements (7005 degrees of freedom), the desired contact angle is set at 90°. Much the same response is seen as the previous smaller droplet but over a longer time scale. Initially, violent oscillations occur during the first 0.03 seconds and the height of the droplet changes from initially 0.127 cm to a maximum of 0.225 cm and a minimum of 0.113 cm. The oscillations then become periodic (the period is approximately 13.1 ms) and decay with each period. After this time, the droplet has conformed to a semi-circular shape and oscillates slightly to achieve its equilibrium shape at approximately 0.5 seconds. Figure 7.33 depicts the change in droplet height in time over the first 0.03 seconds. As there is ten-times more volume than the previous droplet, oscillations to equilibrium last for a much longer time. Figure 7.34 depicts the evolution of the droplet over 0.5 seconds; note the similarities to the previous droplet, not just in terms of geometry but also in terms of pressure distribution. It is very interesting that, in these two cases, the droplet will exhibit the same behaviour regardless of volume. Of course, the behaviour will change as the droplet volume increases and the effect of gravity increases. Figure 7.35 demonstrates a very good correlation between the calculated equilibrium geometry and that from the analytical solution by Pozrikidis [52]. There is a 0.27% increase in volume during the course of the simulation as a result of the use of a coarse mesh. It should be noted here that during the analysis of both droplets, capillary waves were observed travelling across the surface of the droplets.

```
SURFACE EDGES FOUND = 40        BOUNDARY EDGES FOUND = 80
step = 37, time = 0.000000536732008661
  0 SNES Function norm 8.960528559665e-03
  1 SNES Function norm 9.347989547979e-09
  2 SNES Function norm 1.185280555938e-09
  3 SNES Function norm 4.569074204420e-13
Nonlinear solve converged due to CONVERGED_FNORM_ABS
Number of Newton iterations = 3
AAA     step= 37   time= 0.000000536732008661  H= 0.0588299138  R= 0.0588321899  phi= 90.000702
V= 0.0006396389 == -0.0000000%   gy= -9.81000e+02 New dt = +8.96882e-08
-----------------------------------------------------------------------------------------------

SURFACE EDGES FOUND = 40        BOUNDARY EDGES FOUND = 80
step = 38, time = 0.000000626420251011
  0 SNES Function norm 8.960327827458e-03
  1 SNES Function norm 9.797064032428e-09
  2 SNES Function norm 1.157202908346e-09
  3 SNES Function norm 7.548940442462e-13
Nonlinear solve converged due to CONVERGED_FNORM_ABS
Number of Newton iterations = 3
AAA     step= 38   time= 0.000000626420251011  H= 0.0588300195  R= 0.0588331549  phi= 90.000826
V= 0.0006396389 == -0.0000000%   gy= -9.81000e+02 New dt = +8.96882e-08
-----------------------------------------------------------------------------------------------

SURFACE EDGES FOUND = 40        BOUNDARY EDGES FOUND = 80
step = 39, time = 0.000000716108493362
  0 SNES Function norm 8.961290240692e-03
  1 SNES Function norm 1.029781635668e-08
  2 SNES Function norm 1.130007807521e-09
  3 SNES Function norm 1.062571372256e-12
Nonlinear solve converged due to CONVERGED_FNORM_ABS
Number of Newton iterations = 3
AAA     step= 39   time= 0.000000716108493362  H= 0.0588301294  R= 0.0588342965  phi= 90.000939
V= 0.0006396389 == -0.0000000%   gy= -9.81000e+02 New dt = +8.96882e-08
-----------------------------------------------------------------------------------------------

SURFACE EDGES FOUND = 40        BOUNDARY EDGES FOUND = 80
step = 40, time = 0.000000805796735712
  0 SNES Function norm 8.962923497183e-03
  1 SNES Function norm 1.083778666114e-08
  2 SNES Function norm 1.103514333386e-09
  3 SNES Function norm 1.367808603661e-12
Nonlinear solve converged due to CONVERGED_FNORM_ABS
Number of Newton iterations = 3
AAA     step= 40   time= 0.000000805796735712  H= 0.0588302419  R= 0.0588356184  phi= 90.001039
V= 0.0006396389 == -0.0000000%   gy= -9.81000e+02 New dt = +8.96882e-08
```

Figure 7.32: Four representative steps for dynamic analysis of $E = 0.01$ and 90° contact angle

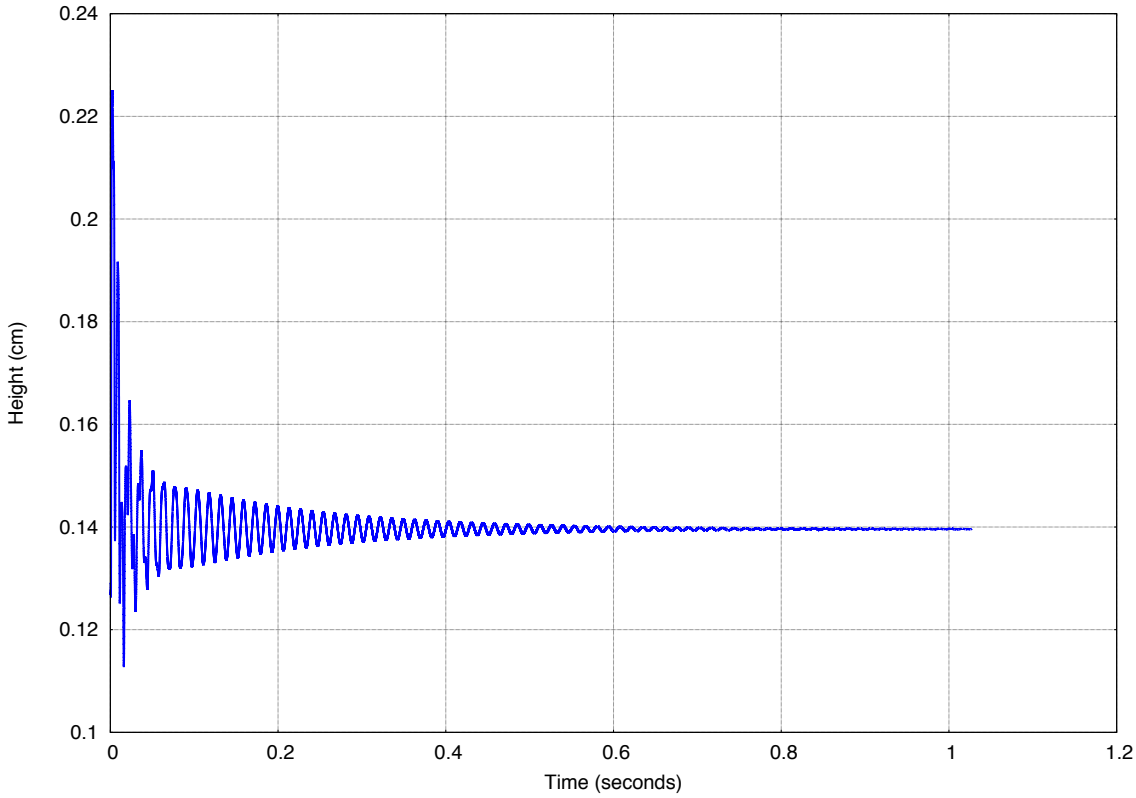

Figure 7.33: Dynamic droplet height in time for $E = 0.1$

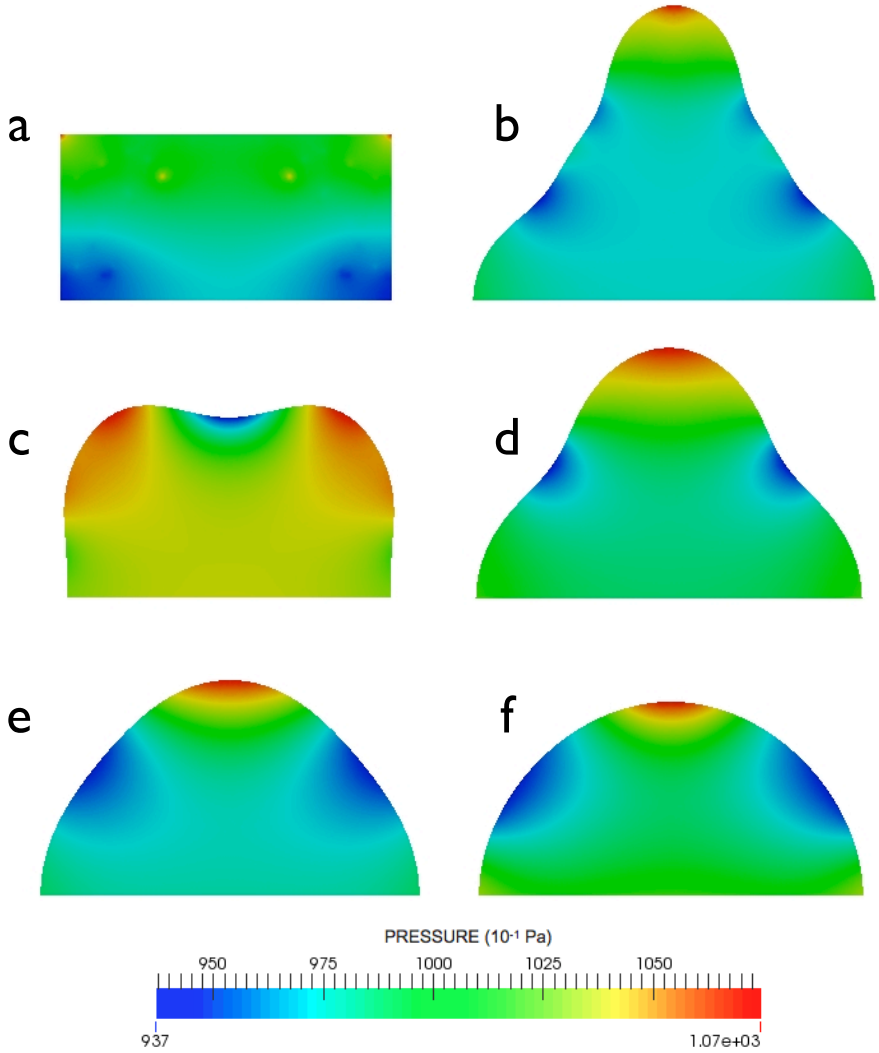

Figure 7.34: Dynamic droplet geometry evolution in first 0.03 seconds for 90° contact angle, $E = 0.1$ with pressure contours: (a) t = 0 ms, (b) t = 2.5 ms, (c) t = 5.55 ms, (d) t = 9.0 ms, (e) t = 23.0 ms, (f) t = 33.5 ms

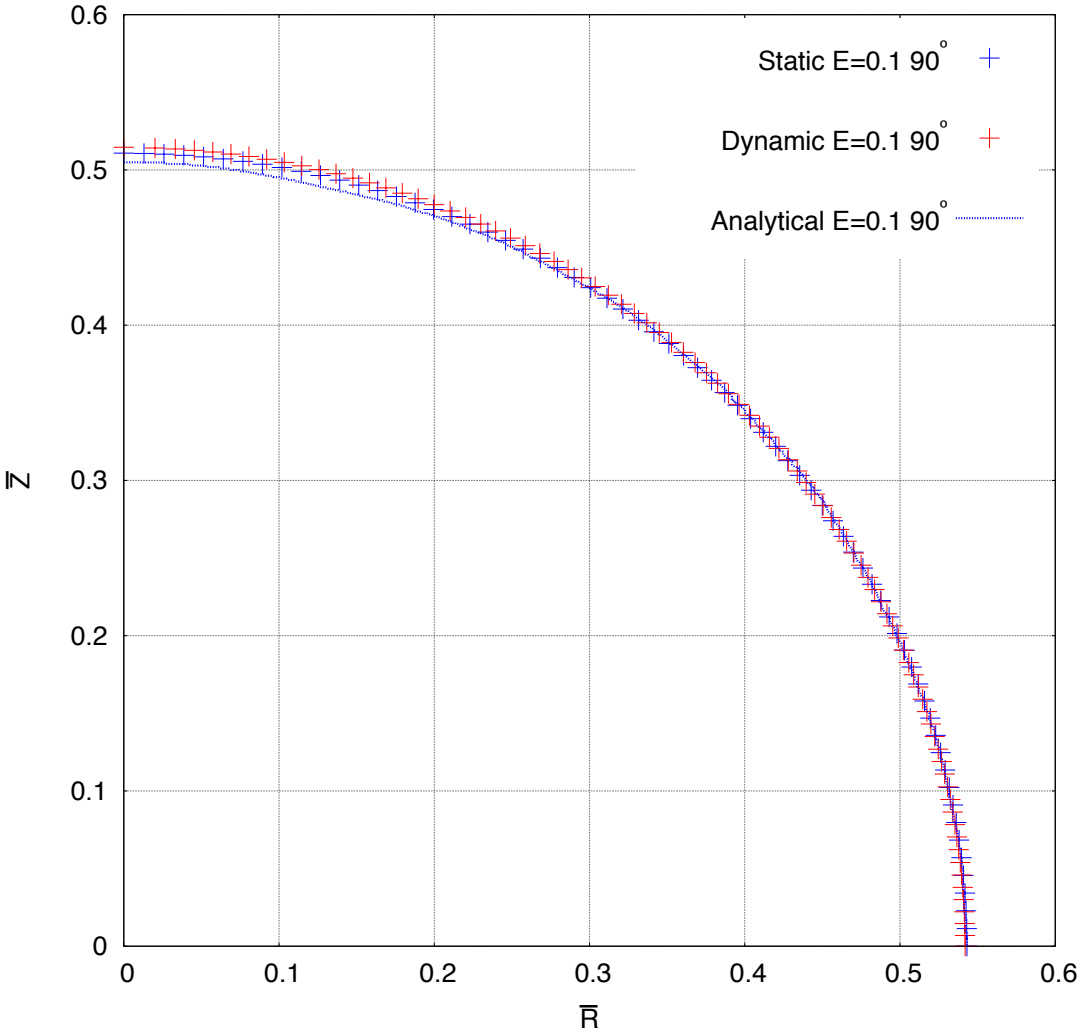

Figure 7.35: Comparison of computational and analytical equilibrium geometry for $E = 0.1$, 90° contact angle for quasi-static and dynamic methods

7.3.3 Dynamic Hanging Droplets and Surfactants

As noted in Chapter 5, surfactants reduce the surface tension of water by at least one third. This change in the surface tension will be most noticeable and most dramatic when the droplet is hanging from a surface. The following analyses compare a hanging water droplet before and after such a lowering of surface tension. The water droplet to be assessed is quite large, with a volume of 17.13 μL (dimensionless volume $E = 0.267$); approximately 58,377 droplets this size are in 1 litre of water. A finite element mesh is created with the same initial cylindrical shape as previously, consisting of 553 nodes and 1020 triangular elements (2765 degrees of freedom), with the boundary conditions as shown in Figure 7.18. One analysis will use the standard value of surface tension for water at 20°C, $\gamma = 73$ dyne/cm, and the

other will use a value one-fifth of this, $\gamma_{surfactant} = 14.6\,\text{dyne/cm}$ to simulate interaction with a surfactant, for example cleaning product residue on a water tap. The equilibrium contact angle will be set at 60°.

Figure 7.36a depicts the evolution of a droplet of water dripping from a tap produced by the Itai Cohen Group at Cornell University using a high speed camera capturing 10,000 frames per second. One can see the elongation of the liquid specimen with surface tension pinching occurring between the developing two main liquid entities. Separation occurs and this first large droplet begins to fall due to gravity, whilst the narrow pinched jet of water bounces back upwards and then also separates, oscillating violently causing the separation of a third, much smaller, droplet. All three droplets conform to near perfect spheres when falling due to gravity, not the classical tear-drop shape one might assume.

Figure 7.36 shows the geometric evolution for the two modelled hanging droplets, one with the standard value of surface tension (Figure 7.36b), and the other with one-fifth of the standard value (Figure 7.36c). The evolution of geometry is initially similar, however, it quickly becomes apparent that the surfactant droplet does not have the surface tension capacity to counter the gravitational pull on its fluid mass, and as such, this droplet elongates rapidly. The droplet with the standard surface tension value droops somewhat before beginning to oscillate towards the now familiar semi-circular shape. The surfactant droplet stretches more and more with surface tension pinching occurring immediately before cast-off. It should be noted here that cast-off occurs as a consequence of the distortion of the mesh; there is no physical law within the computational framework that govern this. Therefore, it is unknown if the pinching recorded is representative of that which would be recorded in a laboratory. Pinching occurs very rapidly in reality and the time step could be too large to capture this effectively. Furthermore, no smaller satellite droplets are created as is seen in the high-speed video and this too is a consequence of both the mesh density and the time step. The newly formed separated droplet has a volume of approximately $13\,\mu$L; taking into account a 1.12% volume loss; this accounts for 77% of the total volume. In terms of geometric shape, the separated droplet has an almost circular geometry and the fluid left behind on the surface now oscillates towards a semi-circular shape. This smaller semi-circular shape, consisting of a lower volume of liquid, can be maintained, i.e. the surface tension force is balanced by the gravitational potential. The two analyses demonstrate a dramatic difference in response as a result of different surface tensions, and demonstrates how important surface tension is in these simulations. The droplet with the standard value of surface tension suffers from a 0.3%

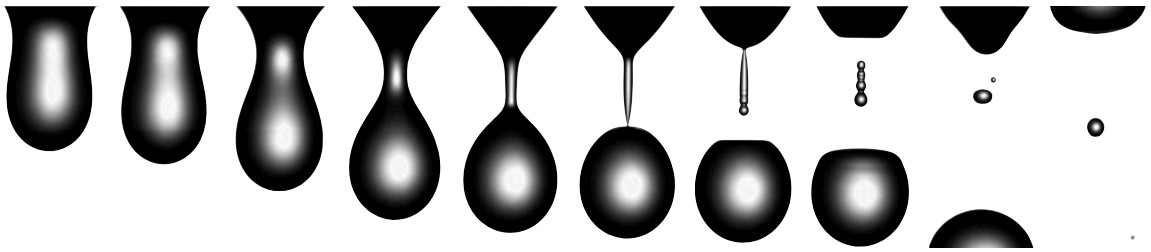

(a) Evolution of water dripping from a tap [9]

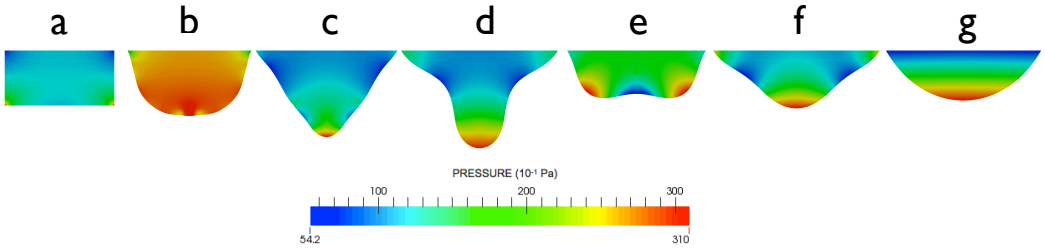

(b) Standard value of surface tension with pressure contours: (a) 0 ms, (b) 1.5 ms, (c) 2.5 ms, (d) 4.4 ms, (e) 10.8 ms, (f) 14.4 ms, (g) 353.8 ms

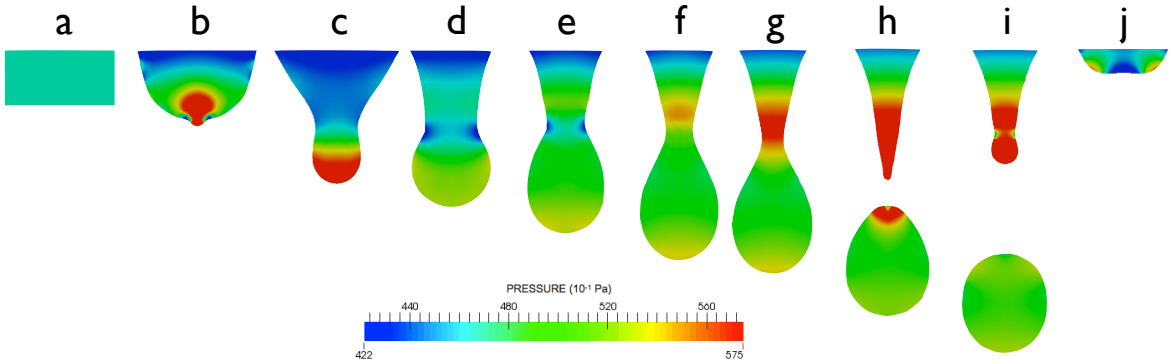

(c) Lower value of surface tension with pressure contours: (a) 0 ms, (b) 3.9 ms, (c) 16.6 ms, (d) 34.4 ms, (e) 39.8 ms, (f) 44.9 ms, (g) 47.8 ms, (h) 54.4 ms, (i) 59.2 ms, (j) 89.8 ms

Figure 7.36: Evolution of hanging droplets

volume loss, whilst the surfactant droplet suffers from considerably higher volume loss. The latter experiences oscillations and as a result suffers a higher degree of non-physical element deletion, especially when cast-off occurs. This can be attributed to the remeshing algorithm. This is discussed in more detail in Chapter 4. Overall, the observed response when lowering the surface tension resembles the droplet in the high-speed video, however, the remeshing algorithm needs to be updated to prevent mesh-dependent results.

In terms of the form of convergence, Figure 7.37 shows four consecutive representative steps for the analysis with the lower value of surface tension. It can be seen that the convergence is

```
SURFACE EDGES FOUND = 42        BOUNDARY EDGES FOUND = 84
step = 34, time = 0.000003609614020542
  0 SNES Function norm 2.411922493279e-02
  1 SNES Function norm 1.266796528133e-07
  2 SNES Function norm 1.152383269202e-09
  3 SNES Function norm 3.620849483042e-12
Nonlinear solve converged due to CONVERGED_FNORM_ABS
Number of Newton iterations = 3
AAA     step= 34   time= 0.000003609614020542  H= 0.1760003815  R= 0.1760101369  phi= 89.920045
V= 0.0171272594 == -0.0000002%   gy= -9.81000e+02 New dt = +5.11423e-07
-----------------------------------------------------------------------------------------------

SURFACE EDGES FOUND = 42        BOUNDARY EDGES FOUND = 84
step = 35, time = 0.000004121036547596
  0 SNES Function norm 2.382998851681e-02
  1 SNES Function norm 1.232149575948e-07
  2 SNES Function norm 1.130861395382e-09
  3 SNES Function norm 3.441986975978e-12
Nonlinear solve converged due to CONVERGED_FNORM_ABS
Number of Newton iterations = 3
AAA     step= 35   time= 0.000004121036547596  H= 0.1760004601  R= 0.1760128301  phi= 89.898507
V= 0.0171272594 == -0.0000002%   gy= -9.81000e+02 New dt = +5.11423e-07
-----------------------------------------------------------------------------------------------

SURFACE EDGES FOUND = 42        BOUNDARY EDGES FOUND = 84
step = 36, time = 0.000004632459074650
  0 SNES Function norm 2.354398196549e-02
  1 SNES Function norm 1.198898203824e-07
  2 SNES Function norm 1.110341167485e-09
  3 SNES Function norm 3.266891268824e-12
Nonlinear solve converged due to CONVERGED_FNORM_ABS
Number of Newton iterations = 3
AAA     step= 36   time= 0.000004632459074650  H= 0.1760005415  R= 0.1760158578  phi= 89.874202
V= 0.0171272594 == -0.0000002%   gy= -9.81000e+02 New dt = +5.11423e-07
-----------------------------------------------------------------------------------------------

SURFACE EDGES FOUND = 42        BOUNDARY EDGES FOUND = 84
step = 37, time = 0.000005143881601704
  0 SNES Function norm 2.326118407740e-02
  1 SNES Function norm 1.166925249732e-07
  2 SNES Function norm 1.090717439201e-09
  3 SNES Function norm 3.095976000192e-12
Nonlinear solve converged due to CONVERGED_FNORM_ABS
Number of Newton iterations = 3
AAA     step= 37   time= 0.000005143881601704  H= 0.1760006248  R= 0.1760192163  phi= 89.847146
V= 0.0171272594 == -0.0000003%   gy= -9.81000e+02 New dt = +5.11423e-07
```

Figure 7.37: Four representative steps for surfactant analysis

quadratic, with the residual after each Newton iteration shown. Additional data noted at each step includes the current time, the height of the droplet, the radius of the droplet, the current contact angle, the current volume and percentage volume loss, gravitational acceleration and the new adaptive time step.

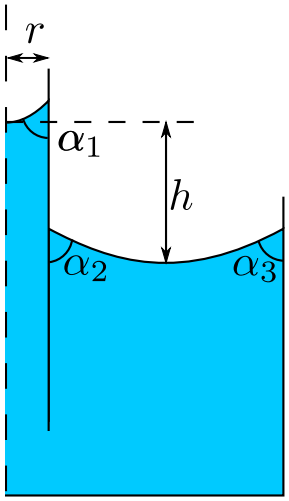

Figure 7.38: Cross-section of capillary problem showing the three contact angles

7.3.4 Dynamic Capillary Tube

The computational framework has been adapted to examine capillary problems [18]. The problem presented here consists of a capillary tube partly submerged in a beaker of water and will examine both the predicted height difference between the tube meniscus and the reservoir meniscus and compare them to the empirical formula given in Chapter 5, Section 5.1.3. The computational framework required significant modification for this problem, which involves more than one contact angle; three contact angles are present in the modelled cross-section, Figure 7.38.

The problem is shown in Figure 7.38 and special attention can be drawn to the three contact angles as shown. Initially, the height of water in the capillary tube is the same as that in the reservoir and the aim is to find the height to which the water in the tube will rise above that in the reservoir, which can be compared to the empirical formula [16]:

$$h = \frac{2\gamma\cos\alpha_1}{\rho g r} \tag{7.8}$$

The values of surface tension, fluid density and gravitational acceleration are $\gamma = 73\,\text{dyne/cm}$, $\rho = 0.998\,\text{g/cm}^3$ and $g = -981\,\text{cm/s}^2$ respectively. It can be clearly seen from Equation 7.8 that the narrower the capillary tube, the higher the level of fluid in the tube will be. The beaker diameter is 0.5 cm and height is 0.09 cm. A capillary tube of diameter 0.03 cm (diameter of 0.05 cm when including wall thickness of 0.01 cm) is placed into the centre of the reservoir; the open end of the tube is 0.015 cm from the base of the beaker. Only half the domain needs to be modelled due to axisymmetric conditions. The volume of water at

Parameter	Value
Fluid viscosity, μ	1.01×10^{-2} dyne·s/cm^2
Fluid density, ρ	0.998 g/cm^3
Surface tension, γ	73 dyne/cm
Contact angles, $\alpha_1, \alpha_2, \alpha_3$	85°, 89°, 90.25°
Stabilisation parameter, β	1.0
Mesh viscosity, μ_{mesh}	1×10^{-4} dyne·s/cm^2
Gravitational acceleration, g	-981 cm/s^2

Table 7.5: Parameters for capillary tube analyses

the start of the analysis is 1.76 μL. The level of water in the capillary tube is initially the same as that in the reservoir, and using the above equation for a contact angle of 89° means the height of fluid in the tube, with a radius of 0.015 cm should be 0.1735 cm above that in the reservoir. Using a contact angle of just less than 90° ensures that the rise of water in the capillary tube is kept to a minimum and therefore so is the computational time; for example if the contact angle was set to 5°, the anticipated capillary rise would be 9.9 cm. Note that an angle just over 90° could be used to the same end, but with the water level in the capillary tube falling below that in the reservoir.

Using the parameters for water at 20°C, listed in Table 7.5, and setting all the contact angles to 89°, resulted in the fluid in the tube rising to a height of 0.1651 cm above that in the reservoir. As with previous problems, the contact angles are approximately achieved very early into the analysis, with the fluid then evolving into a geometry that maintains these angles. The fluid oscillated towards this equilibrium level, as can be seen from Figure 7.39, with a maximum height of 0.2256 cm very early on in the analysis. Capillary waves are clearly seen on the reservoir surface throughout the simulation and Figure 7.40 depicts the change in water level in both the reservoir and capillary tube during the simulation. The pressure field is also shown; however, the magnitude of the pressures is unimportant at this time.

Two other contact angles were also examined: 85° to examine a further increase in the height of fluid in the tube, and 90.25° which will result in a reduction of height in the tube (angles larger than 90.43° will result in all the fluid exiting the bottom of the capillary tube). For the two contact angles less than 90° the water in the tube rises rapidly and then oscillates towards an equilibrium position, and the reverse is true for the contact angle greater than 90°,

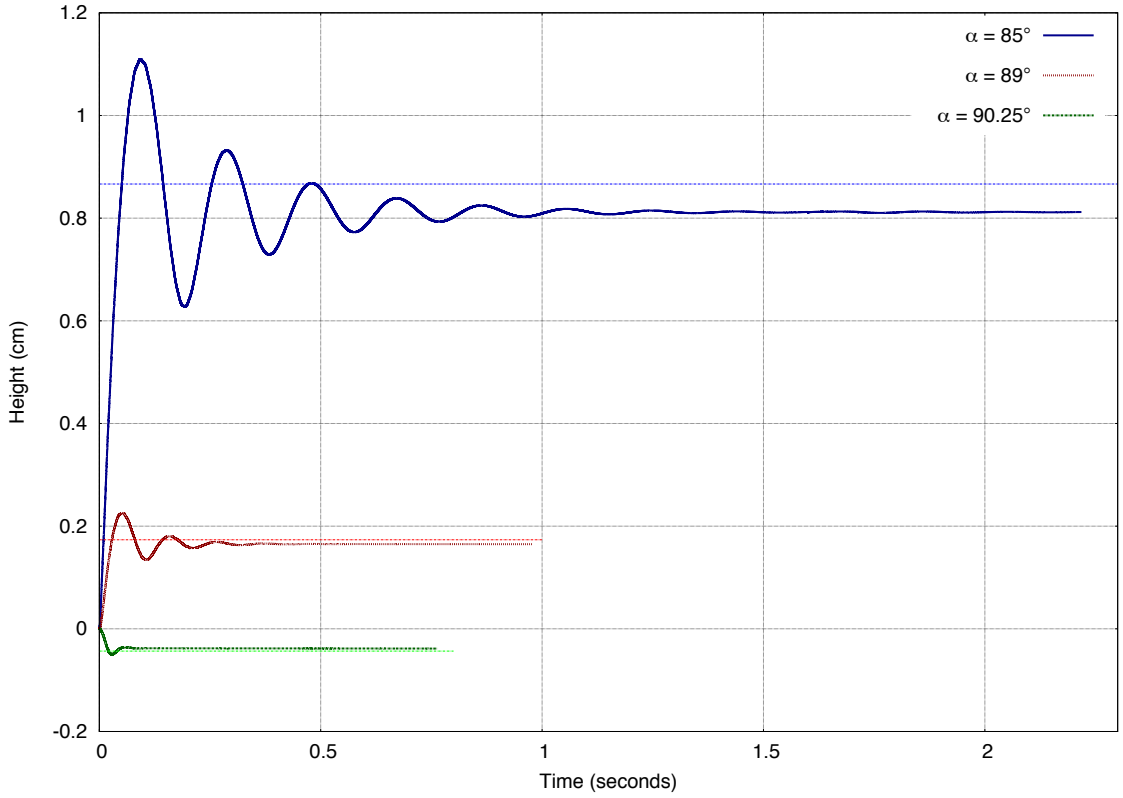

Figure 7.39: Height difference between capillary tube water level and reservoir water level for a range of contact angles; horizontal lines shows the predicted height using Equation 5.3

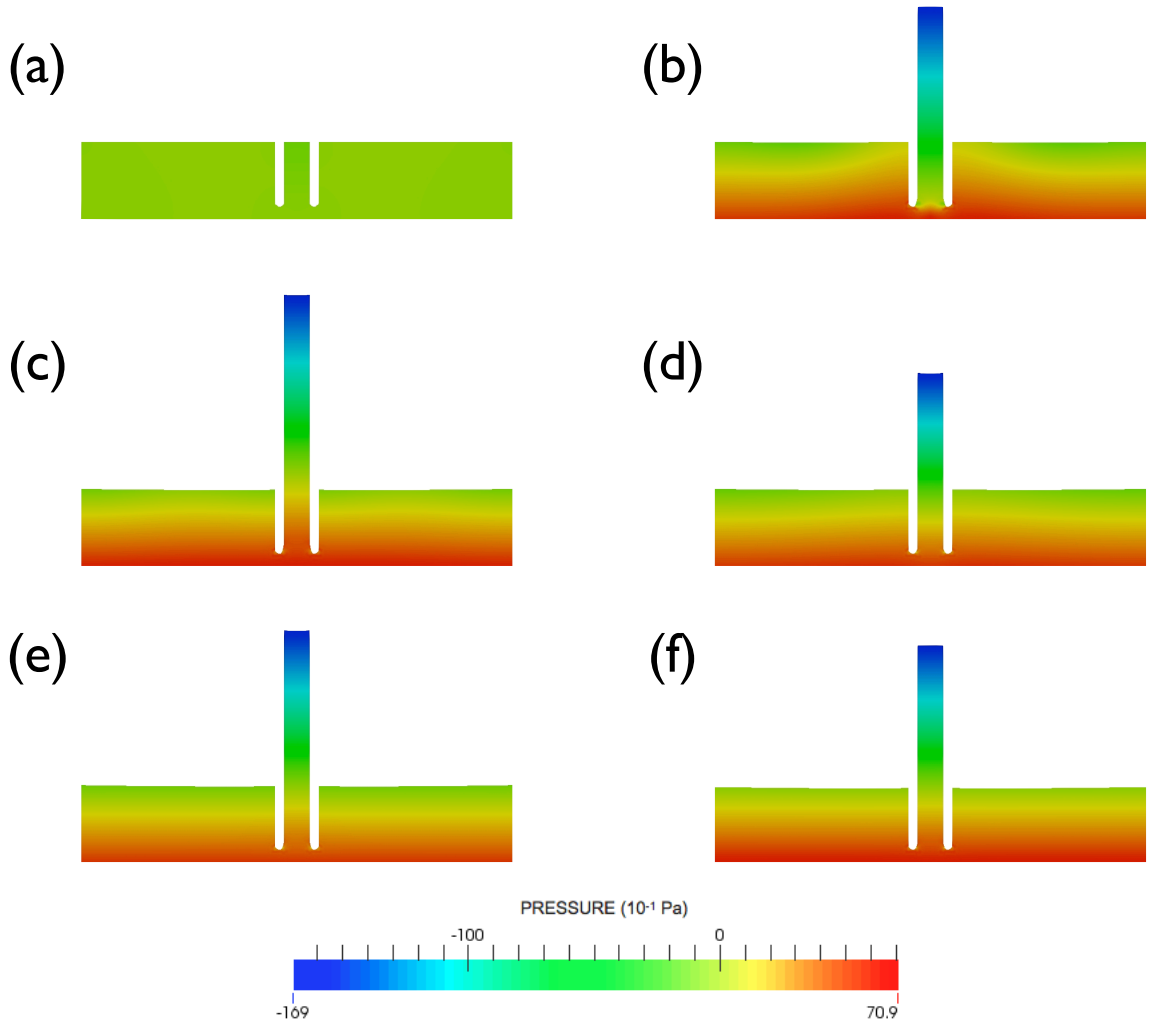

Figure 7.40: Evolution of reservoir and capillary tube water level for a contact angle of 89° with pressure contours: (a) t = 0 ms, (b) t = 25.5 ms, (c) t = 49.6 ms, (d) t = 107.0 ms, (e) t = 159.8 ms, (f) t = 185.8 ms

Contact angle $\alpha_1 = \alpha_2 = \alpha_3$	Analytical height difference	Predicted height difference	Percentage difference
85°	0.8665 cm	0.8120 cm	6.29%
89°	0.1735 cm	0.1651 cm	4.83%
90.25°	-0.0434 cm	-0.0381 cm	12.20%

Table 7.6: Capillary rise analysis - height summary

see Figure 7.39. The calculated height difference using Equation 7.8 and that found using the computational framework are summarised in Table 7.6. The percentage difference between analytical and predicted heights are also given. It can be noted that the computational framework underestimates the height difference for contact angles less than 90° and overestimates the height difference for contact angles greater than 90°. The change in volume during the three analyses performed is 1.93%, 3.37% and 2.28% respectively for contact angles of 85°, 89° and 90.25°. This loss of volume will of course affect the predicted height difference to a degree. Moreover, in problems such as this it would be desirable to refine the mesh locally within the capillary tube. However, this is not possible using Laplacian smoothing, see Chapter 4. Overall, the computational framework is relatively successful in predicting the height of water in the capillary tube for the micro-scale configuration described.

7.4 The Effect of Mesh Density

Previous to this section, the density of the mesh for each problem was selected using a mesh density study. Several mesh of different densities were used for each problem and the best one selected according to the closeness to the analytical solution (where applicable) and taking computational time into consideration. One such study is presented here to highlight the differences the density of mesh makes upon the solution.

Returning to the dynamic analysis of sessile droplets with a dimensionless volume $E = 0.01$ three mesh are assessed and the differences, if any, in results compared. The three mesh are: a coarse mesh consisting of 504 nodes and 926 triangular elements (2520 degrees of freedom), a medium mesh consisting of 1026 nodes and 1934 triangular elements (5130 degrees of freedom), and a fine mesh consisting of 2645 nodes and 5100 triangular elements (13225 degrees of freedom). The coarse mesh is the same as that assessed previously in Sections 7.1.2, 7.1.5 and 7.3.1. This mesh was selected for these previous analyses as the equilibrium shape was highly comparable to the analytical solution and the number of degrees of freedom was low, keeping computational time to a minimum. The parameters used in the analysis of

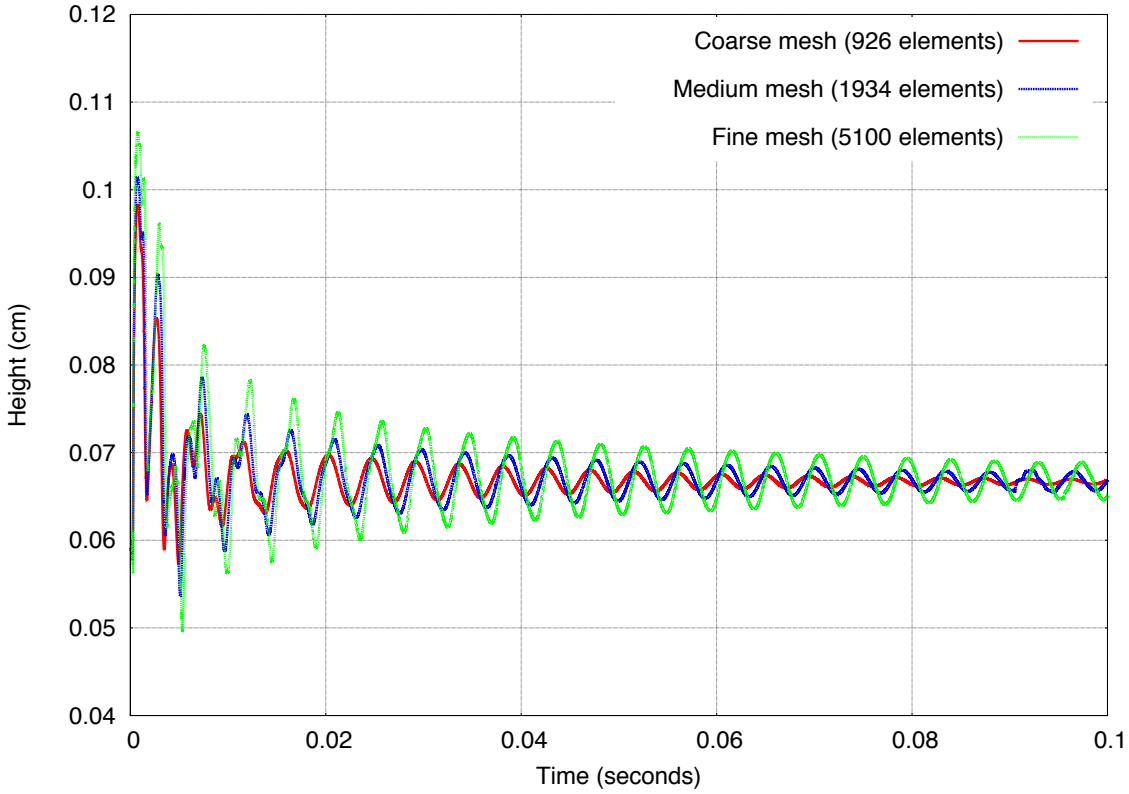

Figure 7.41: Height of the droplet in time for three different mesh densities

the three meshes are the same as those listed in Table 7.3. Figure 7.41 depicts the change in height of the top of the droplet in time for the first 0.1 seconds, as this is the time at which the droplet has approximately reached its equilibrium geometry. It can be seen from the figure that increasing the mesh density causes higher magnitude oscillations to occur. There is a minor shift in period, however, the most noticeable change is in the amplitude of oscillation. Table 7.7 lists the geometric details for each mesh along with the average time step and the percentage volume change. It is immediately apparent that the average time step reduces as the density of the mesh increases and as such the denser the mesh, the longer the time to produce results. Comparing the average time step for the coarse mesh, there is a reduction of 40.2% for the medium mesh, and a reduction of 67.4% for the fine mesh in the respective average time step. However, it is also apparent that for the droplet under inspection the problem of volume loss reduces with increasing mesh density. The volume loss for the fine mesh is approximately 26.9% of that for the coarse mesh.

	Coarse mesh	Medium mesh	Fine mesh
No. nodes	504	1026	2645
No. elements	926	1934	5100
No. dof	2520	5130	13225
Average Δt	1.427×10^{-6} sec	8.532×10^{-7} sec	4.650×10^{-7} sec
Volume change	-0.584%	-0.327%	-0.157%

Table 7.7: Overview of results from mesh density comparison

7.5 Conclusions

This chapter has detailed the results of a number of different analyses. The quasi-static analysis of sessile droplets resting on a flat surface, whereby the fluid viscosity was artificially changed to prevent oscillations demonstrated a good correlation for the contact angles assessed at the three different volumes. A good correlation was also found when the droplet was hanging from a surface and a quasi-static analysis undertaken.

The dynamic analysis of floating droplets, akin to the analytical solutions by Rayleigh, produced a very good correlation between the analytical and computational results. In fact, the analytical period was predicted to within 3% for $n = 2,3,4$ modes of oscillation. The difference can be attributed to Rayleigh neglecting viscous effects and assuming small amplitude oscillations, whereas the computational framework includes viscous effects and assumes large deformations. The results of this analysis also out perform the work of Saksono and Perić [58].

The dynamic analysis of sessile droplets resting on a flat surface showed a very close similarity in response for both examined volumes but with a higher duration for the larger volume. Both droplets conformed to the theoretical semi-circular equilibrium shape with a good correlation to the analytical solution. In terms of dynamic analysis of hanging droplets and surfactants, the importance of surface tension was demonstrated. For the droplet with one-fifth of the surface tension of water, the behaviour was similar to that from a high-speed video, with the droplets that broke off conforming to near-perfect circles. The effect of the density of the mesh in the dynamic analyses showed, as predicted, changes to the amplitude of the oscillations but no change to the frequency of the oscillations. The amplitude of oscillations was found to be higher for a finer mesh, however, this does come at a cost with

analysis using a fine mesh having an average time step one-third of that for a coarse mesh. In all cases examining water droplets, capillary waves were observed on the surface of each droplet.

However, due care and attention must be shown to the problem of volume loss seen in some of the simulations. The quasi-static cases examined have negligible volume loss with all experiencing changes of less than 0.1%. However, in the dynamic cases, the volume loss is exacerbated. For the smaller droplet, 0.67% volume loss occurred and for the larger droplet, 0.27% volume was gained and just over 1% loss is experienced for the surfactant droplet. Interestingly, a denser mesh resulted in a lower volume loss. For the floating droplets, the volume change was negligible, but oscillation of the mesh was minor compared to the other problems examined. Clearly, there is an issue with volume change for problems involving major oscillation of the mesh, especially if a coarse mesh is used. With this in mind, it can be suggested that the current mesh improvement adopted in the framework, Laplacian smoothing, be replaced, as the change of volume could be attributed to non-physical deletion of elements.

Volumetric problems aside, the many analyses undertaken have verified that the computational framework developed not only predicts the correct equilibrium shape of sessile and floating droplets, but also oscillates to this final geometry in the correct manner. Additionally, more complex problems such as capillary tubes and surfactants produced results very close indeed to analytical solutions. Moreover, quadratic convergence was observed for each of the problems assessed. Therefore, confidence can be placed in the framework and the analysis of more complex and testing problems can now be undertaken.

Chapter 8

Surface Acoustic Wave Analysis

Prior to this chapter, all analyses undertaken examine the response of fluid droplets to either the combination of gravitational forces and surface tension forces, or solely surface tension forces. This chapter discusses the most interesting stage of analysis performed by the computational framework on micro-fluid specimens. The analyses examine the acoustic excitation of droplets to model surface acoustic wave (SAW) excitation as performed in the laboratory. Working in collaboration with the Bioelectronics group at the University of Glasgow provides access to data from high-speed cameras of SAW analyses and hence, comparison of this data to the results from the computational framework is possible. A velocity is calculated from laboratory data and applied to the base of the droplet; this provides excitation of the fluid and results in different responses of the fluid domain. The merits of this method and its similarities, if any, to the laboratory data will be outlined.

Additionally a new hypothesis is tested that proposes a different interaction when surface acoustic waves meet the droplet surface than is currently held others. This hypothesis is tested firstly by exciting the membrane upon which the fluid rests and then using a time-dependent contact angle. Both methods induce capillary waves up the droplet surface to cause motion. The merits of each method will be discussed and the validity of the hypothesis will be commented upon.

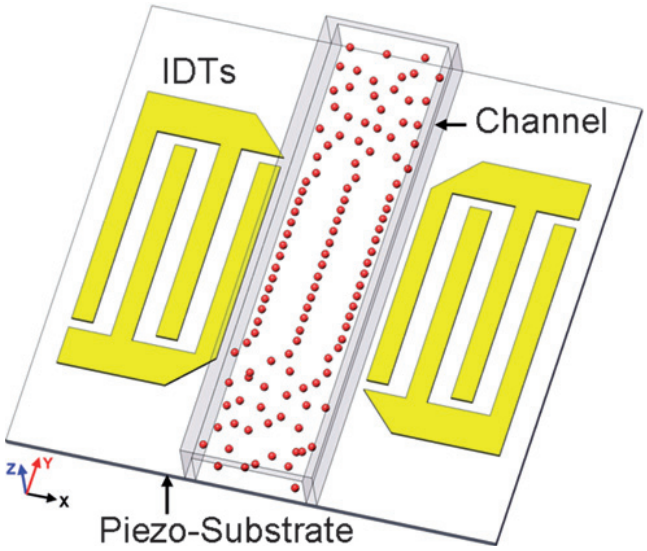

Figure 8.1: Surface acoustic wave patterning from [59]

8.1 Background

The Bioelectronics Group, (Cooper, Wilson and Reboud) [2] conducts research into various areas including advanced diagnostics, lab-on-a-chip diagnostics, synthetic biology and bio-nanophotonics. In the context of this work, lab-on-a-chip diagnostics is the most closely linked area of research. The work in this area aims to offer an alternative method of disease diagnosis in the Developing World where access to sterile laboratories may not be possible, there is poor infrastructure and current diagnostic tools are expensive. In particular, lab-on-a-chip technologies including microfluidics, optical tweezers, dielectrophoresis, optoelectronic tweezers and acoustic tweezing are all tools that can be used to create such a device, refer to [22, 54, 69, 35, 38, 55, 45] and the references therein. Figure 8.1 depicts the use of SAWs to manipulate the position of cells passing through a channel with interdigital transducers (IDTs) on either side. Notice the random distribution of cells either side of the IDTs, and the linear pattern of cells when passing between the IDTs.

Whilst these tools are very much areas of ongoing research, production of prototypes is expensive and time-consuming. As such, development of a computational tool that can predict the response of fluid droplets subject to external excitation, mimicking the aforementioned tools, is extremely useful in contributing to the future design of these devices. In particular, the computational framework will predict the response of excitation via surface acoustic waves. SAWs are used to spin a blood sample, much like a traditional centrifuge, thus separating the different parts of the blood sample to enable disease testing. Current techniques

using a traditional centrifuge can cause damage to cells and struggle with a small number of cells; SAWs do not damage the cells and can cope with both small and large numbers of cells. Working in collaboration with the Bioelectronics Group, the computational framework will first attempt to replicate laboratory testing of water droplets resting on a speaker oscillating with a given frequency. Then, a new hypothesis regarding the interaction of SAWs and the droplet surface will be proposed and tested.

8.2 Water Droplet on a Speaker

High-speed video of a $10\,\mu$L droplet of water with an approximate equilibrium contact angle of 65° resting on a speaker excited at a frequency of 100 Hz for $D = 0.0555$ sec, where D is the duration of excitation, was provided by the Bioelectronics Group. A hydrophobic surface surrounds the droplet preventing it from spreading horizontally, effectively pinning the droplet in place. The displacement, at $\Delta t^* = 0.0005$ sec intervals, of a point on the speaker during excitation without the droplet mass was also provided. This was used to calculate the prescribed velocity to be applied to the nodes in direct contact with the speaker, i.e. at the base of the droplet. This will simulate the vertical motion induced on these nodes by the vibrating surface of the speaker. The current velocity $\mathbf{v}_{n+1}$ can be expressed as:

$$\mathbf{v}_{n+1} = \frac{2}{\Delta t}\left(\mathbf{x}_{n+1} - \mathbf{x}_n\right) - \mathbf{v}_n \tag{8.1}$$

where $\mathbf{x}_{n+1}$ is the current nodal displacement, $\mathbf{x}_n$ is the previous nodal displacement, $\mathbf{v}_n$ is the previous nodal velocity and Δt is the time step. The computational time step is generally less than that used to record the displacement of the point on the speaker, i.e. $\Delta t < \Delta t^*$. Assuming that the acceleration is constant between successive known time instants, the current nodal acceleration and current nodal velocity can be expressed as:

$$\mathbf{a}_{n+1} = \frac{\mathbf{v}_{n+1} - \mathbf{v}_n}{\Delta t^*} \tag{8.2}$$

$$\mathbf{v}_{n+1} = \mathbf{v}_n + \mathbf{a}_{n+1}\Delta t \tag{8.3}$$

The motion of the vibrating surface of the speaker is assumed to be uniform, hence, the nodal velocity is the same for all nodes and is not position-dependent.

Beginning with a cylindrical cross-section and using a quasi-static analysis with an increased viscosity (removing dynamic oscillations, see Chapter 7), the equilibrium geometry is obtained for a contact angle of 65° using a finite element mesh consisting of 1656 nodes and

3162 triangular elements (8280 degrees of freedom). The resulting geometry at this equilibrium position is a good match to the initial geometry from the high-speed video. At equilibrium, the droplet has dimensions of 0.13841 cm height and 0.40454 cm width at the base. Algorithm 8.1 is added to the computational framework and reads the boundary conditions of each node to identify those on the base of the droplet. Once identified and placed into a group, the algorithm calculates the magnitude of the velocity to be applied to these nodes. Then, for each node in turn, the solution vector is set equal to the applied nodal velocity for both vertical fluid velocity and vertical mesh velocity and this results in both the mesh and fluid moving vertically as time passes.

```
Input: all mesh vertices
Output: Mesh vertices on the membrane
Define: ranges all_verts, base_verts;
Identify all vertices and insert into all_verts (MOAB);
for all_verts i do
    Read type tag (MOAB);
    if type is fixed_y then
        Insert vertice into base_verts;
    end
end
Calculate the acceleration during each time instant, see Equation 8.2,
where v_n and v_{n+1} are the velocities at the previous and current time
intervals as recorded;
Calculate the applied velocity, see Equation 8.3, where v_n is the
applied velocity from the previous (Newton) time step;
for base_verts i do
    Set solution vector equal to applied velocity;
    Set applied_velocity tag (MOAB);
end
```

Algorithm 8.1: Identification of vertices on the droplet base and application of the prescribed velocity

For simplicity, the membrane is assumed to be perfectly flat. Starting from the equilibrium geometry obtained using a quasi-static analysis (as described in Chapter 7), the node on the contact line is identified and a horizontal fixity added to its boundary conditions. This has the effect of pinning the droplet therefore replicating the hydrophobic surface surrounding the droplet. Figure 8.2 shows the boundary conditions applied to the mesh and the variables to be used in the analysis are given in Table 8.1. Upon application of the velocity calculated from the provided data, the response from the computational framework is compared to the high-speed video. Figure 8.3a shows the velocity as calculated from the laboratory data and

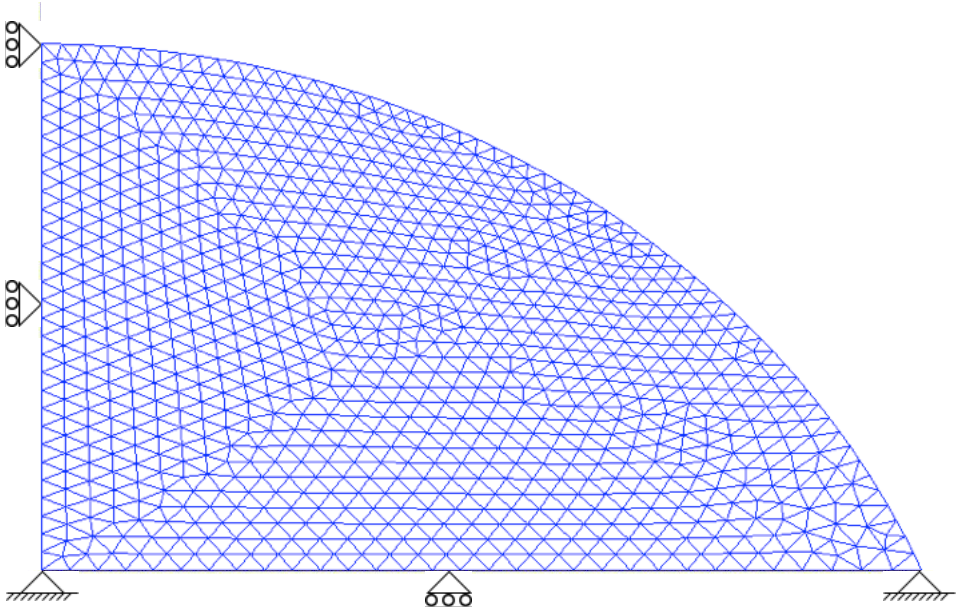

Figure 8.2: Boundary conditions for analysis of a droplet on a speaker

Parameter	Value
Fluid viscosity, μ	$1.01 \times 10^{-2}\,\mathrm{dyne \cdot s/cm^2}$
Fluid density, ρ	$0.998\,\mathrm{g/cm^3}$
Surface tension, γ	$73\,\mathrm{dyne/cm}$
Contact angle, α	65°
Stabilisation parameter, β	1.0
Mesh viscosity, μ_{mesh}	$1 \times 10^{-4}\,\mathrm{dyne \cdot s/cm^2}$
Gravitational acceleration, g	$-981\,\mathrm{cm/s^2}$

Table 8.1: Parameters for droplet on a speaker analysis

applied to the base of the droplet whilst Figure 8.3b shows that the displacement of the base of the droplet over time corresponds to that from the provided laboratory data.

Comparing the geometric evolution of the response from the computational framework and that from the laboratory video, Figure 8.4, it appears that, at least initially, there is some difference in the phase of oscillation. However, after a very short time, the two droplets begin to oscillate in phase and with the same amplitude. The discrepancy at the beginning can be attributed to a difference in momentum, and the fact that the computational framework is unable to capture three-dimensional effects. Additionally, the applied velocity is calculated from the tracking of the membrane when there is no droplet present; whilst the volume of the droplet is very small, it is sufficient to affect the movement of the membrane and as such, the data provided is not a true representation of the membrane motion when a droplet is present. Figure 8.4 shows the predicted response from the framework overlaid with the response from the laboratory, and Figure 8.5 shows the same cross-sections side by side for clarity. Note, due to the low quality of the images captured in the laboratory, some noise is present above and around the droplet, however, the general shape of the droplet is clear. Here it is interesting to note that the occurrence of capillary waves on the surface of the droplet as seen in the laboratory experiment has also been captured in the computational analysis. The capillary waves originate at the contact point and travel up the surface of the droplet towards the axisymmetric boundary.

To investigate the influence of the initial equilibrium contact angle on the solution, two new equilibrium geometries are considered with the same initial number of elements and vertices but with contact angles of 62° and 68°. The velocity is then applied to the base of each droplet in the same manner as before. This change in contact angle makes no major difference in the form of oscillation and only slight differences in the amplitude, with no difference greater than 1%. Increasing the density of the mesh also leads to no major change in the form of oscillation, only the amplitude, as seen in the previous chapter. The change in amplitude was once again less than 1%. Overall, the implementation of a prescribed velocity applied to the node at the base of the droplet produced comparable results to the laboratory data.

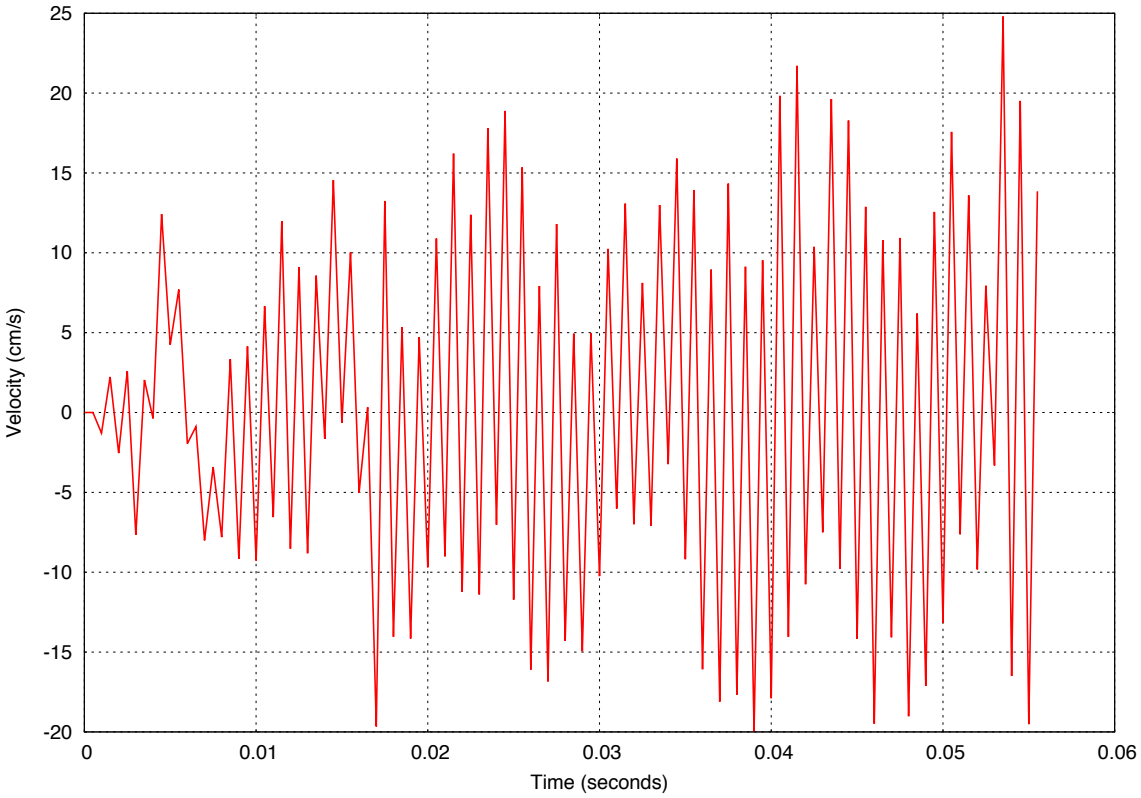

(a) Velocity time history

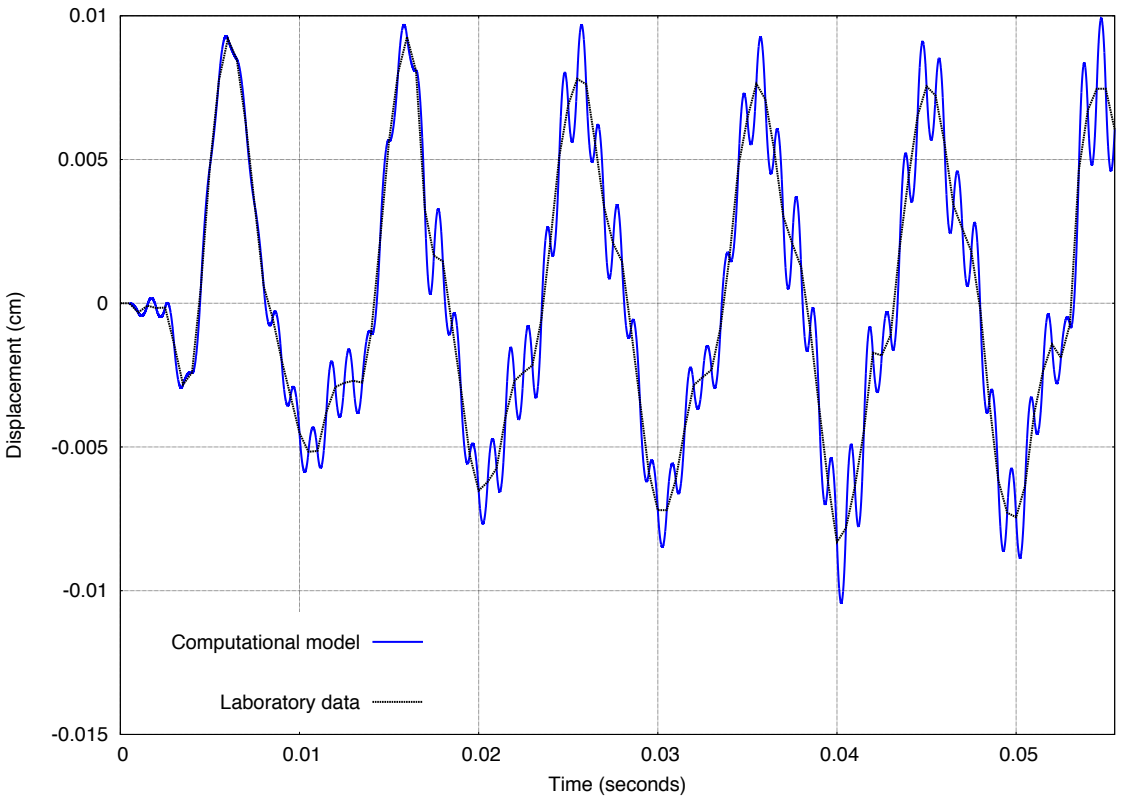

(b) Displacement over time

Figure 8.3: Velocity and displacement

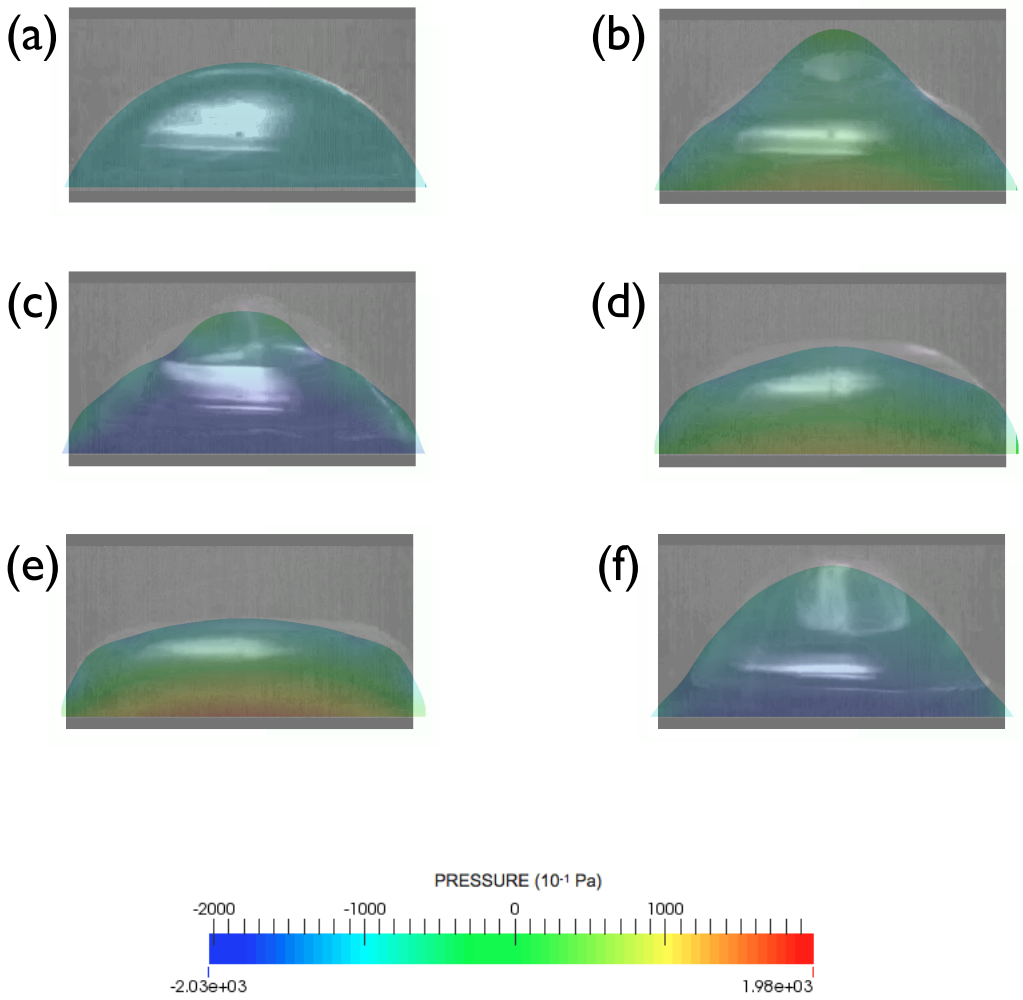

Figure 8.4: Comparison of geometric evolution of a droplet on a speaker with computational results overlaid with data from the laboratory: (a) $t = 0$, (b) $t = D/3$, (c) $t = D/2$, (d) $t = 2D/3$, (e) $t = 4D/5$, (f) $t = 9D/10$

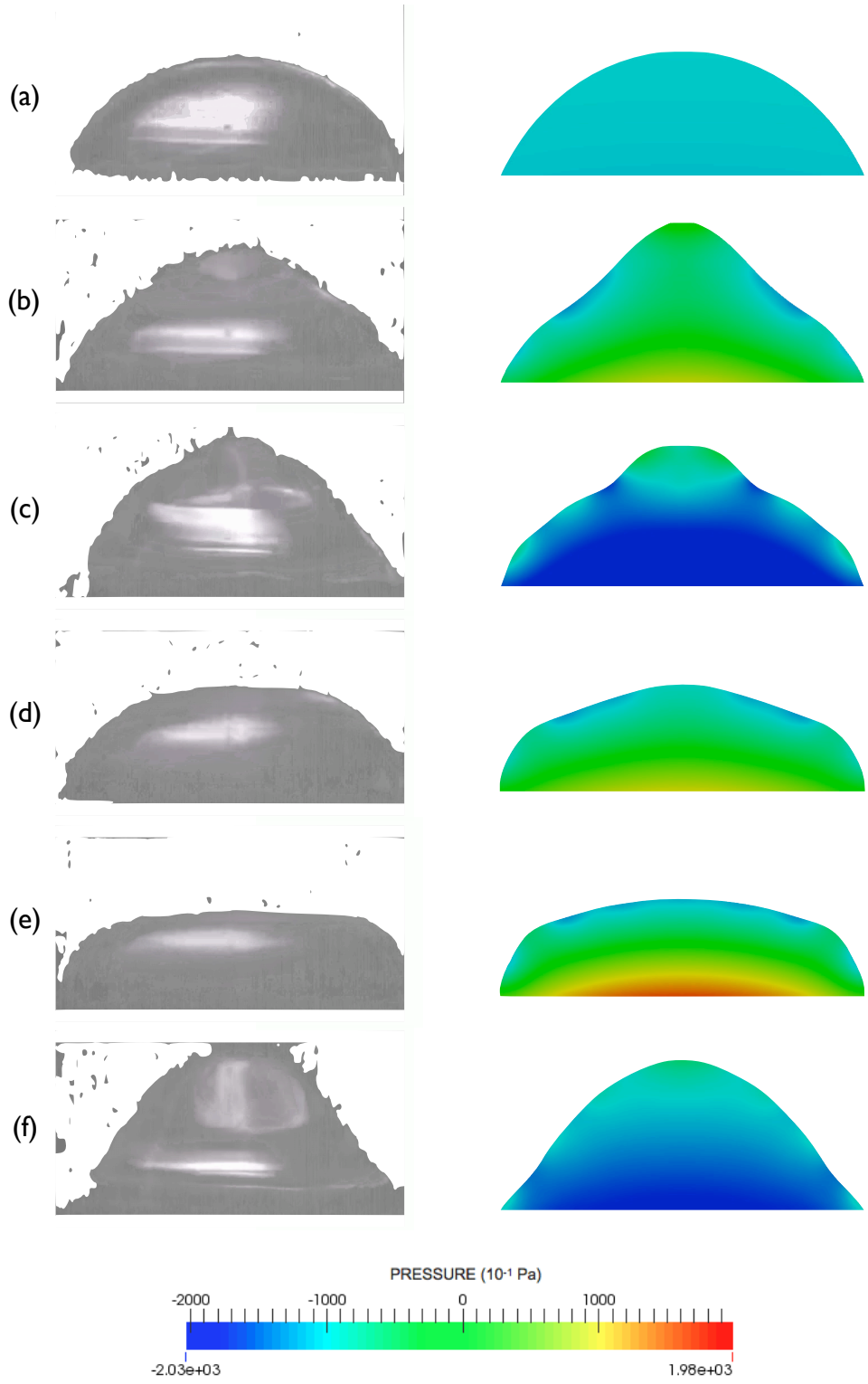

Figure 8.5: Comparison of geometric evolution of a droplet on a speaker with computational results placed side by side with data from the laboratory: (a) $t = 0$, (b) $t = D/3$, (c) $t = D/2$, (d) $t = 2D/3$, (e) $t = 4D/5$, (f) $t = 9D/10$. Note, due to the low quality of the images captured in the laboratory, some noise is present above and around the droplet.

8.3 A New Hypothesis on SAW-Fluid Interaction

There is a general hypothesis within the SAW research community concerning the interaction of SAWs and a droplet and the inducing of jetting and nebulisation. This hypothesis suggests that when the SAW is emitted it travels along the substrate towards the droplet and upon reaching the boundary between the solid and liquid phases, it changes mode. It is assumed that this 'leaky' SAW produces longitudinal waves that propagate into the droplet, pumping energy into the system and causing the droplet to move [12, 60], see Figure 8.6.

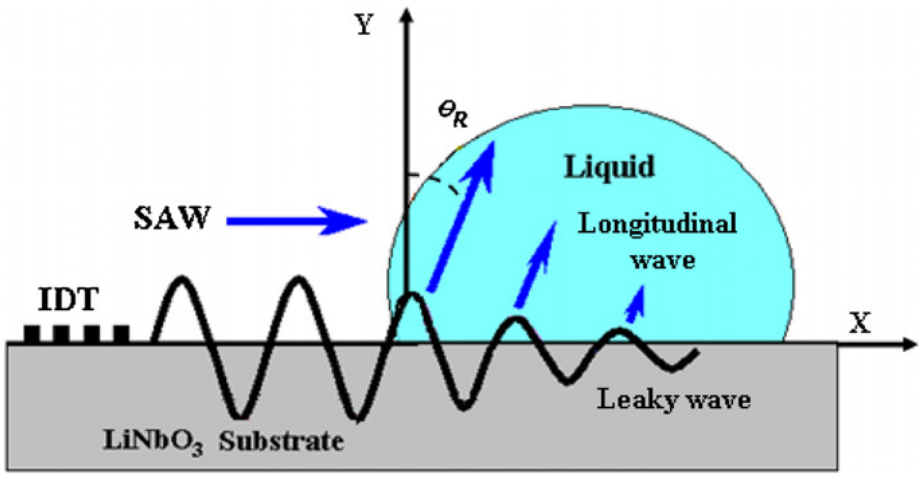

Figure 8.6: Upon reaching the boundary, the SAW produces longitudinal waves that propagate into the droplet at the Rayleigh angle θ_R, from [12]

However, an alternative hypothesis is proposed here. It is proposed that when the SAW reaches the boundary, it propagates capillary waves up the surface of the droplet. As these capillary waves propagate up the droplet surface, they cause a change in the apparent wetting angle and this change in angle causes motion of the droplet. Drastic changes in the wetting angle will cause violet motions in the fluid and it is hoped that the framework will capture jetting and nebulisation. As has been noted in Chapter 7, when determining the equilibrium shape of a droplet starting from an arbitrary geometry, the contact angle approximately conforms to the desired equilibrium contact angle very quickly and the geometry then adapts into a shape that maintains this angle. Additionally, capillary waves were observed in each of the dynamic problems studied. Thus, this hypothesis can be examined by changing the contact angle in time, thereby exciting the droplet, causing oscillations within the droplet.

Two methods of changing the contact angle shall be examined. Firstly, the membrane profile

shall change in time using a penalty method, and secondly, the contact angle itself shall be changed in time.

8.3.1 A Penalty Method to Model a SAW Induced Moving Membrane

When SAWs travel along the membrane, the membrane will move, undulating and changing the apparent wetting angle. In order to model the affect of SAWs upon a membrane, a penalty method is implemented. The penalty method prevents certain nodes from moving away from a defined boundary. The motion of the membrane is approximated as sinusoidal. At the start of the analysis, the nodes along the base of the droplet are identified from their boundary conditions. All boundary conditions are then removed from these nodes apart from the node on the axisymmetric boundary. Each iteration, the distance, d, from each of the identified nodes to the closest point on the membrane profile is calculated, see Figure 8.7. We want to minimise this distance to ensure that the nodes move only along the predefined membrane profile.

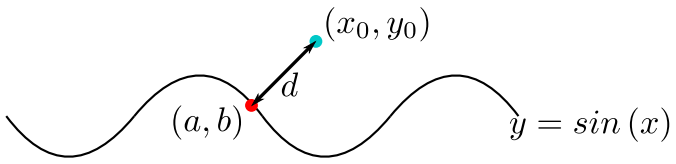

Figure 8.7: Point (a,b) is the closest point on the curve $y = \sin(x)$ to the point (x_0, y_0)

For a node with coordinates (x_0, y_0) the closest point on the membrane defined by the equation $y = \sin(x)$ is the point (a,b), as shown in Figure 8.7. The coordinates of this point are found by minimising the square of the distance between the two points:

- First, assume the current node on the base of the droplet is already on the membrane. Therefore, the node on the base of the droplet and the node on the membrane have the same x coordinate.
- Next, calculate the first derivative in x of the square of the distance and divide it by the second derivative in x of the square of the distance; this gives the residual which is added to the x coordinate.
- The above step is repeated until the residual is smaller than 1×10^{-8} at which point the x coordinate is now that of the point on the membrane and the y coordinate can be calculated from the membrane profile equation.

Once the coordinates of the point on the membrane are known, the distance between these two points, d, is calculated as:

$$d = \left[(x_0 - a)^2 + (y_0 - b)^2\right]^{\frac{1}{2}} \tag{8.4}$$

$$d^2 = \left[(x_0 - a)^2 + (y_0 - b)^2\right] \tag{8.5}$$

Following the derivation in Appendix F, the square of the distance is used to define a penalty stiffness matrix $\mathbf{K_{pen}}$ and a penalty force vector $\mathbf{F_{pen}}$:

$$\mathbf{K_{pen}} = \mathbf{C}^{\mathrm{T}} \kappa \mathbf{C} \underline{\delta \mathbf{v}} \tag{8.6}$$

$$\mathbf{F_{pen}} = \mathbf{C}^{\mathrm{T}} \kappa \mathbf{Q} \tag{8.7}$$

where:

$$\begin{aligned} \mathbf{Q} \;=\; & x_n^2 + \left(\Delta t \left(v_{n+1}^i\right)^x\right)^2 + a^2 + 2x_n \Delta t \left(v_{n+1}^i\right)^x - 2x_n a - 2a\Delta t \left(v_{n+1}^i\right)^x \\ & + y_n^2 + \left(\Delta t \left(v_{n+1}^i\right)^y\right)^2 + b^2 + 2y_n \Delta t \left(v_{n+1}^i\right)^y - 2y_n b - 2b\Delta t \left(v_{n+1}^i\right)^y \end{aligned} \tag{8.8}$$

$$\mathbf{C} = \begin{bmatrix} x_n \Delta t + \Delta t^2 \left(v_{n+1}^i\right)^x - a\Delta t \\ \\ y_n \Delta t + \Delta t^2 \left(v_{n+1}^i\right)^y - b\Delta t \end{bmatrix}^{\mathrm{T}} \tag{8.9}$$

and $\kappa > 0$ is a user defined penalty factor. The value of κ must be selected to give the desired result and therefore a degree of trial and error is required. However, the value of κ must not be so large as to cause ill-conditioning of the global stiffness matrix. The penalty stiffness matrix and force vector are assembled into the global system and are calculated at every iteration.

Consider now that the surface of the speaker evolves in time, and thus, the membrane profile must also evolve in time. This can be achieved by time-dependent scaling. The changing membrane profile is now defined by the equation $y(t) = a(t)\sin(x)$ where $a(t)$ is a triangle function with a period of 0.01 seconds, varying between -1 and $+1$.

The $10\,\mu$L droplet at equilibrium with an initial contact angle of 65° resting on an initially flat surface was subjected to vibrations due to a membrane profile defined by the equation

$y = 0.001a(t)\sin(200x) + 1$. This profile was selected to give several peaks and troughs within the cross-section whilst attempting to avoid meshing issues such as meshing across a trough when the frequency is large. The contact node is not pinned and is free to move along the curve profile. This is because, whilst the hydrophobic surface surrounding the droplet prevents the droplet from spreading outwards, it does not prevent it from receding inwards. Minimal excitation was caused by this vibration in the membrane, as can be seen from both Figure 8.8a depicting an evolution of the droplet geometry, and Figure 8.8b depicting the change in droplet height over time. The change in height of the droplet is approximately 0.02 cm during the course of the excitation, which lasted for 0.02 seconds longer than the laboratory testing. The change in overall droplet geometry is minimal, even though it is apparent that the membrane is changing shape throughout the simulation. The observed contact angle varies by up to 110° during the simulation.

In order to provide some additional momentum, two changes are now made. The droplet is assessed from an initial non-equilibrium position, and the droplet rests on an initial non-flat surface now defined by the equation $y = 0.001a(t)\sin(500x) + 1$. The combination of the additional potential energy and an initially curved membrane profile is made as it is thought this will produce the most dramatic response. Figure 8.9a depicts the evolution of the droplet geometry and Figure 8.9b the change in droplet height over time. In this case, the geometry of the droplet varies greatly and the change in height is much greater; approximately 0.09 cm over the course of the excitation. In this case, there is also a much greater change in the contact angle during the simulation, with the observed angle varying by up to 165°.

Changing the membrane profile in time to induce capillary waves upon the droplet surface did cause motion of the fluid droplet, but proved difficult to implement and unsuccessful in terms of inducing violent jetting. Additionally, due to limitations with the mesh and a desire to minimise analysis time, the profile of the membrane has been kept to a rather simple sine curve. In reality, the membrane profile is significantly more complicated.

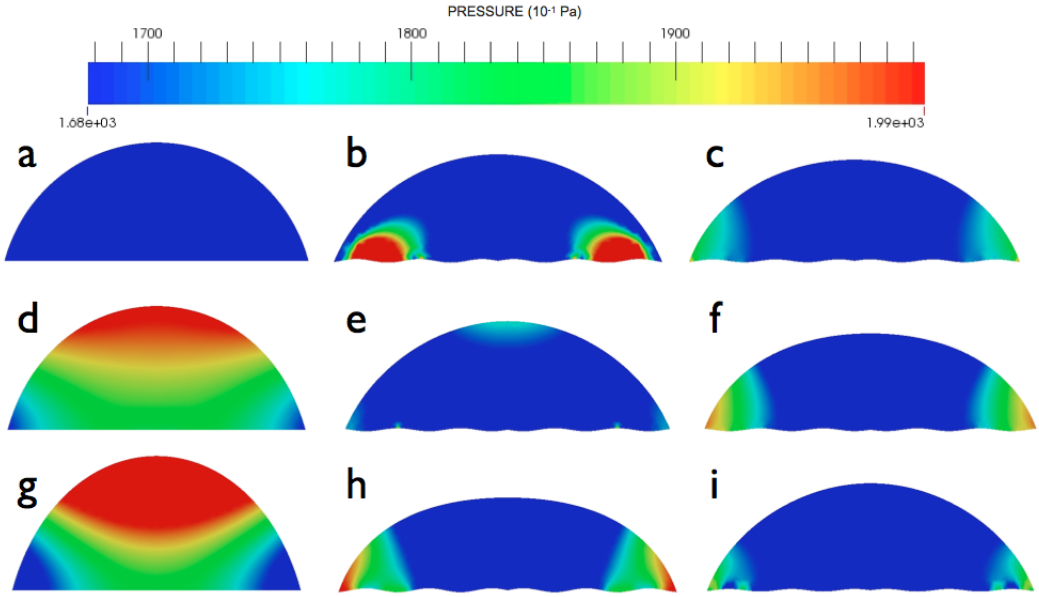

(a) Change in droplet geometry over time

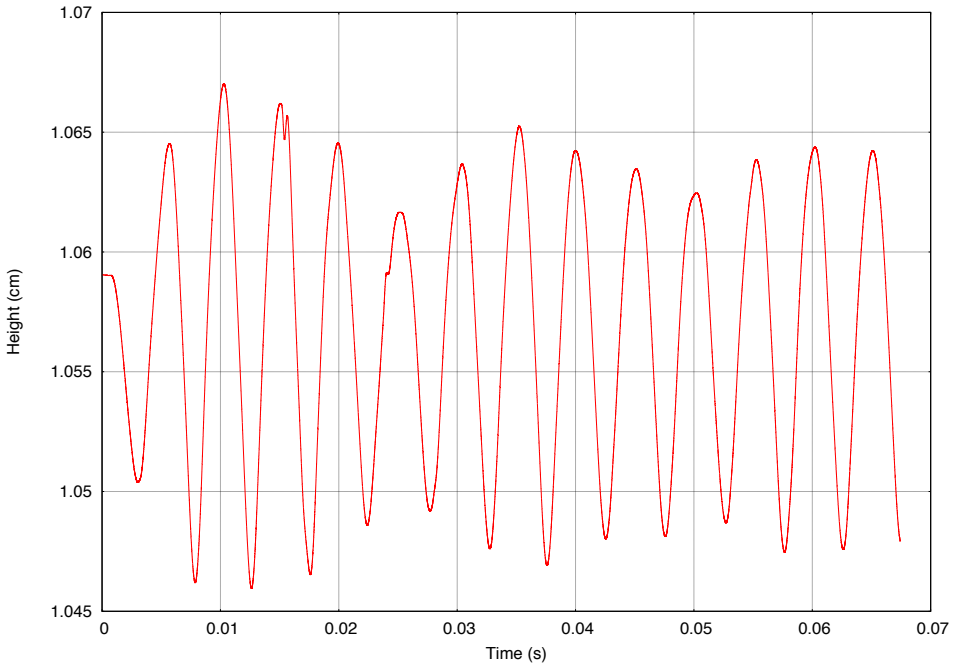

(b) Change in droplet height over time

Figure 8.8: Response of a water droplet to membrane excitation from an initial equilibrium position resting on an initially flat surface

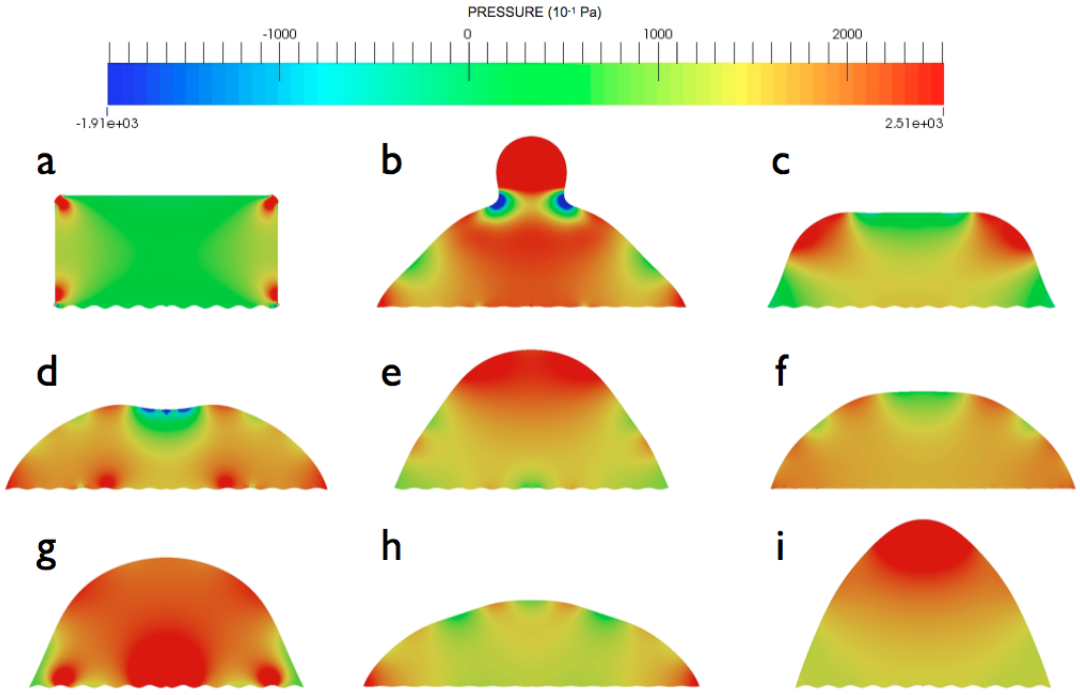

(a) Change in droplet geometry over time

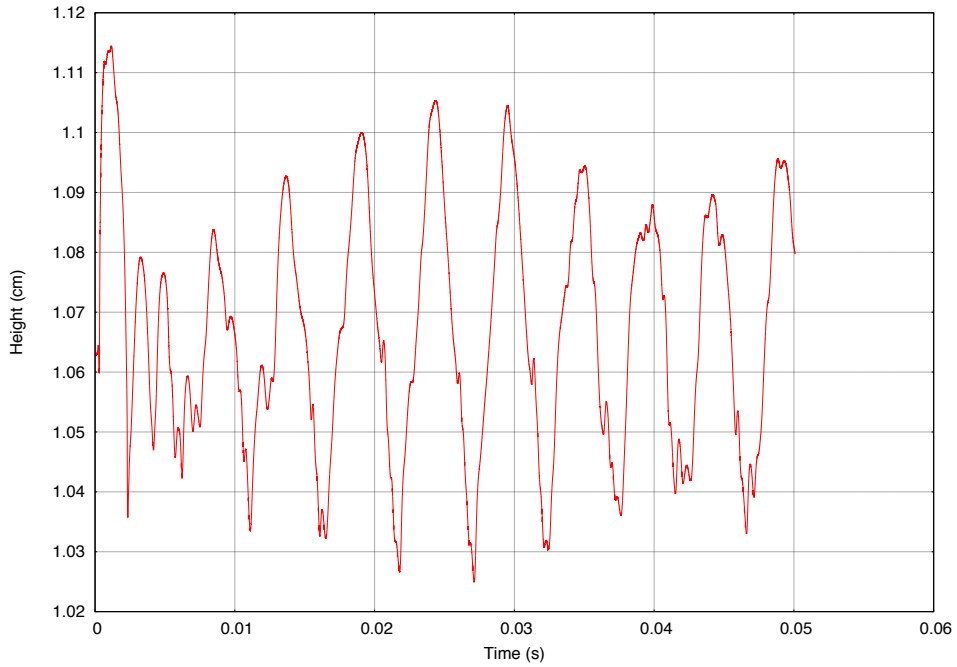

(b) Change in droplet height over time

Figure 8.9: Response of a water droplet to membrane excitation from a non-initial equilibrium position resting on an initially non-flat surface

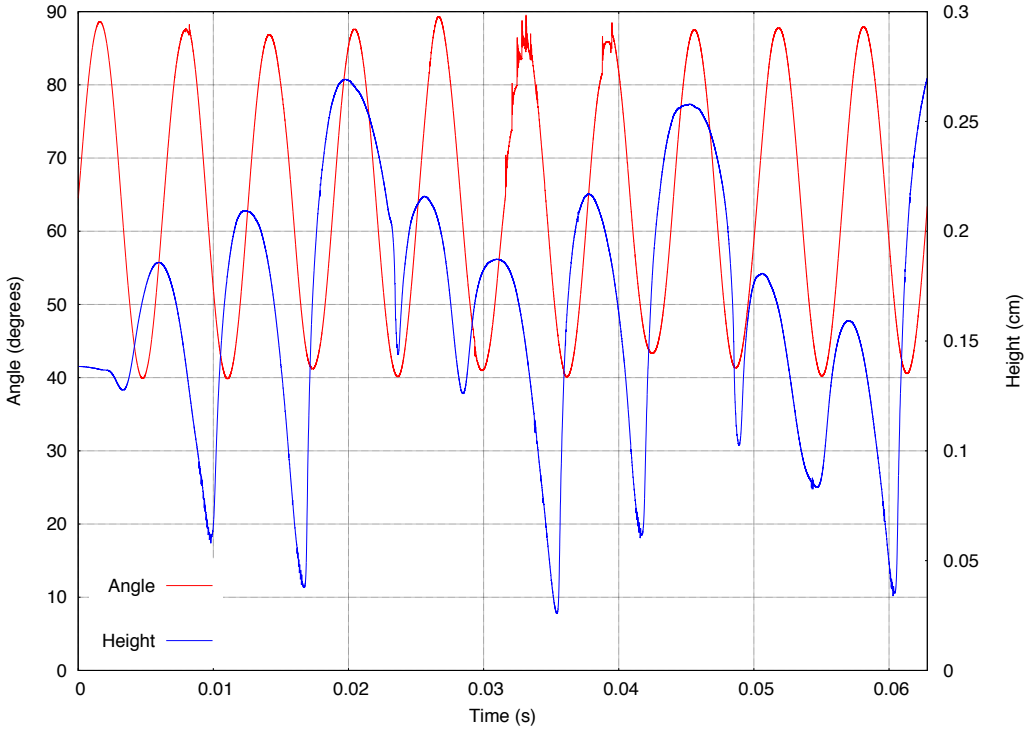

Figure 8.10: Droplet height and contact angle over time

8.3.2 Time Dependent Contact Angle

The equilibrium contact angle shall now be changed in time as a way of modelling the action of the SAWs. The membrane profile shall remain flat. To simulate this computationally, the contact angle is changed according to Equation 8.10, where α_0 is the initial contact angle, A is the amplitude, ω is the angular frequency and t is the current time.

$$\Delta\alpha = \alpha_0 + A\sin(\omega t) \tag{8.10}$$

Using the $10\,\mu$L droplet at equilibrium with an initial contact angle of 65°, the amplitude and frequency can be manipulated so that the angle changes over a given range; for example, if $A = 25$ the contact angle will range from 40° to 90° during the course of one period. It should be noted that for this simulation, the contact node is not pinned. Pinning of the contact node in conjunction with a time-dependent contact angle produced only very minor oscillations in the droplet and there was no ejection of material. Additionally, pinning prevents the droplet from receding inwards which the hydrophobic surface in the laboratory does not. An angular frequency of 1000 Hz (and therefore a period of 6.283×10^{-3} seconds) produces the fluctuations in droplet height and contact angle shown in Figure 8.10 for the first ten periods of oscillation. It can be seen that there is a delay in the change of droplet height relative to the change in contact angle, and in fact, the change in droplet height is approximately one

period behind the change in contact angle. The height of the droplet ranges from 0.02 cm to a maximum of 0.275 cm during this time. The droplet reacts quite violently in some instances and after thirteen periods of contact angle oscillation (approximately 0.079 seconds), there is upward ejection of material from the droplet specimen. Figure 8.12 shows the evolution of the droplet shape from the initial equilibrium position to a point just after ejection of material; note the varied geometries that the droplet undergoes in this time. Figure 8.13 shows the evolution of the droplet for the time period between that of Figures 8.12(i) and 8.12(j) when ejection occurs; note the surface tension pinching occurring on the jet rising up from the main fluid bulk and the near perfect circular shape of the two ejected droplets. It should be noted that pinching is captured as a consequence of the mesh distorting; it is unclear if this is how pinching would occur in the laboratory. It is clear that there is a sudden change in pressure which causes the ejection of the material and the vertical velocity of these two ejected droplets, with approximate volumes of 10.5 nL for the upper and 6.5 nL for the lower, is very high indeed at approximately 4.5 m/sec and 3.5 m/sec respectively. The two ejected droplets continue to travel upwards, with the velocity gradually reducing. Up to a point 0.143 seconds into the analysis, the two ejected droplets are still travelling upwards with the upper (larger) droplet 26.8 cm and the lower (smaller) droplet 20.2 cm above the level of the surface upon which the droplet initially rested. At this point, the velocities of the droplets has reduced to 3.9 cm/s for the upper and 2.9 cm/s for the lower. The velocity of the two ejected droplets will eventually decrease to zero before they both then fall back towards the remainder of the fluid. However, it is also possible that further ejections take place. If both these eventualities were to happen simultaneously, there would be a collision between upwards-moving droplets and downwards-moving droplets. Such behaviour is outwith the scope of this work but would make an interesting study. The changing of the contact angle, producing lateral motion, causes the extreme behaviour experienced.

Figure 8.11 shows four consecutive representative steps from this analysis. It can be seen that the convergence is quadratic, with the residual after each Newton iteration shown. Also included is some geometric information and the contact angle that is being enforced on the system.

It would appear that the hypothesis has been proved, that capillary waves propagating up the surface of a droplet change the wetting angle and cause motion of the droplet. However, further testing is required to experiment with a range of frequencies and amplitudes to better understand this interaction.

```
SURFACE EDGES FOUND = 62        BOUNDARY EDGES FOUND = 125
step = 7404, time = 0.00622688429298002
  0 SNES Function norm 1.202537331284e-02
  1 SNES Function norm 1.017684274530e-07
  2 SNES Function norm 3.056276366061e-08
  3 SNES Function norm 2.753148985666e-10
Nonlinear solve converged due to CONVERGED_FNORM_ABS
Number of Newton iterations = 3
AAA     step= 7404   time= 0.00622688429298002  H= 0.1849798291  R= 0.2247576723  phi= 61.661738
V= 0.0099983351 == -0.0166490%   gy= -9.81e+02   delta_calpha= 63.593218  New dt= 7.29823e-07
-----------------------------------------------------------------------------------------------

SURFACE EDGES FOUND = 62        BOUNDARY EDGES FOUND = 125
step = 7405, time = 0.00622761411612993
  0 SNES Function norm 1.189978358142e-02
  1 SNES Function norm 7.097851101263e-08
  2 SNES Function norm 1.863018222738e-08
  3 SNES Function norm 6.750800521848e-11
Nonlinear solve converged due to CONVERGED_FNORM_ABS
Number of Newton iterations = 3
AAA     step= 7405   time= 0.00622761411612993  H= 0.1849760489  R= 0.2247554814  phi= 61.676335
V= 0.0099983351 == -0.0166491%   gy= -9.81e+02   delta_calpha= 63.611435  New dt= 6.32045e-07
-----------------------------------------------------------------------------------------------

SURFACE EDGES FOUND = 62        BOUNDARY EDGES FOUND = 125
step = 7406, time = 0.00622824616151973
  0 SNES Function norm 1.180809692406e-02
  1 SNES Function norm 5.854196794293e-08
  2 SNES Function norm 1.127144070453e-08
  3 SNES Function norm 4.106028499841e-11
Nonlinear solve converged due to CONVERGED_FNORM_ABS
Number of Newton iterations = 3
AAA     step= 7406   time= 0.00622824616151973  H= 0.1849727671  R= 0.2247535781  phi= 61.688990
V= 0.0099983351 == -0.0166491%   gy= -9.81e+02   delta_calpha= 63.627212  New dt= 5.47367e-07
-----------------------------------------------------------------------------------------------

SURFACE EDGES FOUND = 62        BOUNDARY EDGES FOUND = 125
step = 7407, time = 0.00622879352888006
  0 SNES Function norm 1.174067852635e-02
  1 SNES Function norm 4.989828800604e-08
  2 SNES Function norm 6.804869440401e-09
  3 SNES Function norm 4.159477225130e-11
Nonlinear solve converged due to CONVERGED_FNORM_ABS
Number of Newton iterations = 3
AAA     step= 7407   time= 0.00622879352888006  H= 0.1849699190  R= 0.2247519251  phi= 61.699964
V= 0.0099983351 == -0.0166491%   gy= -9.81e+02   delta_calpha= 63.640876  New dt= 4.74034e-07
```

Figure 8.11: Four representative steps for analysis with time dependent contact angle

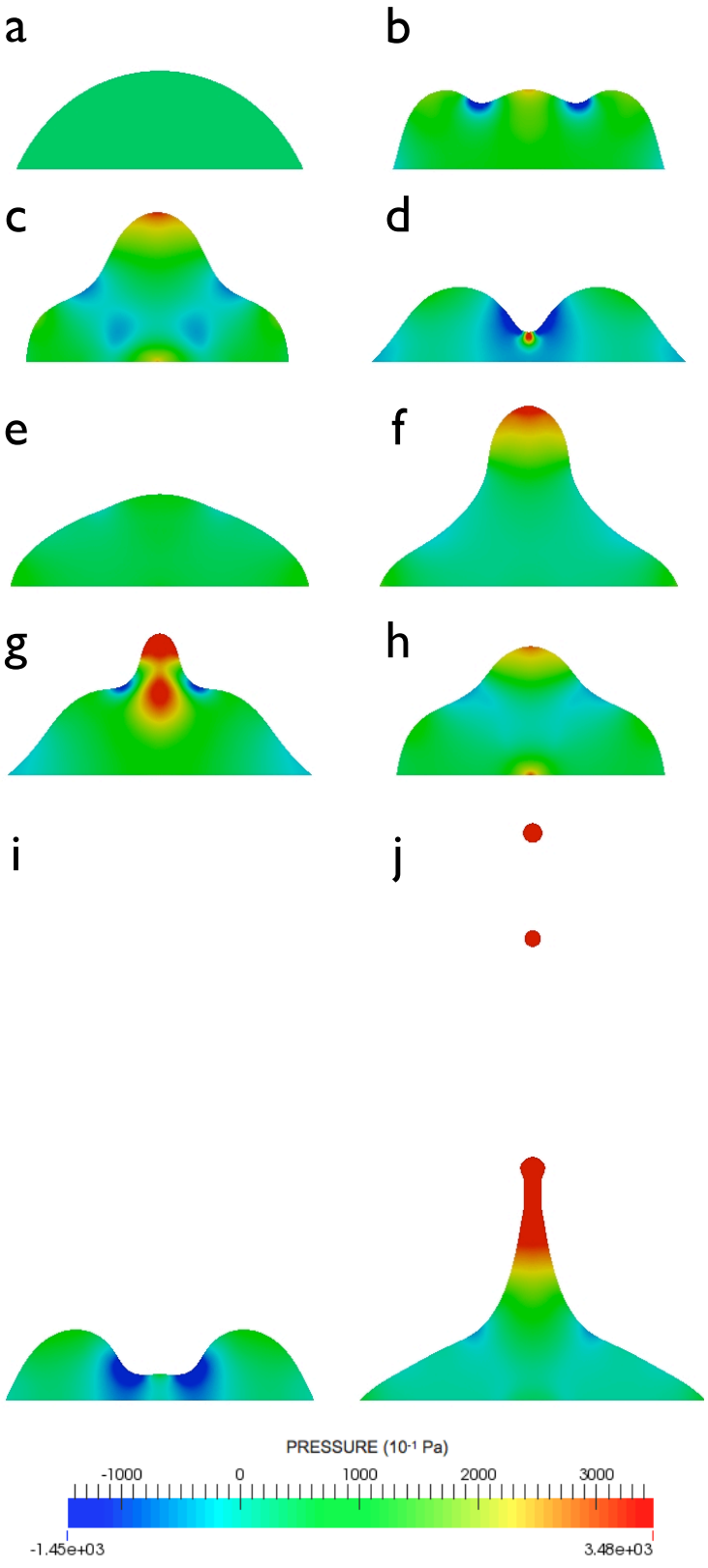

Figure 8.12: Evolution of droplet from equilibrium to ejection of material, contours showing pressure: (a) t = 0 ms, (b) t = 15.3 ms, (c) t = 26.3 ms, (d) t = 35.6 ms, (e) t = 40.0 ms, (f) t = 44.3 ms, (g) t = 61.4 ms, (h) t = 69.9 ms, (i) t = 78.5 ms, (j) t = 81.0 ms

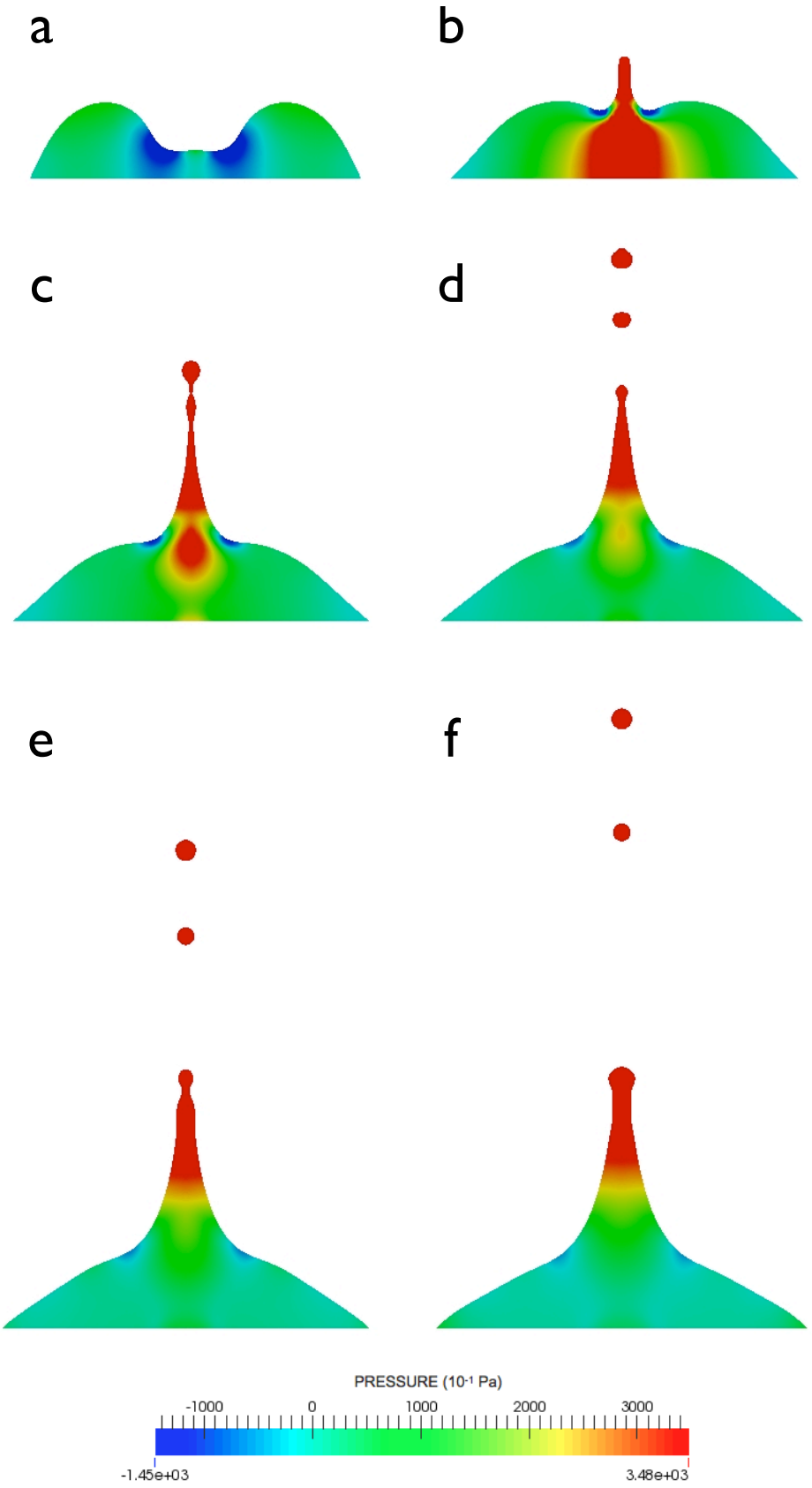

Figure 8.13: Evolution of droplet for the time period between that of Figure 8.12(i) and Figure 8.12(j), showing ejection of material, contours showing pressure: (a) t = 78.5 ms, (b) t = 79.5 ms, (c) t = 79.9 ms, (d) t = 80.3 ms, (e) t = 80.6 ms, (f) t = 81.0 ms

8.4 Conclusions

A method of external excitation has been implemented to replicate laboratory testing and the response of a water droplet has been assessed. Laboratory data was used to apply a velocity to the nodes on the base of the droplet and the resulting response of the droplet was a very close match to the response as filmed using a high-speed camera in the laboratory. No major change in response was experienced when changing the contact angle by up to $\pm 3^{\circ}$ and by increasing the density of the mesh. Whilst there was a slight discrepancy between the response in the laboratory and the response from the computational framework, which can be attributed to momentum differences and data collection issues, there was a good correlation between both the phase and amplitude of oscillation. Changes to the mesh and initial contact angle attributed to no major difference in the response. Therefore, this method is recommended for future problems involving droplets on a speaker.

A new hypothesis was tested that proposed upon reaching the solid-liquid boundary, SAWs propagate capillary waves up the surface of the droplet. These capillary waves cause a change in the contact angle inducing motion. Firstly, a penalty method was implemented in an attempt to model the undulating nature of the surface of the speaker. A rather simplistic profile was selected due to constrictions with the mesh and this method proved unsuccessful in causing jetting. Secondly, the contact angle was changed in time to replicate the action of SAWs with a frequency of 1000 Hz in the range of 40° to 90°. It very quickly became clear that this change in angle was inducing motion within the droplet and after several periods of oscillation, upward ejection of fluid from the droplet was observed. It is clear that the contact angle is extremely influential in the geometry of the droplet, even causing ejection of material. Hence, the proposed hypothesis is correct, but further testing is required. Additionally, the resulting response is very useful if splitting a sample into sub-samples is required.

Chapter 9

Conclusions

The work in this thesis has presented a computational framework for analysing fluids at the micro-scale under axisymmetric conditions. Several distinct novel aspects of the framework were presented in this thesis. The use of an updated Arbitrary Lagrangian Eulerian formulation (UALE) enabled an accurate description of the fluid surface whilst minimising remeshing. Additional contributions, derived directly from the Young-Laplace equation, were included to take account of surface tension. The framework is able to model a variety of scenarios including zero-gravity environments, capillary tubes and excitation via external loading.

The Navier-Stokes equations for an incompressible Newtonian fluid were derived in full, firstly for 2D and then for axisymmetric conditions. A time and space discretised *weak form* of the Navier-Stokes equations was then developed for use in an iterative Newton-Raphson solver. Surface tension is the most dominant force at the micro-scale. Examining the relationship between surface tension and the curvature of the interface between two fluids enabled the inclusion of surface tension in the framework.

The use of equal order interpolation functions for the velocity and pressure fields caused spurious oscillations in the pressure field. To mitigate these oscillations, the pressure Laplacian stabilisation technique (PLS) was implemented. A study into the magnitude of the stabilisation parameter showed that the larger the parameter, the smoother the pressure field, but at

the cost of increased computational time.

Comprehensive validation and verification of the framework was performed. This focused on calculating the equilibrium geometries for various configurations, whilst also varying the fluid volume and equilibrium contact angle. The framework was shown to accurately predict not only the equilibrium shape but also the form of oscillation. This allowed for more complex problems to be examined with a degree of confidence.

To replicate laboratory testing of a water droplet on a vibrating speaker a prescribed velocity was applied to the nodes along the base of the droplet. This method proved quite successful, producing oscillations in phase and with approximately the same amplitude as the laboratory testing.

In order to induce jetting and nebulisation, within the literature there is a hypothesis that upon reaching the solid-fluid boundary, SAWs produce longitudinal waves that propagate into the droplet, pumping energy into the system and causing the droplet to move. However, no computational models exist that examine this directly. In this thesis we offer an alternative hypothesis we believe is closer to reality and we can support this through the use of a computational model. It is proposed that upon reaching the boundary between the fluid and the surface, surface acoustic waves propagate capillary waves up the surface of the droplet, altering the apparent wetting angle and inducing motion. The hypothesis was tested using two different modelling approaches. The first approach changed the profile of the membrane in time, assuming a sinusoidal profile. However, due the complexity of discretising the changing membrane profile, this method was deemed impractical, even though moderate motion was induced. The second approach changed the contact angle in time as a way of modelling the action of the SAWs and proved much more successful in generating the proposed capillary waves and subsequently induced jetting and surface tension pinching, as observed in reality. This indicates that the new hypothesis has some validity. More testing is required before a definitive relationship can be developed between the frequency and amplitude of the excitation and the droplet motion.

Several aspects of the framework can be further developed in the future:

- parallelisation, cleaning and streamlining of the code should be undertaken to improve the overall performance in terms of speed and efficiency
- the methodology can be easily extended to 3D
- extension to examine non-Newtonian fluids by inclusion of different shear stress-shear strain rate relationships
- extension to examine compressible fluids
- the use of automatic differentiation as an alternative to linearisation by hand.

In several of the examples presented, the problem of volume loss arose and this was attributed, in part, to Laplacian smoothing and remeshing. Moreover, Laplacian smoothing is ineffective in 3D and requires a mesh viscosity modelling parameter that is difficult to determine. Kelly [36] has proposed two alternative methods, mesh quality improvement and mesh quality preservation. The former was successful in reducing the level of remeshing and reducing volume loss, however, there was a major detrimental effect on the average time step and therefore this method was deemed too aggressive. The latter almost eradicated volume loss, whilst the time step was much closer to that experienced when using Laplacian smoothing. However, due to the reduction in time step, Laplacian smoothing is recommended until the framework extends to 3D problems.

Overall, the computational framework has been very successful in modelling various microscale problems. The underlying physics has been presented, the computational strategy outlined and several algorithms presented in a way that others can implement this code. The next stage for this work is extension into 3D.

Appendix A

Derivation of Mathematical Operators

Inverse of a Differential Equation

From Bonet and Wood [21]:

$$\text{Let} \quad \frac{\partial \mathbf{x}}{\partial \chi} = \mathbf{S} + \mathbf{U} \tag{A.1}$$

$$\begin{aligned} \left(\frac{\partial \mathbf{x}}{\partial \chi}\right)^{-1} &= \frac{\partial \chi}{\partial \mathbf{x}} = (\mathbf{S}+\mathbf{U})^{-1} \\ &\approx \mathbf{S}^{-1} + D\left(\mathbf{S}^{-1}\right)[\mathbf{U}] \end{aligned} \tag{A.2}$$

where $D\left(\mathbf{S}^{-1}\right)[\mathbf{U}]$ is the directional derivative which can also be expressed as:

$$D\left(\mathbf{S}^{-1}\right)[\mathbf{U}] = \left|\frac{d}{d\varepsilon}\left(\mathbf{S}+\varepsilon\mathbf{U}\right)\right|_{\varepsilon=0} \tag{A.3}$$

Using the product rule, this becomes:

$$D\left(\mathbf{S}^{-1}\right)[\mathbf{U}] = -\mathbf{S}^{-1}\mathbf{U}\mathbf{S}^{-1} \tag{A.4}$$

Therefore:

$$\frac{\partial \chi}{\partial \mathbf{x}} = \mathbf{S}^{-1} - \mathbf{S}^{-1}\mathbf{U}\mathbf{S}^{-1} \tag{A.5}$$

Thus, for:

$$\frac{\partial \mathbf{x}}{\partial \chi} = 1 + \frac{\Delta t}{2}\frac{\partial \delta \hat{\mathbf{v}}}{\partial \chi} \tag{A.6}$$

$$\text{Let } \mathbf{S} = 1 \text{ and } \mathbf{U} = \frac{\Delta t}{2}\frac{\partial \delta \hat{\mathbf{v}}}{\partial \chi} \tag{A.7}$$

Therefore:

$$\begin{aligned}
\frac{\partial \chi}{\partial \mathbf{x}} &= \mathbf{S}^{-1} - \mathbf{S}^{-1}\mathbf{U}\mathbf{S}^{-1} \\
&= (1)^{-1} - (1)^{-1}\left(\frac{\Delta t}{2}\frac{\partial \delta \hat{\mathbf{v}}}{\partial \chi}\right)(1)^{-1} \\
&= 1 - \frac{\Delta t}{2}\frac{\partial \delta \hat{\mathbf{v}}}{\partial \chi}
\end{aligned} \tag{A.8}$$

Nodal Acceleration

It can be seen that the first term of the acceleration equation (Equation 4.11) is the time derivative of the fluid velocity, which can also be written as:

$$\frac{\partial \mathbf{v}}{\partial t} = \frac{\Delta \mathbf{v}}{\Delta t} + \frac{\delta \mathbf{v}_i}{\Delta t} \tag{A.9}$$

The second term of Equation 4.11 is the product of the derivative of the fluid velocity in the reference configuration and the convective velocity. Expanding and writing in full:

$$\begin{aligned}
\frac{\partial \mathbf{v}}{\partial \chi}\mathbf{c} &= \frac{\partial \mathbf{v}}{\partial \chi}(\mathbf{v} - \hat{\mathbf{v}}) \\
&= \frac{\partial (\mathbf{v}_i + \delta \mathbf{v}_i)}{\partial \chi}((\mathbf{v}_i + \delta \mathbf{v}_i) - (\hat{\mathbf{v}}_i + \delta \hat{\mathbf{v}}_i)) \\
&= \frac{\partial \mathbf{v}_i}{\partial \chi}\mathbf{v}_i + \frac{\partial \mathbf{v}_i}{\partial \chi}\delta \mathbf{v}_i + \frac{\partial \delta \mathbf{v}_i}{\partial \chi}\mathbf{v}_i - \frac{\partial \mathbf{v}_i}{\partial \chi}\hat{\mathbf{v}}_i - \frac{\partial \mathbf{v}_i}{\partial \chi}\delta \hat{\mathbf{v}}_i - \frac{\partial \delta \mathbf{v}_i}{\partial \chi}\hat{\mathbf{v}}_i
\end{aligned} \tag{A.10}$$

The product of two iterative change in velocity terms is negligible and ignored. The third term of Equation 4.11 can be expanded:

$$
\begin{aligned}
-\frac{\Delta t}{2}\frac{\partial \mathbf{v}}{\partial \chi}\frac{\partial \delta\hat{\mathbf{v}}_i}{\partial \chi}\mathbf{c} &= -\frac{\Delta t}{2}\frac{\partial \mathbf{v}}{\partial \chi}\frac{\partial \delta\hat{\mathbf{v}}_i}{\partial \chi}(\mathbf{v}-\hat{\mathbf{v}}) \\
&= -\frac{\Delta t}{2}\frac{\partial (\mathbf{v}_i+\delta\mathbf{v}_i)}{\partial \chi}\frac{\partial \delta\hat{\mathbf{v}}_i}{\partial \chi}((\mathbf{v}_i+\delta\mathbf{v}_i)-(\hat{\mathbf{v}}_i+\delta\hat{\mathbf{v}}_i)) \\
&= -\frac{\Delta t}{2}\frac{\partial \delta\hat{\mathbf{v}}_i}{\partial \chi}\left(\frac{\partial \mathbf{v}_i}{\partial \chi}\mathbf{v}_i+\frac{\partial \mathbf{v}_i}{\partial \chi}\delta\mathbf{v}_i+\frac{\partial \delta\mathbf{v}_i}{\partial \chi}\mathbf{v}_i-\frac{\partial \mathbf{v}_i}{\partial \chi}\hat{\mathbf{v}}_i-\frac{\partial \mathbf{v}_i}{\partial \chi}\delta\hat{\mathbf{v}}_i-\frac{\partial \delta\mathbf{v}_i}{\partial \chi}\hat{\mathbf{v}}_i\right) \\
&= -\frac{\Delta t}{2}\frac{\partial \mathbf{v}_i}{\partial \chi}\frac{\partial \delta\hat{\mathbf{v}}_i}{\partial \chi}\mathbf{v}_i+\frac{\Delta t}{2}\frac{\partial \mathbf{v}_i}{\partial \chi}\frac{\partial \delta\hat{\mathbf{v}}_i}{\partial \chi}\hat{\mathbf{v}}_i \qquad \text{(A.11)}
\end{aligned}
$$

Hence, the acceleration of a node is found from:

$$
\begin{aligned}
\mathbf{a} &= \frac{\Delta \mathbf{v}}{\Delta t}+\frac{\delta \mathbf{v}_i}{\Delta t} \\
&\quad +\frac{\partial \mathbf{v}_i}{\partial \chi}\mathbf{v}_i+\frac{\partial \mathbf{v}_i}{\partial \chi}\delta\mathbf{v}_i+\frac{\partial \delta\mathbf{v}_i}{\partial \chi}\mathbf{v}_i-\frac{\partial \mathbf{v}_i}{\partial \chi}\hat{\mathbf{v}}_i-\frac{\partial \mathbf{v}_i}{\partial \chi}\delta\hat{\mathbf{v}}_i-\frac{\partial \delta\mathbf{v}_i}{\partial \chi}\hat{\mathbf{v}}_i \\
&\quad -\frac{\Delta t}{2}\frac{\partial \mathbf{v}_i}{\partial \chi}\frac{\partial \delta\hat{\mathbf{v}}_i}{\partial \chi}\mathbf{v}_i+\frac{\Delta t}{2}\frac{\partial \mathbf{v}_i}{\partial \chi}\frac{\partial \delta\hat{\mathbf{v}}_i}{\partial \chi}\hat{\mathbf{v}}_i \qquad \text{(A.12)}
\end{aligned}
$$

Appendix B

The Symmetric Part of the Deviatoric Stress Tensor

From Equation 3.24:

$$\begin{aligned}\mathbf{e} &= \frac{1}{2}(\nabla\mathbf{v}) + \frac{1}{2}(\nabla\mathbf{v})^{\mathrm{T}} \\ &= \frac{\partial\mathbf{v}}{\partial\mathbf{x}} - \frac{1}{3}tr\left(\frac{\partial\mathbf{v}}{\partial\mathbf{x}}\right)\end{aligned}$$

Mapping to the reference domain using Equation 4.8:

$$\begin{aligned}\mathbf{e} &= \left(\frac{\partial\mathbf{v}}{\partial\chi} - \frac{\Delta t}{2}\frac{\partial\mathbf{v}}{\partial\chi}\frac{\partial\delta\hat{\mathbf{v}}}{\partial\chi}\right) - \frac{1}{3}tr\left(\frac{\partial\mathbf{v}}{\partial\chi} - \frac{\Delta t}{2}\frac{\partial\mathbf{v}}{\partial\chi}\frac{\partial\delta\hat{\mathbf{v}}}{\partial\chi}\right) \\ &= \left(\frac{\partial(\mathbf{v}_i+\delta\mathbf{v})}{\partial\chi} - \frac{\Delta t}{2}\frac{\partial(\mathbf{v}_i+\delta\mathbf{v})}{\partial\chi}\frac{\partial\delta\hat{\mathbf{v}}}{\partial\chi}\right) - \frac{1}{3}tr\left(\frac{\partial(\mathbf{v}_i+\delta\mathbf{v})}{\partial\chi} - \frac{\Delta t}{2}\frac{\partial(\mathbf{v}_i+\delta\mathbf{v})}{\partial\chi}\frac{\partial\delta\hat{\mathbf{v}}}{\partial\chi}\right) \\ &= \left[\frac{\partial\mathbf{v}_i}{\partial\chi} - \frac{1}{3}tr\left(\frac{\partial\mathbf{v}_i}{\partial\chi}\right)\right] + \left[\frac{\partial\delta\mathbf{v}}{\partial\chi} - \frac{1}{3}tr\left(\frac{\partial\delta\mathbf{v}}{\partial\chi}\right)\right] - \left[\frac{\Delta t}{2}\frac{\partial\mathbf{v}_i}{\partial\chi}\frac{\partial\delta\hat{\mathbf{v}}}{\partial\chi} - \frac{1}{3}tr\left(\frac{\Delta t}{2}\frac{\partial\mathbf{v}_i}{\partial\chi}\frac{\partial\delta\hat{\mathbf{v}}}{\partial\chi}\right)\right] \\ &= \mathbf{e}_i + \delta\mathbf{e} + \delta\hat{\mathbf{e}} \qquad \text{(B.1)}\end{aligned}$$

where:

$$\mathbf{e}_i = \frac{\partial\mathbf{v}_i}{\partial\chi} - \frac{1}{3}tr\left(\frac{\partial\mathbf{v}_i}{\partial\chi}\right) \qquad \text{(B.2)}$$

$$\delta\mathbf{e} = \frac{\partial \delta\mathbf{v}}{\partial \chi} - \frac{1}{3} tr\left(\frac{\partial \delta\mathbf{v}}{\partial \chi}\right) \tag{B.3}$$

$$\delta\hat{\mathbf{e}} = -\frac{\Delta t}{2}\frac{\partial \mathbf{v}_i}{\partial \chi}\frac{\partial \delta\hat{\mathbf{v}}}{\partial \chi} + \frac{1}{3} tr\left(\frac{\Delta t}{2}\frac{\partial \mathbf{v}_i}{\partial \chi}\frac{\partial \delta\hat{\mathbf{v}}}{\partial \chi}\right) \tag{B.4}$$

Axisymmetric Form of the Symmetric Part of the Deviatoric Stress Tensor

Cartesian Form

Using cartesian coordinates, the velocity vector is:

$$\mathbf{v} = \begin{bmatrix} v_x \\ v_y \\ v_z \end{bmatrix} \tag{B.5}$$

and the gradient of the velocity is:

$$\begin{aligned} \nabla\mathbf{v} &= \frac{\partial v_x}{\partial x} + \frac{\partial v_y}{\partial y} + \frac{\partial v_z}{\partial z} \\ &= \begin{bmatrix} \frac{\partial v_x}{\partial x} & \frac{\partial v_x}{\partial y} & \frac{\partial v_x}{\partial z} \\ \frac{\partial v_y}{\partial x} & \frac{\partial v_y}{\partial y} & \frac{\partial v_y}{\partial z} \\ \frac{\partial v_z}{\partial x} & \frac{\partial v_z}{\partial y} & \frac{\partial v_z}{\partial z} \end{bmatrix} \end{aligned} \tag{B.6}$$

which, in 2D conditions, becomes:

$$\nabla\mathbf{v} = \begin{bmatrix} \frac{\partial v_x}{\partial x} & \frac{\partial v_x}{\partial y} \\ \frac{\partial v_y}{\partial x} & \frac{\partial v_y}{\partial y} \end{bmatrix} \tag{B.7}$$

The symmetric part of the deviatoric stress tensor is calculated as:

$$\begin{aligned} \mathbf{e} &= dev(\mathbf{v}) \\ &= \frac{1}{2}\left(\nabla\mathbf{v} + \nabla\mathbf{v}^{\mathrm{T}}\right) - \frac{1}{3}tr(\nabla\mathbf{v}) \end{aligned} \tag{B.8}$$

where $tr(\nabla\mathbf{v})$ is the trace of the gradient of the velocity. Expanding this, and using Voigt notation latterly, it becomes:

$$\begin{aligned} \mathbf{e} &= \frac{1}{2}\left(\begin{bmatrix} \frac{\partial v_x}{\partial x} & \frac{\partial v_x}{\partial y} \\ \frac{\partial v_y}{\partial x} & \frac{\partial v_y}{\partial y} \end{bmatrix} + \begin{bmatrix} \frac{\partial v_x}{\partial x} & \frac{\partial v_x}{\partial y} \\ \frac{\partial v_y}{\partial x} & \frac{\partial v_y}{\partial y} \end{bmatrix}^{\mathrm{T}}\right) - \frac{1}{3}tr\left(\begin{bmatrix} \frac{\partial v_x}{\partial x} & \frac{\partial v_x}{\partial y} \\ \frac{\partial v_y}{\partial x} & \frac{\partial v_y}{\partial y} \end{bmatrix}\right) \\ &= \begin{bmatrix} \frac{\partial v_x}{\partial x} & \frac{1}{2}\left(\frac{\partial v_x}{\partial y} + \frac{\partial v_y}{\partial x}\right) \\ \frac{1}{2}\left(\frac{\partial v_x}{\partial y} + \frac{\partial v_y}{\partial x}\right) & \frac{\partial v_y}{\partial y} \end{bmatrix} - \frac{1}{3}\begin{bmatrix} \frac{\partial v_x}{\partial x} + \frac{\partial v_y}{\partial y} & 0 \\ 0 & \frac{\partial v_x}{\partial x} + \frac{\partial v_y}{\partial y} \end{bmatrix} \\ &= \begin{bmatrix} \frac{\partial v_x}{\partial x} - \frac{1}{3}\left(\frac{\partial v_x}{\partial x} + \frac{\partial v_y}{\partial y}\right) & \frac{1}{2}\left(\frac{\partial v_x}{\partial y} + \frac{\partial v_y}{\partial x}\right) \\ \frac{1}{2}\left(\frac{\partial v_x}{\partial y} + \frac{\partial v_y}{\partial x}\right) & \frac{\partial v_y}{\partial y} - \frac{1}{3}\left(\frac{\partial v_x}{\partial x} + \frac{\partial v_y}{\partial y}\right) \end{bmatrix} \\ &= \begin{bmatrix} \frac{2}{3}\frac{\partial v_x}{\partial x} - \frac{1}{3}\frac{\partial v_y}{\partial y} \\ \frac{2}{3}\frac{\partial v_y}{\partial y} - \frac{1}{3}\frac{\partial v_x}{\partial x} \\ \frac{1}{2}\left(\frac{\partial v_x}{\partial y} + \frac{\partial v_y}{\partial x}\right) \\ \frac{1}{2}\left(\frac{\partial v_x}{\partial y} + \frac{\partial v_y}{\partial x}\right) \end{bmatrix} \end{aligned} \tag{B.9}$$

Cylindrical Form

In cylindrical coordinates, the velocity vector is:

$$\mathbf{v} = \begin{bmatrix} v_r \\ v_\phi \\ v_z \end{bmatrix} \tag{B.10}$$

and the gradient of the velocity is:

$$\begin{aligned} \nabla \mathbf{v} &= \frac{\partial \mathbf{v}}{\partial r}\hat{\mathbf{r}} + \frac{\partial \mathbf{v}}{\partial \phi}\frac{\hat{\phi}}{r} + \frac{\partial \mathbf{v}}{\partial z}\hat{\mathbf{z}} \\ &= \begin{bmatrix} \frac{\partial v_r}{\partial r} & \frac{1}{r}\frac{\partial v_r}{\partial \phi} & \frac{\partial v_r}{\partial z} \\ \frac{\partial v_\phi}{\partial r} & \frac{\partial v_\phi}{\partial \phi} & \frac{\partial v_\phi}{\partial z} \\ \frac{\partial v_z}{\partial r} & \frac{\partial v_z}{\partial \phi} & \frac{\partial v_z}{\partial z} \end{bmatrix} \end{aligned} \tag{B.11}$$

which, in axisymmetric conditions (no tangential velocity and $\phi = 0$), becomes:

$$\nabla \mathbf{v} = \begin{bmatrix} \frac{\partial v_r}{\partial r} & \frac{\partial v_r}{\partial z} \\ \frac{\partial v_z}{\partial r} & \frac{\partial v_z}{\partial z} \end{bmatrix} \tag{B.12}$$

Calculating the symmetric part of the deviatoric stress tensor, we obtain:

$$
\begin{aligned}
\mathbf{e} &= \frac{1}{2}\left(\begin{bmatrix} \frac{\partial v_r}{\partial r} & \frac{\partial v_r}{\partial z} \\ \frac{\partial v_z}{\partial r} & \frac{\partial v_z}{\partial z} \end{bmatrix} + \begin{bmatrix} \frac{\partial v_r}{\partial r} & \frac{\partial v_r}{\partial z} \\ \frac{\partial v_z}{\partial r} & \frac{\partial v_z}{\partial z} \end{bmatrix}^{\mathrm{T}}\right) - \frac{1}{3}tr\left(\begin{bmatrix} \frac{\partial v_r}{\partial r} & \frac{\partial v_r}{\partial z} \\ \frac{\partial v_z}{\partial r} & \frac{\partial v_z}{\partial z} \end{bmatrix}\right) \\
&= \begin{bmatrix} \frac{\partial v_r}{\partial r} & \frac{1}{2}\left(\frac{\partial v_r}{\partial z} + \frac{\partial v_z}{\partial r}\right) \\ \frac{1}{2}\left(\frac{\partial v_r}{\partial z} + \frac{\partial v_z}{\partial r}\right) & \frac{\partial v_z}{\partial z} \end{bmatrix} - \frac{1}{3}\begin{bmatrix} \frac{\partial v_r}{\partial r} + \frac{\partial v_z}{\partial z} & 0 \\ 0 & \frac{\partial v_r}{\partial r} + \frac{\partial v_z}{\partial z} \end{bmatrix} \\
&= \begin{bmatrix} \frac{\partial v_r}{\partial r} - \frac{1}{3}\left(\frac{\partial v_r}{\partial r} + \frac{\partial v_z}{\partial z}\right) & \frac{1}{2}\left(\frac{\partial v_r}{\partial z} + \frac{\partial v_z}{\partial r}\right) \\ \frac{1}{2}\left(\frac{\partial v_r}{\partial z} + \frac{\partial v_z}{\partial r}\right) & \frac{\partial v_z}{\partial z} - \frac{1}{3}\left(\frac{\partial v_r}{\partial r} + \frac{\partial v_z}{\partial z}\right) \end{bmatrix} \\
&= \begin{bmatrix} \frac{2}{3}\frac{\partial v_r}{\partial r} - \frac{1}{3}\frac{\partial v_z}{\partial z} \\ \frac{2}{3}\frac{\partial v_z}{\partial z} - \frac{1}{3}\frac{\partial v_r}{\partial r} \\ \frac{1}{2}\left(\frac{\partial v_r}{\partial z} + \frac{\partial v_z}{\partial r}\right) \\ \frac{1}{2}\left(\frac{\partial v_r}{\partial z} + \frac{\partial v_z}{\partial r}\right) \end{bmatrix}
\end{aligned}
\tag{B.13}
$$

To map between cartesian and cylindrical coordinate systems, and when $\phi = 0$:

$$
x = r\cos\phi = r \qquad y = z \qquad z = r\sin\phi = 0 \tag{B.14}
$$

Therefore, the deviatoric part of the stress tensor becomes:

$$
\mathbf{e} = \begin{bmatrix} \frac{2}{3}\frac{\partial v_x}{\partial x} - \frac{1}{3}\frac{\partial v_y}{\partial y} \\ \frac{2}{3}\frac{\partial v_y}{\partial y} - \frac{1}{3}\frac{\partial v_x}{\partial x} \\ \frac{1}{2}\left(\frac{\partial v_x}{\partial y} + \frac{\partial v_y}{\partial x}\right) \\ \frac{1}{2}\left(\frac{\partial v_x}{\partial y} + \frac{\partial v_y}{\partial x}\right) \end{bmatrix} \tag{B.15}
$$

which is identical to the form found in a cartesian coordinate system. Hence, no change is required for the symmetric part of the deviatoric stress tensor during the transition from cartesian to cylindrical coordinates.

Appendix C

Mapping from Cartesian to Cylindrical Coordinate Systems

To transform from a cartesian to a cylindrical coordinate system:

$$x = r\cos\phi \tag{C.1}$$

$$y = r\sin\phi \tag{C.2}$$

$$z = z \tag{C.3}$$

The unit vectors in the cylindrical system are functions of position. They are expressed in terms of the cylindrical coordinates and the unit vectors of the cartesian coordinate system which are not functions of position.

$$\hat{\mathbf{r}} = \hat{\mathbf{x}}\cos\phi + \hat{\mathbf{y}}\sin\phi \tag{C.4}$$

$$\hat{\phi} = \hat{\mathbf{y}}\cos\phi - \hat{\mathbf{x}}\sin\phi \tag{C.5}$$

$$\hat{\mathbf{z}} = \hat{\mathbf{z}} \tag{C.6}$$

Using the above expressions, we can derive the following nine relationships:

$$\frac{\partial \hat{\mathbf{r}}}{\partial r} = 0 \tag{C.7}$$

$$\frac{\partial \hat{\mathbf{r}}}{\partial \phi} = \hat{\mathbf{y}}\cos\phi - \hat{\mathbf{x}}\sin\phi = \hat{\phi} \tag{C.8}$$

$$\frac{\partial \hat{\mathbf{r}}}{\partial z} = 0 \tag{C.9}$$

$$\frac{\partial \hat{\phi}}{\partial r} = 0 \tag{C.10}$$

$$\frac{\partial \hat{\phi}}{\partial \phi} = -\hat{\mathbf{x}}\cos\phi - \hat{\mathbf{y}}\sin\phi = -\hat{\mathbf{r}} \tag{C.11}$$

$$\frac{\partial \hat{\phi}}{\partial z} = 0 \tag{C.12}$$

$$\frac{\partial \hat{\mathbf{z}}}{\partial r} = 0 \tag{C.13}$$

$$\frac{\partial \hat{\mathbf{z}}}{\partial \phi} = 0 \tag{C.14}$$

$$\frac{\partial \hat{\mathbf{z}}}{\partial z} = 0 \tag{C.15}$$

The two coordinate systems are linked by the Jacobian:

$$\mathbf{J} = \begin{bmatrix} \frac{\partial x}{\partial r} & \frac{\partial x}{\partial \phi} & \frac{\partial x}{\partial z} \\ \frac{\partial y}{\partial r} & \frac{\partial y}{\partial \phi} & \frac{\partial y}{\partial z} \\ \frac{\partial z}{\partial r} & \frac{\partial z}{\partial \phi} & \frac{\partial z}{\partial z} \end{bmatrix} = \begin{bmatrix} \cos\phi & -r\sin\phi & 0 \\ \sin\phi & r\cos\phi & 0 \\ 0 & 0 & 1 \end{bmatrix} \tag{C.16}$$

and the inverse of the Jacobian is:

$$\mathbf{J}^{-1} = \begin{bmatrix} \frac{\partial r}{\partial x} & \frac{\partial r}{\partial y} & \frac{\partial r}{\partial z} \\ \frac{\partial \phi}{\partial x} & \frac{\partial \phi}{\partial y} & \frac{\partial \phi}{\partial z} \\ \frac{\partial z}{\partial x} & \frac{\partial z}{\partial y} & \frac{\partial z}{\partial z} \end{bmatrix} = \begin{bmatrix} \cos\phi & \sin\phi & 0 \\ -\frac{\sin\phi}{r} & \frac{\cos\phi}{r} & 0 \\ 0 & 0 & 1 \end{bmatrix} \tag{C.17}$$

Now, the gradient of the pressure, for example, in the spatial domain can be mapped from cartesian to cylindrical coordinate systems:

$$\begin{aligned}\frac{\partial p}{\partial \mathbf{x}} &= \left(\frac{\partial p}{\partial r}\frac{\partial r}{\partial x}+\frac{\partial p}{\partial \phi}\frac{\partial \phi}{\partial x}+\frac{\partial p}{\partial z}\frac{\partial z}{\partial x}\right)\hat{\mathbf{x}} \\ &+\left(\frac{\partial p}{\partial r}\frac{\partial r}{\partial y}+\frac{\partial p}{\partial \phi}\frac{\partial \phi}{\partial y}+\frac{\partial p}{\partial z}\frac{\partial z}{\partial y}\right)\hat{\mathbf{y}} \\ &+\left(\frac{\partial p}{\partial r}\frac{\partial r}{\partial z}+\frac{\partial p}{\partial \phi}\frac{\partial \phi}{\partial z}+\frac{\partial p}{\partial z}\frac{\partial z}{\partial z}\right)\hat{\mathbf{z}} \end{aligned} \tag{C.18}$$

Substituting the relevant terms from Equation C.17:

$$\frac{\partial p}{\partial \mathbf{x}} = \left(\frac{\partial p}{\partial r}\cos\phi - \frac{\partial p}{\partial \phi}\frac{\sin\phi}{r}\right)\hat{\mathbf{x}} + \left(\frac{\partial p}{\partial r}\sin\phi + \frac{\partial p}{\partial \phi}\frac{\cos\phi}{r}\right)\hat{\mathbf{y}} + \frac{\partial p}{\partial z}\hat{\mathbf{z}} \tag{C.19}$$

Grouping like terms:

$$\frac{\partial p}{\partial \mathbf{x}} = \frac{\partial p}{\partial r}\left(\hat{\mathbf{x}}\cos\phi + \hat{\mathbf{y}}\sin\phi\right) + \frac{\partial p}{\partial \phi}\frac{1}{r}\left(-\hat{\mathbf{x}}\sin\phi + \hat{\mathbf{y}}\cos\phi\right) + \frac{\partial p}{\partial z}\hat{\mathbf{z}} \tag{C.20}$$

Simplifying using the unit vectors in Equations C.4 - C.6 we arrive at the gradient of the pressure expressed in a cylindrical coordinate system:

$$\frac{\partial p}{\partial \mathbf{x}} = \frac{\partial p}{\partial r}\hat{\mathbf{r}} + \frac{1}{r}\frac{\partial p}{\partial \phi}\hat{\phi} + \frac{\partial p}{\partial z}\hat{\mathbf{z}} \tag{C.21}$$

Hence, the divergence of the pressure is found from:

$$\nabla\cdot\mathbf{p} = \left(\frac{\partial}{\partial r}\hat{\mathbf{r}} + \frac{1}{r}\frac{\partial}{\partial \phi}\hat{\phi} + \frac{\partial}{\partial z}\hat{\mathbf{z}}\right)\cdot\left(p_r\hat{\mathbf{r}} + p_\phi\hat{\phi} + p_z\hat{\mathbf{z}}\right) \tag{C.22}$$

where the derivatives must be taken before the dot product, i.e. :

$$\begin{aligned}\nabla\cdot\mathbf{p} &= \frac{\partial \mathbf{p}}{\partial r}\hat{\mathbf{r}} + \frac{1}{r}\frac{\partial \mathbf{p}}{\partial \phi}\hat{\phi} + \frac{\partial \mathbf{p}}{\partial z}\hat{\mathbf{z}} \\ &= \hat{\mathbf{r}}\left(\frac{\partial p_r}{\partial r}\hat{\mathbf{r}} + \frac{\partial p_\phi}{\partial r}\hat{\phi} + \frac{\partial p_z}{\partial r}\hat{\mathbf{z}} + p_r\frac{\partial \hat{\mathbf{r}}}{\partial r} + p_\phi\frac{\partial \hat{\phi}}{\partial r} + p_z\frac{\partial \hat{\mathbf{z}}}{\partial r}\right) \\ &\quad + \frac{\hat{\phi}}{r}\left(\frac{\partial p_r}{\partial \phi}\hat{\mathbf{r}} + \frac{\partial p_\phi}{\partial \phi}\hat{\phi} + \frac{\partial p_z}{\partial \phi}\hat{\mathbf{z}} + p_r\frac{\partial \hat{\mathbf{r}}}{\partial \phi} + p_\phi\frac{\partial \hat{\phi}}{\partial \phi} + p_z\frac{\partial \hat{\mathbf{z}}}{\partial \phi}\right) \\ &\quad + \hat{\mathbf{z}}\left(\frac{\partial p_r}{\partial z}\hat{\mathbf{r}} + \frac{\partial p_\phi}{\partial z}\hat{\phi} + \frac{\partial p_z}{\partial z}\hat{\mathbf{z}} + p_r\frac{\partial \hat{\mathbf{r}}}{\partial z} + p_\phi\frac{\partial \hat{\phi}}{\partial z} + p_z\frac{\partial \hat{\mathbf{z}}}{\partial z}\right)\end{aligned} \tag{C.23}$$

Using the nine relationships derived earlier in Equations C.7 - C.15:

$$\begin{aligned}\nabla\cdot\mathbf{p} &= \hat{\mathbf{r}}\left(\frac{\partial p_r}{\partial r}\hat{\mathbf{r}}+\frac{\partial p_\phi}{\partial r}\hat{\phi}+\frac{\partial p_z}{\partial r}\hat{\mathbf{z}}\right)\\ &\quad+\frac{\hat{\phi}}{r}\left(\frac{\partial p_r}{\partial \phi}\hat{\mathbf{r}}+\frac{\partial p_\phi}{\partial \phi}\hat{\phi}+\frac{\partial p_z}{\partial \phi}\hat{\mathbf{z}}+p_r\hat{\phi}-p_\phi\hat{\mathbf{r}}\right)\\ &\quad+\hat{\mathbf{z}}\left(\frac{\partial p_r}{\partial z}\hat{\mathbf{r}}+\frac{\partial p_\phi}{\partial z}\hat{\phi}+\frac{\partial p_z}{\partial z}\hat{\mathbf{z}}\right)\end{aligned} \tag{C.24}$$

Recognising that the product of a unit vector with itself is one, the product of two different unit vectors is zero, and using the product rule, the above expression simplifies to:

$$\begin{aligned}\nabla\cdot\mathbf{p} &= \frac{\partial p_r}{\partial r}+\frac{1}{r}\left(\frac{\partial p_\phi}{\partial \phi}+p_r\right)+\frac{\partial p_z}{\partial z}\\ &= \left(\frac{\partial p_r}{\partial r}+\frac{p_r}{r}\right)+\frac{1}{r}\frac{\partial p_\phi}{\partial \phi}+\frac{\partial p_z}{\partial z}\\ &= \frac{1}{r}\frac{\partial}{\partial r}(p_r r)+\frac{1}{r}\frac{\partial p_\phi}{\partial \phi}+\frac{\partial p_z}{\partial z}\end{aligned} \tag{C.25}$$

Hence, an extra term requires to be calculated when in cylindrical coordinates. Following a similar procedure, the divergence of the velocity in cylindrical coordinates is:

$$\nabla\cdot\mathbf{v}=\frac{1}{r}\frac{\partial}{\partial r}(v_r r)+\frac{1}{r}\frac{\partial v_\phi}{\partial \phi}+\frac{\partial v_z}{\partial z} \tag{C.26}$$

However, there is no tangential flow and therefore $v_\phi = 0$, thus:

$$\nabla\cdot\mathbf{v}=\frac{1}{r}\frac{\partial}{\partial r}(v_r r)+\frac{\partial v_z}{\partial z} \tag{C.27}$$

Appendix D

Full Axisymmetric Weak Form of the Navier-Stokes Equations

Conservation of Mass

From Equation 4.14, the *weak form* of the conservation of mass is:

$$R_v(\mathbf{v},\hat{\mathbf{v}}) = \int_{V(\mathbf{x})} \mathbf{w_p} tr\left(\frac{\partial \mathbf{v}}{\partial \mathbf{x}}\right) dV \tag{D.1}$$

An additional term due to axisymmetric divergence of velocity, see Equation 4.31, is required:

$$R_v(\mathbf{v},\hat{\mathbf{v}}) = \int_{V(\mathbf{x})} \mathbf{w_p} tr\left(\frac{\partial \mathbf{v}}{\partial \mathbf{x}}\right) dV + \int_{V(\mathbf{x})} \mathbf{w_p} \cdot \left(\frac{v_r}{r}\right)_r dV \tag{D.2}$$

where the subscript $(\ldots)_r$ denotes only the radial component is required. Applying Equation 4.8 to map from spatial to reference domains:

$$R_v(\mathbf{v},\hat{\mathbf{v}}) = \int_{V} \mathbf{w_p} tr\left(\frac{\partial \mathbf{v}}{\partial \chi} - \frac{\Delta t}{2}\frac{\partial \mathbf{v}}{\partial \chi}\frac{\partial \delta\hat{\mathbf{v}}}{\partial \chi}\right) dV + \int_{V} \mathbf{w_p} \cdot \left(\frac{v_r}{r}\right)_r dV \tag{D.3}$$

Expanding and applying Equation 4.1:

$$R_v(\mathbf{v},\hat{\mathbf{v}}) = \int_V \mathbf{w_p} tr\left(\frac{\partial \mathbf{v}_i}{\partial \chi}\right) dV + \int_V \mathbf{w_p} tr\left(\frac{\partial \delta\mathbf{v}}{\partial \chi}\right) dV - \int_V \mathbf{w_p} tr\left(\frac{\Delta t}{2}\frac{\partial \mathbf{v}_i}{\partial \chi}\frac{\partial \delta\mathbf{v}}{\partial \chi}\right) dV + \int_V \mathbf{w_p}\cdot\left(\frac{v_i}{r}\right)_r dV + \int_V \mathbf{w_p}\cdot\left(\frac{\delta v}{r}\right)_r dV \quad \text{(D.4)}$$

Integrating from 0 to $2\pi r$ using Equation 4.35:

$$\begin{aligned} R_v(\mathbf{v},\hat{\mathbf{v}}) = {} & 2\pi\int_r\int_z \mathbf{w_p} r_n tr\left(\frac{\partial \mathbf{v}_i}{\partial \chi}\right) drdz + \Delta t\pi\int_r\int_z \mathbf{w_p} tr\left(\frac{\partial \mathbf{v}_i}{\partial \chi}\right)(\delta\hat{\mathbf{v}})_r drdz \\ & + 2\pi\int_r\int_z \mathbf{w_p} r_n tr\left(\frac{\partial \delta\mathbf{v}}{\partial \chi}\right) dV r dz \\ & - 2\pi\int_r\int_z \mathbf{w_p} r_n tr\left(\frac{\Delta t}{2}\frac{\partial \mathbf{v}_i}{\partial \chi}\frac{\partial \delta\mathbf{v}}{\partial \chi}\right) drdz + 2\pi\int_r\int_z \mathbf{w_p}\cdot(v_i)_r drdz \\ & + 2\pi\int_r\int_z \mathbf{w_p}\cdot(\delta v)_r drdz \end{aligned} \quad \text{(D.5)}$$

Let:

$$\mathbf{f_{pv}} = 2\pi\int_r\int_z \mathbf{w_p} r_n \frac{\partial \mathbf{v}_i}{\partial \chi} : \mathbf{I}\, drdz \quad \text{(D.6)}$$

$$\mathbf{K_{pv}^{fr}} = \Delta t\pi\int_r\int_z \mathbf{w_p}\frac{\partial \mathbf{v}_i}{\partial \chi} : \mathbf{I}\mathbf{N_r}\underline{\delta\hat{\mathbf{v}}} drdz \quad \text{(D.7)}$$

$$\mathbf{K_{pv}} = 2\pi\int_r\int_z \mathbf{w_p} r_n \frac{\partial \mathbf{N}}{\partial \chi} : \mathbf{I}\underline{\delta\mathbf{v}} drdz \quad \text{(D.8)}$$

$$\mathbf{K_{p\hat{v}}} = -2\pi\int_r\int_z \mathbf{w_p} r_n \frac{\Delta t}{2}\left[\frac{\partial \mathbf{v}_i}{\partial \chi}\right]^{\mathrm{T}} : \frac{\partial \mathbf{N}}{\partial \chi}\underline{\delta\hat{\mathbf{v}}} drdz \quad \text{(D.9)}$$

$$\mathbf{f_{pv}^{axi}} = 2\pi\int_r\int_z \mathbf{w_p}\cdot(v_i)_r drdz \quad \text{(D.10)}$$

$$\mathbf{K_{pv}^{axi}} = 2\pi\int_r\int_z \mathbf{w_p}\cdot(\mathbf{N_r})\,\underline{\delta\mathbf{v}} drdz \quad \text{(D.11)}$$

Therefore:

$$\left(\mathbf{K_{pv}} + \mathbf{K_{pv}^{axi}}\right)\underline{\delta\mathbf{v}} + \left(\mathbf{K_{p\hat{v}}} + \mathbf{K_{pv}^{fr}}\right)\underline{\delta\hat{\mathbf{v}}} = -\left(\mathbf{f_{pv}} + \mathbf{f_{pv}^{axi}}\right) \quad \text{(D.12)}$$

Conservation of Momentum

From Equation 4.15, the *weak form* of the conservation of momentum is:

$$R_v(\mathbf{v},\hat{\mathbf{v}},p) = \int_{V(\mathbf{x})} \rho \mathbf{w_v}\cdot\mathbf{a} - tr\left(\frac{\partial \mathbf{w_v}}{\partial \mathbf{x}}\right) p + 2\mu\left(\frac{\partial \mathbf{w_v}}{\partial \mathbf{x}} : \mathbf{e}\right) - \mathbf{w_v}\cdot\mathbf{b}\, dV \tag{D.13}$$

Additional terms due to axisymmetric divergence of pressure and divergence of velocity, see Equations 4.30 and 4.31, are required:

$$\begin{aligned} R_v(\mathbf{v},\hat{\mathbf{v}},p) &= \int_{V(\mathbf{x})} \rho \mathbf{w_v}\cdot\mathbf{a} - tr\left(\frac{\partial \mathbf{w_v}}{\partial \mathbf{x}}\right) p + 2\mu\left(\frac{\partial \mathbf{w_v}}{\partial \mathbf{x}} : \mathbf{e}\right) - \mathbf{w_v}\cdot\mathbf{b}\, dV \\ &\quad - \int_{V(\mathbf{x})} w_v \cdot \frac{p_r}{r} dV + \int_{V(\mathbf{x})} 2\mu\left(w_v\cdot\frac{v_r}{r}\right) dV \end{aligned} \tag{D.14}$$

Applying Equation 4.8 to map from spatial to reference domains:

$$\begin{aligned} R_v(\mathbf{v},\hat{\mathbf{v}},p) &= \int_{V} \rho \mathbf{w_v}\cdot\mathbf{a} - tr\left(\frac{\partial \mathbf{w_v}}{\partial \chi} - \frac{\Delta t}{2}\frac{\partial \mathbf{w_v}}{\partial \chi}\frac{\partial \delta\hat{\mathbf{v}}}{\partial \chi}\right) p + 2\mu\left(\frac{\partial \mathbf{w_v}}{\partial \chi} - \frac{\Delta t}{2}\frac{\partial \mathbf{w_v}}{\partial \chi}\frac{\partial \delta\hat{\mathbf{v}}}{\partial \chi}\right) : \mathbf{e} \\ &\quad - \mathbf{w_v}\cdot\mathbf{b}\, dV - \int_{V} w_v \cdot \frac{p_r}{r} dV + \int_{V} 2\mu\left(w_v\cdot\frac{v_r}{r}\right) dV \end{aligned} \tag{D.15}$$

Expanding and applying Equations 4.2 and 4.18:

$$\begin{aligned} R_v(\mathbf{v},\hat{\mathbf{v}},p) &= \int_{V} \rho \mathbf{w_v}\cdot\mathbf{a} - tr\left(\frac{\partial \mathbf{w_v}}{\partial \chi}\right) p_i - tr\left(\frac{\partial \mathbf{w_v}}{\partial \chi}\right) \delta p_i + tr\left(\frac{\Delta t}{2}\frac{\partial \mathbf{w_v}}{\partial \chi}\frac{\partial \delta\hat{\mathbf{v}}}{\partial \chi}\right) p_i \\ &\quad + 2\mu\left(\frac{\partial \mathbf{w_v}}{\partial \chi}\right) : \mathbf{e}_i + 2\mu\left(\frac{\partial \mathbf{w_v}}{\partial \chi}\right) : \delta\mathbf{e} + 2\mu\left(\frac{\partial \mathbf{w_v}}{\partial \chi}\right) : \delta\hat{\mathbf{e}} \\ &\quad - 2\mu\left(\frac{\Delta t}{2}\frac{\partial \mathbf{w_v}}{\partial \chi}\frac{\partial \delta\hat{\mathbf{v}}}{\partial \chi}\right) : \mathbf{e}_i - \mathbf{w_v}\cdot\mathbf{b}\, dV - \int_{V}\left(w_v\cdot\frac{p_i}{r}\right)_r dV \\ &\quad - \int_{V}\left(w_v\cdot\frac{\delta p}{r}\right)_r dV + \int_{V} 2\mu\left(w_v\cdot\frac{v_i}{r}\right)_r dV \\ &\quad + \int_{V} 2\mu\left(w_v\cdot\frac{\delta v}{r}\right)_r dV \end{aligned} \tag{D.16}$$

Integrating from 0 to $2\pi r$ using Equations 4.35 and 4.37:

$$\begin{aligned}
R_v(\mathbf{v},\hat{\mathbf{v}},p) &= 2\pi\int_r\int_z r_n\rho\mathbf{w}_\mathbf{v}\cdot\mathbf{a}drdz+\Delta t\pi\int_r\int_z\rho\mathbf{w}_\mathbf{v}\cdot\mathbf{a}\left(\delta\hat{\mathbf{v}}\right)_r drdz \\
&\quad -2\pi\int_r\int_z r_n tr\left(\frac{\partial\mathbf{w}_\mathbf{v}}{\partial\chi}\right)p_i drdz-\Delta t\pi\int_r\int_z tr\left(\frac{\partial\mathbf{w}_\mathbf{v}}{\partial\chi}\right)p_i\left(\delta\hat{\mathbf{v}}\right)_r drdz \\
&\quad -2\pi\int_r\int_z r_n tr\left(\frac{\partial\mathbf{w}_\mathbf{v}}{\partial\chi}\right)\delta p drdz+2\pi\int_r\int_z r_n tr\left(\frac{\Delta t}{2}\frac{\partial\mathbf{w}_\mathbf{v}}{\partial\chi}\frac{\partial\delta\hat{\mathbf{v}}}{\partial\chi}\right)p_i drdz \\
&\quad +2\pi\int_r\int_z 2\mu r_n\left(\frac{\partial\mathbf{w}_\mathbf{v}}{\partial\chi}\right):\mathbf{e}_i drdz+\Delta t\pi\int_r\int_z 2\mu\left(\frac{\partial\mathbf{w}_\mathbf{v}}{\partial\chi}\right):\mathbf{e}_i\left(\delta\hat{\mathbf{v}}\right)_r drdz \\
&\quad +2\pi\int_r\int_z 2\mu r_n\left(\frac{\partial\mathbf{w}_\mathbf{v}}{\partial\chi}\right):\delta\mathbf{e}drdz+2\pi\int_r\int_z 2\mu r_n\left(\frac{\partial\mathbf{w}_\mathbf{v}}{\partial\chi}\right):\delta\hat{\mathbf{e}}drdz \\
&\quad -2\pi\int_r\int_z 2\mu r_n\left(\frac{\Delta t}{2}\frac{\partial\mathbf{w}_\mathbf{v}}{\partial\chi}\frac{\partial\delta\hat{\mathbf{v}}}{\partial\chi}\right):\mathbf{e}_i drdz-2\pi\int_r\int_z r_n\left(\mathbf{w}_\mathbf{v}\cdot\mathbf{b}\right)drdz \\
&\quad -\Delta t\pi\int_r\int_z\left(\mathbf{w}_\mathbf{v}\cdot\mathbf{b}\right)\left(\delta\hat{\mathbf{v}}\right)_r drdz-2\pi\int_r\int_z\left(w_v\cdot p_i\right)_r drdz \\
&\quad -2\pi\int_r\int_z\left(w_v\cdot\delta p\right)_r drdz+2\pi\int_r\int_z\frac{2\mu}{r_n}\left(w_v\cdot v_i\right)_r drdz \\
&\quad -2\pi\int_r\int_z\frac{2\mu}{r_n^2}\left(w_v\cdot v_i\right)_r\left(\frac{\Delta t}{2}\delta\hat{\mathbf{v}}\right)drdz+2\pi\int_r\int_z\frac{2\mu}{r_n}\left(w_v\cdot\delta v\right)_r drdz \qquad \text{(D.17)}
\end{aligned}$$

Expanding the first two terms using the full form of the acceleration from Equation 4.13:

$$\begin{aligned}
2\pi\int_r\int_z r_n\rho\mathbf{w}_\mathbf{v}\cdot\mathbf{a}drdz &= 2\pi\int_r\int_z r_n\rho\mathbf{w}_\mathbf{v}\cdot\left(\frac{\Delta\mathbf{v}}{\Delta t}+\frac{\delta\mathbf{v}}{\Delta t}+\frac{\partial\mathbf{v}_i}{\partial\chi}\left(\mathbf{v}_i-\hat{\mathbf{v}}_i\right)\right)drdz \\
&\quad +2\pi\int_r\int_z r_n\rho\mathbf{w}_\mathbf{v}\cdot\left(\frac{\partial\mathbf{v}_i}{\partial\chi}\left(\delta\mathbf{v}-\delta\hat{\mathbf{v}}\right)\right)drdz \\
&\quad +2\pi\int_r\int_z r_n\rho\mathbf{w}_\mathbf{v}\cdot\left(\frac{\partial\delta\mathbf{v}}{\partial\chi}\left(\mathbf{v}_i-\hat{\mathbf{v}}_i\right)\right)drdz \\
&\quad +2\pi\int_r\int_z r_n\rho\mathbf{w}_\mathbf{v}\cdot\left(\frac{\Delta t}{2}\frac{\partial\mathbf{v}_i}{\partial\chi}\frac{\partial\delta\hat{\mathbf{v}}}{\partial\chi}\left(\hat{\mathbf{v}}_i-\mathbf{v}_i\right)\right)drdz \qquad \text{(D.18)}
\end{aligned}$$

$$\Delta t\pi\int_r\int_z\rho\mathbf{w}_\mathbf{v}\cdot\mathbf{a}\left(\delta\hat{\mathbf{v}}\right)_r drdz=\Delta t\pi\int_r\int_z\rho\mathbf{w}_\mathbf{v}\cdot\left(\frac{\Delta\mathbf{v}}{\Delta t}+\frac{\partial\mathbf{v}_i}{\partial\chi}\left(\mathbf{v}_i-\hat{\mathbf{v}}_i\right)\right)\left(\delta\hat{\mathbf{v}}\right)_r drdz \qquad \text{(D.19)}$$

Let:

$$\mathbf{f_{vm}} = 2\pi \int_r \int_z r_n \rho \mathbf{w_v} \cdot \left(\frac{\Delta \mathbf{v}}{\Delta t} + \frac{\partial \mathbf{v}_i}{\partial \chi} (\mathbf{v}_i - \hat{\mathbf{v}}_i) \right) - r_n (\mathbf{w_v} \cdot \mathbf{b}) \, dr dz \tag{D.20}$$

$$\mathbf{M_{vv}} = 2\pi \int_r \int_z r_n \rho \mathbf{w_v} \cdot \left(\frac{\mathbf{N}}{\Delta t} + \frac{\partial \mathbf{v}_i}{\partial \chi} \mathbf{N} + \frac{\partial \mathbf{N}}{\partial \chi} (\mathbf{v}_i - \hat{\mathbf{v}}_i) \right) \underline{\delta \mathbf{v}} dr dz \tag{D.21}$$

$$\mathbf{M_{v\hat{v}}} = 2\pi \int_r \int_z r_n \rho \mathbf{w_v} \cdot \left(\frac{\Delta t}{2} \frac{\partial \mathbf{v}_i}{\partial \chi} \frac{\partial \mathbf{N}}{\partial \chi} (\hat{\mathbf{v}}_i - \mathbf{v}_i) - \frac{\partial \mathbf{v}_i}{\partial \chi} \mathbf{N} \right) \underline{\delta \hat{\mathbf{v}}} dr dz \tag{D.22}$$

$$\mathbf{K_{vm}^{fr}} = \Delta t \pi \int_r \int_z \left(\rho \mathbf{w_v} \cdot \left(\frac{\Delta \mathbf{v}}{\Delta t} + \frac{\partial \mathbf{v}_i}{\partial \chi} (\mathbf{v}_i - \hat{\mathbf{v}}_i) \right) - \mathbf{w_v} \cdot \mathbf{b} \right) \mathbf{N_r} \underline{\delta \hat{\mathbf{v}}} dr dz \tag{D.23}$$

$$\mathbf{f_{vp}} = -2\pi \int_r \int_z r_n \frac{\partial \mathbf{w_v}}{\partial \chi} : \mathbf{I} p_i dr dz \tag{D.24}$$

$$\mathbf{K_{vp}^{fr}} = -\Delta t \pi \int_r \int_z \left(\frac{\partial \mathbf{w_v}}{\partial \chi} : \mathbf{I} p_i \right) \mathbf{N_r} \underline{\delta \hat{\mathbf{v}}} dr dz \tag{D.25}$$

$$\mathbf{K_{vp}} = -2\pi \int_r \int_z r_n \frac{\partial \mathbf{w_v}}{\partial \chi} : \mathbf{I} \mathbf{N} \underline{\delta p} dr dz \tag{D.26}$$

$$\mathbf{K_{vp\hat{v}}} = 2\pi \int_r \int_z r_n \frac{\Delta t}{2} \left[\frac{\partial \mathbf{w_v}}{\partial \chi} \right]^{\mathrm{T}} : p_i \frac{\partial \mathbf{N}}{\partial \chi} \underline{\delta \hat{\mathbf{v}}} dr dz \tag{D.27}$$

$$\mathbf{f_{vv}} = 2\pi \int_r \int_z 2\mu r_n \frac{\partial \mathbf{w_v}}{\partial \chi} : \mathbf{e}_i dr dz \tag{D.28}$$

$$\mathbf{K_{vv}^{fr}} = \Delta t \pi \int_r \int_z \left(2\mu \frac{\partial \mathbf{w_v}}{\partial \chi} : \mathbf{e}_i \right) \mathbf{N_r} \underline{\delta \hat{\mathbf{v}}} dr dz \tag{D.29}$$

$$\mathbf{K_{vv}} = 2\pi \int_r \int_z 2\mu r_n \frac{\partial \mathbf{w_v}}{\partial \chi} : \delta \mathbf{e} dr dz \tag{D.30}$$

$$\mathbf{K_{v\hat{v}}} = 2\pi \int_r \int_z 2\mu r_n \frac{\partial \mathbf{w_v}}{\partial \chi} : \delta \hat{\mathbf{e}} dr dz - 2\pi \int_r \int_z 2\mu r_n \frac{\Delta t}{2} \left(\frac{\partial \mathbf{w_v}}{\partial \chi} (\mathbf{e}_i)^{\mathrm{T}} \right) : \frac{\partial \mathbf{N}}{\partial \chi} \underline{\delta \hat{\mathbf{v}}} dr dz \tag{D.31}$$

$$\mathbf{f_{vp}^{axi}} = -2\pi \int_r \int_z (w_v \cdot p_i)_r dr dz \tag{D.32}$$

$$\mathbf{K_{vp}^{axi}} = -2\pi \int_r \int_z (w_v \cdot \mathbf{N_r}) \underline{\delta p} dr dz \tag{D.33}$$

$$\mathbf{f_{vv}^{axi}} = 2\pi \int_r \int_z \frac{2\mu}{r_n} (w_v \cdot v_i)_r dr dz \tag{D.34}$$

$$\mathbf{K_{v\hat{v}}^{axi}} = -2\pi \int_r \int_z \frac{\mu \Delta t}{r_n^2} (w_v \cdot v_i)_r \mathbf{N_r} \underline{\delta \hat{\mathbf{v}}} dr dz \tag{D.35}$$

$$\mathbf{K_{vv}^{axi}} = 2\pi \int_r \int_z \frac{2\mu}{r_n} (w_v \cdot \mathbf{N_r}) \underline{\delta \mathbf{v}} dr dz \tag{D.36}$$

Therefore:

$$\frac{1}{2\Delta t}\left(\mathbf{M_{vv}}\underline{\delta \mathbf{v}}+\mathbf{M_{v\hat{v}}}\underline{\delta \hat{\mathbf{v}}}\right)+\left(\mathbf{K_{vv}}+\mathbf{K_{vv}^{axi}}\right)\underline{\delta \mathbf{v}}+\left(\mathbf{K_{vp}}+\mathbf{K_{vp}^{axi}}\right)\underline{\delta p}$$

$$+\left(\mathbf{K_{vp\hat{v}}}+\mathbf{K_{v\hat{v}}}+\mathbf{K_{v\hat{v}}^{axi}}+\mathbf{K_{vv}^{fr}}+\mathbf{K_{vm}^{fr}}+\mathbf{K_{vp}^{fr}}\right)\underline{\delta \hat{\mathbf{v}}}$$

$$=-\left(\mathbf{f_{vv}}+\mathbf{f_{vv}^{axi}}+\mathbf{f_{vm}}+\mathbf{f_{vp}}+\mathbf{f_{vp}^{axi}}\right) \tag{D.37}$$

Final System of Governing Equations

Including the terms derived for pressure stabilisation in Chapter 6, Equation 6.16, and combining with Equations D.12 and D.37, in diagrammatic form, the system of governing equations is shown below:

$$\begin{bmatrix} \mathbf{A_{vv}} & \mathbf{A_{vp}} & \mathbf{A_{v\hat{v}}} \\ \mathbf{A_{pv}} & \mathbf{A_{pp}} & \mathbf{A_{p\hat{v}}} \\ \mathbf{A_{\hat{v}v}} & \mathbf{A_{\hat{v}p}} & \mathbf{A_{\hat{v}\hat{v}}} \end{bmatrix} \begin{bmatrix} \underline{\delta \mathbf{v}} \\ \underline{\delta \mathbf{p}} \\ \underline{\delta \hat{\mathbf{v}}} \end{bmatrix} = - \begin{bmatrix} \mathbf{F_v} \\ \mathbf{F_p} \\ \mathbf{F_{\hat{v}}} \end{bmatrix}$$

Figure D.1: Diagrammatic form of the system of governing equations

where:

$$\mathbf{A_{vv}}=\frac{\mathbf{M_{vv}}}{2\Delta t}+\mathbf{K_{vv}}+\mathbf{K_{vv}^{axi}} \tag{D.38}$$

$$\mathbf{A_{vp}}=\mathbf{K_{vp}}+\mathbf{K_{vp}^{axi}} \tag{D.39}$$

$$\mathbf{A_{v\hat{v}}}=\frac{\mathbf{M_{v\hat{v}}}}{2\Delta t}+\mathbf{K_{v\hat{v}}}+\mathbf{K_{v\hat{v}}^{axi}}+\mathbf{K_{vp\hat{v}}}+\mathbf{K_{vv}^{fr}}+\mathbf{K_{vm}^{fr}}+\mathbf{K_{vp}^{fr}} \tag{D.40}$$

$$\mathbf{A_{pv}} = \mathbf{K_{pv}} + \mathbf{K_{pv}^{axi}} \tag{D.41}$$

$$\mathbf{A_{pp}} = \mathbf{K_{pp}^{s}} + \mathbf{K_{pp}^{b}} \tag{D.42}$$

$$\mathbf{A_{p\hat{v}}} = \mathbf{K_{p\hat{v}}} + \mathbf{K_{pv}^{fr}} + \mathbf{K_{p\hat{v}}^{s}} + \mathbf{K_{p\hat{v}}^{b}} + \mathbf{K_{pp}^{s,fr}} + \mathbf{K_{pp}^{b,fr}} + \mathbf{K_{pp}^{b,n}} \tag{D.43}$$

$$\mathbf{A_{\hat{v}p}} = 0 \tag{D.44}$$

$$\mathbf{F_{v}} = \mathbf{f_{vv}} + \mathbf{f_{vv}^{axi}} + \mathbf{f_{vm}} + \mathbf{f_{vp}} + \mathbf{f_{vp}^{axi}} \tag{D.45}$$

$$\mathbf{F_{p}} = \mathbf{f_{pv}} + \mathbf{f_{pv}^{axi}} + \mathbf{f_{pp}^{s}} + \mathbf{f_{pp}^{b}} \tag{D.46}$$

The first row of global system is reserved for momentum terms and the second row is reserved for mass terms and pressure stabilisation terms. In the third row, the term $\mathbf{A_{\hat{v}p}}$ is zero for all entries, the terms $\mathbf{A_{\hat{v}\hat{v}}}$ and $\mathbf{F_{\hat{v}}}$ are reserved for mesh improvement, and the term $\mathbf{A_{\hat{v}v}}$ is involved with the ALE formulation. Surface nodes are designated as Lagrangian nodes and for those nodes the diagonal terms (for example, $\hat{v}_x \times \hat{v}_x$) are set to 1 and the off diagonal terms (for example $v_x \times \hat{v}_x$) are set to -1 to reflect that the particle and mesh velocities are coupled and therefore move together.

Appendix E

The Surface Gradient, Metric Tensor and the Surface Tension Contribution

Surface Gradient

The following derivation is from Weatherburn [68]. A surface can be thought of as the locus of a point, and the position vector $\mathbf{r}$ of this is a function of two independent variables u, v. Any relation between these two variables represents a curve on the surface. Using subscript $[\ldots]_1$ to denote partial derivatives with respect to u and $[\ldots]_2$ to denote partial derivatives with respect to v, we can write:

$$\mathbf{r}_1 = \frac{\partial \mathbf{r}}{\partial u} \tag{E.1}$$

$$\mathbf{r}_2 = \frac{\partial \mathbf{r}}{\partial v} \tag{E.2}$$

$$\mathbf{r}_{11} = \frac{\partial^2 \mathbf{r}}{\partial u^2} \tag{E.3}$$

$$\mathbf{r}_{12} = \frac{\partial^2 \mathbf{r}}{\partial u \partial v} \tag{E.4}$$

$$\mathbf{r}_{22} = \frac{\partial^2 \mathbf{r}}{\partial v^2} \tag{E.5}$$

and so forth. Vector $\mathbf{r}_1$ is tangential to the curve $v = \text{const}$ at the point $\mathbf{r}$; for its direction is that of the displacement $d\mathbf{r}$, due to a variation du in the first variable only. Simplifying the

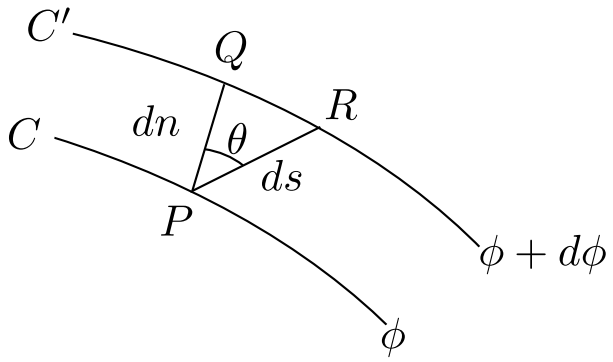

Figure E.1: Two consecutive curves

above:

$$\mathbf{E} = \mathbf{r}_1^2 = \mathbf{r}_{11} = \frac{\partial^2 \mathbf{r}}{\partial u^2} \tag{E.6}$$

$$\mathbf{G} = \mathbf{r}_2^2 = \mathbf{r}_{22} = \frac{\partial^2 \mathbf{r}}{\partial v^2} \tag{E.7}$$

$$\mathbf{F} = \mathbf{r}_1 \cdot \mathbf{r}_2 \tag{E.8}$$

$$\mathbf{H} = \mathbf{EG} - \mathbf{F}^2 \tag{E.9}$$

The quantities **E**, **F** and **G** are the fundamental magnitudes of the first order. Consider now a scalar function of position $\phi(u,v)$; the gradient of this function at any point P is a vector quantity whose direction is the direction on the surface at which P gives the maximum arc-rate of increase of ϕ and whose magnitude is this maximum rate of increase. Two consecutive level curves are denoted C, C', Figure E.1. These curves correspond to the values ϕ and $\phi + d\phi$ of the function, where $d\phi$ is positive. Let PQ be an element of the orthogonal trajectory of the level curves, intercepted between C, C', and let the length of this element be dn. Let ds be the length of PR, an element of arc of another curve through P, cutting C'. It can be seen that PQ is the shortest distance from P to the curve C'; the direction of PQ gives the maximum rate of increase of ϕ at P. Therefore, the gradient of ϕ at P has the direction PQ and the magnitude $d\phi/dn$, which will be denoted $\nabla\phi$.

Although $\nabla\phi$ is independent of any choice of variables, it is convenient to derive an expression for the function in terms of the coordinates u, v. Defining $\delta u, \delta v$ as an infinitesimal displacement along the curve $\phi(u,v) = \text{const}$:

$$\phi_1 \delta u + \phi_2 \delta v = 0 \tag{E.10}$$

Hence, a displacement du, dv orthogonal to this is given by:

$$\frac{du}{dv} = \frac{\mathbf{G}\phi_1 - \mathbf{F}\phi_2}{\mathbf{E}\phi_2 - \mathbf{F}\phi_1} \tag{E.11}$$

The vector $\mathbf{v}$ is parallel to $\nabla\phi$ and found from:

$$\mathbf{V} = (\mathbf{G}\phi_1 - \mathbf{F}\phi_2)\,\mathbf{r}_1 + (\mathbf{E}\phi_2 - \mathbf{F}\phi_1)\,\mathbf{r}_2 \tag{E.12}$$

The resolved part of this in the direction of $\mathbf{r}_1$ is equal to:

$$\begin{aligned} \frac{1}{\sqrt{\mathbf{E}}}\mathbf{r}_1 \cdot \mathbf{V} &= (\mathbf{G}\phi_1 - \mathbf{F}\phi_2)\frac{\mathbf{E}}{\sqrt{\mathbf{E}}} + (\mathbf{E}\phi_2 - \mathbf{F}\phi_1)\frac{\mathbf{F}}{\sqrt{\mathbf{E}}} \\ &= \frac{\mathbf{H}^2}{\sqrt{\mathbf{E}}}\phi_1 \\ &= \mathbf{H}^2\frac{1}{\sqrt{\mathbf{E}}}\frac{\partial\phi}{\partial u} \end{aligned} \tag{E.13}$$

which is equal to the product of $\mathbf{H}^2$ and the derivative of ϕ in the direction of $\mathbf{r}_1$. Hence:

$$\begin{aligned} \nabla\phi &= \frac{\mathbf{V}}{\mathbf{H}^2} \\ &= \frac{(\mathbf{G}\phi_1 - \mathbf{F}\phi_2)}{\mathbf{H}^2}\mathbf{r}_1 + \frac{(\mathbf{E}\phi_2 - \mathbf{F}\phi_1)}{\mathbf{H}^2}\mathbf{r}_2 \end{aligned} \tag{E.14}$$

This result can be obtained by operating the vectorial differential operator ∇ on the function ϕ:

$$\nabla = \frac{1}{\mathbf{H}^2}\mathbf{r}_1\left(\mathbf{G}\frac{\partial}{\partial u} - \mathbf{F}\frac{\partial}{\partial v}\right) + \frac{1}{\mathbf{H}^2}\mathbf{r}_2\left(\mathbf{E}\frac{\partial}{\partial v} - \mathbf{F}\frac{\partial}{\partial u}\right) \tag{E.15}$$

The definition of $\nabla\phi$ was independent of variables and therefore this operator is invariant. When the parametric curves are orthogonal, the operator takes a much simpler form as:

$$\mathbf{F} = \mathbf{r}_1 \cdot \mathbf{r}_2 = 0 \tag{E.16}$$

and therefore:

$$\mathbf{H}^2 = \mathbf{EG} \tag{E.17}$$

so that:

$$\nabla = \frac{1}{\mathbf{E}}\mathbf{r}_1\frac{\partial}{\partial u} + \frac{1}{\mathbf{G}}\mathbf{r}_2\frac{\partial}{\partial v} \tag{E.18}$$

$\mathbf{E}$ and $\mathbf{G}$ are the components of the metric tensor which we will rename A_{mt} and B_{mt}. Sub-

stituting in the forms for $\mathbf{r}_1$ and $\mathbf{r}_2$ from Equations E.1 and E.2, and calculating in the same coordinate system as the shape functions (ξ,θ) the surface gradient ∇_s is found from:

$$\nabla_s = \frac{1}{A_{mt}}\frac{\partial \mathbf{x}(\xi,\theta)}{\partial \xi}\frac{\partial}{\partial \xi} + \frac{1}{B_{mt}}\frac{\partial \mathbf{x}(\xi,\theta)}{\partial \theta}\frac{\partial}{\partial \theta} \tag{E.19}$$

The Metric Tensor

From Equation 5.13, the position of a single point on the line 1-2, Figure 5.7, can be expressed:

$$\begin{aligned}\mathbf{x}(\xi,\theta) &= \begin{bmatrix} \frac{1}{2}(1-\xi)\cos\theta & 0 & \frac{1}{2}(1+\xi)\cos\theta & 0 \\ \frac{1}{2}(1-\xi)\sin\theta & 0 & \frac{1}{2}(1+\xi)\sin\theta & 0 \\ 0 & \frac{1}{2}(1-\xi) & 0 & \frac{1}{2}(1+\xi) \end{bmatrix} \begin{bmatrix} r_1 \\ z_1 \\ r_2 \\ z_2 \end{bmatrix} \\ &= \begin{bmatrix} \frac{1}{2}r_1(1-\xi)\cos\theta + \frac{1}{2}r_2(1+\xi)\cos\theta \\ \frac{1}{2}r_1(1-\xi)\sin\theta + \frac{1}{2}r_2(1+\xi)\sin\theta \\ \frac{1}{2}z_1(1-\xi) + \frac{1}{2}z_2(1+\xi) \end{bmatrix}\end{aligned} \tag{E.20}$$

Taking the derivative of $\mathbf{x}$ in terms of both ξ and θ gives:

$$\frac{\partial \mathbf{x}}{\partial \xi} = \begin{bmatrix} -\frac{1}{2}r_1\cos\theta + \frac{1}{2}r_2\cos\theta \\ -\frac{1}{2}r_1\sin\theta + \frac{1}{2}r_2\sin\theta \\ -\frac{1}{2}z_1 + \frac{1}{2}z_2 \end{bmatrix} \tag{E.21}$$

$$\frac{\partial \mathbf{x}}{\partial \theta} = \begin{bmatrix} -\frac{1}{2}r_1(1-\xi)\sin\theta - \frac{1}{2}r_2(1+\xi)\sin\theta \\ \frac{1}{2}r_1(1-\xi)\cos\theta + \frac{1}{2}r_2(1+\xi)\cos\theta \\ 0 \end{bmatrix} \tag{E.22}$$

The components of the metric tensor are:

$$\begin{aligned} A_{\text{mt}} &= \frac{\partial \mathbf{x}}{\partial \xi} \cdot \frac{\partial \mathbf{x}}{\partial \xi} \\ &= \left(-\frac{1}{2} r_1 \cos\theta + \frac{1}{2} r_2 \cos\theta\right)^2 + \left(-\frac{1}{2} r_1 \sin\theta + \frac{1}{2} r_2 \sin\theta\right)^2 \\ &\quad + \left(-\frac{1}{2} z_1 + \frac{1}{2} z_2\right)^2 \\ &= \frac{1}{4}\left[(r_1 - r_2)^2 + (z_1 - z_2)^2\right] \end{aligned} \tag{E.23}$$

and:

$$\begin{aligned} B_{\text{mt}} &= \frac{\partial \mathbf{x}}{\partial \theta} \cdot \frac{\partial \mathbf{x}}{\partial \theta} \\ &= \left(-\frac{1}{2} r_1 (1-\xi) \sin\theta - \frac{1}{2} r_2 (1+\xi) \sin\theta\right)^2 \\ &\quad + \left(\frac{1}{2} r_1 (1-\xi) \cos\theta + \frac{1}{2} r_2 (1+\xi) \cos\theta\right)^2 \\ &= \frac{1}{4}\left[r_1 (1-\xi) + r_2 (1+\xi)\right]^2 \end{aligned} \tag{E.24}$$

Additionally, the derivative of the transverse of the shape function matrix for the surface of revolution generated by line 1-2 (Figure 5.7), in terms of firstly ξ and then θ gives:

$$\frac{\partial \mathbf{N}_{12}^{\text{T}}}{\partial \xi} = \begin{bmatrix} -\frac{1}{2}\cos\theta & -\frac{1}{2}\sin\theta & 0 \\ 0 & 0 & -\frac{1}{2} \\ \frac{1}{2}\cos\theta & \frac{1}{2}\sin\theta & 0 \\ 0 & 0 & \frac{1}{2} \end{bmatrix} \tag{E.25}$$

$$\frac{\partial \mathbf{N}_{12}^{\text{T}}}{\partial \theta} = \begin{bmatrix} -\frac{1}{2}(1-\xi)\sin\theta & \frac{1}{2}(1-\xi)\cos\theta & 0 \\ 0 & 0 & 0 \\ -\frac{1}{2}(1+\xi)\sin\theta & \frac{1}{2}(1+\xi)\cos\theta & 0 \\ 0 & 0 & 0 \end{bmatrix} \tag{E.26}$$

Surface Tension Contributions

The calculation of the surface tension force vector is:

$$\mathbf{F}^{\mathbf{ST}} = \int_{-1}^{1}\int_{0}^{2\pi}\left\{\frac{\sqrt{A_{\mathrm{mt}}B_{\mathrm{mt}}}}{A_{\mathrm{mt}}}\frac{\partial \mathbf{N}_{12}^{\mathrm{T}}}{\partial \xi}\frac{\partial \mathbf{x}(\xi,\theta)}{\partial \xi} + \frac{\sqrt{A_{\mathrm{mt}}B_{\mathrm{mt}}}}{B_{\mathrm{mt}}}\frac{\partial \mathbf{N}_{12}^{\mathrm{T}}}{\partial \theta}\frac{\partial \mathbf{x}(\xi,\theta)}{\partial \theta}\right\} d\xi\, d\theta \tag{E.27}$$

Examining the term $A_{\mathrm{mt}}B_{\mathrm{mt}}$ first:

$$A_{\mathrm{mt}}B_{\mathrm{mt}} = \frac{1}{16}\left[(r_1-r_2)^2+(z_1-z_2)^2\right]\left[r_1(1-\xi)+r_2(1+\xi)\right]^2 \tag{E.28}$$

$$\frac{\sqrt{A_{\mathrm{mt}}B_{\mathrm{mt}}}}{A_{\mathrm{mt}}} = \frac{r_1(1-\xi)+r_2(1+\xi)}{\sqrt{(r_1-r_2)^2+(z_1-z_2)^2}} = \frac{r_1(1-\xi)+r_2(1+\xi)}{L} \tag{E.29}$$

$$\frac{\sqrt{A_{\mathrm{mt}}B_{\mathrm{mt}}}}{B_{\mathrm{mt}}} = \frac{\sqrt{(r_1-r_2)^2+(z_1-z_2)^2}}{r_1(1-\xi)+r_2(1+\xi)} = \frac{L}{r_1(1-\xi)+r_2(1+\xi)} \tag{E.30}$$

where $L = \sqrt{(r_1-r_2)^2+(z_1-z_2)^2}$ is the length of the edge. Examining the first group of terms inside the double integral:

$$\begin{aligned}
\frac{\sqrt{A_{\mathrm{mt}}B_{\mathrm{mt}}}}{A_{\mathrm{mt}}}\frac{\partial \mathbf{N}_{12}^{\mathrm{T}}}{\partial \xi}\frac{\partial \mathbf{x}(\xi,\theta)}{\partial \xi} &= \frac{\sqrt{A_{\mathrm{mt}}B_{\mathrm{mt}}}}{A_{\mathrm{mt}}}\begin{bmatrix} -\frac{1}{2}\cos\theta & -\frac{1}{2}\sin\theta & 0 \\ 0 & 0 & -\frac{1}{2} \\ \frac{1}{2}\cos\theta & \frac{1}{2}\sin\theta & 0 \\ 0 & 0 & \frac{1}{2} \end{bmatrix} \\
&\quad \begin{bmatrix} -\frac{1}{2}r_1\cos\theta + \frac{1}{2}r_2\cos\theta \\ -\frac{1}{2}r_1\sin\theta + \frac{1}{2}r_2\sin\theta \\ -\frac{1}{2}z_1 + \frac{1}{2}z_2 \end{bmatrix} \\
&= \frac{\sqrt{A_{\mathrm{mt}}B_{\mathrm{mt}}}}{A_{\mathrm{mt}}}\frac{1}{4}\begin{bmatrix} r_1-r_2 \\ z_1-z_2 \\ r_2-r_1 \\ z_2-z_1 \end{bmatrix} \\
&= \frac{r_1(1-\xi)+r_2(1+\xi)}{L}\frac{1}{4}\begin{bmatrix} r_1-r_2 \\ z_1-z_2 \\ r_2-r_1 \\ z_2-z_1 \end{bmatrix}
\end{aligned} \tag{E.31}$$

Therefore, the double integral of this becomes:

$$\int_{-1}^{1}\int_{0}^{2\pi}\left\{\frac{\sqrt{A_{\mathrm{mt}}B_{\mathrm{mt}}}}{A_{\mathrm{mt}}}\frac{\partial \mathbf{N}_{12}^{\mathrm{T}}}{\partial \xi}\frac{\partial \mathbf{x}(\xi,\theta)}{\partial \xi}\right\}d\xi d\theta = \frac{\pi\gamma(r_1+r_2)}{L}\begin{bmatrix} r_1-r_2 \\ z_1-z_2 \\ r_2-r_1 \\ z_2-z_1 \end{bmatrix} \tag{E.32}$$

Examining now the second group of terms inside the double integral:

$$\begin{aligned}\frac{\sqrt{A_{\mathrm{mt}}B}}{B_{\mathrm{mt}}}\frac{\partial \mathbf{N}_{12}^{\mathrm{T}}}{\partial \theta}\frac{\partial \mathbf{x}(\xi,\theta)}{\partial \theta} &= \frac{\sqrt{A_{\mathrm{mt}}B_{\mathrm{mt}}}}{B_{\mathrm{mt}}}\begin{bmatrix} -\frac{1}{2}(1-\xi)\sin\theta & \frac{1}{2}(1-\xi)\cos\theta & 0 \\ 0 & 0 & 0 \\ -\frac{1}{2}(1+\xi)\sin\theta & \frac{1}{2}(1+\xi)\cos\theta & 0 \\ 0 & 0 & 0 \end{bmatrix} \\ &\quad \begin{bmatrix} -\frac{1}{2}r_1(1-\xi)\sin\theta - \frac{1}{2}r_2(1+\xi)\sin\theta \\ \frac{1}{2}r_1(1-\xi)\cos\theta + \frac{1}{2}r_2(1+\xi)\cos\theta \\ 0 \end{bmatrix}\end{aligned} \tag{E.33}$$

$$\begin{aligned}\frac{\sqrt{A_{\mathrm{mt}}B_{\mathrm{mt}}}}{B_{\mathrm{mt}}}\frac{\partial \mathbf{N}_{12}^{\mathrm{T}}}{\partial \theta}\frac{\partial \mathbf{x}(\xi,\theta)}{\partial \theta} &= \frac{\sqrt{A_{\mathrm{mt}}B_{\mathrm{mt}}}}{B_{\mathrm{mt}}}\frac{1}{4}\begin{bmatrix} r_1(1-\xi)^2 + r_2(1-\xi)(1+\xi) \\ 0 \\ r_1(1-\xi)(1+\xi) + r_2(1+\xi)^2 \\ 0 \end{bmatrix} \\ &= \frac{L}{r_1(1-\xi)+r_2(1+\xi)} \\ &\quad \frac{1}{4}\begin{bmatrix} r_1(1-\xi)^2 + r_2(1-\xi)(1+\xi) \\ 0 \\ r_1(1-\xi)(1+\xi) + r_2(1+\xi)^2 \\ 0 \end{bmatrix}\end{aligned} \tag{E.34}$$

Therefore, the double integral of this becomes:

$$\int_{-1}^{1}\int_{0}^{2\pi}\left\{\frac{\sqrt{A_{\mathrm{mt}}B_{\mathrm{mt}}}}{B_{\mathrm{mt}}}\frac{\partial \mathbf{N}_{12}^{\mathrm{T}}}{\partial\theta}\frac{\partial \mathbf{x}(\xi,\theta)}{\partial\theta}\right\}d\xi d\theta = \pi\gamma L\begin{bmatrix}1\\0\\1\\0\end{bmatrix} \tag{E.35}$$

Appendix F

Derivation of The Penalty Stiffness

For a point on the base of the droplet with coordinates (x_0, y_0), the closest point on a membrane defined by the equation $y = \sin(x)$ is the point (a, b), see Figure 8.7. The distance between these two nodes is calculated as:

$$d = \left[(x_0 - a)^2 + (y_0 - b)^2\right]^{\frac{1}{2}} \tag{F.1}$$

$$d^2 = \left[(x_0 - a)^2 + (y_0 - b)^2\right] \tag{F.2}$$

Following Equation 4.4, the coordinates of the point on the base of the droplet can be expressed as:

$$x_0 = x_n + \Delta t \left(v^i_{n+1}\right)^x + \frac{\Delta t}{2}\left(\delta v^{i+1}_{n+1}\right)^x \tag{F.3}$$

$$y_0 = y_n + \Delta t \left(v^i_{n+1}\right)^y + \frac{\Delta t}{2}\left(\delta v^{i+1}_{n+1}\right)^y \tag{F.4}$$

Substituting Equations F.3 and F.4 into Equation F.2:

$$\begin{aligned} d^2 &= \left(x_n + \Delta t \left(v^i_{n+1}\right)^x + \frac{\Delta t}{2}\left(\delta v^{i+1}_{n+1}\right)^x - a\right)^2 \\ &\quad + \left(y_n + \Delta t \left(v^i_{n+1}\right)^y + \frac{\Delta t}{2}\left(\delta v^{i+1}_{n+1}\right)^y - b\right)^2 \end{aligned} \tag{F.5}$$

Examining the first set of terms in parenthesis:

$$\begin{aligned}\left(x_n+\Delta t\left(v_{n+1}^i\right)^x+\frac{\Delta t}{2}\left(\delta v_{n+1}^{i+1}\right)^x-a\right)^2 &= x_n^2+\left(\Delta t\left(v_{n+1}^i\right)^x\right)^2+\cancel{\left(\frac{\Delta t}{2}\left(\delta v_{n+1}^{i+1}\right)^x\right)^2}+a^2\\ &\quad +2x_n\Delta t\left(v_{n+1}^i\right)^x+x_n\Delta t\left(\delta v_{n+1}^{i+1}\right)^x-2x_na\\ &\quad +\Delta t^2\left(v_{n+1}^i\right)^x\left(\delta v_{n+1}^{i+1}\right)^x-2a\Delta t\left(v_{n+1}^i\right)^x\\ &\quad -a\Delta t\left(\delta v_{n+1}^{i+1}\right)^x \end{aligned} \tag{F.6}$$

Examining the second set of terms in parenthesis:

$$\begin{aligned}\left(y_n+\Delta t\left(v_{n+1}^i\right)^y+\frac{\Delta t}{2}\left(\delta v_{n+1}^{i+1}\right)^y-b\right)^2 &= y_n^2+\left(\Delta t\left(v_{n+1}^i\right)^y\right)^2+\cancel{\left(\frac{\Delta t}{2}\left(\delta v_{n+1}^{i+1}\right)^y\right)^2}+b^2\\ &\quad +2y_n\Delta t\left(v_{n+1}^i\right)^y+y_n\Delta t\left(\delta v_{n+1}^{i+1}\right)^y-2y_nb\\ &\quad +\Delta t^2\left(v_{n+1}^i\right)^y\left(\delta v_{n+1}^{i+1}\right)^y-2b\Delta t\left(v_{n+1}^i\right)^y\\ &\quad -b\Delta t\left(\delta v_{n+1}^{i+1}\right)^y \end{aligned} \tag{F.7}$$

Defining $\mathbf{Q}$ as a vector is known terms and $\mathbf{C}$ as a matrix of unknown terms [40]:

$$\begin{aligned}\mathbf{Q} &= x_n^2+\left(\Delta t\left(v_{n+1}^i\right)^x\right)^2+a^2+2x_n\Delta t\left(v_{n+1}^i\right)^x-2x_na-2a\Delta t\left(v_{n+1}^i\right)^x\\ &\quad +y_n^2+\left(\Delta t\left(v_{n+1}^i\right)^y\right)^2+b^2+2y_n\Delta t\left(v_{n+1}^i\right)^y-2y_nb-2b\Delta t\left(v_{n+1}^i\right)^y \end{aligned} \tag{F.8}$$

$$\mathbf{C}\underline{\delta\mathbf{v}}=\begin{bmatrix} x_n\Delta t+\Delta t^2\left(v_{n+1}^i\right)^x-a\Delta t \\ \\ y_n\Delta t+\Delta t^2\left(v_{n+1}^i\right)^y-b\Delta t \end{bmatrix}^{\mathrm{T}}\underline{\delta\mathbf{v}} \tag{F.9}$$

Following the penalty method as described by Liu and Quek [40], the penalty stiffness matrix and penalty force vector are defined as:

$$\mathbf{K_{pen}}=\mathbf{C}^{\mathrm{T}}\kappa\mathbf{C}\underline{\delta\mathbf{v}} \tag{F.10}$$

$$\mathbf{F_{pen}}=\mathbf{C}^{\mathrm{T}}\kappa\mathbf{Q} \tag{F.11}$$

where $\kappa>0$ is a user defined penalty factor.

References

[1] OpenCFD Ltd 2008, OpenFOAM user guide Version 1.5 Edition.

[2] "Bioelectronics Group, University of Glasgow". http://www.gla.ac.uk/schools/engineering/research/divisions/biomedical/advancedmedicaldiagnosticsloac/.

[3] "Bubbles". Retrived 06/08/2013 from https://sites.google.com/site/scienceshowsforschools2/fairyliquidandtheburstbubble.

[4] "Dripping Tap". Retrived 06/08/2013 from http://physics.stackexchange.com/questions/53516/satellite-droplets-in-a-breaking-liquid-jet.

[5] "Ripples on a pond". Retrieved 21/08/2013 from http://followingthevoicewithin.blogspot.co.uk/2011/12/pebbles.html.

[6] "CGAL, Computational Geometry Algorithms Library". http://www.cgal.org.

[7] "CUBIT". https://cubit.sandia.gov/.

[8] "Wasp on water". Retrived 06/08/2013 from http://www.tickld.com/images/content/48470.jpg.

[9] "Water Dripping". Still images taken from a video produced by The Itai Cohen Group, Cornell University, retrieved 12/12/2013 from http://cohengroup.lassp.cornell.edu/media.php?show=9.

[10] "Water droplets on leaf". Retrived 06/08/2013 from http://wallpaperdreams.com/background/114/water-droplet-cluster-on-leaf.html.

[11] D. Acheson. *Elementary Fluid Dynamics*. First edition. Oxford University Press (1990). ISBN 978-0-19-859679-0.

[12] M. Alghane, B. X. Chen, Y. Q. Fu, Y. Li, J. K. Luo & A. J. Walton. "Experimental and numerical investigation of acoustic streaming excited by using a surface acoustic wave device on a 128° YX-$LiNbO_3$ substrate". *Journal of Micromechanics and Microengineering*, 21(1):015005 (2011).

[13] Archimedes. "On Floating Bodies" (250BC).

[14] H. Askes, E. Kuhl & P. Steinmann. "An {ALE} formulation based on spatial and material settings of continuum mechanics. Part 2: Classification and applications". *Computer Methods in Applied Mechanics and Engineering*, 193(39âĂŞ41):4223 – 4245 (2004).

[15] I. Babuška. "The finite element method with Lagrangian multipliers". *Numerische Mathematik*, 20(3):179–192 (1973).

[16] G. Batchelor. *An Introduction to Fluid Dyanmics*. Cambridge University Press (1967).

[17] K.-J. Bathe & E. L. Wilson. *Numerical Methods in Finite Element Analysis*. Prentice-Hall (1976). ISBN 0-13-627190-1.

[18] Q. Bausiere. "CFD Microfluidic Development". Technical report, University of Glasgow (2013).

[19] T. Belytschko & J. Kennedy. "Computer models for subassembly simulation". *Nuclear Engineering and Design*, 49(1-2):17–38 (1978).

[20] T. Belytschko, W. K. Liu & B. Moran. *Nonlinear Finite Elements for Continua and Structures*. John Wiley & Sons (2000). ISBN 0-471-98774-3.

[21] J. Bonet & R. D. Wood. *Nonlinear Continuum Mechanics for Finite Element Analysis*. Cambridge University Press (1997). ISBN 0-521-57272-X.

[22] Y. Bourquin, J. Reboud, R. Wilson & J. M. Cooper. "Tuneable surface acoustic waves for fluid and particle manipulations on disposable chips". *Lab on a Chip*, 10:1898–1901 (2010).

[23] J. Brackbill, D. Kothe & C. Zemach. "A continuum method for modeling surface tension". *Journal of computational physics*, (100):335–354 (1992).

[24] F. Brezzi. "On the existence, uniqueness and approximation of saddle-point problems arising from Lagrangian multipliers". *ESAIM: Mathematical Modelling and Numerical Analysis - Modélisation Mathématique et Analyse Numérique*, 8(R2):129–151 (1974).

[25] F. Brezzi & J. Pitkäranta. "On the stabilisation of finite element approximations of the Stokes equations". *Efficient Solutions of Elliptic Systems, Notes on Numerical Fluid Mechanics*, 10:11–19 (1984).

[26] A. N. Brooks & T. J. Hughes. "Streamline upwind/Petrov-Galerkin formulations for convection dominated flows with particular emphasis on the incompressible Navier-Stokes equations". *Computer Methods in Applied Mechanics and Engineering*, 32(1-3):199–259 (1982).

[27] W. Dettmer & D. Peric. "A computational framework for free surface fluid flows accounting for surface tension". *Computer Methods in Applied Mechanics and Engineering*, 195(23-24):3038–3071 (2006).

[28] W. Dettmer, P. H. Saksono & D. Perić. "On a finite element formulation for incompressible Newtonian fluid flows on moving domains in the presence of surface tension". *Communications in Numerical Methods in Engineering*, 19(9):659–668 (2003).

[29] J. Donea & A. Huerta. *Finite Element Methods for Flow Problems*. John Wiley & Sons (2003). ISBN 9780471496663.

[30] J. Donea, A. Huerta, J.-P. Ponthot & A. Rodriguez-Ferran. "Arbitrary Lagrangian Eulerian Methods". *Computer Methods in Applied Mechanics and Engineering*, 193(45-47):4819–4836 (2004).

[31] C. A. Felippa. "Review of Continuum Mechanics". In "Nonlinear Finite Element Methods", chapter 7. Univeristy of Colorado at Boulder (2012).

[32] R. Franck & R. Lazarus. "Mixed Eulerian-Lagrangian method". *Methods in Computational Physics*, 3:47–67 (1964).

[33] C. Hirt, A. Amsden & J. Cook. "An Arbitrary Lagrangian Eulerian Computing Method for All Flow Speeds". *Journal of Computational Physics*, 14(3):227–253 (1974).

[34] T. J. Hughes, L. P. Franca & M. Balestra. "A New Finite Element Formulation for Computational Fluid Dynamics: V. Circumventing the Babuška-Brezzi Condition: a Stable Petrov-Galerkin Formulation of the Stokes Problem Accommodating Equal-Order Interpolations". *Computer Methods in Applied Mechanics and Engineering*, 59(1):85–99 (1986).

[35] E. A. Johannessen, L. Wang, L. Cui, T. B. Tang, M. Ahmadian, A. Astaras, S. W. J. Reid, P. S. Yam, A. F. Murray, B. W. Flynn, S. P. Beaumont, D. R. S. Cumming & J. M. Cooper. "Implementation of multichannel sensors for remote biomedical measurements

in a microsystems format". *IEEE transactions on bio-medical engineering*, 51(3):525–35 (2004).

[36] A. Kelly. *The Optimisation of Finite Element Meshes*. Ph.D. thesis, School of Engineering, University of Glasgow, Scotland (2014).

[37] P. Knupp, L. G. Margolin & M. Shashkov. "Reference Jacobian Optimization-based Rezone Strategies for Arbitrary Lagrangian Eulerian Methods". *Journal of Computational Physics*, 176(1):93–128 (2002).

[38] J. Leach, K. Wulff, G. Sinclair, P. Jordan, J. Courtial, L. Thomson, G. Gibson, K. Karunwi, J. Cooper, Z. J. Laczik & M. Padgett. "Interactive approach to optical tweezers control". *Applied optics*, 45(5):897–903 (2006).

[39] R. J. LeVeque & Z. Li. "Immersed Interface Methods for Stokes Flow with Elastic Boundaries or Surface Tension". *SIAM Journal on Scientific Computing*, 18(3):709–735 (1997).

[40] G. Liu & S. Quek. *The Finite Element Method: A Practical Course*. Butterworth-Heinemann (2003). ISBN 0-7506-5866 5.

[41] Y. J. Liu, X. Ding, S.-C. S. Lin, J. Shi, I.-K. Chiang & T. J. Huang. "Surface acoustic wave driven light shutters using polymer-dispersed liquid crystals". *Advanced materials (Deerfield Beach, Fla.)*, 23(14):1656–9 (2011).

[42] E. MacCurdy. *The notebooks of Leonardo da Vinci*, volume I and II. Reynal and Hitchcock (1938).

[43] X. Mao, J. R. Waldeisen & T. J. Huang. ""Microfluidic drifting"-implementing three-dimensional hydrodynamic focusing with a single-layer planar microfluidic device". *Lab on a chip*, 7(10):1260–2 (2007).

[44] MOAB. "Mesh-Oriented datABase". *http://trac.mcs.anl.gov/projects/ITAPS/wiki/MOAB*.

[45] S. L. Neale, C. Witte, Y. Bourquin, C. Kremer, A. Menachery, Y. Zhang, R. Wilson, J. Reboud & J. M. Cooper. "New optical, acoustic, and electrical diagnostics for the developing world" (2012).

[46] W. Noh. "CEL: A time-dependent two-space dimensional coupled Eulerian-Lagrangian code". *Methods in Computational Physics*, 3 (1964).

[47] E. Oñate, S. Idelsohn, F. Del Pin & R. Aubry. "The Particle Finite Element Method-An Overview". *International Journal of Computational Methods*, 1(2):267–307 (2004).

[48] E. Oñate, S. R. Idelsohn & C. A. Felippa. "Consistent pressure Laplacian stabilization for incompressible continua via higher-order finite calculus". *International Journal for Numerical Methods in Engineering*, 87(1-5):171–195 (2011).

[49] B. Pascal. "Experiences nouvelles touchant le vide (New Experiments with the Vacuum)" (1647).

[50] M. Pastor, M. Quecedo & O. Zienkiewicz. "A Mixed Displacement-Pressure Formulation for Numerical Analysis of Plastic Failure". *Computers & Structures*, 62(I):13–23 (1997).

[51] D. Perić & P. Saksono. "On finite element modelling of surface tension: variational formulation and applications". CIMNE: Barcelona (2001).

[52] C. Pozrikidis. *Introduction to Theoretical and Computational Fluid Dynamics*. First edition. Oxford University Press (1997). ISBN 0-19509320-8.

[53] L. Rayleigh. "On the Capillary Phenomena of Jets". *Proceedings of the Royal Society of London*, 29(196-199):71–97 (1879).

[54] J. Reboud, Y. Bourquin, R. Wilson, G. S. Pall, M. Jiwaji, A. R. Pitt, A. Graham, A. P. Waters & J. M. Cooper. "Shaping acoustic fields as a toolset for microfluidic manipulations in diagnostic technologies". *Proceedings of the National Academy of Sciences*, 109(38):15162–15167 (2012).

[55] J. Reboud, R. Wilson, Y. Bourquin, Y. Zhang, S. L. Neale & J. M. Cooper. "Phononic fluidics: acoustically activated droplet manipulations" (2011).

[56] P. Saksono. *On finite element modelling of surface tension phenomena*. Ph.D. thesis, Department of Civil Engineering, University of Swansea, Wales (2002).

[57] P. H. Saksono & D. Perić. "On Finite Element Modelling of Surface Tension Variational Formulation and Applications - Part I: Quasistatic Problems". *Computational Mechanics*, 38(3):265–281 (2005).

[58] P. H. Saksono & D. Perić. "On Finite Element Modelling of Surface Tension: Variational Formulation and Applications - Part II: Dynamic Problems". *Computational Mechanics*, 38(3):251–263 (2005).

[59] J. Shi, D. Ahmed, X. Mao, S.-C. S. Lin, A. Lawit & T. J. Huang. "Acoustic tweezers: patterning cells and microparticles using standing surface acoustic waves (SSAW)". *Lab on a chip*, 9(20):2890–5 (2009).

[60] S. Shiokawa, Y. Matsui & T. Ueda. "Liquid Streaming and Droplet Formation Caused by Leaky Rayleigh Waves". *Ultrasonics*, pages 643–646 (1989).

[61] A. Syred & Getty Images. "Red blood cells". Retrived 06/08/2013 from http://static.guim.co.uk/sys-images/Guardian/Archive/Search/2011/9/29/1317292397802/human-red-blood-cells-007.jpg.

[62] R. Tadmor. "Line energy and the relation between advancing, receding, and young contact angles." *Langmuir : the ACS journal of surfaces and colloids*, 20(18):7659–64 (2004).

[63] T. J. Tautges, R. Meyers, K. Merkley, C. Stimpson & C. Ernst. "MOAB: A Mesh-Oriented Database". SAND 2004-1592, Sandia National Laboratories (2004). Report.

[64] T. E. Tezduyar. "Stabilized Finite Element Formulations for Incompressible Flow Computations". *Advances in Applied Mechanics*, 28:1–44 (1992).

[65] N. Thürey, C. Wojtan, M. Gross & G. Turk. "A multiscale approach to mesh-based surface tension flows". *ACM Transactions on Graphics (SIGGRAPH 2010)*, 29(4):48:1–48:10 (2010).

[66] D. Tritton. *Physical Fluid Dynamics*. Second edition. Oxford University Press (1988). ISBN 0-19-854493-6.

[67] A. Truty. *On Certain Cases of Mixed and Stabilized Mixed Finite Element Formulations for Single and Two-Phase Geomaterials*. Ph.D. thesis, Cracow University of Technology (2004).

[68] C. Weatherburn. *Differential Geometry of Three Dimensions*, volume 1. Cambridge University Press (1927).

[69] D. Wlodkowic, S. Faley, M. Zagnoni, J. P. Wikswo & J. M. Cooper. "Microfluidic single-cell array cytometry for the analysis of tumor apoptosis". *Analytical chemistry*, 81(13):5517–23 (2009).

[70] T. Young. "An Essay on the Cohesion of Fluids". *Philosophical Transactions of the Royal Society of London*, 95:65–87 (1805).